Systematic Design of Multiport Antennas for MIMO-enabled Mobile Wireless Terminals

Von der Fakultät für Ingenieurwissenschaften,
Abteilung Elektrotechnik und Informationstechnik
der Universität Duisburg-Essen

zur Erlangung des akademischen Grades

Doktor der Ingenieurwissenschaften

genehmigte Dissertation

von

Aleksander Krewski
aus
Kiew, Ukraine

Datum der Einreichung:
06/03/2014

Tag der mündlichen Prüfung:
07/07/2014

Gutachter: Prof. Dr.-Ing. Klaus Solbach
Gutachter: Prof. Dr.-Ing. Werner L. Schroeder

To my beloved mother Antonina

Acknowledgements

The work leading to completion of this dissertation was carried out at RheinMain University of Applied Sciences (Rüsselsheim, Germany) as a part of the ADVANT (ADVanced ANTenna) project funded by Option N.V (Leuven, Belgium). The author would like to thank Dr. Jan Vercruysse from Option N.V. for his guidance and support.

Many thanks, first and foremost, go to the author's adviser Prof. Dr.-Ing. Werner L. Schroeder for his patience during many useful discussions which led to the completion of this dissertation. His experience and extensive knowledge were crucial in author's understanding of the research subject. With immense gratitude the author would also like to thank his supervisor Univ.-Prof. Dr.-Ing. Klaus Solbach for his insight and helpful guidance.

The author cannot find words to express his gratitude to his friends and colleagues especially Dr. Yifei Feng for countless discussions on mobile wireless communication related subjects and beyond. Mr. Oliver Strack and Mr. Ringo Helleis fabricated two prototypes shown in this dissertation for which the author is immensely grateful.

Contents

Chapter 1

Introduction

1.1. Motivation

Over the past twenty years commercial mobile wireless communication has been evolving extremely fast. The growth has been stimulated particularly by advancements in semiconductor technology. Customers demand combined with new technologies allowed miniaturization of mobile wireless devices. Design of antennas followed the same trend leading to significant changes in their design and integration with mobile wireless terminals. For instance whip antennas, used in early days of mobile communication, were superseded by planar inverted-F antennas (PIFAs) and inverted-F antennas (IFAs) around the end of the century. For the past decade these types of antennas, optimized so as to maximize bandwidth and total efficiency, were frequently exploited in commercial handsets. Initially, voice transmission and short messages were the only services provided by network operators. However, since introduction of the Internet in the early nineties the demand for data transmission has been increasing exponentially. In order to cope with this demand Multiple Input – Multiple Output (MIMO) techniques which allow to transmit and receive multiple independent signal streams were introduced. They have created a need for design of multiport antennas featuring high isolation between antenna ports at both ends of the wireless communication link in order for the system to achieve required performance. The main challenge remains design of multiport antennas for small MIMO-enabled mobile wireless devices. At present the major

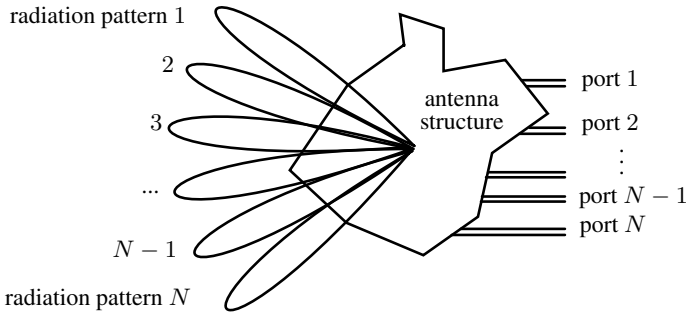

Fig. 1.1.: Schematic representation of an N-port antenna structure where N orthogonal radiation patterns ("beam patterns") are mapped to N output ports after [1].

issue is to fit these antennas into the same volume as available for single feed antennas without compromising the performance. At the same time the bandwidth requirements for multiport antennas for MIMO application in small mobile wireless devices are much tougher than for single feed antennas. In order not to repeat the same long evolution as that of single feed antennas it is necessary to examine first available literature in an attempt to find proper analytical tools suitable as a starting point in research and development of multiport antennas. The next section of the present chapter provides an outlook on the state of the art characterization and design techniques for multiport antennas. They have to be considered as a base for development of proper description and systematic design approach shown in the present dissertation. The approach allows, without trade-offs, to achieve high total per port efficiencies and high isolation between ports while covering desired frequency bands.

1.2. State of the Art

In order to address the problem of multiport antenna design for mobile wireless devices proper characterization of these antennas is required. Early work related to the subject of descriptive quantities for multiport antennas was conducted for antenna arrays. Comprehensive theory was given in [1]. The concepts of "beam patterns" and "beam-coupling factors" were introduced (see Fig. 1.1). Based on the power balance relation the general solution which relates the scattering matrix of a multiport antenna with reflectances corresponding to "beam patterns" was found. Four decades later in the series of

papers [2, 3, 4, 5] this theory was refreshed and new terminology, more appropriate to describe multiport antennas for MIMO application, was introduced. Since then various antenna designs for MIMO-enabled mobile wireless devices appeared in literature. *Modal analysis* based on the spectrum of *radiation matrix* [6] provides meaningful description of multiport antennas. At present it is important to understand the difference between multiport antennas considered in this dissertation and antenna arrays. In MIMO transmission it is typically assumed that the power distribution among ports is, on average, equal and signals applied to different ports are uncorrelated. In antenna arrays power, fed into a single port, distributed among array elements and phase of the signal are typically varied so as to achieve spatial scanning of a radiation pattern. Also spacing between elements of an antenna array is a subject of optimization in order to achieve the desired performance. In case of multiport antennas for MIMO application the size of a device chassis is constrained by the definition of the form factor. The number of *radiation modes* [7, 8] (eigenvectors of the *radiation matrix*) which can be exploited for design of multiport antenna diminishes rapidly with increasing mode index. Therefore, the "overall" radiation quality factor of a multiport antenna system is significantly influenced by the "weakest" *radiation mode* i.e. *radiation mode* with the highest radiation quality factor. These statements are in line, but not directly comparable, with an interpretation given in terms of *spherical modes* [9], where the "overall" radiation quality factor for multiport antennas was found to be an arithmetic average of radiation quality factors of the *spherical modes*. In this dissertation the above stated claims are shown to be valid using *the theory of characteristic modes for conducting bodies* [10]. *Characteristic modes* are solutions of a generalized eigenvalue problem, where the system matrix has physical interpretation of the impedance matrix. Real eigenvectors, referred to as eigencurrents, which exist on the surface of a conducting body without its presence, are called characteristic modes. Eigenvalues are associated with reactive energies of characteristic modes. Computation of characteristic modes does not require prior assumptions relative to antenna physical structure and port location. Electrical size of an arbitrarily shaped surface is sufficient in order to obtain the solution which leads to an antenna design concept and allows to draw fundamental conclusions on the performance of an antenna design in terms of radiation quality factor before an actual design is produced. The results bring about a realization that chassis of a mobile wireless device is the main *radiator* and only a small *coupler* capable of exciting a superposition of *characteristic modes* on the chassis is sufficient to complete an antenna design [11]. Comprehensive numerical investigations of which characteristic

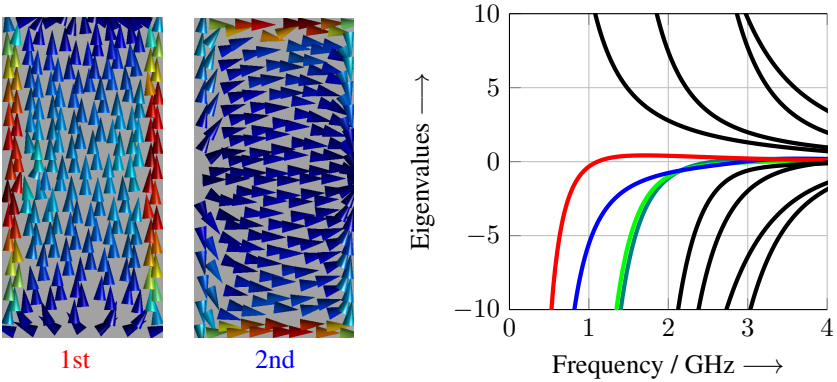

Fig. 1.2.: Characteristic modes on $60 \times 120\ \mathrm{mm}^2$ smartphone chassis. Surface current densities of the 1st and the 2nd characteristic modes at 850 MHz (left) and eigenvalues of the first few characteristic modes (right). The first four capacitive characteristic modes are given by color curves.

modes can be excited on a chassis of a bar-type and clamshell mobile phones, so as to devise a concept for multiport antenna design, were given in [12, 13] (e.g. see Fig. 1.2). Inspection of eigenvalues of the smartphone chassis with small volume for antenna placement revealed that the number of characteristic modes which can be effectively excited at frequencies below 1 GHz is constrained by the aspect ratio of the chassis to only the 1st characteristic mode (smallest magnitude of eigenvalue, see Fig. 1.2). The 2nd characteristic mode already features a substantially larger eigenvalue which indicates that more electromagnetic energy is stored in the near-field than in case of the 1st characteristic modes. In general, the higher the frequency the more characteristic modes with low magnitude eigenvalues are available thus rendering the design of multiport antennas feasible assuming these characteristic modes or alternatively some orthogonal superpositions of these modes can be independently excited. This statement applies if chassis of a device is not significantly modified. Interesting work, where a 4-port MIMO antenna for Wireless Local Area Network (WLAN) 2.4 GHz frequency band was designed, was presented in a series of publications [14, 15, 16, 17, 18]. Four *capacitive couplers* located in four corners of the mobile phone chassis excite superpositions of the first four *capacitive characteristic modes*. Additional fairly complex circuitry is required to map characteristic modes to output ports of the antenna system. This design aspect brings about an illustration of the relation between *characteristic*

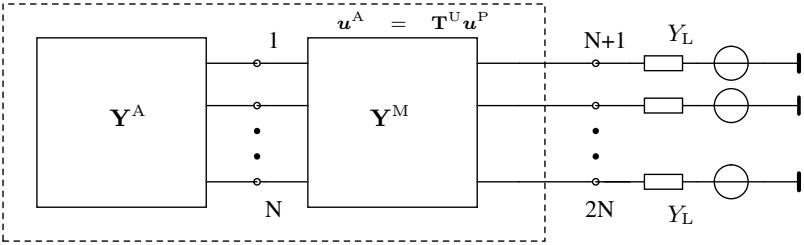

Fig. 1.3.: Simplified schematic representation of an N-port antenna matching problem as given in [28]. $\mathbf{Y}^{\mathrm{A}}$ and $\mathbf{Y}^{\mathrm{M}}$ denote admittance matrix of an antenna and a matching network, respectively. Voltages at the reference plane between the antenna and matching network $\boldsymbol{u}^{\mathrm{A}}$ are related to the voltages at the output port of the cascade $\boldsymbol{u}^{\mathrm{P}}$ are given by voltage transfer function $\mathbf{T}^{\mathrm{U}}$.

modes and *radiation modes*. More recently use of *inductive couplers* to excite *capacitive characteristic modes* was proposed [19, 20, 21, 22]. Eight coupling elements, located around the edges of the chassis, are used to excite three capacitive characteristic modes. The feeding network is simple since each set of couplers is excited independent from the others. All three feeding networks are buried in a thick multilayer chassis. Also this design is dedicated to WLAN 2.4 GHz frequency band. If chassis of a device can be modified to an extent which allows to significantly change intrinsic resonance frequencies of some characteristic modes then, assuming these modified characteristic modes can be effectively excited, a design of multiport antenna for frequency bands below 1 GHz is feasible. Proposed techniques for smartphone chassis modification include adding bezel ring or strips along the chassis. Possible realizations of 2-port MIMO antennas for smartphones exploiting these design techniques were shown in [23, 24]. All above recalled designs based on characteristic chassis modes require some type of feeding network which should allow for the maximum power transfer from sources to couplers. Theoretical treatment of the problem of multiport antenna matching, at a fundamental level, was given in [25, 26], where different types of match were investigated. It was found that the optimum match, called multiport match, is achieved when the scattering matrix approximately vanishes about the desired frequency. Similar work, with respect to generality and results, was reported in [27]. However, practical realization of the multiport match has proven to be difficult. The technique, for synthesizing a single $2N$-port matching network, was given in [28, 29] (see Fig. 1.3). For lossless antennas it gives explicitly an admittance matrix of a

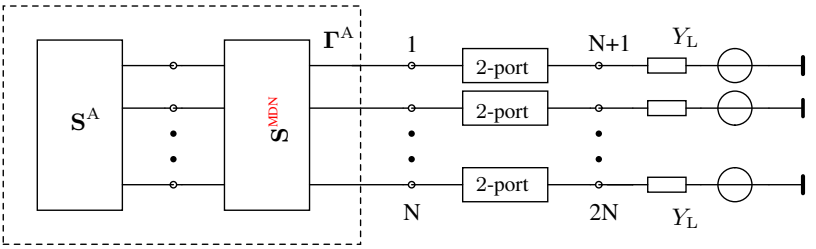

Fig. 1.4.: Modified Youla approach after [32] as used in e.g. [31, 33] and [17, 18]. $\mathbf{S}^{\mathrm{A}}$ and $\mathbf{S}^{\mathrm{MDN}}$ denote scattering matrix of an antenna and an MDN, respectively.

matching network by calculating the voltage transfer function using Cholesky decomposition of the conductance matrix of an antenna. The approach is applicable to lossy antennas and realistic matching networks which are also lossy. The output ports are matched to the same load impedances and at each of the ports a particular linear superposition of *radiation modes* is seen. Thus, the "overall" bandwidth is constrained by a *radiation mode* featuring the highest radiation quality factor. The "overall" bandwidth of a multiport antenna has to be defined via a single descriptive quantity analogous to reflectance for single port antenna. This quantity must take into account both per port Return Loss (RL) and isolation between ports simultaneously. Absence of such descriptive quantity, which allows to distinguish two different antenna designs in terms of the "overall" bandwidth, results in ambiguous matching requirements. Typically, such requirements are expressed in terms of higher per port RL and lower isolation or *vice versa*. A quantity which shows how well multiport antenna is match was originally introduced in [30] for antenna arrays. It is called Active Reflection Coefficient (ARC). Also the scattering matrix of a network capable of mapping *radiation modes* to external ports, as used in [31], was derived in [30]. Use of this network allows to exploit individual *modal bandwidths* of a multiport antenna which is advantageous as compared to use of a network after [28] only. A design technique exploiting network for mapping *radiation modes* to external ports was presented in [32] and later simplified in [31, 33] (see Fig. 1.4). The approach is based on the theory after [1, 3] which indicated that matching and mapping of *radiation modes* can be performed separately using two different networks. Mapping of *radiation modes* to external ports, referred to, in the present dissertation, as mode decomposition is performed without change of the impedance level. The complete network which

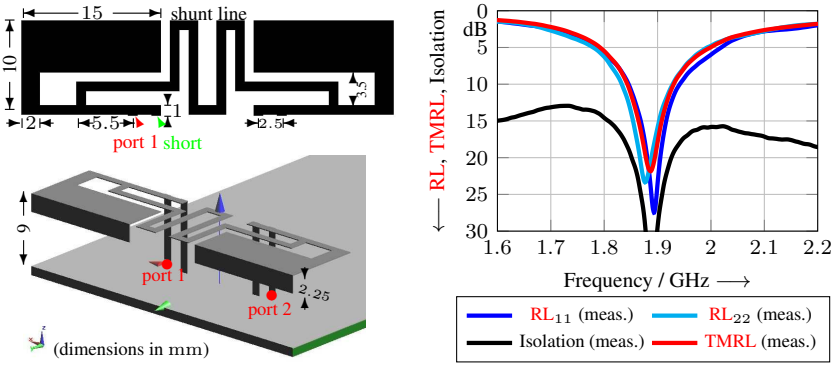

Fig. 1.5.: Measured per port RL, isolation and TMRL [38] for a geometrically symmetric 2-port MIMO antenna exploiting "connecting line" after [39].

realizes both multiport match and mode decomposition for an N-port antenna comprises $2N$-port Mode Decomposition Network (MDN), featuring hybrids with a particular phase shift and power division, and N 2-port matching networks. This approach of matching and mode decomposition was used to map characteristic modes to output ports of the 4-port MIMO antenna after [18]. It is well-motivated and systematic, but practical implications of the design were not addressed. Further investigations of the subject were presented in [34]. The approach employes Givens rotations of the real and the imaginary parts of antenna impedance matrix. It is systematic and allows to obtain multiport match using fairly complex network.

In this dissertation it is shown that if chassis of a device features high aspect ratio relative to wavelength then advantage from excitation of characteristic modes can be drawn for a single superposition of characteristic modes only. For this reason, some other techniques for design of 2-port MIMO antennas have been sought. Most notably, so-called "connecting lines" have been used [35]. The approach was taken up again in [36] where physical explanation of how high isolation between ports is achieved was given based on observations of the surface currents on an example of a 2-port antenna arrangement comprising two co-linear dipoles and a "connecting line". A number of other designs which exploit this realization of multiport match have been spawned over the past few years (see e.g. Fig. 1.5), including a design covering frequency bands below 1 GHz reported in [37]. This design technique has also been patented [40, 41, 42, 43]. Antennas exploiting "connecting line" are fixed-

frequency and feature the same per port RL. Extension toward multi-band operation and electrical switching is not straightforward. An other proposed technique is use of filters in order to isolate antenna ports. Two basic realizations are known in the literature. Use of slots in chassis of a mobile wireless device was proposed in [44], [45]. In practice, application of this design method is limited only to higher than 1 GHz frequency bands. The method requires introduction of significant changes to a chassis (introdction of slots in the middle of a chassis) which renders the approach not practical for use in commercial mobile wireless devices. Direct use of band stop filters in the physical structure of antenna elements was proposed in [46]. Due to the worst possible placement of antenna elements on the opposite short sides of a chassis reported isolation between antenna ports is high but "overall" bandwidth is extremely narrow and the total per port efficiencies are very low. However, rapid increase of the number of frequency bands to cover led to realization that fixed-frequency multiport antennas featuring the same per port RL (e.g. designs exploiting "connecting line") are insufficient for mobile wireless devices. Moreover, in recent year the subject of detrimental influence of a user and operating environment of a device on the performance of antennas has been addressed. It was found that certain level of electrical reconfigurability can help to improve antenna performance to some extent. Therefore, electrically switchable and electrically tunable antennas, which in addition feature significantly different RL observed at both ports, have gained much interest from both academia and industry. Nevertheless, the number of designs pertinent to electrically tunable 2-port MIMO antennas for small mobile wireless devices covering frequency bands below 1 GHz is limited to [47, 48]. This design is a specific realization of a more general solution reported in [49] (see Fig. 1.6). It features monopole and dipole antennas placed on two opposite short edges of a smarthphone chassis. An electrically tunable antenna after [47] employes varactor diodes placed at the feed of a dipole. The fixed-frequency version of this design where both antennas were placed on the same edge of a chassis and used for Receiver (RX)-Transmitter (TX) isolation, as in [49], was shown in [50]. An other approach, where a magnetic dipole (loop antenna) and a monopole antennas placed at the same short edge of the chassis, was described in [51]. It was reported that the design can be extended toward electrical tuning by exploiting electrically tunable radio frequency (RF)-Micro Electro-Mechanical System (MEMS) capacitors.

In this dissertation special attention is given to design of 2-port antennas for MIMO-enabled devices which are plugged into host devices (e.g. laptops) such as datacards and Universal Serial Bus (USB) dongles. These devices re-

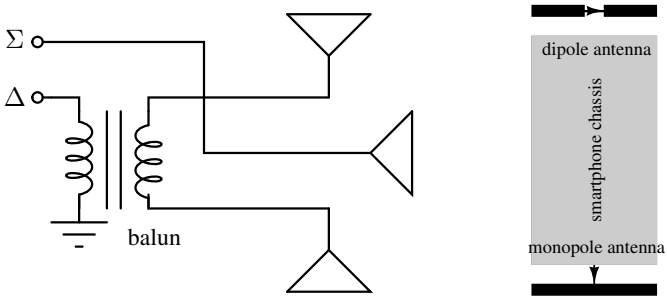

Fig. 1.6.: State of the art 2-port MIMO antenna after [49] (left) and realization on a smartphone chassis as given in [47, 52] (right).

quire specific antenna design considerations since an antenna can be placed on one short edge of a device only. Furthermore, given an "extremely" small size of these devices (much smaller than that of modern smartphones) covering frequency bands below 1 GHz is problematic even if an advantage from an electrically large chassis of a host device, to improve antenna performance, can be drawn. Designs, reported so far in literature, have tried to address these challenges [53, 54, 55]. However, all of them cover only a single frequency band and their performance in terms of "overall" bandwidth and total per port efficiencies is found to be insufficient. More recently, a design featuring relatively high total per port efficiencies for larger chassis of a USB dongle was reported [56]. However, all above described designs feature the same per port RL just like designs exploiting a "connecting line". They are much more suitable for covering frequency bands above 2 GHz. Design of internal multiport antennas for laptops is also considered in the present dissertation. State of the art single feed antennas usually cover only WLAN and Bluetooth frequency bands. The form factor and typical operating scenario suggest that the best possible location for an antenna is at the top of the lid [57] and [58]. However, in recent years a new design trend emerged where plastic enclosures of the laptops were superseded by aluminium shells hence the term monocoque laptop was coined. The solutions for this type of laptops involve placing antennas for WLAN and Bluetooth frequency bands behind designer's logo as in [59] or mounting them on the frame of optical drive [60]. In both of these solutions antennas are likely to feature narrow bandwidth, since more electromagnetic energy is stored in the near-field of the cavity rather than is being radiated, and low total efficiency at WLAN and Bluetooth frequency bands. With high

number of frequency bands required to be covered by the Long Term Evolution (LTE) standard the above described designs may be insufficient, especially if their extension to design multiport antennas is considered.

1.3. Overview of the Dissertation

Beginning from an overview of the state of the art in characterization of multiport antennas and available design techniques it becomes clear that understanding of existing descriptive quantities and conception of new systematic design method remain of high practical interest. Design procedures based on the *theory of characteristic chassis modes* and *modal analysis*, which uses the spectrum of the *radiation matrix*, are employed in this dissertation. Using *characteristic modes* it is established that higher order *radiation modes*, which feature high radiation quality factors, significantly limit the useful "overall" bandwidth of the antenna system. To exploit *modal bandwidths* of the higher order *radiation modes* the DL-MIMO concept, where subsets of *radiation modes* are assigned to different portions of a frequency band, is introduced. Systematic design of feeding network so as to realize the above described concept is proposed. Further, it is shown that in many cases exploitation of *modal bandwidths* alone may be still insufficient to cover desired frequency bands. In order to cover multiple frequency bands multiport antennas must then employ electrical switching and electrical tuning as an integral part of their design. Nevertheless, it is important to remember that the design of the radiating structure itself still remains the key aspect to be solved to achieve high total per port efficiencies of an antenna system. In order to devise systematic design techniques the present dissertation focuses on multiport antennas for extremely small mobile wireless terminals which are used in a nearly stationary operating environment featuring negligible user interaction, i.e. USB dongles and their host devices (laptops). An other important aspect covered in the present dissertation is the choice of proper semiconductor components and their integration with an antenna which in turn allows realization of a low-loss electrical switching and electrical tuning of multiport antennas.

The main result of this dissertation is systematic design technique which, with aid of *modal analysis*, allows to design multiport antennas and circuitry for variety of MIMO-enabled mobile wireless devices from laptops to small USB dongles. The procedure follows from systematic construction of the desired *radiation modes* from orthogonal subsets of *characteristic modes*. It is based on

the relation between *radiation modes* and *characteristic modes*. For laptops a concept which allows to systematically design, in principle, an N-port MIMO antenna by exciting *characteristic chassis modes* using extremely small couplers is devised. The design procedure is verified by measurements of prototype of a multi-band 2-port MIMO antenna for 13" laptop. An other systematic procedure is shown to aid design of a small 2-port DL-MIMO antenna for USB dongles. An optimum antenna physical structure is found so as to maximize attainable modal bandwidths and modal efficiencies given small volume for antenna placement. In order for an antenna to cover multiple frequency bands while maintaining high total efficiency a concept of separation coarse electrical switching from fine electrical tuning is developed. Electrical switching is applied in the antenna physical structure so as to, at least approximately, cover the desired frequency bands. Electrical tuning, to exactly cover the desired frequency bands, can then be performed using a separate module located on the chassis of a device. The tuning module shown in the present dissertation allows to map *radiation modes* to external ports while providing independent electrical tuning of both *radiation modes* to the required extent. The merit of the established design procedure and achieved high total per port efficiencies are confirmed by measurements of two antenna prototypes for small MIMO-enabled USB dongle.

Chapter 2

Radiation Modes of Multiport Antennas

In the present chapter, beginning from recalling well-known quantitative description of single port antennas, the general characterization for multiport antennas is given. A set of quantities capable of describing multiport antennas for MIMO application cannot consider input ports of the antenna system separately but has to take into account also mutual relations between all pairs of ports. Further, characterization of multiport antennas using e.g. scattering matrix is by itself meaningless and, as was indicated in [61], only the invariant properties of the matrix description are of interest. Subsequently, *modal analysis* of multiport antennas, based on the spectrum of *radiation matrix* [6], after [1, 3, 5] is introduced. *Modal analysis* is a logical generalization of a single port antenna description to multiport antennas. Detailed overview of modal descriptive quantities and discussion of their usefulness to characterize multiport antennas is provided. Moreover, it is recognized that if the *radiation modes* [7, 8] are not mapped to the external ports of the N-port antenna then a unique definition of the "overall" bandwidth for such antenna system can be given [38]. The quantity takes into account the complete spectrum of the scattering matrix.

2.1. Single Port Antenna Description

A convenient starting point, before discussing proper characterization of multiport antennas, is the description of single port antennas. Single port linearly polarized antennas for mobile wireless devices are characterized often by only two quantities: complex reflection coefficient $|s_{11}|$ (equivalently Return Loss (RL) or Voltage Standing Wave Ratio (VSWR)) and total efficiency η_{tot}. The magnitude of the complex reflection coefficient $|s_{11}|$ uniquely describes relation between power reflected at the antenna feed and incident power at the feed, which is equal to the available power of the source, (see Fig. 2.5a)

$$P_{\text{refl}} = |s_{11}|^2 P_{\text{av}}. \tag{2.1}$$

where the complex reflection coefficient s_{11} is defined, using the antenna impedance Z and the load impedance Z_{L}, as

$$s_{11} = \frac{Z - Z_{\text{L}}}{Z + Z_{\text{L}}}. \tag{2.2}$$

For the typical real load impedance $Z_{\text{L}} = 50\ \Omega$ the magnitude of reflection coefficient is ideally zero when $Z = Z_{\text{L}}$ (match) and one when $Z = 0$ (short) or $Z = \infty$ (open). In general $|s_{11}| \in [0, 1]$. Often, the complementary quantities called Return Loss (RL) and Voltage Standing Wave Ratio (VSWR) both of which take only positive values are used in practice

$$\text{RL} = -20 \log_{10} |s_{11}|, \quad \text{where} \quad \text{RL} \in [0, \infty) \tag{2.3}$$

$$\text{VSWR} = \frac{1 + |s_{11}|}{1 - |s_{11}|}, \quad \text{where} \quad \text{VSWR} \in [1, \infty). \tag{2.4}$$

The magnitude of the reflection coefficient is related to the total efficiency, which is the ratio of radiated power to the input power, via

$$\eta_{\text{tot}} = \eta_{\text{rad}} \eta_{\text{m}} = \eta_{\text{rad}} (1 - |s_{11}|^2), \tag{2.5}$$

where η_{rad} and η_{m} are the radiation efficiency and the matching efficiency of an antenna, respectively. Therefore, the $|s_{11}|$, RL, VSWR and η_{tot} are a basic quantities for comparison of different single port antenna designs. The bandwidth is, from a practical point of view, related to either of the above quantities. The characterization is completed by the magnitude of the radiation pattern.

Analogous considerations, as the above for a single port antennas, are carried out for multiport antennas in order to characterize them using meaningful descriptive quantities in section 2.2.

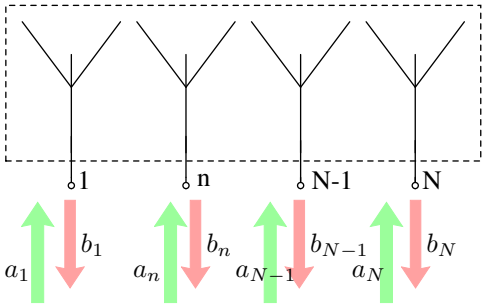

Fig. 2.1.: Illustration of an input and output wave quantities for a N-port antenna system.

2.2. Introduction to *Radiation Modes* of Multiport Antennas

2.2.1. Compound pattern

Consider an N-port antenna system as shown conceptually in Fig. 2.1. In the receive mode of operation an incident electromagnetic wave described by its electric field $\boldsymbol{E}_{\text{inc}}(\Omega) = (E_{\text{inc},\vartheta}(\Omega), E_{\text{inc},\varphi}(\Omega))^{\top}$, where $\Omega = (\vartheta, \varphi)$ is its Angle of Arrival (AoA) and $(\cdot)^{\top}$ denotes transpose, generates at the antenna feed ports a vector of outgoing wave quantities $\boldsymbol{b}(\Omega) = (b_1(\Omega), b_2(\Omega), ..., b_N(\Omega))^{\top}$ traveling toward the load impedances. Formally, this is given by [3]

$$\boldsymbol{b}(\Omega) = \frac{\lambda_0}{\sqrt{4\pi\eta_0}} \mathbf{T}(\Omega) \boldsymbol{E}_{\text{inc}}(\Omega), \tag{2.6}$$

where elements of $\boldsymbol{b}(\Omega)$ are given by $b_n = \frac{u_n - Z_{\text{L}} i_n}{2\sqrt{Z_{\text{L}}}}$ with equal load impedances i.e. $Z_{\text{L},1} = \cdots = Z_{\text{L},N} = Z_{\text{L}}$. i_n and u_n are current and voltage observed at n-th port, respectively. λ_0 denotes wavelength in free space and η_0 the wave impedance of the free space. All angles, field amplitudes and phases are referenced to a unique origin of the coordinate system. The definition assumes, in agreement with measurement practice, that each port is terminated with the reference impedance (e.g. 50 Ω). The function that fully describes the relation between $\boldsymbol{b}(\Omega)$ and $\boldsymbol{E}_{\text{inc}}(\Omega)$, given by (2.6), is the $N \times 2$ complex

matrix function known as *compound pattern*

$$\mathbf{T}(\Omega) = \begin{pmatrix} T_{\vartheta,1}(\Omega) & T_{\varphi,1}(\Omega) \\ T_{\vartheta,2}(\Omega) & T_{\varphi,2}(\Omega) \\ \vdots & \vdots \\ T_{\vartheta,N}(\Omega) & T_{\varphi,N}(\Omega) \end{pmatrix}. \tag{2.7}$$

The n-th row of $\mathbf{T}(\Omega)$ contains radiation pattern relative to n-th feed port. The first and the second column corresponds to the ϑ and φ polarized components of the radiation pattern, respectively. Therefore, relative phases and amplitudes between antenna ports and full polarimetric response is retained in $\mathbf{T}(\Omega)$. It is important to note that $\mathbf{T}(\Omega)$ is fixed by definition (2.6) where terminations at all ports are equal i.e. $Z_\mathrm{L} = 50\ \Omega$. Measurements with other terminations may lead to different radiation patterns. The compound pattern is dimensionless. For a single port antenna ($N = 1$), single polarization and co-polarized incident electric field $\boldsymbol{E}_\mathrm{inc}(\Omega)$ the definition (2.6) is related to the conventional gain pattern by

$$G(\Omega) = |T(\Omega)|^2. \tag{2.8}$$

2.2.2. Radiation matrix

To write the corresponding to (2.6) expression for the transmit mode operation, assume that the antenna is fed by a vector of incoming wave quantities $\boldsymbol{a} = (a_1, a_2, ..., a_N)^\top$. The electric field vector $\boldsymbol{E}_\mathrm{rad}(\Omega, r) = (E_{\mathrm{rad},\vartheta}(\Omega, r), E_{\mathrm{rad},\varphi}(\Omega, r))^\top$ of the antenna into direction $\Omega = (\vartheta, \varphi)$ and observed at distance r from the origin of the coordinate system is given by [3]

$$\boldsymbol{E}_\mathrm{rad}(\Omega, r) = \mathrm{j}\sqrt{\frac{\eta_0}{4\pi}}\frac{\mathrm{e}^{-\mathrm{j}k_0 r}}{r}\mathbf{T}(\Omega)^\top \boldsymbol{a}, \tag{2.9}$$

where k_0 is the propagation constant in free space. The total power radiated by the antenna is given by

$$P_\mathrm{rad} = \frac{1}{2\eta_0}\oiint_\Omega |\boldsymbol{E}_\mathrm{rad}(\Omega, r)|^2 r^2 \mathrm{d}\Omega, \tag{2.10}$$

with $\mathrm{d}\Omega = \sin\vartheta \mathrm{d}\vartheta\mathrm{d}\varphi$. Substitution of (2.9) into (2.10) leads to the following expression on the total radiated power

$$P_\mathrm{rad} = \frac{1}{2}\boldsymbol{a}^\dagger \mathbf{R}\boldsymbol{a}, \tag{2.11}$$

where $N \times N$ Hermitian matrix $\mathbf{R}$ is referred to as *radiation matrix* [6] and $(\cdot)^\dagger$ denotes Hermitian transpose. The *radiation matrix* is given by

$$\mathbf{R} = \frac{1}{4\pi} \oiint_{\Omega} \mathbf{T}(\Omega)^* \mathbf{T}(\Omega)^\top \mathrm{d}\Omega, \tag{2.12}$$

where $(\cdot)^*$ denotes complex conjugate. The *radiation matrix* describes radiation pattern overlap and efficiency. The diagonal elements are per port efficiencies

$$\eta_n^{\mathrm{port}} = R_{nn}. \tag{2.13}$$

The off-diagonal elements of $\mathbf{R}$ are overlap integrals between the radiation patterns related to mth and nth feed ports and obtained therefrom as

$$\rho_{mn} = \frac{R_{mn}}{\sqrt{R_{mm} R_{nn}}}. \tag{2.14}$$

ρ_{mn} is called *radiation pattern overlap*. For a statistically isotropic propagation environment with Rayleigh fading and zero mean complex Gaussian random process of the channel matrix elements the following relation between the radiation pattern overlap and the Power Envelope Correlation Coeffient (PECC) holds [62]

$$\rho_{mn}^{\mathrm{P}} = |\rho_{mn}|^2, \tag{2.15}$$

where ρ_{mn}^{P} is usually given in data sheets due to its smaller value as compared to radiation pattern overlap. It is also simpler to measure and has its merits for multiport antennas exploiting diversity. A more detailed discussion about radiation pattern overlap is given in section 2.5 of the present chapter.

2.2.3. Relation between radiation matrix and scattering matrix

The purpose of the present subsection is to show the derivation and importance of the power balance relation for a lossy multiport antennas. Refer to Fig. 2.1. The available power $\frac{1}{2}\boldsymbol{a}^\dagger \boldsymbol{a}$ is equal to the sum of the radiated power, P_{rad}, and the dissipated power, P_{diss} in the antenna and the reflected power $\frac{1}{2}\boldsymbol{b}^\dagger \boldsymbol{b}$. Formally, this is described by [63, 64, 65]

$$P_{\mathrm{rad}} = \frac{1}{2}\boldsymbol{a}^\dagger \boldsymbol{a} - \frac{1}{2}\boldsymbol{b}^\dagger \boldsymbol{b} - P_{\mathrm{diss}}. \tag{2.16}$$

The radiated power, after (2.11), is given by

$$P_{\mathrm{rad}} = \frac{1}{2}\boldsymbol{a}^{\dagger}\mathbf{R}\boldsymbol{a}. \tag{2.17}$$

The vector of incoming wave quantities $\boldsymbol{a}$ and the vector of outgoing wave quantities $\boldsymbol{b}$ are related via the scattering matrix $\mathbf{S}$ of an antenna

$$\boldsymbol{b} = \mathbf{S}\boldsymbol{a}. \tag{2.18}$$

Substitution of (2.17) and (2.18) into (2.16) yields

$$\frac{1}{2}\boldsymbol{a}^{\dagger}\mathbf{R}\boldsymbol{a} = \frac{1}{2}\boldsymbol{a}^{\dagger}\boldsymbol{a} - \frac{1}{2}\boldsymbol{a}^{\dagger}\mathbf{S}^{\dagger}\mathbf{S}\boldsymbol{a} - P_{\mathrm{diss}}. \tag{2.19}$$

Assuming that $P_{\mathrm{diss}} = \frac{1}{2}\boldsymbol{a}^{\dagger}\mathbf{D}\boldsymbol{a}$, where $\mathbf{D}$ is a real symmetric matrix, referred to as the *dissipation matrix*, contains loss coefficients of the multiport antenna system the power balance relations can be written in the matrix form as

$$\mathbf{R} = \mathbf{I} - \mathbf{S}^{\dagger}\mathbf{S} - \mathbf{D}, \tag{2.20}$$

The power balance relation (2.20) is of particular interest for lossless multiport antennas in which case $\mathbf{D} = \mathbf{0}$. It allows to express radiation pattern overlap in terms of S-parameters as was frequently shown in the literature e.g. [65]. Moreover, if the antenna is not only lossless but also ideally matched, i.e. $\mathbf{S} = \mathbf{0}$, then the *radiation matrix* must coincide with the identity matrix, i.e. $\mathbf{R} = \mathbf{I}$. The per port efficiencies are all equal to unity and the radiation pattern overlap after (2.14) between each pair of ports equals zero.

2.3. *Radiation Mode* Based Descriptive Quantities for Multiport Antennas

2.3.1. Modal efficiencies

In the Closed-loop Spatial Multiplexing (CL-SM) mode of operation the evolved Node-B (eNB)'s precoder and the User Equipment (UE)'s MIMO detector via exchange of Channel State Information (CSI) jointly attempt to diagonalize the channel matrix. This amounts to applying unitary transforms to the channel matrix. The only properties of the channel matrix which survive

the unitary transformation are the invariant properties of the *radiation matrix*, i.e. its eigenvalues and eigenvectors. Since *radiation matrix* is Hermitian there is a unique unitary matrix $\mathbf{V}$ such that it diagonalizes *radiation matrix* [1, 3]

$$\mathbf{C} = \mathbf{diag}(\eta_1, \ldots, \eta_N) = \mathbf{V}^\dagger \mathbf{R} \mathbf{V}. \tag{2.21}$$

The columns of $\mathbf{V}$, i.e. the eigenvectors $\boldsymbol{V}_n$ of $\mathbf{R}$, are called *radiation modes* [7, 8]. The elements of the diagonal matrix $\mathbf{C}$ (*modal efficiency matrix*) are the *modal efficiencies* $\eta_1, ..., \eta_N$. The far-field radiation patterns associated with different *radiation modes* are mutually orthogonal because the eigenvectors of the matrix $\mathbf{V}$ are orthogonal. The power radiated by the nth *radiation mode* is given by

$$P_{\mathrm{rad},n} = \frac{1}{2} a^\dagger \boldsymbol{V}_n^\dagger \mathbf{R} \boldsymbol{V}_n a = \frac{1}{2} \eta_n |a|^2, \tag{2.22}$$

where η_n is the efficiency of the nth *radiation mode* and $a = |\boldsymbol{a}|$ is the magnitude of the vector $\boldsymbol{a}$ which describes incoming modal wave quantities.

2.3.2. Modal reflectances

The definition of *modal reflectances* is analogous as that of the reflection coefficient of a single port antenna but using incoming and outgoing *modal wave quantities*. Without knowing *a priori* the vector of incoming wave quantities necessary to excite the *radiation mode* of interest direct measurement of *modal reflectances* is not feasible. For this reason the relation between the scattering matrix of the antenna system and *modal reflectances* is of interest. *Modal reflectances* are the generalization of the reflection coefficient s_{11}, for a single feed antenna, to multiport antennas. Further for completeness of the argument, the relation between *modal efficiencies* and *modal reflectances* for a lossless antenna system, analogous to (2.5) for a lossless single feed antenna, is shown.

The power balance relation for lossless multiport antennas (i.e. for $\mathbf{D} = \mathbf{0}$) was explored in [31], [66]. In case of lossless multiport antennas the power balance relation takes the form

$$\mathbf{R} = \mathbf{I} - \mathbf{S}^\dagger \mathbf{S} \quad (\text{if} \quad \text{lossless}), \tag{2.23}$$

The scattering matrix of a reciprocal antenna is complex symmetric, i.e. $\mathbf{S} = \mathbf{S}^\top$. Obviously, then

$$\mathbf{C} = \mathbf{V}^\dagger (\mathbf{I} - \mathbf{S}^* \mathbf{S}) \mathbf{V} = \mathbf{I} - \mathbf{V}^\dagger \mathbf{S}^* \mathbf{S} \mathbf{V}. \tag{2.24}$$

Further, if, in addition, the eigenvalues of $\mathbf{S}^*\mathbf{S}$ are, at this point of considerations, distinct [67] and

$$\mathbf{S}^*\mathbf{S} = \mathbf{V}\mathbf{\Sigma}^2\mathbf{V}^\dagger \tag{2.25}$$

is a diagonalization of $\mathbf{S}^*\mathbf{S}$, then there exists a diagonal matrix

$$\mathbf{\Theta} = \mathbf{diag}(\mathrm{e}^{\mathrm{j}\,\theta_1}, \mathrm{e}^{\mathrm{j}\,\theta_2}, ..., \mathrm{e}^{\mathrm{j}\,\theta_N}) \quad \theta_\mathrm{j} \in \mathbb{R} \tag{2.26}$$

such that

$$\mathbf{S} = \mathbf{U}^*\mathbf{\Sigma}\mathbf{U}^\dagger \quad \text{with} \quad \mathbf{U}^* = \mathbf{V}^*\mathbf{\Theta}. \tag{2.27}$$

Note, that the matrix $\mathbf{V}$ in this section is the same matrix $\mathbf{V}$ as in (2.21). Moreover, the specific case of non-distinct modal efficiencies was discussed in [31]. However, it was found that in practice even then the unique matrix $\mathbf{V}$ can be associated with the decomposition (2.21) if the antenna system features multiport symmetry. As an illustrative example consider a square plate with two symmetrically placed capacitive couplers. Two radiation modes appear to be non-distinct. However, if degeneracy occurs it can be mend by selection of proper eigenvectors from the respective subspace. The decomposition $\mathbf{S} = \mathbf{U}^*\mathbf{\Sigma}\mathbf{U}^\dagger$ is known as Takagi factorization [67]. It is a special case of singular value decomposition $\mathbf{S} = \mathbf{W}\mathbf{\Sigma}\mathbf{U}^\dagger$ with $\mathbf{W} = \mathbf{U}^*$ and applicable also to singular matrices. Relation (2.27) leads to

$$\mathbf{S} = \mathbf{V}^*(\mathbf{\Theta}\mathbf{\Sigma}\mathbf{\Theta}^\top)\mathbf{V}^\dagger = \mathbf{V}^*\mathbf{\Gamma}\mathbf{V}^\dagger, \tag{2.28}$$

where

$$\mathbf{\Gamma} = \mathbf{\Theta}^2\mathbf{\Sigma} \tag{2.29}$$

is the diagonal matrix with complex values. If (2.28) is multiplied from the right by the matrix $\mathbf{V}$ then $\mathbf{S}\mathbf{V} = \mathbf{V}^*\mathbf{\Sigma}\mathbf{\Theta}^2 = \mathbf{V}^*\mathbf{\Gamma}$, which gives

$$\mathbf{\Gamma} = \mathbf{V}^\top\mathbf{S}\mathbf{V}. \tag{2.30}$$

$\mathbf{\Gamma}$ is a diagonal matrix with complex entries $\mathbf{\Gamma} = \mathbf{diag}(\Gamma_1, \Gamma_2, ..., \Gamma_N)$. These complex values represent the *modal reflection coefficients* (*modal reflectances*) of all N *radiation modes*. It is apparent from (2.29) that the matrix $\mathbf{\Theta}$ contains the phase component of $\mathbf{\Gamma}$ and that $\mathbf{\Sigma}$ is the magnitude of $\mathbf{\Gamma}$ ($\mathbf{\Sigma}^2 = \mathbf{\Gamma}^*\mathbf{\Gamma}$). The phase of $\mathbf{\Gamma}$ is not arbitrary but uniquely given by the decomposition of $\mathbf{S}^*\mathbf{S}$ (2.30). However the interpretation of the phase is different from that for a single port antenna. For a multi-port antennas (2.30) can be written with respect to n-th eigenvector of $\mathbf{S}^*\mathbf{S}$ as

$$\mathbf{S}\boldsymbol{V}_n = \boldsymbol{V}_n^*\Gamma_n. \tag{2.31}$$

The relation shows that if an eigenvector $\boldsymbol{V}_n$ is incident at the feed ports the reflected vector $\boldsymbol{V}_n^*\Gamma_n$ is its conjugate complex copy (phase reversed), multiplied in addition by the modal reflection coefficient Γ_n [68]. Based on the previous results it is possible to write the relation between *modal efficiencies* and *modal reflectances* in the form [1, 3, 31]

$$\mathbf{C} = \mathbf{I} - \mathbf{\Gamma}^*\mathbf{\Gamma}. \tag{2.32}$$

This relation between modal quantities that fully characterize lossless multiport antenna is equivalent to (2.23) when $\mathbf{V}$ is known. Any matched lossless multiport antenna always features maximum per port efficiencies, zero overlap between radiation patterns of all ports because $\mathbf{S} = \mathbf{0}$ implies $\mathbf{R} = \mathbf{I}$. Equivalently, in terms of modal quantities, the ideal match occurs when $\mathbf{\Gamma} = \mathbf{0}$ which leads to $\mathbf{C} = \mathbf{I}$. Modal radiation patterns and per port radiation patterns differ in general. Only for antenna systems, where *radiation modes* are mapped to external ports the per port radiation patterns correspond to modal radiation patterns.

2.3.3. Multiport symmetric antennas

Multiport antenna is called symmetric if its scattering matrix remains unchanged when exchanging port indices. It was shown in [18] after [69] that in case of a permutation of port indices $\mathbf{\Pi}$ leaves unchanged scattering matrix $\mathbf{S}$, i.e. if

$$\mathbf{\Pi S \Pi} = \mathbf{S} \tag{2.33}$$

then $\mathbf{\Pi}$ and $\mathbf{S}$ commute. Equivalently, given that $\mathbf{\Pi}^{-1} = \mathbf{\Pi}$, (2.33) can be given in the form $\mathbf{\Pi S} = \mathbf{S\Pi}$ which shows that the commutator of $\mathbf{\Pi}$ and $\mathbf{S}$ is zero. $\mathbf{\Pi}$ and $\mathbf{S}$ have common basis of eigenvectors. In general, matrix multiplication is not commutative. This allows to uniquely define multiport symmetry of antenna systems via real and explicitly known matrix $\mathbf{V}$. The real matrix $\mathbf{V}$ leads to $\mathbf{V}\mathbf{V}^\top = \mathbf{I}$. Then, (2.30) can be written as

$$\mathbf{V\Gamma} = \mathbf{SV}. \tag{2.34}$$

The definition of multiport symmetry via commutation of the $\mathbf{\Pi}$ and $\mathbf{S}$ is general. Taking a recourse to the less general but more intuitive geometrical symmetry [5] is thus unnecessary.

2.3.4. Modal impedances

The goal of the present subsection is to introduce the notion of *modal impedances* which has to be consistent with the *modal analysis* based on the spectrum of *radiation matrix*. In order to satisfy the goal the impedance matrix has to be diagonalizable by the unitary matrix $\mathbf{V}$. Then, a straightforward relation between *modal reflectances* and *modal impedances* exist. Unfortunately, in the general case of lossless N-port antenna the relation between *modal reflectances* and *modal impedances* cannot be directly found. In order to understand the problem consider substitution of (2.28) into well-known relation between scattering matrix and normalized impedance matrix which leads to

$$\mathbf{z} = (\mathbf{I} + \mathbf{V}^*\boldsymbol{\Gamma}\mathbf{V}^\dagger)(\mathbf{I} - \mathbf{V}^*\boldsymbol{\Gamma}\mathbf{V}^\dagger)^{-1}. \tag{2.35}$$

It is easy to see that $(\mathbf{I} - \mathbf{V}^*\boldsymbol{\Gamma}\mathbf{V}^\dagger) \neq \mathbf{V}^*(\mathbf{I} - \boldsymbol{\Gamma})\mathbf{V}^\dagger$ because of the fact that matrix $\mathbf{V}$ is unitary but not necessarily orthogonal, i.e. $\mathbf{V}\mathbf{V}^\top \neq \mathbf{I}$ in general. Therefore, the impedance matrix cannot be diagonalized is a straightforward manner by the unitary matrix $\mathbf{V}$. Expressing $\mathbf{S}^*\mathbf{S}$ in terms of the normalized impedance matrix leads to the matrix quadratic equation with respect to $\mathbf{z}$. The solution of the matrix quadratic equation is given in [28] and can be written using *modal efficiencies matrix* in the form

$$\mathbf{z} = \mathbf{V}\left(2\mathbf{C}^{-1} - \mathbf{I}\right)\mathbf{V}^\dagger + \mathcal{C}(\mathbf{V}\mathbf{C}\mathbf{V}^\dagger)^{-1}\boldsymbol{\Psi}\mathcal{C}\left(4\mathbf{V}(\mathbf{C}^{-1} - \mathbf{I})\mathbf{V}^\dagger\right), \tag{2.36}$$

where $\boldsymbol{\Psi}$ is an arbitrary unitary matrix and $\mathcal{C}$ denotes Cholesky decomposition. The first component of (2.36) represents eigenvalue decomposition of $\mathbf{z}$ with real diagonal normalized modal impedance matrix $\boldsymbol{\zeta} = 2\mathbf{C}^{-1} - \mathbf{I}$. For matched lossless antenna, i.e. when $\mathbf{C} = \mathbf{I}$, (2.36) reduces ideally to $\mathbf{z} = \mathbf{I}$ assuming all ports are terminated with the same real load impedances Z_L.

Only if a lossless antenna system features multiport symmetry (see previous subsection), i.e. when (2.34) applies, then the following relation between *normalized modal impedance matrix* $\boldsymbol{\zeta}$ (normalized to the load impedance Z_L, which are assumed equal for all *radiation modes*), and *modal reflectance matrix* $\boldsymbol{\Gamma}$ is fulfilled

$$\boldsymbol{\zeta} = (\mathbf{I} + \boldsymbol{\Gamma})(\mathbf{I} - \boldsymbol{\Gamma})^{-1}, \tag{2.37}$$

and the normalized impedance matrix $\mathbf{z}$ is diagonalized by the same $\mathbf{V}$ as in (2.21). The general (not only applicable to multiport symmetric antennas) and fairly complex relation between modal impedances and modal reflectances was

derived using relations given in [28]. The resulting expression (2.36) is cumbersome and has very little practical significance since typically in engineering practice it is not only convenient to exploit multiport symmetry but also beneficial. If the antenna system features multiport symmetry, in the sense of a real matrix $\mathbf{V}$, then *radiation modes* do not change over frequency. This fact is also clearly desirable in construction of matching and mode decomposition networks as shown later in chapter 4. Therefore, since (2.37) allows to obtain modal impedances from modal reflectances of a multiport symmetric antennas it is of significant practical importance.

2.3.5. Modal bandwidths and radiation quality factors

Modal bandwidths

Proper definition of modal reflectances, modal impedances and the relation between both quantities for multiport symmetric antennas given in the previous subsections allow to consider introduction of *modal bandwidths*. The fractional x dB bandwidth of nth radiation mode is defined as

$$b_n^{x\mathrm{dB}} = \frac{f_{n,2} - f_{n,1}}{f_{n,0}}, \tag{2.38}$$

where RL_n is the return loss of the nth radiation mode and $f_{n,1}$, and $f_{n,2}$ are the lower and the upper frequencies, respectively, for which $\mathrm{RL}_n \geq x\mathrm{dB}$. The relation between three frequencies is $f_{n,1} < f_{n,0} < f_{n,2}$, where $f_{n,0}$ is the center frequency. If modal reflectance is known it is possible to obtain the x dB bandwidth using analytical expression (both *radiation mode* and its matching network are assumed lossless) or numerical analysis (losses may be included) by matching the mode at single frequency $f_{n,0}$.

Modal radiation quality factors

Estimation of modal bandwidths for lossless multiport antennas can also be performed using the notion of modal radiation quality factors. The inverse of the modal radiation quality factors correspond to the fractional 7 dB modal return loss bandwidths (assuming single narrowband resonance) [70]

$$b_n^{7\mathrm{dB}} = \frac{1}{Q_{\mathrm{rad},n}}, \tag{2.39}$$

where superscript 7 dB refers to the level of *modal return loss* at which it is obtained. According to [71] (2.39) is valid for $Q_{\mathrm{rad},n} > 4$.

For the purpose of the present chapter it is appropriate to introduce *modal radiation quality factors* as in [3] using the textbook definition of the radiation quality factor after [72]. For the nth *radiation mode* it is given by

$$Q_{\mathrm{rad},n} = \frac{2\omega \max\left(\langle W_{\mathrm{M},n}\rangle, \langle W_{\mathrm{E},n}\rangle\right)}{P_{\mathrm{rad},n}}, \tag{2.40}$$

where $\langle W_{\mathrm{E},n}\rangle$ and $\langle W_{\mathrm{M},n}\rangle$ are the time-average electric and magnetic energies of the nth radiation mode stored in the near-field, respectively and $P_{\mathrm{rad},n}$ is the power radiated by the nth *radiation mode*. The definition assumes that the input impedance can be made real at any given frequency using a lossless external matching circuit. In order to determine a much more suitable in engineering practice expression than that given by (2.40) so as to be able to calculate modal radiation quality factors it is convenient to take a recourse to the established expressions for single port antennas. Since modal impedances are invariant quantities of the multiport antennas an expression valid for radiation quality factor of a single port antenna will also be applicable to calculating radiation quality factor of *radiation modes*. The most general expression for the radiation quality factor was given in [71]. It was derived from both Maxwell's equations and using Equivalent Circuit Models (ECMs) assuming that the matching network comprises a single series reactance or shunt reactance for series or shunt ECM of an antenna, respectively (for details see appendix A). For further discussion consider that *normalized modal impedances* of a lossless antenna system, assuming a single resonance mode, are given by $\zeta_n = \rho_{\mathrm{rad},n} + \mathrm{j}\xi_n$, where $\rho_{\mathrm{rad},n}$ and ξ_n are normalized radiation resistance and normalized reactance of the n-th modal impedance, respectively. In case of multiport symmetry, defined in the previous subsection via real matrix $\mathbf{V}$, *modal impedances* can be explicitly obtained from (2.37). If the mode-specific matching network comprising a single reactance is used to match a *radiation mode* then the radiation quality factor of the complete arrangement is given by Yaghjian [71]

$$Q_{\mathrm{rad},n}(\omega_0) = \frac{\omega_0}{2\rho_{\mathrm{rad},n}} \sqrt{\left(\frac{\mathrm{d}\rho_{\mathrm{rad},n}}{\mathrm{d}\omega}\right)^2\Bigg|_{\omega_0} + \left(\frac{\mathrm{d}\xi_n}{\mathrm{d}\omega}\Bigg|_{\omega_0} + \frac{|\xi_n(\omega_0)|}{\omega_0}\right)^2}, \tag{2.41}$$

where ω_0 denotes the radian frequency of interest. The absolute value $|\xi_n(\omega_0)|$ in the second term on the rhs of (2.41) comes from realization that the matching network can comprise either a series capacitance or a series inductance.

The same result, i.e. (2.41), can be analogously obtained if a shunt ECM of the antenna is matched with a shunt inductance or capacitance. The above most general expression for calculation of the radiation quality factor takes into account change over frequency of both the real part and the imaginary part of the impedance and is valid over a wide range of frequencies. In [73] it was shown that (2.41) reduces to the radiation quality factor after [74] if the change of the real part of impedance is negligible as compared to frequency derivative of the reactance, which is expected behavior of the higher order *radiation modes*. With respect to nth *radiation mode* the relation after [74] is given by

$$Q_{\mathrm{rad},n}(\omega_0) = \frac{\omega_0}{2\rho_{\mathrm{rad},n}} \left| \frac{\mathrm{d}\xi_n}{\mathrm{d}\omega}\bigg|_{\omega_0} + \frac{|\xi_n(\omega_0)|}{\omega_0} \right|. \tag{2.42}$$

The term $|\mathrm{d}\xi_n(\omega_0)|\,/\mathrm{d}\omega$ is typically larger than $|\xi_n(\omega_0)|\,/\omega_0$ for *radiation modes* featuring high radiation quality factors. The radiation quality factor of the nth *radiation mode* at resonance (at which $\xi_n(\omega_0) = 0$) can be expressed in the form [75]

$$Q_{\mathrm{rad},n}(\omega_0) = \frac{\omega_0}{2\rho_{\mathrm{rad},n}} \left| \frac{\mathrm{d}\xi_n}{\mathrm{d}\omega}\bigg|_{\omega_0} \right|. \tag{2.43}$$

The difference in determination of the radiation quality factor using (2.42) and (2.43) away from resonance is about factor of two except when $|\mathrm{d}\xi_n(\omega_0)|\,/\mathrm{d}\omega \approx 0$. Then the difference becomes significant and use of (2.42) is mandatory.

In case of multiport antennas for small mobile wireless terminals with high aspect ratio it is often observed that already the second *radiation mode* features high radiation quality factor. Illustrative numerical examples supporting this statement are given in Chapter 3 using *characteristic modes* [10].

2.4. Total Multiport Efficiency and Modal Efficiency Imbalance

2.4.1. Total multiport efficiency

In the Receive Diversity (RD) mode of operation RF signals are combined at the receiver typically using Maximum Ratio Combining (MRC) scheme. If the

weighting coefficients are equal the method reduces to Equal Gain Combining (EGC). In this method after phase compensation RF signals are simply added without checking the quality of signal individually in all branches. Thus a branch with weak signal contributes only additional noise to the output signal. A descriptive quantity which allows to properly account for degradation of the expected value of the channel capacity with correspondence to the EGC scheme is necessary to introduce. The definition of *total multiport efficiency* assumes that all ports are fed with uncorrelated signals (random phases) of equal power which describe MIMO operation of a wireless communication system. The total multiport efficiency is a ratio of the total radiated power P_{rad} to the available power P_{av} [76]

$$\overline{\eta_{\mathrm{tot}}} = \frac{P_{\mathrm{rad}}}{P_{\mathrm{av}}} = \frac{1}{N}\mathrm{tr}(\mathbf{R}) = \frac{1}{N}\sum_{n=1}^{N} R_{nn} = \frac{1}{N}\sum_{n=1}^{N} \eta_n^{\mathrm{port}}. \tag{2.44}$$

The relation does apply neither to antenna arrays nor to beamforming. (2.44) is applicable also in case of lossy antennas [38]. The trace is invariant under similarity transformation so that $\mathrm{tr}\,(\mathbf{R}) = \mathrm{tr}\,(\mathbf{C})$ which shows that the total multiport efficiency is an arithmetic average of the per port efficiencies

$$\overline{\eta_{\mathrm{tot}}} = \frac{1}{N}\mathrm{tr}(\mathbf{C}). \tag{2.45}$$

The same result can also be obtained using *modal analysis* based on the spectrum of the *radiation matrix*. Let index n to identify the nth *radiation mode* so that $P_{\mathrm{rad},n}$ and $P_{\mathrm{av},n}$ are the total radiated power and the available power of the nth radiation mode, respectively. The maximization of the per port efficiencies yields maximization of the total multiport efficiency. The off-diagonal elements of $\mathbf{R}$ are not taken into account which seems to be in conflict with the expectation that in addition minimization of these elements is required in order to maximize the total multiport efficiency. However, this is not the case since the trace is invariant under similarity transformation as shown above. Therefore, the design goal of maximization of the per port efficiencies is equivalent to maximization of *modal efficiencies*. The latter goal leads simultaneously to minimization of the *condition number* $\kappa = \eta_{\max}/\eta_{\min}$ of the matrix $\mathbf{R}$ (see section 2.5) or equivalently to minimization of the *modal efficiency imbalance* β [61] (see the next subsection). No additional design goals related to radiation pattern overlap are required i.e. the pattern overlap becomes a redundant descriptive quantity as shown in section 2.5.

2.4.2. Modal efficiency imbalance

In the Spatial Multiplexing (SM) mode of operation, assuming high Signal to Noise Ratio (SNR) regime, it was shown by Feng [61, 77] that the quantity which describes degradation of the expected value of the channel capacity is the *modal efficiency imbalance*. It is the ratio of the *total multiport efficiency* to the geometric average of *modal efficiencies* [61]

$$\beta = \frac{\overline{\eta_{\text{tot}}}}{\sqrt[N]{\eta_1 \eta_2 \cdots \eta_N}}. \tag{2.46}$$

For a perfectly balanced, i.e. $\eta_1 = \eta_2 = \cdots = \eta_N$, lossless multiport antenna $\beta = 1$ and the expected value of the channel capacity is maximized. In general $\beta \geq 1$. To complete the definition it is convenient to introduce $\beta^{(\text{dB})}$ which is the *modal imbalance figure* [61]

$$\beta^{(\text{dB})} = 10\text{dB} \log_{10} \left(\frac{\overline{\eta_{\text{tot}}}}{\sqrt[N]{\eta_1 \eta_2 \cdots \eta_N}} \right). \tag{2.47}$$

Equalization of modal efficiencies over the desired "overall" bandwidth remains the design goal for multiport antennas. To illustrate this consider comparing two symmetric 2-port MIMO antennas against each other. The first antenna features $\eta_1 = 90\ \%$ and $\eta_2 = 10\ \%$ and the second $\eta_1 = 60\ \%$ and $\eta_2 = 40\ \%$. Both antennas have the same $\overline{\eta_{\text{tot}}} = 50\ \%$ equal to per port efficiencies. However, in terms of β the antenna systems expose significant differences since for the first antenna $\beta = 1.66$ and for the second antenna $\beta = 1.02$. Therefore, the second antenna system features better performance in terms of expected capacity in the SM mode of operation assuming high SNR regime due to lower *modal efficiency imbalance* β. This is an important conclusion especially for the most practical antenna designs for mobile wireless terminals which often feature multiport symmetry and where one of the *radiation modes* features low modal efficiency.

2.5. Upper Bound on Radiation Pattern Overlap

The radiation pattern overlap was introduced in subsection 2.2.2 as overlap integral between two radiation patterns related to a pair of ports. It is used

in the context of multiport antennas for MIMO application. However, it shall be noted that in literature often quantities like Complex Envelope Correlation Coeffient (CECC) and Power Envelope Correlation Coeffient (PECC) are used in the same context. Both are statistical quantities related, in addition, to RF signals in a certain propagation environment. The expectation value of their correlation coincides with the normalized radiation pattern overlap (2.14) under an assumption of an isotropic Rayleigh scattering scenario. It important to realize that radiation pattern correlation has no relation with the envelope of the RF signal. Therefore, it shall be, more appropriately, referred to as radiation pattern overlap. Its direct calculation using (2.14) requires knowledge of per port radiation patterns. Therefore, many attempts have been made to derive useful practical expressions for explicit calculation of pattern overlap using S-parameters. The expressions applicable to lossless multiport antennas are given in e.g. [64] while for lossy antennas use of equivalent circuit models was proposed [78, 79]. Another interesting work was dedicated to extending an upper bound on *radiation pattern overlap* which in [80] was found to be related to the minimum per port efficiency. In the present section, following [81, 82], it is shown that it is unnecessary to directly calculate radiation pattern overlap using (2.14). It is sufficient to consider an upper bound on pattern overlap which can be given in terms of the ratio of the maximum to the minimum *modal efficiencies* both of which are invariant properties of the *radiation matrix*. Detailed derivation is given in Appendix B. For the purpose of the present section the upper bound on radiation pattern overlap for a lossy N-port antenna is expressed in terms of the *condition number* $\kappa = \eta_{\max}/\eta_{\min}$ of the *radiation matrix* $\mathbf{R}$, where $\eta_{\max}$ and $\eta_{\min}$ are maximum and minimum modal efficiencies, as [82]

$$|\rho_{mn}| \leq \frac{\kappa - 1}{\kappa + 1}. \tag{2.48}$$

Small values of the modal efficiency condition number yield small pattern overlap (see Fig. 2.2). In other words large values of $\eta_{\max}$ and $\eta_{\min}$ and small *modal efficiency imbalance* [61] lead to low radiation pattern overlap. Therefore, pattern overlap by itself is of relatively low relevance as a descriptive quantity because it is usually small even for lossy antennas provided that an approximate match is achieved. Moreover, if *radiation modes* of an antenna system are directly mapped to external ports then multiport antenna features near-zero overlap independently from how well its *radiation modes* are matched. The concept of mapping *radiation modes* to external ports (see Chapter 4 and 5) not only allows to exploit significantly different bandwidths of all

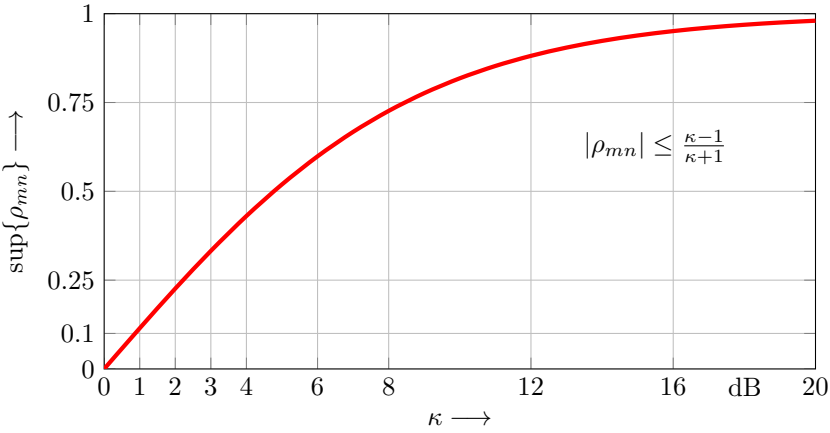

Fig. 2.2.: Tight upper bound on the radiation pattern overlap versus condition number for an N-port antenna, where *radiation modes* are *not* mapped to external ports, after (2.48).

radiation modes and achieve high isolation between antenna ports but also simultaneously leads to near-zero radiation pattern overlap. Therefore, the major limiting factor in design of multiport antennas for small mobile wireless devices is bandwidth of higher order radiation modes and not radiation pattern overlap.

2.6. Total Multiport Return Loss

2.6.1. Total active reflection coefficient

Multiport antennas are usually characterized by the per port return loss (or s_{ii}), isolation (or s_{ij} for $i \neq j$) and pattern overlap (often using PECC instead of radiation pattern overlap). In the present chapter and subsequently in Appendix B it is shown that radiation pattern overlap is not an independent descriptive quantity from the antenna scattering matrix $\mathbf{S}$ and thus should not be considered as useful design parameter. Often, performance comparisons between different designs of multiport antennas are made in terms of "better match" but "worst isolation" and *vice versa*. Consider two antenna systems with the same losses but different performance in terms of both return loss and isolation (see e.g. Fig. 2.3). The definition of the "overall" bandwidth is not

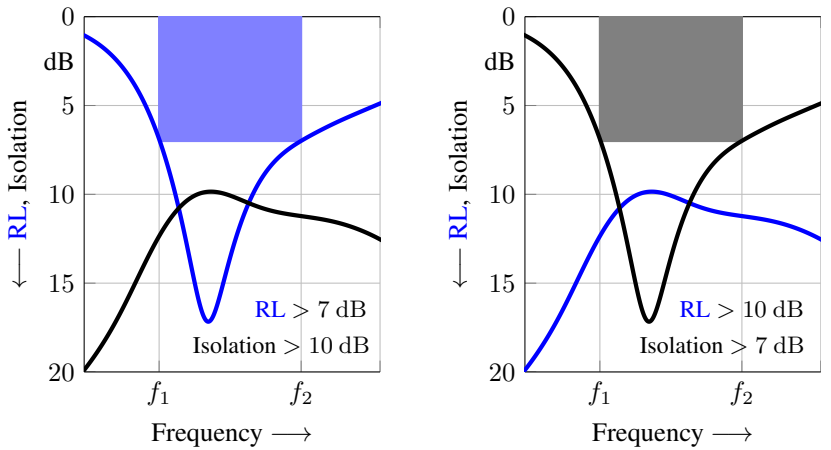

Fig. 2.3.: Illustrative examples of the performance of two symmetric 2-port MIMO antennas which have different RL and isolation but the same performance in terms of a single descriptive quantity that takes into account all S-parameters of the antenna.

unique. In order to define the bandwidth of multiport antenna, where *radiation modes* are not mapped to external ports, it is necessary to introduce a single descriptive quantity.

In order to illustrate the problem consider a pathological example of the "ideal" 2-port antenna depicted in Fig. 2.4. Per port matching indicates that $s_{11} = s_{22} = 0$ but due to $s_{21} = 1$ the antenna does not radiate. Power applied to one port simply exits at the other port. The mistake of characterizing multiport antennas by looking only at per port return loss often leads to wrong conclusions [83, 84]. The new quantity has to takes into account more than just s_{nn} to be appropriate for general characterization of the N-port MIMO antennas. A single descriptive quantity for multiport antennas called Total Active Reflection Coefficient (TARC) was defined in [85]. TARC is a square root of the available power at all ports of the antenna minus radiated power, normalized to the available power

$$\mathrm{TARC} = \sqrt{\frac{P_{\mathrm{av}} - P_{\mathrm{rad}}}{P_{\mathrm{av}}}}. \tag{2.49}$$

The definition, generally applies to all multiport antennas, but does not specify neither the distribution of power among the ports ($P_{\mathrm{av},n}/P_{\mathrm{av}}$), nor the

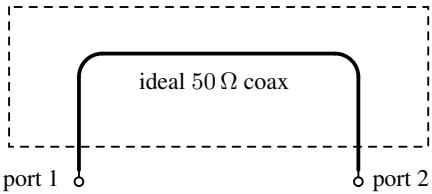

Fig. 2.4.: Pathological example of a lossless 2-port antenna "enclosed in a black box" that has infinite return loss, $\mathrm{RL}_{11} = \mathrm{RL}_{22} = \infty$ but does not radiate [38].

correlation between signals at different ports. In MIMO transmission one may assume that the power distribution among the ports is, on average, equal ($P_{\mathrm{av},n} = 1/N P_{\mathrm{av}}$) and signals applied to different ports have to be uncorrelated. The TARC, for lossless antennas it can be calculated using [85]

$$\mathrm{TARC} = \sqrt{\frac{\sum_{i=1}^{N} |b_i|^2}{\sum_{i=1}^{N} |a_i|^2}} \tag{2.50}$$

for certain excitation vector $\boldsymbol{a}$. Worth noticing is the fact that the TARC has real values since the phase reference plane does not have any physical meaning for a multiport antennas. The TARC is not sufficient for description of multiport antennas for MIMO application. The proper descriptive quantity for these antennas, i.e. Total Multiport Return Loss (TMRL), is introduced after [38] following [30] in the next subsection using power relations at the feeds of a multiport antenna.

2.6.2. Multiport reflectance and total multiport reflectance

The relation (2.1) can be naturally extended to multiport antennas. Consider a N-port antenna system shown in Fig. 2.5b. The available power is distributed equally among all ports, i.e. $P_{\mathrm{av},n} = \frac{1}{N} P_{\mathrm{av}}$. When port n is fed with wave quantity a_n the power reflected back from all ports is

$$P_{\mathrm{refl},n} = \sum_{m=1}^{N} |s_{mn}|^2 P_{\mathrm{av},n}. \tag{2.51}$$

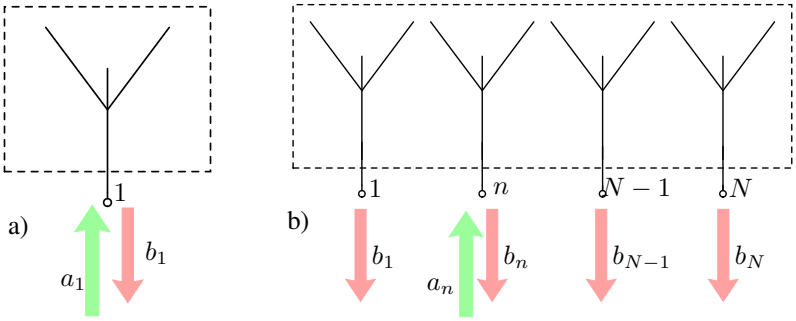

Fig. 2.5.: Illustration of an input and output wave quantities for a single port antenna (left) and multiport antenna system (right).

The quantity, which retains information equivalent to $|s_{11}|$ in the single antenna case, is named *multiport reflectance*. For an N-port antenna it was given in [38] as

$$\Gamma_n^{\text{port}} = \sqrt{\sum_{m=1}^{N} |s_{mn}|^2}. \tag{2.52}$$

The quantity Γ_n^{port} is relative to port n of an N-port antenna system and may also be called effective reflectance of port n, because it relates reflected power through all ports to available power at the (single) feed port n. To complete the definition it is possible to introduce *multiport return loss* relative to port n of an N-port antenna system

$$\text{MRL}_n = -10\text{dB}\log_{10}\left(\sum_{m=1}^{N} |s_{mn}|^2\right). \tag{2.53}$$

A multiport reflectance is a per port generalization of $|s_{11}|$ for a single port antenna. However a single descriptive quantity characterizing reflectance for all ports of a multiport antenna is of interest. A key requirement for multiport antenna for MIMO application is low imbalance between per port reflectances (approximately equal values of Γ_n^{port}) which is equivalent to the requirement of low *modal reflectance imbalance* as described in section 2.4 with respect to *modal efficiency imbalance*. The new descriptive quantity should reflect this requirement. The generalization of *multiport reflectance* to a quantity which describes "overall" matching efficiency is the root-mean-squared value of the multiport reflectances, $\Gamma_1^{\text{port}}, \Gamma_2^{\text{port}}, ..., \Gamma_n^{\text{port}}$ of all ports of a multiport antenna.

The *normalized total multiport reflectance* of an N-port antenna system was defined in [38] as

$$\Gamma_{\mathrm{tot}} = \sqrt{\frac{1}{N}\sum_{n=1}^{N}\left(\Gamma_n^{\mathrm{port}}\right)^2} = \sqrt{\frac{1}{N}\sum_{m,n=1}^{N}|s_{mn}|^2} = \frac{1}{\sqrt{N}}\left\|\mathbf{S}\right\|_{\mathrm{F}}, \tag{2.54}$$

where $\left\|\mathbf{S}\right\|_{\mathrm{F}}$ denotes the Frobenius norm of the antenna scattering matrix. The corresponding *normalized total multiport return loss* of an N-port antenna system is defined by

$$\mathrm{TMRL} = -20\mathrm{dB}\log_{10}\left(\Gamma_{\mathrm{tot}}\right) = -20\mathrm{dB}\log_{10}\left(\frac{1}{\sqrt{N}}\left\|\mathbf{S}\right\|_{\mathrm{F}}\right). \tag{2.55}$$

TMRL is a logical generalization of RL to N-port antennas for MIMO application. Due to normalization $(1/\sqrt{N})$, Γ_{tot} takes its values in the same interval as the antenna S-parameters $[0, 1]$. Furthermore, since $||\mathbf{S}||_{\mathrm{F}} = ||\mathbf{\Gamma}||_{\mathrm{F}}$ the following relations are true

$$\Gamma_{\mathrm{tot}} = \frac{1}{\sqrt{N}}||\mathbf{\Gamma}||_{\mathrm{F}} \tag{2.56}$$

and

$$\mathrm{TMRL} = -20\mathrm{dB}\log_{10}(\Gamma_{\mathrm{tot}}) = -20\mathrm{dB}\log_{10}(\frac{1}{\sqrt{N}}||\mathbf{\Gamma}||_{\mathrm{F}}). \tag{2.57}$$

Based on (2.56) and using (2.44) and (2.32) it is possible to derive the expected value of the *total multiport efficiency* for a lossless antenna system

$$\overline{\eta_{\mathrm{tot}}} = 1 - \Gamma_{\mathrm{tot}}^2, \tag{2.58}$$

which depends on the total multiport reflectance only. Minimization of Γ_{tot} or equivalently maximization of TMRL leads to maximization of $\overline{\eta_{\mathrm{tot}}}$ similarly as for a single port antenna.

As a descriptive quantity TMRL is applicable to any number of antenna ports. However, there are two special cases that are worth to mention. For a single port antenna ($N = 1$) obviously the following is true $\Gamma_{\mathrm{tot}} = \Gamma_1^{\mathrm{port}} = |s_{11}|$ and TMRL $=$ MRL $=$ RL. In case of symmetric N-port antennas $\Gamma_{\mathrm{tot}} = \Gamma_n^{\mathrm{port}}$ (TMRL $=$ MRL$_n$). If all S-parameters of the multiport antenna are the same (i.e. $s_{11} = s_{mn} = \cdots = s$, for all m and n) then $\Gamma_{\mathrm{tot}} = \sqrt{N}s$. This

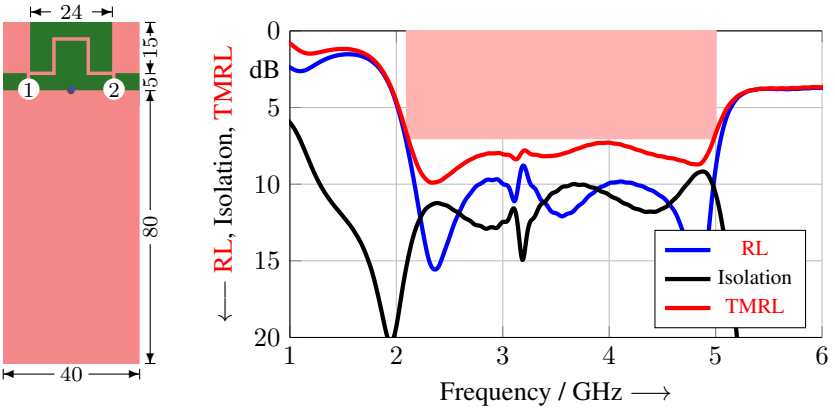

Fig. 2.6.: Planar, symmetric 2-port MIMO antenna featuring wideband frequency response from 2.1 GHz to 5 GHz (Red rectangle shows 7 dB TMRL bandwidth) [38]. All dimensions are given in mm.

means that Γ_{tot} is $\sqrt{N}$ times higher then the corresponding S-parameters. For a symmetric 2-port MIMO antenna with $s_{11} = s_{22} = s_{12} = s_{21}$ the *total multiport reflectance* is 3 dB higher than the S-parameters. As an example consider the design shown in Fig. 2.6 which has wideband characteristics. Per port return loss and isolation are well equalized at about 10 dB over bandwidth of almost 3 GHz. However, matching efficiency described in terms of TMRL is approximately 7 dB only. Inspection of TMRL reveals that the true matching efficiency is about 3 dB worse than what a plot of per port RL only would suggest (since RL $\approx$ Isolation).

Chapter 3

Characteristic Chassis Modes

In the previous chapter descriptive quantities capable of meaningful characterization of multiport antennas for MIMO application were introduced. Once an antenna design is proposed, and ports introduced, these quantities can be used to further aid a systematic design procedure and evaluate results. However, in order arrive at a design concept more fundamental considerations are necessary which allow to predict modal radiation quality factors and to identify the "optimum" location of antenna ports prior to any detailed design study. The starting point for design of antennas for small mobile wireless devices is the size of the chassis itself. The *theory of characteristic modes* introduced by Harrington [10] and Garbacz [86] allows to analyze chassis of a device where only its shape and electrical size are required input parameters. No prior assumptions on an antenna physical structure and port locations are necessary. Extensive computations of characteristic modes for various device form factors led to identification of the chassis of a device as the main contributor to the radiation [11, 12, 87]. This important observation advance antenna design for small mobile wireless terminals to a concept of "extremely" small *couplers* which excite characteristic chassis modes. Application of characteristic modes to design of antennas for mobile wireless devices were most notably researched by Fabres [88], Obeidat [89], Chaudhury [18] and Ethier [90]. Characteristic modes provide valuable information regarding optimum type of a coupler and their placement so as to excite characteristic modes of interest for the purpose

of multiport antenna design [18, 21]. Further, if couplers selectively excite the desired *characteristic modes* then they approximately correspond to the *radiation modes*. The relation between *characteristic chassis modes* and *radiation modes* constitutes the cornerstone of the procedure for systematic design of multiport antennas outlined in this dissertation. In this chapter an illustration of the relation between *characteristic chassis modes* and *radiation modes* is given using an example design of a multi-band 2-port MIMO antenna for LTE-enabled laptops.

3.1. Theory of Characteristic Modes

The purpose of this section is to give a brief description of the theory of characteristic modes for conducting bodies introduced in [10, 86].

3.1.1. Notation

For the purpose of further analysis it is convenient to introduce the following notation. The product of two vector functions $\boldsymbol{A}$ and $\boldsymbol{B}$ on the surface S is defined as

$$\langle \boldsymbol{A}|\boldsymbol{B}\rangle_S = \oiint_S \boldsymbol{A}\cdot\boldsymbol{B}\,\mathrm{d}s. \tag{3.1}$$

As a shorthand for the *inner product* in the complex Hilbert space, over surface S, on which square-integrable vector functions $\boldsymbol{A}$ and $\boldsymbol{B}$ are defined we use notation

$$\langle \boldsymbol{A}^*|\boldsymbol{B}\rangle_S = \oiint_S \boldsymbol{A}^*\cdot\boldsymbol{B}\,\mathrm{d}s, \tag{3.2}$$

where asterisk denotes complex conjugate. The subscript S on the left hand side of (3.2) denotes integration over the surface S. An operator $\widehat{\mathbf{K}}$ is *symmetric*, if the following relation between two vector fields holds

$$\langle \boldsymbol{A}|\widehat{\mathbf{K}}\boldsymbol{B}\rangle_S = \langle \widehat{\mathbf{K}}\boldsymbol{A}|\boldsymbol{B}\rangle_S. \tag{3.3}$$

The concept of the *reaction integral* was introduced in [91]. The reaction of electric field a on source b after [92] is defined as

$$\langle \boldsymbol{E}^a|\boldsymbol{J}^b\rangle_S = \oiint_S \boldsymbol{E}^a\cdot\boldsymbol{J}^b\mathrm{d}s, \tag{3.4}$$

where $\boldsymbol{E}$ and $\boldsymbol{J}$ are the electric field and current due to this field, respectively. Analogous definition applies to the magnetic field and magnetic current due to this electric field. The reciprocity theorem $\langle \boldsymbol{E}^a | \boldsymbol{J}^b \rangle_S = \langle \boldsymbol{E}^b | \boldsymbol{J}^a \rangle_S$ states that the reaction of field a on source b is equal to the reaction of field b on source a.

3.1.2. Field quantities and impedance operator

The current density $\boldsymbol{J}_\mathrm{s}$ induced on the surface S of a conducting body by an externally impressed electric field $\boldsymbol{E}^\mathrm{ex}$ is related to this field by the boundary condition [10]

$$\left[\widehat{\mathbf{L}}(\boldsymbol{J}_\mathrm{s}) - \boldsymbol{E}^\mathrm{ex}\right]_\mathrm{tan} = \mathbf{o}, \tag{3.5}$$

where the subscript "tan" indicates tangential component of any vectors on surface S_0. The operator $\widehat{\mathbf{L}}$ allows to relate externally impressed electric field to unknown current density which represents classic description of radiation problem in the frequency domain. For a scattering problem it gives a relation between known incident electric field and unknown current. The operator is given by the gradient $\nabla\Phi$ of the scalar potential Φ and vector potential $\boldsymbol{A}$ via [10]

$$\widehat{\mathbf{L}}(\boldsymbol{J}_\mathrm{s}) = \mathrm{j}\omega\boldsymbol{A}(\boldsymbol{J}_\mathrm{s}) + \nabla\Phi(\boldsymbol{J}_\mathrm{s}). \tag{3.6}$$

The vector potential and the scalar potentials observed at a distance $\boldsymbol{r}$ from the source point $\boldsymbol{r}'$ are given by

$$\boldsymbol{A}(\boldsymbol{J}_\mathrm{s}) = \mu \iint\limits_S \boldsymbol{J}_\mathrm{s}(\boldsymbol{r}')G(\boldsymbol{r},\boldsymbol{r}')\mathrm{d}s \tag{3.7}$$

and

$$\Phi(\boldsymbol{J}_\mathrm{s}) = \frac{-1}{\mathrm{j}\omega\epsilon} \iint\limits_S \nabla' \cdot \boldsymbol{J}_\mathrm{s}(\boldsymbol{r}')G(\boldsymbol{r},\boldsymbol{r}')\mathrm{d}s, \tag{3.8}$$

respectively where ϵ denotes permittivity, μ denotes permability and k is the wavenumber. Operator ∇' denotes divergence with respect to r'. The Green's function has a well-known form

$$G(\boldsymbol{r},\boldsymbol{r}') = \frac{\mathrm{e}^{-\mathrm{j}\,k|\boldsymbol{r}-\boldsymbol{r}'|}}{4\pi\,|\boldsymbol{r}-\boldsymbol{r}'|}. \tag{3.9}$$

Substitution of potentials after (3.7) and (3.8) into (3.6) yields an expression for operator $\widehat{\mathbf{L}}(\boldsymbol{J})$ in terms of current $\boldsymbol{J}_\mathrm{s}$ induced on the surface S_0 [15]

$$\widehat{\mathbf{L}}(\boldsymbol{J}_\mathrm{s}) = \frac{1}{\mathrm{j}\omega\epsilon} \iint\limits_S \boldsymbol{J}_\mathrm{s}(\boldsymbol{r}') \cdot (\nabla'\nabla' + k^2)G(\boldsymbol{r},\boldsymbol{r}')\mathrm{d}s. \tag{3.10}$$

The operator $\widehat{\mathbf{L}}(\boldsymbol{J}_\mathrm{s})$ is symmetric but not Hermitian. The real and the imaginary parts of $\widehat{\mathbf{L}}$ are real and symmetric, and are given by

$$\Re\{\widehat{\mathbf{L}}\} = \frac{1}{2}(\widehat{\mathbf{L}} + \widehat{\mathbf{L}}^*) \quad \text{and} \quad \Im\{\widehat{\mathbf{L}}\} = \frac{1}{2\mathrm{j}}(\widehat{\mathbf{L}} - \widehat{\mathbf{L}}^*), \tag{3.11}$$

respectively. For the purpose of further discussion it is advantageous to introduce the notation $\widehat{\mathbf{Z}} = \widehat{\mathbf{L}}_\mathrm{tan}$. The operator $\widehat{\mathbf{Z}}$, called *impedance matrix*, maps $\boldsymbol{J}_\mathrm{s}$ onto $\boldsymbol{E}_\mathrm{tan}$.

3.1.3. Characteristic modes

The complex operator $\widehat{\mathbf{Z}}$, which has dimension of impedance, can be split into symmetric and real operators $\widehat{\mathbf{R}}$ (real part of $\widehat{\mathbf{Z}}$) and $\widehat{\mathbf{X}}$ (imaginary part of $\widehat{\mathbf{Z}}$). The characteristic modes are solutions of the eigenvalue problem

$$\widehat{\mathbf{X}}\boldsymbol{J}_{\mathrm{s},m} = \lambda_m \widehat{\mathbf{R}}\boldsymbol{J}_{\mathrm{s},m}, \tag{3.12}$$

with real eigenvalues λ_m and eigenvectors $\boldsymbol{J}_{\mathrm{s},m}$. The $\boldsymbol{J}_{\mathrm{s},m}$ are called *characteristic, modal currents or eigencurrents* on the surface S of the conducting body. Since the λ_m are frequency dependent, the *eigencurrents* $\boldsymbol{J}_{\mathrm{s},m}$ also are frequency dependent. The range of eigenvalues is from $-\infty$ to $+\infty$. In general, $\lambda_m \to 0$ with increasing size of the conducting body relative to wavelength. Characteristic modes which feature positive eigenvalues are called *inductive characteristic modes* and those which have negative eigenvalues are referred to as *capacitive characteristic modes*. For the purpose of further discussion, it is convenient to scale $\boldsymbol{J}_\mathrm{s}$ and $\boldsymbol{J}_{\mathrm{s},m}$, which are peak values, to the total radiated power P_0, as

$$P_0 = \frac{1}{2}\langle \boldsymbol{J}_{\mathrm{s},m} | \widehat{\mathbf{R}}\boldsymbol{J}_{\mathrm{s},m} \rangle_{S_0}. \tag{3.13}$$

The orthogonality relation between the mth and nth characteristic mode then takes the form

$$\langle \boldsymbol{J}_{\mathrm{s},m} | \widehat{\mathbf{R}}\boldsymbol{J}_{\mathrm{s},n} \rangle_{S_0} = 2P_0\delta_{mn}, \tag{3.14}$$

$$\langle \boldsymbol{J}_{\mathrm{s},m} | \widehat{\mathbf{X}}\boldsymbol{J}_{\mathrm{s},n} \rangle_{S_0} = \lambda_m 2P_0\delta_{mn}, \tag{3.15}$$

$$\langle \boldsymbol{J}_{\mathrm{s},m} | \widehat{\mathbf{Z}}\boldsymbol{J}_{\mathrm{s},n} \rangle_{S_0} = (1 + \mathrm{j}\lambda_m) 2P_0\delta_{mn}, \tag{3.16}$$

where δ_{mn} is the Kronecker delta (1 for $m = n$ and 0 otherwise). The surface current density $\boldsymbol{J}_\mathrm{s}$ on a conducting body can be represented as a linear combination of scaled modal surface current densities $\boldsymbol{J}_{\mathrm{s},m}$ as

$$\boldsymbol{J}_\mathrm{s} = \sum_m \alpha_m \boldsymbol{J}_{\mathrm{s},m}, \tag{3.17}$$

with α_m denoting complex expansion coefficients of the surface current density. Further, the inner product between the surface current density of the mth characteristic mode and the total current density gives

$$\langle \boldsymbol{J}_{\mathrm{s},m} | \widehat{\mathbf{R}} \boldsymbol{J}_\mathrm{s} \rangle_{S_0} = \langle \boldsymbol{J}_{\mathrm{s},m} | \widehat{\mathbf{R}} \sum_n \alpha_n \boldsymbol{J}_{\mathrm{s},n} \rangle_{S_0} = \alpha_n 2P_0 \delta_{mn}, \tag{3.18}$$

$$\alpha_m = \frac{1}{2P_0} \langle \boldsymbol{J}_{\mathrm{s},m} | \widehat{\mathbf{R}} \boldsymbol{J}_\mathrm{s} \rangle_{S_0} = \frac{1}{(1+\mathrm{j}\lambda_m)2P_0} \langle \boldsymbol{J}_{\mathrm{s},m} | \widehat{\mathbf{Z}} \boldsymbol{J}_\mathrm{s} \rangle_{S_0}. \tag{3.19}$$

Scaling of the surface current density according to (3.13) renders the sum of squares of the magnitudes of the expansion coefficients unity

$$\frac{1}{2} \langle \boldsymbol{J}_\mathrm{s} | \widehat{\mathbf{R}} \boldsymbol{J}_\mathrm{s} \rangle_{S_0} = P_0 \sum_n \sum_m \alpha_n^* \alpha_m \delta_{mn} = P_0 \sum_m |\alpha_m|^2 = P_0. \tag{3.20}$$

The magnitude of a coefficient α_m indicates how strongly the particular modal surface current density $\boldsymbol{J}_{\mathrm{s},m}$ contributes to the total surface current density $\boldsymbol{J}_\mathrm{s}$ at a given frequency.

3.1.4. Modal power factors

The purpose of this section is to discuss physical meaning of eigenvalues and subsequently to define modal power factors as an alternative and practically useful representation of eigenvalues. The first step is to relate eigenvalues to physical quantities such as the total radiated power P_rad and reactive energy. If the domain G is bounded outside by a sphere in the far-field region S_∞ and inside by the surface S_0 of the body (see Fig. F.1) then using the complex Poynting theorem, used in e.g. [74, 12], gives

$$\frac{1}{2} \oiint_S (\boldsymbol{E} \times \boldsymbol{H}^*) \boldsymbol{n} \, \mathrm{d}S = P_\mathrm{rad} + 2\,\mathrm{j}\,\omega(\langle W_\mathrm{M} \rangle - \langle W_\mathrm{E} \rangle), \tag{3.21}$$

where vector $\boldsymbol{n}$ is normal to the surface S_0 of the body and is pointing towards the far-field sphere surface S_∞. $\langle W_\mathrm{M} \rangle$ is the time average of stored magnetic

energy and $\langle W_{\mathrm{E}} \rangle$ is the time average of the stored electric energy. On the surface S_0 of a body $\boldsymbol{E}|_{S_0} = -\widehat{\mathbf{Z}}[\boldsymbol{J}_{\mathrm{s}}]$. Further, since the scalar triple product is invariant under circular shift and the equivalence principle holds (i.e. $\boldsymbol{J}_{\mathrm{s}} = \boldsymbol{n} \times \boldsymbol{H}|_{S_0}$) it is easy to obtain

$$(\boldsymbol{E} \times \boldsymbol{H}^*)\boldsymbol{n} = (\boldsymbol{n} \times \boldsymbol{H}^*)\widehat{\mathbf{Z}}\boldsymbol{J}_{\mathrm{s}} = \boldsymbol{J}_{\mathrm{s}}^*\widehat{\mathbf{Z}}\boldsymbol{J}_{\mathrm{s}}. \tag{3.22}$$

Therefore, the power balance relation can be written as

$$\frac{1}{2}\langle \boldsymbol{J}_{\mathrm{s}}^* | \widehat{\mathbf{Z}}\boldsymbol{J}_{\mathrm{s}} \rangle_{S_0} = P_{\mathrm{rad}} + 2\,\mathrm{j}\,\omega(\langle W_{\mathrm{M}} \rangle - \langle W_{\mathrm{E}} \rangle) \tag{3.23}$$

Use of the orthogonality relation (3.16) with respect to the mth characteristic mode allows to rewrite (3.23) into

$$P_0(1 + \mathrm{j}\,\lambda_m) = P_0 + 2\,\mathrm{j}\,\omega(\langle W_{\mathrm{M},m} \rangle - \langle W_{\mathrm{E},m} \rangle). \tag{3.24}$$

Comparison of the imaginary parts on the lhs and the rhs of (3.24) leads to

$$\lambda_m = 2\omega \frac{\langle W_{\mathrm{M},m} \rangle - \langle W_{\mathrm{E},m} \rangle}{P_0}. \tag{3.25}$$

The resonance occurs when $\langle W_{\mathrm{M},m} \rangle = \langle W_{\mathrm{E},m} \rangle$ which leads to $\lambda_m = 0$. Eigenvalues are proportional to the difference between time average of stored magnetic energy and time average of stored electric energy. For a single characteristic mode *modal power factors* is defined as ratio of the total radiated power to the apparent power. Thus, using (3.25) it can be shown that the *modal power factors* are given by

$$p_{\mathrm{f},m} = \left| \frac{1}{1 + \mathrm{j}\lambda_m} \right|^2. \tag{3.26}$$

Modal power factors are useful as an alternative representation of eigenvalues. Higher order modes with high reactive power will have diminishing contribution to the radiated power. The notion of modal power factor does not discriminate between capacitive and inductive characteristic modes. The modal power factors are similar to, so called, modal significance [93]. However, it makes sense to use $p_{\mathrm{f},m}$ as an alternative representation of eigenvalues because of its physical meaning. It depends only on the shape and size of the conducting body and takes convenient interval $[0, 1]$.

3.2. Characteristic Mode Impedances

3.2.1. Definition

The purpose of this subsection is to define characteristic mode impedances and discuss their application in antenna design. The impedance of the mth characteristic mode is defined via *Rayleigh quotient* [67] (pp. 176–180) as

$$Z_m := \frac{\langle \boldsymbol{J}_{\mathrm{s},m} | \widehat{\mathbf{Z}} \boldsymbol{J}_{\mathrm{s},m} \rangle_{S_0}}{\langle \boldsymbol{J}_{\mathrm{s},m} | \boldsymbol{J}_{\mathrm{s},m} \rangle_{S_0}}. \tag{3.27}$$

Using orthogonality relation (3.16) the impedance of a characteristic mode becomes

$$Z_m := \frac{\langle \boldsymbol{J}_{\mathrm{s},m} | \widehat{\mathbf{R}} \boldsymbol{J}_{\mathrm{s},m} \rangle_{S_0}}{\langle \boldsymbol{J}_{\mathrm{s},m} | \boldsymbol{J}_{\mathrm{s},m} \rangle_{S_0}} (1 + \mathrm{j}\,\lambda_m), \tag{3.28}$$

where R_m is the radiation resistance of a characteristic mode is defined by

$$R_m := \frac{\langle \boldsymbol{J}_{\mathrm{s},m} | \widehat{\mathbf{R}} \boldsymbol{J}_{\mathrm{s},m} \rangle_{S_0}}{\langle \boldsymbol{J}_{\mathrm{s},m} | \boldsymbol{J}_{\mathrm{s},m} \rangle_{S_0}}. \tag{3.29}$$

Note that the nominator of (3.29) equals $2P_0$ due to scaling (3.13). Characteristic mode radiation resistance R_m depends on the shape of the body which determines magnitude of the surface current density over frequency, i.e. $i_m^2 = \langle \boldsymbol{J}_{\mathrm{s},m} | \boldsymbol{J}_{\mathrm{s},m} \rangle_{S_0}$ in the denominator of (3.29). Note that the radiation resistance R_m defined by (3.29) is the far-field property of a characteristic mode and therefore it is a different quantity than the radiation resistance discussed in the subsection 3.4.3. The radiation resistance in section 3.4.3 refers to the near-field considerations relative to a fictitious small coupler. Using (3.28) and (3.29) the impedance of a characteristic mode is given by [94, 90, 95]

$$Z_m := R_m + \mathrm{j}\,X_m = R_m(1 + \mathrm{j}\,\lambda_m). \tag{3.30}$$

The reactance of a characteristic mode is the product $R_m \lambda_m$.

The definition of characteristic mode impedance allows to further consider introduction of characteristic mode voltages V_m^{ex}, for a given excitation, and characteristic mode currents $I_m = \alpha_m i_m$, where α_m are the surface current density expansion coefficients after (3.17). The total surface current density

Fig. 3.1.: Simple circuit representation of a characteristic mode. V^{ex} is the characteristic mode voltage which is actually present for the given excitation and I_m is the corresponding actual characteristic mode.

can be represented as a sum of real vectors $\boldsymbol{e}_m$, where $\langle \boldsymbol{e}_m | \boldsymbol{e}_m \rangle_{S_0} = 1$, with expansion coefficients I_m

$$\boldsymbol{J}_{\mathrm{s}} = \sum_m \boldsymbol{e}_m I_m, \tag{3.31}$$

where $\boldsymbol{e}_m = i_m^{-1} \boldsymbol{J}_{\mathrm{s},m}$ is the normalized surface current density of a characteristic mode. Following eq.(25-27) from [10] it is easy to obtain

$$\widehat{\mathbf{Z}} \boldsymbol{J}_{\mathrm{s}} - \boldsymbol{E}_{\tan}^{\mathrm{ex}} = 0 \tag{3.32}$$

$$\widehat{\mathbf{Z}} \sum_m \boldsymbol{e}_m I_m - \boldsymbol{E}_{\tan}^{\mathrm{ex}} = 0 \tag{3.33}$$

$$\sum_m \langle \boldsymbol{e}_n | \widehat{\mathbf{Z}} \boldsymbol{e}_m \rangle_{S_0} I_m - \langle \boldsymbol{e}_n | \boldsymbol{E}_{\tan}^{\mathrm{ex}} \rangle_{S_0} = 0. \tag{3.34}$$

Due to the orthogonality relation $\langle \boldsymbol{e}_m | \widehat{\mathbf{Z}} \boldsymbol{e}_n \rangle_{S_0} = R_n (1 + \mathrm{j}\, \lambda_n) \delta_{mn}$ the above relation leads to

$$Z_m I_m = (R_m + \mathrm{j}\, X_m) I_m = \langle \boldsymbol{e}_m | \boldsymbol{E}_{\tan}^{\mathrm{ex}} \rangle_{S_0} =: V_m^{\mathrm{ex}} \tag{3.35}$$

The right hand side $V_m^{\mathrm{ex}} := \langle \boldsymbol{e}_m | \boldsymbol{E}_{\tan}^{\mathrm{ex}} \rangle_{S_0}$ is the characteristic mode voltage which is actually present for the given excitation and I_m the corresponding actual characteristic mode current. This may be considered the starting point for an ECM of a characteristic mode (see Fig. 3.1). The coefficients of expansion are

$$I_m = \frac{V_m^{\mathrm{ex}}}{Z_m} = \alpha_m i_m. \tag{3.36}$$

3.2.2. Application of characteristic mode impedances

The definition of the characteristic mode impedances allows further to define characteristic mode bandwidths and approximately obtain characteristic mode radiation quality factors. Both quantities allow to determine an approximate bandwidth of an antenna before the antenna is designed. Estimation of characteristic mode radiation quality factors and bandwidths is studied in section 3.3.

An other important application of characteristic mode impedances is their use in construction of ECMs of characteristic modes. Synthesis of characteristic mode ECMs from characteristic mode impedances was shown in [95] using as an example a thin wire structure. The approach can be extended toward arbitrary structures if higher order ECMs are used for high order characteristic modes. In this dissertation it is shown that characteristic mode ECMs can be successfully used to derive physics based ECMs of capacitive and inductive couplers (see section 3.5).

3.2.3. Numerical examples

For illustrative purposes two canonical shapes are considered. The sphere with radius $a = 0.1$ m and the cylinder with length $\ell = 0.06$ m and diameter $d = 0.01$ m were chosen as examples. Characteristic mode impedances of the first two characteristic modes were calculated using (3.27) over a broad range of ka's for both volumes. However, due to the fact that the present thesis focuses, for the most part, on design of small multiport antennas only values of $ka < 1$ remain of interest. Nevertheless, observations made in the present subsection are important for subsequent consideration of characteristic mode radiation quality factors and bandwidths discussed in section 3.3 of the present chapter.

Sphere

The radiation resistance and reactance of the 1st characteristic mode are shown in Fig. 3.2 (blue). The radiation resistance of this characteristic mode increases with frequency until the maximum value of nearly $75\ \Omega$ is reached at $ka \approx 1.4$ which corresponds to half-wavelength resonance. Then it decreases with frequency to the minimum of approximately $0.3\ \Omega$ at about double the ka, i.e. $ka \approx 2.8$, which is the non-radiating full-wavelength resonance. It is known

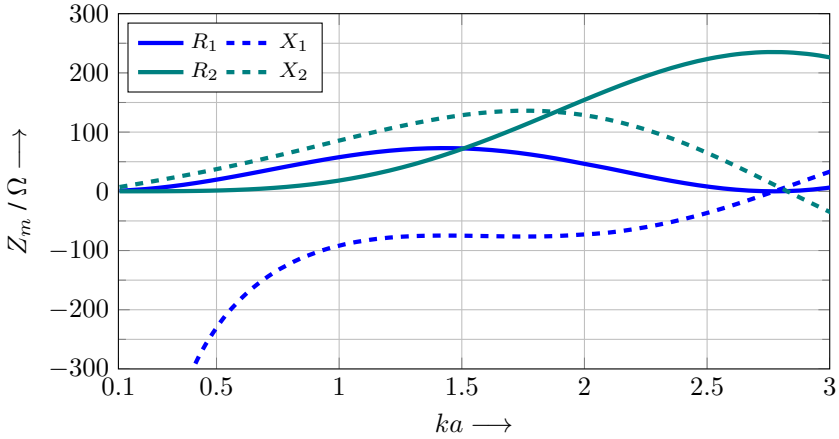

Fig. 3.2.: Characteristic mode impedance Z_m versus ka of the 1st (blue) and the 2nd (teal) characteristic mode on the sphere obtained using (3.27).

that this oscillatory behavior persists for higher ka's. The reactance of the 1st characteristic mode increases with frequency from negative to zero which is consistent with that fact that its a capacitive characteristic mode. Zero value of the reactance (resonance) occurs at $ka \approx 2.8$. From $ka \approx 1$ to $ka \approx 2$ the reactance remains nearly constant at about $-75\ \Omega$.

The teal lines in Fig. 3.2 show the radiation resistance and reactance of the 2nd characteristic mode. The behavior of the the radiation resistance and reactance of this characteristic mode is significantly different than that of the 1st characteristic mode. This characteristic mode remains inductive (positive reactance) until $ka \approx 2.8$. As in the case of the 1st characteristic mode the resonance of the 2nd characteristic mode also occurs at $ka \approx 2.8$. However, for this characteristic mode it is the half-wavelength resonance. The radiation resistance increases with frequency and reaches the local maximum value of about $240\ \Omega$ at $ka \approx 2.8$ (resonance).

Cylinder

The radiation resistance and reactance of the 1st characteristic mode are shown in Fig. 3.3 (blue). The radiation resistance is about $50\ \Omega$ at $ka \approx 1.6$ (which corresponds to $\ell/\lambda = 0.5$). The reactance increases with frequency from neg-

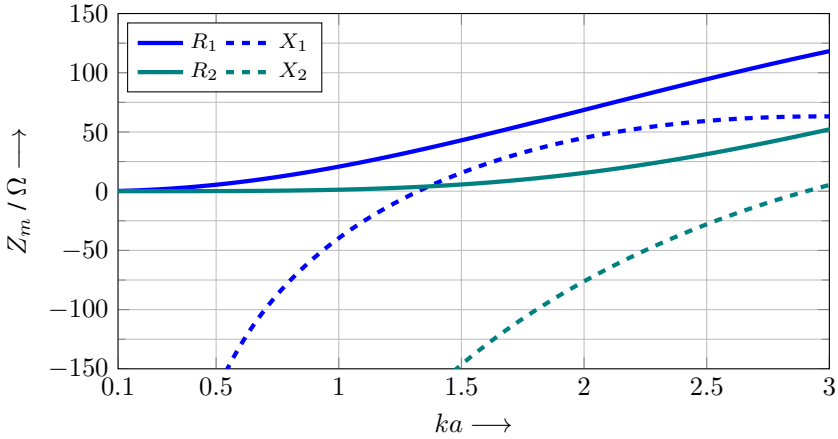

Fig. 3.3.: Characteristic mode impedance Z_m versus ka of the 1st (blue), 2nd (teal) characteristic mode on the cylinder ($\ell/d = 6$) obtained using (3.27).

ative to positive values and attains zero value at approximately $ka \approx 1.35$. The radiation resistance and reactance of the 2nd characteristic mode are shown in Fig. 3.3 (teal). The values of the radiation resistance and its increase with frequency are smaller than in case of the 1st characteristic mode. The reactance is also much higher for this characteristic mode and the resonance occurs at approximately double the resonance of the 1st characteristic mode, i.e. at $ka \approx 2.7$.

3.3. Characteristic Mode Bandwidths and Radiation Quality Factors

3.3.1. Characteristic mode bandwidths

Since characteristic mode impedances are explicitly known from (3.30) it is possible to directly calculate characteristic mode bandwidths numerically (see Chapter 5 section 5.2). The bandwidth of the mth characteristic mode, evaluated numerically using characteristic mode impedance and assuming a lossless π-type matching network, corresponds to the bandwidth of a fictitious single feed antenna designed to feature approximately the same surface current den-

sity as the mth characteristic mode. Therefore, it is possible to treat the bandwidth defined via Z_m as an upper bound for what can be achieved once an antenna is designed. No recourse to any approximate expressions for the characteristic mode radiation quality factors is necessary. However, the radiation quality factor remains the quantity, which under certain conditions, is convenient for estimation of bandwidth without full inspection of the frequency dependence of Z_m. The fractional 7 dB bandwidth of the mth characteristic mode can be approximated (assuming single narrowband resonance) using an expression given in [70], as

$$b_m^{7\mathrm{dB}} = \frac{1}{Q_{\mathrm{rad},m}}. \tag{3.37}$$

The relation holds for $Q_{\mathrm{rad},m} > 4$ as stated in [71]. Numerical results, shown in subsection (3.3.3), illustrate the validity of this statement.

3.3.2. Estimation of characteristic mode radiation quality factors

The radiation quality factor after [75, 72] is the ratio of the maximum of the time-average electric energy or magnetic energy, stored in the near-field, to the total radiated energy per cycle. The definition assumes that the input impedance can be made real at any given frequency using a lossless external matching circuit. Using the above definition, formally, the radiation quality factor of the mth characteristic mode is given by

$$Q_{\mathrm{rad},m}(\omega) = \frac{2\omega \max\left(\langle W_{\mathrm{M},m}\rangle, \langle W_{\mathrm{E},m}\rangle\right)}{P_{\mathrm{rad},m}}, \tag{3.38}$$

where $\langle W_{\mathrm{M},m}\rangle$ is the time-average stored magnetic energy and $\langle W_{\mathrm{E},m}\rangle$ is the time-average stored electric energy and $P_{\mathrm{rad},m}$ is the radiated power. Radiation quality factor is an important descriptive parameter for electrically small and multiport antennas which is frequently used to estimate the bandwidth. The bandwidth remains a measurable quantity whereas the radiation quality factor is not. However, ability to estimate it for the dominant and the first few higher order characteristic modes of an arbitrarily shaped volume using analytical expression is of significant practical interest. Further, it allows to estimate the attainable bandwidth (for sufficiently high radiation quality factors) without neither prior design of the antenna physical structure nor location of the feeds.

The goal of this section is the introduction of a few different expressions for calculation of characteristic mode radiation quality factors and illustrate their accuracy and usefulness.

Expression derived using electromagnetic field theory

In order to obtain characteristic mode radiation quality factors over broad range of frequencies using the definition (3.38) and without taking recourse to any ECM it is necessary to calculate separately the time averaged stored magnetic and electric energies $\langle W_{\mathrm{M},m} \rangle$ and $\langle W_{\mathrm{E},m} \rangle$, respectively. Detailed derivation using complex Poynting theorem and eq.(8-53) [92] is given in Appendix F. The derivation results in the same expression as that shown in [96, 97]

$$Q_{\mathrm{rad},m}(\omega) = \max\left(\frac{\omega}{4P_0} \left\langle \boldsymbol{J}_{\mathrm{s},m} \middle| \frac{\partial \widehat{\mathbf{X}}}{\partial \omega} \boldsymbol{J}_{\mathrm{s},m} \right\rangle_{S_0} \pm \frac{\lambda_m}{2} \right). \tag{3.39}$$

The relation contains the derivative of the imaginary part of $\widehat{\mathbf{Z}}$ and the surface current density $\boldsymbol{J}_{\mathrm{s},m}$ integration over the surface S of a body and an eigenvalue λ_m. In principle, use of (3.39) is not limited to a certain shape but can be applied to an arbitrarily shaped volume. Illustrative examples, considered in detail later in this section, show the practical application of the relation (3.39). (3.39) remains a good approximation for small ka's or sufficiently high values of $Q_{\mathrm{rad},m}$ as noted in [96, 97].

Simplified expression for characteristic mode radiation quality factors

At first glance the expression (3.39) after [96, 97] exposes similarity to the well-known expression by Geyi for [74]. After substitution of $X_m = R_m \lambda_m$, (F.37) and (3.29) into (3.39) one obtains

$$Q_{\mathrm{rad},m}(\omega) = \frac{\omega}{2R_m} \max\left(\frac{\partial \widetilde{X}_m}{\partial \omega} \pm \frac{X_m}{\omega} \right), \tag{3.40}$$

where the derivative $\frac{\partial \widetilde{X}_m}{\partial \omega}$ is defined by (F.37) (see Appendix F). (3.40) is approximately the expression for the radiation quality factor given by Geyi

in [74]. If the change of characteristic mode surface current density over frequency is small then $\frac{\partial \widetilde{X}_m}{\partial \omega} \approx \frac{\partial X_m}{\partial \omega}$ and (3.40) can be expressed as

$$Q_{\mathrm{rad},m}(\omega) \approx \frac{\omega}{2R_m} \max\left(\lambda_m \frac{\partial R_m}{\partial \omega} \pm \lambda_m \frac{R_m}{\omega} + R_m \frac{\partial \lambda_m}{\partial \omega}\right). \tag{3.41}$$

Thus, in this case (3.41) requires only calculation of the derivative of characteristic mode reactance *not* a derivative of the imaginary part of the operator $\widehat{\mathbf{Z}}$ as in (3.39). (3.39) and (3.41) do not contain frequency derivative of the real part of characteristic mode impedance as does the expression introduced by Yaghjian in [71]. Therefore, both (3.39) and (3.41) remain only useful approximations which tend to break down in the vicinity of a resonance. The approximation of the radiation quality factor for the mth characteristic mode after [71], given by

$$Q_{\mathrm{rad},m}(\omega) = \frac{\omega}{2R_m} \sqrt{\left(\frac{\partial R_m}{\partial \omega}\right)^2 + \left(\lambda_m \frac{\partial R_m}{\partial \omega} + |\lambda_m| \frac{R_m}{\omega} + R_m \frac{\partial \lambda_m}{\partial \omega}\right)^2}, \tag{3.42}$$

typically matches very well with numerical results. However, it can be shown that in certain cases even this approximation of the bandwidth breaks down. According to [71] the inverse of any of the following expressions for radiation quality factor (3.39)–(3.42) leads to a useful approximation of the fractional 7 dB bandwidth for $Q_{\mathrm{rad},m} > 4$. Numerical illustration of this fact is shown in subsection 3.3.3.

Characteristic mode radiation quality factors at resonance

If the radiation quality factor is taken at resonance of a characteristic mode then, (3.39) reduces to the expression given in [12]

$$Q_{\mathrm{rad},m,0} = \frac{\omega_{m,0}}{2} \left|\frac{\mathrm{d}\lambda_m}{\mathrm{d}\omega}\right|_{\omega=\omega_{m,0}}, \tag{3.43}$$

where $\omega_{m,0}$ denotes the resonance radian frequency of the mth characteristic mode. The same result was given earlier by Harrington in [98]. Calculation of the radiation quality factor only at resonance brings about very little information. It only allows to compare radiation quality factors of different characteristic modes against each other at their respective resonance frequencies. Values

of radiation quality factors of the first few characteristic modes for typical mobile phone form factors calculated using (3.43) were reported in [12]. The majority of them are in the interval $[1, 5]$, thus estimation of characteristic mode fractional 7 dB bandwidth as the inverse of the radiation quality factor is burdened with high error [73] (see subsection 3.3.3). The radiation quality factor at resonance provides a valid starting point for further discussion. The expression (3.39) remains much more useful in practical applications since typically finding an estimate on the radiation quality factors is of interest for characteristic modes significantly below their respective resonance frequencies.

3.3.3. Numerical examples

The goal of this subsection is to show the usefulness of expressions (3.39)–(3.42) in obtaining characteristic mode radiation quality factors over a broad frequency range and their mutual agreement or lack thereof. The illustrative examples shall indicate the potential of the present analysis for predicting the minimum radiation quality factor of antennas designed with respect to the surface current density given by the characteristic modes on a given shape of the body. Three canonical shapes are considered here for illustration.

Sphere

The radiation quality factor of the 1st capacitive characteristic mode was calculated for the sphere using (3.39) and using approximate expressions given by Geyi [74] (3.41) and Yaghjian [71] (3.42) applied based on the knowledge of characteristic mode impedance defined by (3.27) (see Fig. 3.4, blue). The results are compared against the analytical expression given by Thal and Gustafsson [99, 100] (for TM_{10} spherical mode). Both of these analytical expressions take into account energy stored inside the sphere surrounding a body. They give approximately 1.5 times higher values of radiation quality factor than that given by analytical expression introduced by Chu [75] and re-examined by McLean [101] for linearly polarized lossless single mode antenna enclosed in a sphere. Both numerical and analytical results are in good agreement for $ka < 0.65$ (see Fig. 3.4). Note that according to [73] Thal's and Gustafsson's expressions are applicable for $ka < 0.65$. The radiation quality factor of the 1st capacitive characteristic mode attains its local minimum value at $ka \approx 1.4$ and local maximum value at $ka \approx 2.8$, which correspond to a half-wavelength and

full-wavelength resonances, respectively. In case of the 1st inductive characteristic mode all estimates of the radiation quality factor produce significantly different approximations from $ka \approx 1.25$ to $ka \approx 2.8$, where the latter value corresponds to the half-wavelength resonance. For $ka > 1$ and small values of radiation quality factor the results of (3.39), (3.41), and (3.42) mutually disagree. Furthermore, for $Q_{\mathrm{rad},m} < 4$ the inverse of the radiation quality factor does not approximate the fractional 7 dB bandwidth [73]. This statement can be shown to be true by means of the direct numerical calculation of the fractional 7 dB bandwidth using lossless π-type circuit to match characteristic mode impedance obtained from (3.27). Fig. 3.5 shows the comparison between the fractional 7 dB bandwidth calculated, using the above described numerical analysis, and that obtained as an inverse of the radiation quality factor after (3.39), (3.41), and (3.42). The maximum fractional 7 dB bandwidth is about 0.7 at $ka \approx 1.25$ (see Fig. 3.5, red). Analogous analysis, comparison and observations can be performed for the 1st inductive characteristic mode on the surface of the sphere (see Figs. 3.4, 3.5). Both analytical and numerical analysis suggest that in order to achieve equal bandwidths of both considered characteristic modes the electrical size of the sphere has to be approximately in the interval $ka \in [1.75, 1.9]$.

Cylinder

The radiation quality factor of the 1st characteristic mode for a cylinder, with aspect ratio $\frac{\ell}{d} = 6$, was calculated using (3.39) and compared against results obtained from (3.40) and (3.42) using beforehand calculated characteristic mode impedance after (3.27). The results were compared against the Gustafsson's analytical expression [100, 102] for a cylinder with the same aspect ratio (see Fig. 3.6). All results are in good mutual agreement for $ka < 1$ (see Fig. 3.4). Within this range of ka the radiation quality factor of the 1st characteristic mode is higher than 4, thus approximation of the fractional 7 dB bandwidth as the inverse of the radiation quality factor remains valid.

Thin long wire

Fig. 3.7 shows characteristic mode radiation quality factors obtained using (3.39) for the first three *characteristic modes* on a linear thin long wire over broad range of ka. Fig. 3.7 shows that the numerical result for the 1st characteristic mode is in an excellent agreement with Gustafsson's analytical ex-

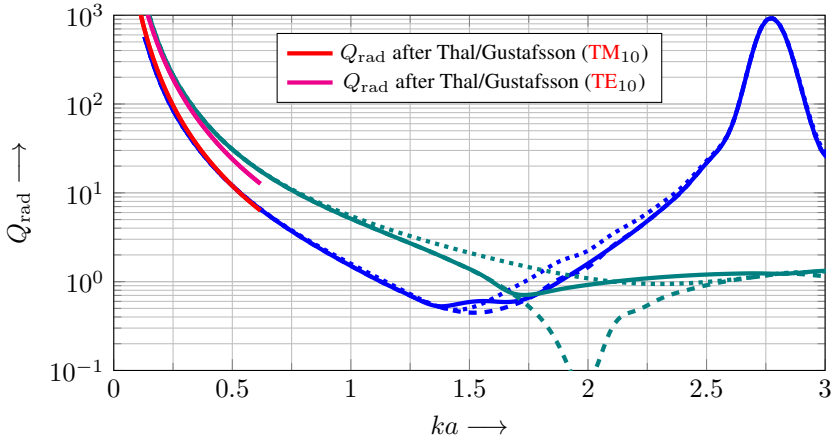

Fig. 3.4.: The radiation quality factor Q_{rad} of the 1st capacitive and inductive characteristic modes on the sphere obtained using (3.39) (solid blue and teal) compared to Geyi's [74] (dashed blue and teal) and Yaghjian's [71] (dotted blue and teal) expressions and analytical expression given by Thal and Gustafssson [99, 100, 102] for spherical modes TM_{10} (red) and TE_{10} (magenta).

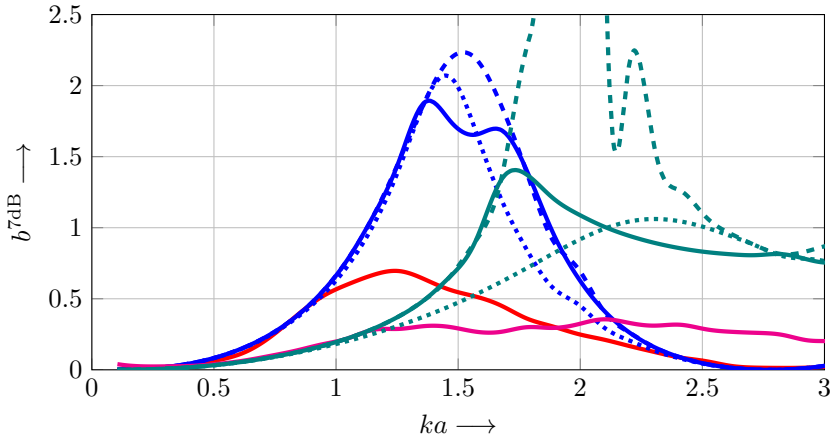

Fig. 3.5.: The fractional 7 dB bandwidth of the 1st capacitive and inductive characteristic modes on the sphere obtained using lossless matching with a π-type circuit (solid red and solid magenta, respectively) and comparison to the results obtained using (3.39) (solid blue and teal) and the comparison to Geyi's [74] (dashed blue and teal) and Yaghjian's [71] (dotted blue and teal) expressions.

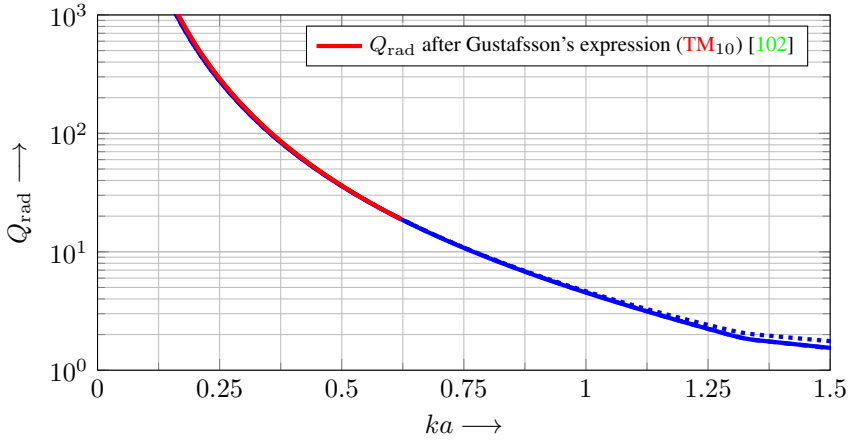

Fig. 3.6.: The radiation quality factor Q_{rad} of the 1st capacitive characteristic mode on a cylinder with $\frac{\ell}{d} = 6$ obtained using (3.39) (solid blue), (3.40) (dashed blue), and (3.42) (dotted blue), and comparison to the analytical expression given by Gustafssson [100, 102] for spherical mode TM_{10} on a cylinder with the same aspect ratio (solid red).

pression [100, 102] for $ka < 0.65$. Higher order characteristic modes feature significantly higher radiation quality factors.

Conclusions

The general conclusion is that aspect ratio of a body has direct impact on characteristic mode radiation quality factors. An approximately one dimensional body such as a thin electric dipole features very high aspect ratio thus the current can flow only along the length of the dipole. Therefore, resonances occur at $mf_{1,0}$ where $f_{1,0}$ is the resonance frequency of the 1st characteristic mode and $m \in M$ which can easily be seen in Fig. 3.7. It can be observed that the characteristic mode radiation quality factors increase by about 100 with the increase of the characteristic mode index m at $ka = 1$. The optimum, with respect to the ratio of volume to the surface, is the sphere. For the sphere it was shown in [97] that the radiation quality factor attains its minimum. In conclusion, use of characteristic modes in calculation of modal radiation quality factor by means of (3.39) provides a valid starting point in design of electrically small antennas and multiport antennas for MIMO application.

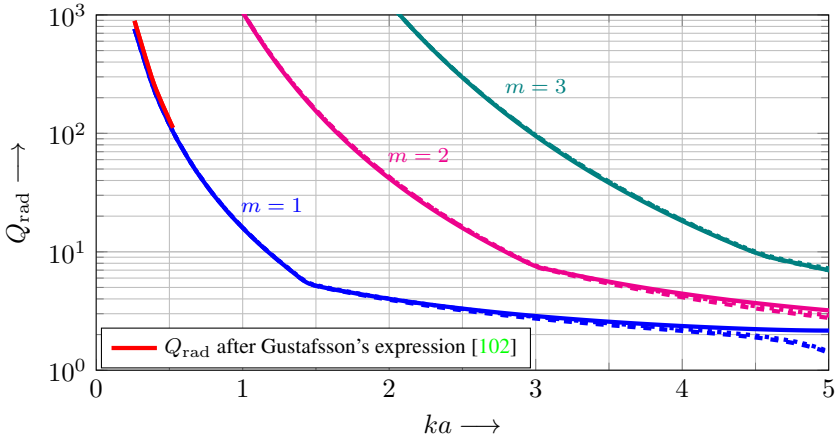

Fig. 3.7.: The radiation quality factor Q_{rad} versus electrical size ka for the first three capacitive characteristic modes on a thin long wire ($\frac{\ell}{d} = 50$) obtained using (3.39) (solid) and the comparison to Geyi's [74] (dashed) and Yaghjian's [71] (dotted) expressions and to analytical expression given by Gustafssson [100, 102] (red).

3.4. Excitation of Characteristic Modes

The theory of characteristic modes is of significant practical importance for design of antennas if the desired set of characteristic modes can be excited. The present section provides insight into the issue of effective excitation of characteristic modes. Qualitative discussion of this subject uses the notion of *reaction integral*. The dimensionless complex surface current density expansion coefficients α_m after (3.17) are given by

$$\alpha_m = \frac{\langle \boldsymbol{J}_{\mathrm{s},m} | \boldsymbol{E}^{\mathrm{ex}}_{\tan} \rangle_{S_0}}{(1 + \mathrm{j}\,\lambda_m) 2P_0}. \tag{3.44}$$

The term $\langle \boldsymbol{J}_{\mathrm{s},m} | \boldsymbol{E}^{\mathrm{ex}}_{\tan} \rangle_{S_0}$ (the *reaction integral*) contains the modal surface current density and the impressed external field as would be present over the surface of the chassis in absence of the chassis. By reciprocity, the reaction integral can be expressed as

$$\langle \boldsymbol{J}_{\mathrm{s},m} | \boldsymbol{E}^{\mathrm{ex}}_{\tan} \rangle_{S_0} = \iiint\limits_{V(\boldsymbol{J}^{\mathrm{ex}})} \boldsymbol{E}_m \boldsymbol{J}^{\mathrm{ex}} \,\mathrm{d}V, \tag{3.45}$$

where the characteristic mode electric field $\boldsymbol{E}_m$ produced by $\boldsymbol{J}_{\mathrm{s},m}$ alone in the absence of the chassis and the current density $\boldsymbol{J}^{\mathrm{ex}}$ is an impressed current density in the volume outside of the conducting body. The reaction integral for the actual structure can be written (by means of reciprocity and assuming delta-gap source [103]) as

$$\langle \boldsymbol{J}_{\mathrm{s},m} | \boldsymbol{E}^{\mathrm{ex}}_{\tan} \rangle_{S_0} = -u_m i^{\mathrm{ex}}, \tag{3.46}$$

where u_m is the voltage at the feed of a coupler due to the impressed surface current density $\boldsymbol{J}_{\mathrm{s},m}$ for zero current at the feed. $\boldsymbol{E}^{\mathrm{ex}}_{\tan}$ is the actual field distribution due to a point like source current i^{ex} on the body (including couplers). The excitation of the characteristic mode is obviously proportional to u_m. Determination of a suitable type of coupler and its optimum location so as to maximize u_m is subject of the next two subsections.

3.4.1. Fictitious capacitive coupler

For a small fictitious capacitive coupler (i.e. capacitive plate without a feed structure) u_m is the voltage at the feed of a coupler when the coupler is not connected to the chassis (only an impressed current i^{ex} flowing from body into the coupler is considered) (see Fig. 3.8a). The voltage u_m can be obtained from the local (near-field) electric field $\boldsymbol{E}_m$ of a characteristic mode. In order for a capacitive coupler to strongly excite the mth characteristic mode the coupler has to be placed where the voltage u_m is the maximum under the constraint for coupler's distance from the chassis. The reaction integral for capacitive couplers becomes maximum if the plate has a shape of an equipotential surface (see Fig. 3.8a, blue lines) and is placed near the maximum of the modal charge density. The larger the distance of the capacitive plate from the chassis the higher the voltage u_m. Further, assuming now that the coupler is no longer fictitious but is connected to the chassis via feed and a real current source is used (see Fig. 3.9a), the reaction increases with frequency and area of the plate. In other words the volume V occupied by a capacitive coupler should be maximized. However, the volume for antennas in small mobile wireless devices is usually constrained so that even a trade-off between the area and the distance cannot be exploited as both parameters are often fixed. Qualitative discussion of optimum capacitive coupler placement, supported by numerical examples, was given in [12]. The numerical evaluation of the voltage u_m and subsequently radiation resistance of a fictitious coupler R_m^{FC} are shown in the subsection 3.4.3 for the example of a $60 \times 120\ \mathrm{mm}^2$ smartphone ground plane.

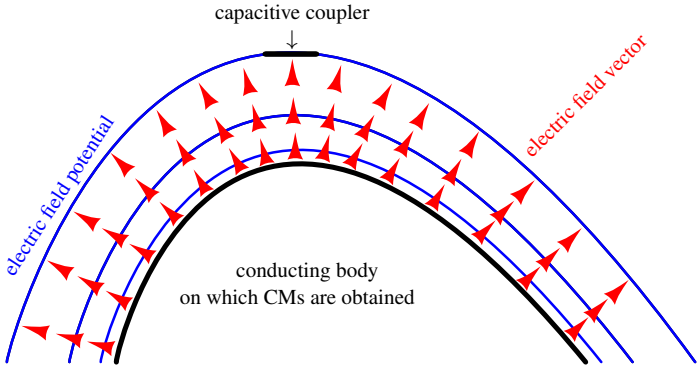

(a) capacitive coupler

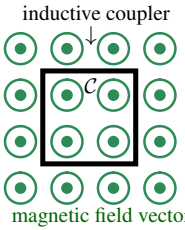

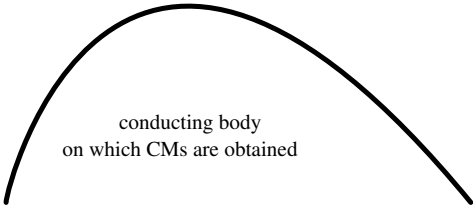

(b) inductive coupler

Fig. 3.8.: Simple representation of fictitious couplers (a) small capacitive coupler (plate) and (b) small inductive coupler (loop) at small distance from a conducting body on which characteristic modes were obtained. Simple graphic representation of an electric field (red arrows) and its potential (blue lines), and magnetic field (green circles) of the 1st characteristic mode are shown under local gradient field approximation.

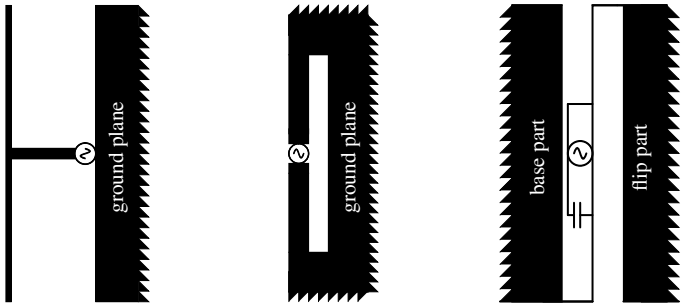

(a) capacitive coupler (b) inductive coupler I (c) inductive coupler II

Fig. 3.9.: Three different state of the art types of couplers: (a) capacitive coupler (capacitive plate), (b) inductive coupler (current loop) used in conjunction with smartphone chassis as shown in [19, 20, 22, 21], and (c) inductive coupler introduced in [104] for clamshell phones.

For design of multiport antennas it is necessary to identify the locations of couplers so as to either selectively excite the desired characteristic modes or to be able to effectively excite orthogonal superpositions of characteristic modes.

3.4.2. Fictitious inductive coupler

A fictitious inductive coupler (thin wire loop along the contour $\mathcal{C} = \partial\mathcal{S}$) with impressed current i^{ex} along the orientation of $\mathcal{C}$ is shown in Fig. 3.8b. $-u_m$ is the voltage induced in the loop by magnetic field $\boldsymbol{H}_m$ of the mth characteristic model. The reaction integral for an inductive couplers becomes maximum if the loop is placed in the maximum of modal magnetic flux and properly oriented. Inductive couplers are capable of exciting both inductive and capacitive characteristic modes. Reverting to a "real" inductive coupler (see Fig. 3.9bc), where the loop is connected to the chassis, excitation of capacitive characteristic modes using practical inductive couplers was shown in [104] and more recently in [19, 20, 21, 22]. An inductive coupler can also be realized as a slot in the conducting body. The slot has to be placed near a maximum of the surface current density of the characteristic mode which is to be excited. Moreover, the area of the slot has to be maximized in order to strongly excite the desired characteristic mode. Obviously, while maximization of the length of a slot may not be an issue, width is typically constrained in case of mobile wireless devices.

3.4.3. Radiation resistance of fictitious couplers

Theory

In the previous section a qualitative discussion of an optimum coupler placement based on the notion of reaction integral and assuming idealized fictitious couplers was given. In this section the goal is to provide a quantitative description of interaction between fictitious couplers and the chassis. For a single fictitious coupler (see Fig. 3.8) the real part of its self-impedance is the radiation resistance. To simplify the discussion assume that the coupler in question is a capacitive coupler. According to the statements given in the previous section it shall be placed in an equipotential surface at some distance from the chassis. A current is impressed but no feed structure is considered. If all characteristic modes under consideration are scaled to P_0 after (3.13) then the power radiated by the mth characteristic mode $P_{\mathrm{rad},m}$ is given by

$$P_{\mathrm{rad},m} = P_0 \left|\alpha_m\right|^2 = P_0 \left| \frac{\langle \boldsymbol{J}_{\mathrm{s},m} | \boldsymbol{E}^{\mathrm{ex}}_{\tan} \rangle_{S_0}}{(1+\mathrm{j}\,\lambda_m) 2P_0} \right|^2 = \frac{\left|\langle \boldsymbol{J}_{\mathrm{s},m} | \boldsymbol{E}^{\mathrm{ex}}_{\tan} \rangle_{S_0}\right|^2}{(1+\lambda_m^2) 4P_0}. \tag{3.47}$$

With the reaction integral given by (3.46) one obtains

$$P_{\mathrm{rad},m} = \frac{\left|u_m\right|^2}{(1+\lambda_m^2) 2P_0} \frac{1}{2} \left|i^{\mathrm{ex}}\right|^2. \tag{3.48}$$

This expression allows to identify the contribution of the mth characteristic mode to the radiation resistance of a fictitious coupler as

$$R^{\mathrm{FC}}_{\mathrm{rad},m} = \frac{1}{(1+\lambda_m^2)} \left| \frac{u_m}{\sqrt{2P_0}} \right|^2, \tag{3.49}$$

where the superscript "FC" denotes fictitious coupler. The total radiated power is the sum of modal contributions (3.20) which implies that

$$R^{\mathrm{FC}}_{\mathrm{rad}} = \sum_m R^{\mathrm{FC}}_{\mathrm{rad},m}, \tag{3.50}$$

i.e. the radiation resistance of a fictitious coupler is the sum of contributions from a number of characteristic modes. Expression (3.49) makes explicit that $R^{\mathrm{FC}}_{\mathrm{rad},m}$ depends on frequency via eigenvalues λ_m and voltages u_m (near field). The radiation resistance of a fictitious coupler is proportional to the magnitude squared of the modal voltage u_m and attains the maximum at resonance $\omega_{m,0}$.

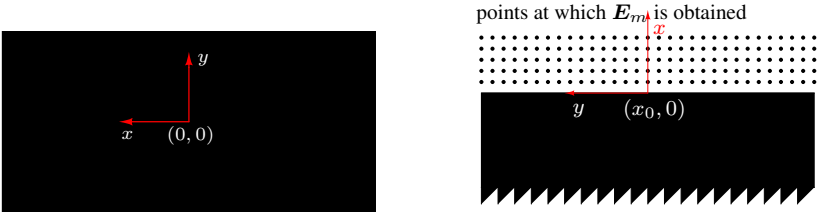

Fig. 3.10.: $60 \times 120\ \mathrm{mm}^2$ ground plane with a coordinate system used in calculation of characteristic mode near-field electric fields, voltages and radiation resistances of a fictitious capacitive coupler.

However, it is important to note that λ_m and u_m are not independent quantities. u_m has to be obtained from line integral and contour integral of the near-field electric field $\boldsymbol{E}_m$ for a capacitive coupler and an inductive coupler, respectively. An illustrative numerical example with important notes related to the practical application of (3.49) and its limitations are given later in the next subsection.

Numerical Example

As an example for calculation of modal voltage u_m and radiation resistance R_m^{FC}, using (3.49), consider a $60 \times 120\ \mathrm{mm}^2$ ground plane of a typical smartphone. Computation of both quantities allows to illustrate criteria for placement of capacitive couplers. The center of the coordinate system is located in the geometric center of the ground plane. The x-axis is perpendicular to the width of the chassis while y-axis is perpendicular to the length of the chassis (see Fig. 3.10). The near-field electric field $\boldsymbol{E}_1$ of the first capacitive characteristic mode was obtained in the vicinity of the chassis along the y-axis over a set of distances d of the fictitious capacitive coupler from the short edge of the ground plane. The voltage $u_1(d)$, due to this characteristic mode,

$$u_1(d) = \int_{x_0}^{x_0+d} \boldsymbol{E}_1 \, \mathrm{d}\boldsymbol{x} \tag{3.51}$$

was calculated along the y-axis at 900 MHz (see Fig. 3.10) for various distance d of a fictitious capacitive coupler from the ground plane (see Fig. 3.11a). It is apparent that the larger the distance d of the capacitive coupler from the edge

of the chassis the higher the voltage. However, this increase is not linear with distance. It is most rapid over the distance of the first few millimeters from the chassis. The larger the distance from the ground plane, the less significant the increase of the voltage becomes. For an infinitesimally thin sheet the voltage u_1 is given by $u_1 \sim \Re(\sqrt{x + \mathrm{j}\, z})$. In the case under study $z = 0$ (u_1 is obtained in the xy plane), therefore the modal voltage is approximately proportional to the square root of the distance x. This fact can also be read from the numerical results (see Fig. 3.11). The results also indicates that it is sufficient for a fictitious capacitive coupler to be located at a distance corresponding to about one-tenth of the length of the ground plane to obtain high voltage u_1 (hence the term *small coupler*). An other useful observation is that the voltage increases when moving from the center of the short edge to the corners of the chassis. This is to be expected since the surface charge density is the maximum at the corners. Therefore, the optimum coupler placement and the feed with respect to the maximization of the voltage u_1 and in turn maximization of the reaction integral after (3.46) is in the four corners of the chassis [12, 13, 15].

According to (3.49) the radiation resistance of a fictitious capacitive coupler placed at the equi-potential surface is proportional to the sum of the square magnitudes of the modal voltages u_m. At 900 MHz contribution of the 1st capacitive characteristic mode among all other characteristic modes to the radiation resistance is the most significant (see Fig. 3.11b). From the sum of the first 24 characteristic mode's radiation resistances it is apparent that the contribution of the higher order characteristic modes to the radiation resistance is small but becomes more prominent when moving from the center of the short edge toward corners of the ground plane (see Fig. 3.11b, red curve). The radiation resistance increases approximately in a linear fashion with distance d of the coupler from the chassis. In practice, a realistic, small coupler is connected to the chassis via feed which changes both the voltage u_1 and impressed current i^{ex} in the reaction integral rendering the present analysis insufficient. However, this does not invalidate the general principles of the analysis and its basic conclusions. Realistic small capacitive coupler comprising $1 \times 9\,\mathrm{mm}^2$ strip, where $1\,\mathrm{mm}$ is left for source placement, is shown in Fig. 3.12b. Extensive FDTD simulations, where position of the coupler along the short edge of the ground plane y was a parameter of the analysis (from $y = -30\,\mathrm{mm}$ to $y = 30\,\mathrm{mm}$), were performed. The values of realistic capacitive coupler radiation resistance, obtained using FDTD simulations, over parameter y are in a good agreement with values of radiation resistance of a fictitious coupler, obtained using (3.50) by considering the first 24 characteristic modes, for y

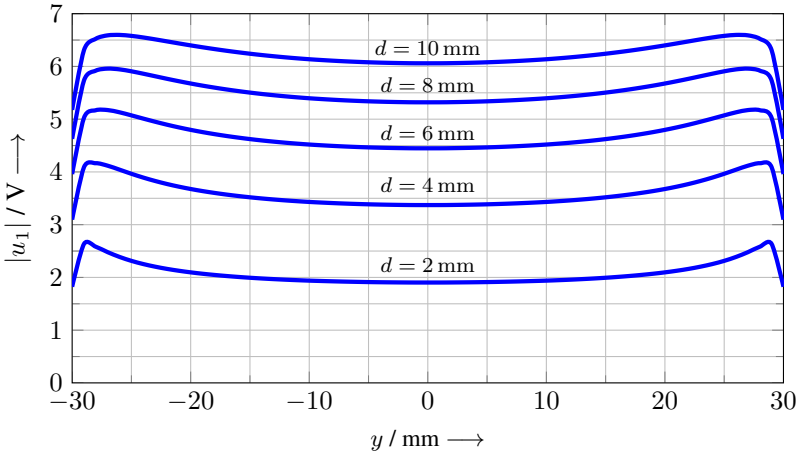

(a) voltage

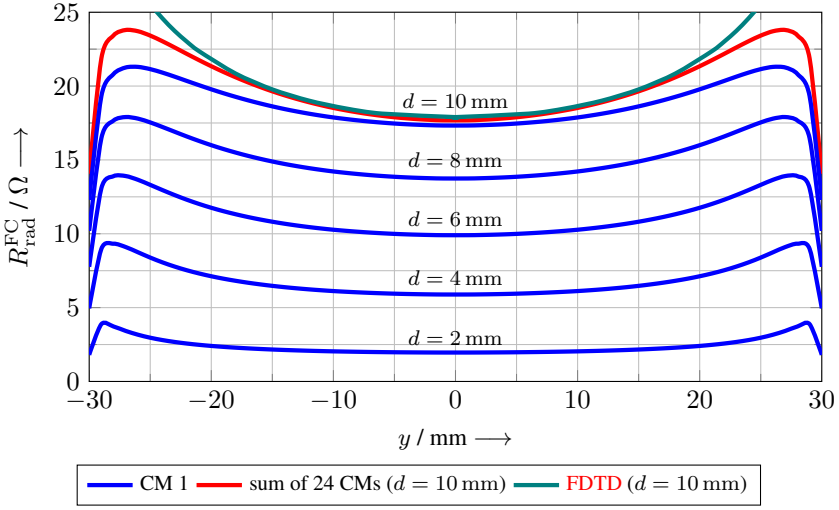

(b) radiation resistance

Fig. 3.11.: (a) Voltage $|u_1|$ and (b) radiation resistance $R_{\mathrm{rad}}^{\mathrm{FC}}$ of a fictitious capacitive coupler due to the 1st characteristic mode on $60 \times 120\,\mathrm{mm}^2$ plate at 900 MHz (blue). The coupler is located along the short edge of the ground plane and at separation $d \in \{2, ..., 10\}\,\mathrm{mm}$. The total radiation resistance of a fictitious capacitive coupler as a sum taken over the first 24 characteristic modes (red). For comparison the radiation resistance of an extremely small capacitive coupler after Fig. 3.12b obtained using FDTD simulation is given (teal).

(a) fictitious capacitive coupler (b) realistic, small capacitive coupler

Fig. 3.12.: (a) fictitious capacitive coupler and points at which near-field electric field of characteristic modes are obtained and (b) realistic small coupler (pin) connected to the 60×120 mm^2 ground plane via feed.

from $-20\,\mathrm{mm}$ to $20\,\mathrm{mm}$ (see Fig. 3.11b, teal and red). The reactance of the pin connected to the chassis can be approximated in terms of self-capacitance of a short strip since the self-inductance is negligible in comparison. However, its calculation is not necessary since it provides very little information. As discussed earlier the radiation resistance brings about much more insight into proper placement of a coupler.

In order to investigate how different characteristic modes contribute to the radiation resistance of a fictitious capacitive coupler over the frequency range from $0.5\,\mathrm{GHz}$ to $3\,\mathrm{GHz}$ a fictitious coupler location relative to the ground plane was fixed to $x_0 + d = 70\,\mathrm{mm}$ and $y_0 = 0\,\mathrm{mm}$ (see Fig. 3.12a). The distance of a fictitious coupler from the ground plane was assumed to be $d = 10\,\mathrm{mm}$ so that the line integration of characteristic mode near-field electric fields was performed from x_0 to $x_0 + d$ using (3.51). Also, the total radiation resistance as a sum of contributions from the first 24 characteristic modes was calculated and compared against the radiation resistance obtained using FDTD simulation of a realistic small coupler shown in Fig. 3.12b. The results are brought together in Fig. 3.13. It is interesting to note that near $1\,\mathrm{GHz}$ the 1st capacitive characteristic mode contributes 90% of the total radiation resistance. At about $2.1\,\mathrm{GHz}$ the 4th characteristic mode contributes about 50% to the total radiation resistance. The higher order characteristic modes have small contributions to the total radiation resistance of a capacitive coupler.

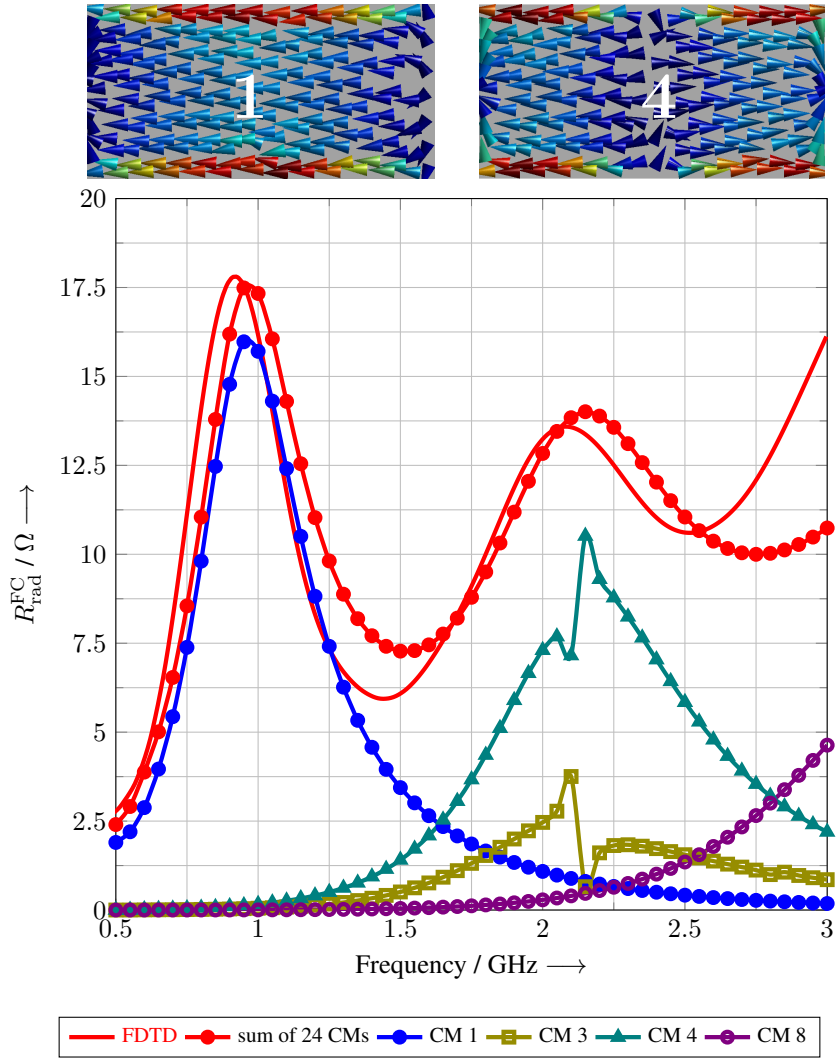

Fig. 3.13.: Characteristic mode radiation resistances of the first few characteristic modes to the radiation resistance of a fictitious capacitive coupler after Fig. 3.12a and comparison to the radiation resistance of the extremely small coupler ($1 \times 9\,\mathrm{mm}^2$ pin) after Fig. 3.12b obtained using FDTD. Both fictitious coupler and pin are placed at the center of the short edge of the $60 \times 120\,\mathrm{mm}^2$ ground plane. Above the plot surface current densities of the 1st and the 4th characteristic modes are shown.

3.5. Equivalent Circuit Models of Characteristic Modes and Couplers

The goal of the present section is introduction of physics based ECMs for characteristic modes and further development of ECMs of capacitive or inductive couplers. As opposed to the use of more or less generic equivalent circuits whose elements are just numerically fitted so as to reproduce simulated or measured scattering parameters [87] equivalent circuit models shown in the present paper provide physical insight and allow to explore the limits of attainable performance. The elements of a physics based equivalent circuits are, as far as possible, obtained from easily calculated descriptive quantities of characteristic modes and from coupler's geometry. Further, a good understanding of the coupling between the chassis and couplers placed on it remains a relevant aspect and is explored here using ECMs.

3.5.1. ECMs of characteristic modes

Knowledge of the characteristic mode impedances (see section 3.2) allows to construct ECMs of characteristic modes which can further be used in development of ECMs of capacitive and inductive couplers. The goal of the present section is to illustrate how to construct these ECMs based on two examples. In order to illustrate usefulness of characteristic mode ECMs a $120 \times 60\ \mathrm{mm}^2$ plate corresponding to the size of the ground plane of a typical smartphone is considered. The impedance of the 1st characteristic mode is obtained using (3.27) (see Fig. 3.14, solid red). The radiation resistance R_1 increases approximately with the square of frequency within a limited frequency range. The radiation quality factor of the 1st capacitive characteristic mode at resonance frequency $f_{1,0} = 1.11\,\mathrm{GHz}$ is found to be $Q_{1,0} = 1.3$ and radiation resistance $R_{1,0} = 26\ \Omega$ for $2P_0 = 1\ \mathrm{W}$. The reactance can be approximated by a series connection of $L_1 = 4.8\ \mathrm{nH}$ and $C_1 = 4.27\ \mathrm{pF}$. The ECM of the 1st capacitive characteristic mode is the second order high pass circuit after [95], which comprises shunt RL circuit with series capacitance C (see Fig. 3.15). The values of ECMs which model the 1st characteristic mode impedance are given in Tab. 3.1. Both ECMs represent the impedance of the 1st characteristic mode very accurately (see Fig. 3.14, dashed blue). Note that for higher order characteristic modes systematic design of ECMs based on template functions given in [95] is feasible. However, further discussion with regards to physics

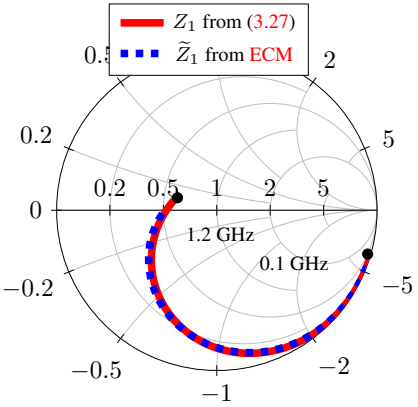

Fig. 3.14.: Impedance of the 1st capacitive characteristic mode on $60 \times 120\ \mathrm{mm}^2$ plate obtained using (3.27) (solid red) and its approximation (dashed blue) using ECM shown in Fig. 3.15 with values given in Tab. 3.1.

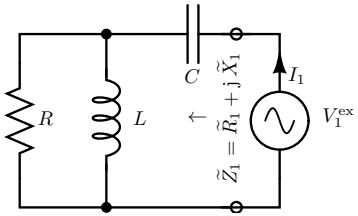

$$\widetilde{R}_1(\omega) = \frac{RL^2\omega^2}{R^2 + (\omega L)^2} \tag{3.52}$$

and

$$\widetilde{X}_1(\omega) = \frac{\omega R^2 L}{R^2 + (\omega L)^2} - \frac{1}{\omega C} \tag{3.53}$$

Fig. 3.15.: ECM of the 1st capacitive characteristic mode. The ECM comprises shunt connection of resistance R and inductance L, and a series capacitance C. The input impedance of the circuit $\widetilde{Z}_1$ approximately matches the impedance of the 1st characteristic mode Z_1 calculated using (3.27) over a broad frequency range. V^{ex} is the modal voltage which is actually present for the given excitation and I_1 the corresponding actual modal current.

Tab. 3.1.: Element values of the second order high pass equivalent circuit model for the 1st capacitive characteristic mode after [95], shown in Fig. 3.15.

element	unit	CM1
R	Ω	65.3
L	nH	7
C	pF	4.43

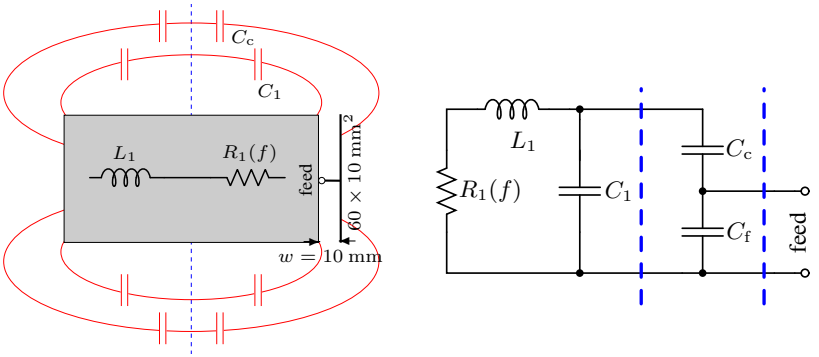

Fig. 3.16.: Illustration of an interaction between capacitive coupler and the 1st characteristic chassis mode and a simple circuit representation of this interaction.

based ECMs of couplers is intentionally constrained to the 1st characteristic mode in order to expose the basic behavior of couplers.

3.5.2. ECM of capacitive coupler

Consider a capacitive coupler of dimensions 10×60 mm^2. It is a vertical plate connected to the 60×120 mm^2 ground plane via 9 mm long pin and the feed. The coupler is placed in front of the short edge of the ground plane (see Fig. 3.16, left). For the purpose of fundamental understanding of the relation between the basic geometry of the coupler–ground plane arrangement circuit elements $R_1(f)$, L_1, C_1 and C_c are drawn so as to correspond to the complete antenna physical structure. Further, based on the location of feed relative to the circuit elements a basic circuit model of the coupler is constructed (see Fig. 3.16, right). C_c is the coupling capacitance which models an interaction between the coupler and the 1st characteristic mode. C_f is the capacitance seen at the coupler's feed.

Excitation of the 1st characteristic mode on the ground plane using a capacitive coupler amounts to "tapping" the capacitive part of the characteristic mode's impedance. The capacitive coupler intercepts major part of the electric flux of the 1st characteristic mode. The ECM of the "tapped" 1st characteristic mode is a shunt RLC circuit with values of R_E, L_E and C_E given in Fig. 3.18.

The arrangement, comprising the chassis and the coupler, can be considered as a transmission line when looking at it from the side. Therefore, the ca-

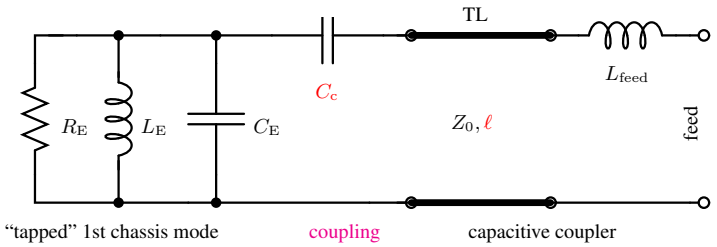

Fig. 3.17.: Equivalent circuit model of the capacitive coupler after Fig. 3.16b. C_{c} (coupling capacitance) and ℓ ("effective length" of the coupler) are the only optimization parameters.

pacitance C_{f} present in the basic circuit model (see Fig. 3.16) is replaced by a transmission line. The line impedance of this transmission line was found, using quasi-static electromagnetic analysis, to be $Z_0 = 175.5\ \Omega$. The pin connecting capacitive plate to the chassis features self inductance which can be approximated by [105]

$$L_{\text{feed}} = \frac{2d}{\text{cm}} \left(\ln\left(\frac{2d}{r}\right) - 1 \right) \text{nH}, \tag{3.54}$$

where r is the radius and d the length of the pin. For $r = 0.05$ cm and $d = 1$ cm the self inductance of a pin equals $L_{\text{feed}} = 5.38$ nH. The length ℓ of the transmission line corresponds to the "effective length" over which the coupling occurs. C_{c} and ℓ are the only optimization parameters in the ECM. In order to find C_{c} and ℓ an optimization was performed from $0.5\,\text{GHz}$ to $1.2\,\text{GHz}$ to finally fit the ECM to the result of FDTD simulation (see Fig. 3.17). The model not only delivers correct frequency dependency (see Fig. 3.18a) but almost all elements can be directly calculated from modal quantities and coupler's geometry. Further, the equivalent circuit model can be used to predict the behavior of the coupler when changing its basic geometry. For instance the distance of the capacitive plate from the edge of the ground plane, i.e. the width of the transmission's line slot w has an impact of the line impedance Z_0. Increase of the distance of a capacitive plate from the ground plane leads to increase of the radiation resistance. The ECM models this by increase of the line impedance.

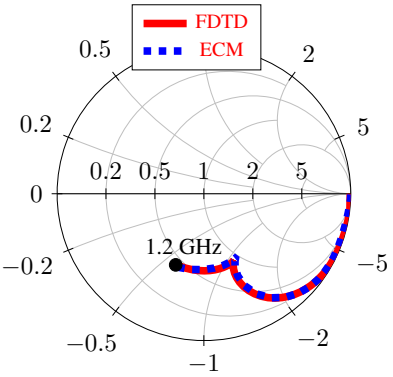

TABLE I
THE VALUE OF COUPLING CAPACITANCE IS $C_c = 1.18\,\mathrm{pF}$.

element	unit	CM 1
R_E	Ω	60.5
L_E	nH	5.5
C_E	pF	5.43
element	unit	Coupler
Z_0	Ω	175.5
ℓ	cm	1.3
L_{feed}	nH	5.4

Fig. 3.18.: Comparison between the input impedance of the capacitive coupler on the 60×120 mm^2 ground plane obtained using FDTD (solid red) and the input impedance predicted by the ECM (dashed blue) after Fig. 3.17.

3.6. *Characteristic Mode* Based Antenna Design

The purpose of the present section is introduction of the systematic approach to design multiport antennas. In a first step the notions of an unperturbed and a perturbed structures are introduced. Further, it is shown that the surface current density expansion coefficients are not appropriate for finding the relation between *characteristic modes* and *radiation modes*. To overcome this obstacle the far-field electric field expansion coefficients for the perturbed structure are defined and it is shown that calculation of these coefficients leads to a meaningful relation between the *characteristic modes* and *radiation modes* and subsequently to a design approach. The theoretical aspects of the design approach are outlined in the present section, whereas its application is shown in section 3.7.

3.6.1. Unperturbed versus perturbed structure

So far in all presented material it was silently assumed that an arbitrarily shaped body itself is the only element under considerations for the purpose of characteristic modes computation. For further discussion it is necessary to define the *unperturbed structure* and the *perturbed structure*.

Characteristic mode analysis is initially applied to the bare chassis of a device in which all exciters i.e. inductive couplers (slots) and capacitive couplers (plates) are intentionally dismissed. Computed characteristic modes corresponds to an *unperturbed structure*. Since the basic properties of *characteristic modes* of moderate order depend mainly on the large scale features of the geometry, the analysis of the *unperturbed structure* yields a valid starting point for further considerations. Exciters are to be introduced later so as to approximately accommodate the surface current density of the desired *characteristic modes* to be excited.

An *unperturbed structure* refers to a body which does not contain any external couplers or does not include any other significant changes made to the basic shape of the body. Inclusion of external couplers or introduction of significant changes to the shape of the body may changes resonance frequencies and surface current densities of characteristic modes. However, if couplers and modifications of the body are small as compared to size of the body and the wavelength then the *perturbation* can be considered negligible. Fictitious couplers (see Fig. 3.8), described in the previous section, relate to the ideally unperturbed structure. In any case a body featuring external realistic couplers or small modifications to its basic shape (e.g. slots) (see Fig. 3.9) it is referred to as *perturbed structure*.

3.6.2. Expansion coefficients for the unperturbed structure

The far-field electric field is related to the surface current density via

$$\boldsymbol{E}(\boldsymbol{r}) = -\mathrm{j}\eta_0 \frac{\mathrm{e}^{-\mathrm{j}kr}}{4\pi kr} \left(\boldsymbol{k} \times \oiint_{\boldsymbol{r}' \in S} \boldsymbol{J}_\mathrm{s}(\boldsymbol{r}') \mathrm{e}^{\mathrm{j}\boldsymbol{k}\boldsymbol{r}'} \mathrm{d}S \right) \times \boldsymbol{k}, \tag{3.55}$$

where $\boldsymbol{k}$ is the propagation vector along the direction of $\boldsymbol{r}$, $k = |\boldsymbol{k}|$ is its magnitude and $\eta_0 = 377\ \Omega$ is the free space impedance. Note, that (3.55) can be rewritten for the mth characteristic mode. The inner product between the electric field of the mth characteristic mode $\boldsymbol{E}_m$ and the total electric field $\boldsymbol{E}$ yields

$$\langle \boldsymbol{E}_m | \boldsymbol{E} \rangle_{S_\infty} = \langle \boldsymbol{E}_m | \sum_n \alpha_n \boldsymbol{E}_n \rangle_{S_\infty} = 2P_0 \eta_0 \alpha_n \delta_{mn}, \tag{3.56}$$

where the subscript S_∞ indicates integration over the far-field sphere surrounding the conducting body and the complex expansion coefficients α_m are the

same as in (3.17). The far-field electric field expansion coefficients are given by [98, 93]

$$\alpha_m = \frac{1}{2P_0\eta_0}\langle \boldsymbol{E}_m|\boldsymbol{E}\rangle_{S_\infty}. \tag{3.57}$$

Due to orthogonality of the characteristic modes both surface current density expansion coefficients and far-field electric field expansion coefficients are the same for the same structure.

3.6.3. Expansion coefficients for the perturbed structure

In order to find which characteristic modes are strongly excited due to electric field $\boldsymbol{E}^{\text{ex}}$ generated by $\boldsymbol{J}^{\text{ex}}$ (see section 3.4) the expansion coefficients have to be calculated using the relation

$$\beta_m = \frac{1}{2P_0\eta_0}\langle \boldsymbol{E}_m|\boldsymbol{E}^{'}\rangle_{S_\infty}, \tag{3.58}$$

where $\boldsymbol{E}^{'}$ is the total electric field of the perturbed structure (i.e. the structure with the coupler). Since β_m can be calculated only if an exciter is present the expansion into the characteristic modes of the original conducting body corresponds to determination of an equivalent source current density, i.e. the contribution of the exciters is mapped to characteristic modes. The actual surface current density on the conducting body is *not* the superposition of the characteristic modes with the calculated coefficients. Note, that for clarity the β_m are normalized in the same way as α_m in (3.13).

3.6.4. The relation between *radiation modes* and *characteristic modes*

Aiming at a systematic design procedure for multiport antennas it is necessary to establish relations between *characteristic modes* and *radiation modes*. To that end consider (3.58) for a P-port antenna system. If an excitation is applied to the pth port (remaining ports matched) the per port electric fields for the perturbed structure $\boldsymbol{E}^{'}_{\text{P},p}$ associated with this port can be represented as linear superposition of electric fields of radiation mode $\boldsymbol{E}^{'}_{\text{R},n}$ with coefficients υ_{pn}, where index n refers to a particular *radiation mode*. Then, electric field

expansion coefficients β_{mp} which represent projection of characteristic mode electric fields $\boldsymbol{E}_{\mathrm{C},m}$ (unperturbed structure) on $\boldsymbol{E}'_{\mathrm{P},p}$ (perturbed structure) are given by

$$\beta_{mp} = \frac{1}{2P_0\eta_0}\langle \boldsymbol{E}_{\mathrm{C},m}|\boldsymbol{E}'_{\mathrm{P},p}\rangle_{S_\infty} = \frac{1}{2P_0\eta_0}\langle \boldsymbol{E}_{\mathrm{C},m}|\sum_n \upsilon_{pn}\boldsymbol{E}'_{\mathrm{R},n}\rangle_{S_\infty}. \quad (3.59)$$

Note that υ_{pn} are, in general, complex coefficient which remain fixed once the feed locations are chosen. Further steps in the derivation yield

$$\beta_{mp} = \sum_n \upsilon_{pn}\frac{1}{2P_0\eta_0}\langle \boldsymbol{E}_{\mathrm{C},m}|\boldsymbol{E}'_{\mathrm{R},n}\rangle_{S_\infty} = \sum_n \xi_{mn}\upsilon_{pn}, \quad (3.60)$$

where ξ_{mn} denotes electric field expansion coefficient which is the far-field projection of electric field of the mth *characteristic mode* (unperturbed structure) on the electric field of the nth *radiation mode* (perturbed structure).

3.6.5. Systematic design procedure

In order to simplify further discussion on (3.60) assume that the location of couplers on the conducting body is fixed (this assumption corresponds to frequent practical design constraint of antenna placement in small mobile wireless devices). This assumption renders the projection of $\boldsymbol{E}'_{\mathrm{R},n}$ on $\boldsymbol{E}'_{\mathrm{P},p}$, and thus all coefficients υ_{pn}, fixed. These coefficients are entries of the unitary matrix $\mathbf{V}$ after (2.21). Through design of *radiation modes* using *characteristic modes*, i.e. proper choice of coefficients ξ_{mn} in (3.60) it is possible to achieve the desired mapping of *characteristic modes* to ports described in terms of coefficients β_{mp}. Specifically, two systematic approaches for design of multiport antennas are possible. Couplers are placed to either interact with disjoint subsets of *characteristic modes* or in such way so that the *characteristic modes* which are excited by pth coupler superimpose to (nearly) zero sum of coefficients at any other coupler. As an example of the first design approach consider two couplers exiting *characteristic modes* of opposite symmetry. An example of the second design approach is 2-port MIMO antenna for laptop presented in [106, 107]. The design aspects are described in more detail in the section 3.7 of the present chapter whereas the prototype is outlined in Chapter 6.

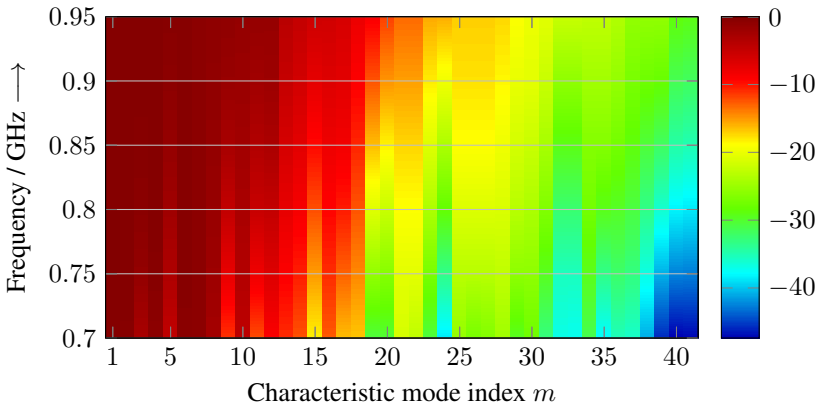

Fig. 3.19.: *Modal power factors*, given in dB scale, of the first 40 characteristic modes for a laptop chassis over LTE low-band frequency range. Characteristic modes are numbered in the sequence of decreasing *modal power factor* at 950 MHz.

3.7. Design of Multiport Antennas for Laptops

In the present section the theory from section 3.6 is applied to introduce the design of a broadband multiport antenna system for laptops. The goal is to construct *radiation modes* from *characteristic modes* using the design procedure outlined in the previous section. Early work on the subject of 2-port MIMO antenna design for LTE low-band was described in [108]. The solution features two couplers, on placed at the top of the lid and the other connects the lid with the base part. Both couplers excite different superpositions of characteristic modes which are mutually orthogonal. The design features high isolation between two ports and high total per port efficiencies. However, an approach to design multiport antenna for laptops, described in the present section, utilizes only a slot between the lid and the base part, which is an inherent feature of laptops, for placement of exciters and conductive strips both of which electrically connect the lid with the base part.

A 15.4" laptop comprising $250 \times 350 \times 20$ mm^2 base part and $250 \times 350 \times 10$ mm^2 lid without any slot between the two parts is initially considered. Characteristic modes are computed for this *unperturbed structure* (see section 3.6). Inspection of Fig. 3.19 reveals that many characteristic modes in the LTE low-band frequency range (from 704 MHz to 940 MHz) with high *modal power*

factors (3.26) are available. They can potentially be excited on the chassis of a laptop provided that a proper *coupler* is used. However, selective excitation of particular characteristic modes is difficult. A solution where different superpositions of characteristic modes which are mutually orthogonal are excited in LTE low-band is more practical. Note, that displaying modal power factors instead of eigenvalues is particularly useful for an electrically large structures where many characteristic modes feature low magnitude eigenvalues.

Examination of the surface current density of some the most significant characteristic modes on the laptop chassis in LTE low-band frequency range reveals that they can be divided according to the symmetry plane of the laptop chassis. For instance the surface current densities of the 6th and the 11th characteristic mode (see Figs. 3.20 and 3.21) are tangential to laptop's symmetry plane. Therefore, the symmetry plane in this case can be associated with a magnetic wall. The surface current densities of the 8th and the 9th characteristic modes (see Figs. 3.22 and 3.23) are normal to the symmetry plane. Hence, this plane can be substituted for by an electric wall. Two orthogonal subsets of characteristic modes are identified. This can be expressed as

$$\boldsymbol{J}_{\mathrm{s}}^{(\Sigma)} \in \{..., \boldsymbol{J}_{\mathrm{s},6}, ..., \boldsymbol{J}_{\mathrm{s},11}, ...\}, \tag{3.61}$$

and

$$\boldsymbol{J}_{\mathrm{s}}^{(\Delta)} \in \{..., \boldsymbol{J}_{\mathrm{s},8}, ..., \boldsymbol{J}_{\mathrm{s},9}, ...\}, \tag{3.62}$$

where $\boldsymbol{J}_{\mathrm{s}}^{(\Sigma)}$ and $\boldsymbol{J}_{\mathrm{s}}^{(\Delta)}$ are subsets of characteristic mode surface current densities here referred to as common (superscript Σ) and differential (superscript Δ) mode subsets, respectively. These observations of characteristic mode surface current density symmetries are important for a proper realization of exciters and their placement. The optimum location of the exciters for either subset of modes is easy to identify from characteristic mode surface current densities. Two current sources are required so as to excite subsets $\boldsymbol{J}_{\mathrm{s}}^{(\Sigma)}$ and $\boldsymbol{J}_{\mathrm{s}}^{(\Delta)}$. To maximize the reaction integral (3.45) the exciters have to be placed where the two subsets of characteristic mode surface current densities attain their respective maxima. The slot between the lid and the base part of the laptop, which is an inherent feature of laptops, is taken advantage of. Two exciters, both of which connect lid with the base part of a laptop, are placed symmetrically as shown in Fig. 3.24. Two conductive hinges that connect lid and the base part are placed symmetrically in the slot near the laptop's symmetry plane. Their purpose is to close the current loops generated by the two exciters. In order to

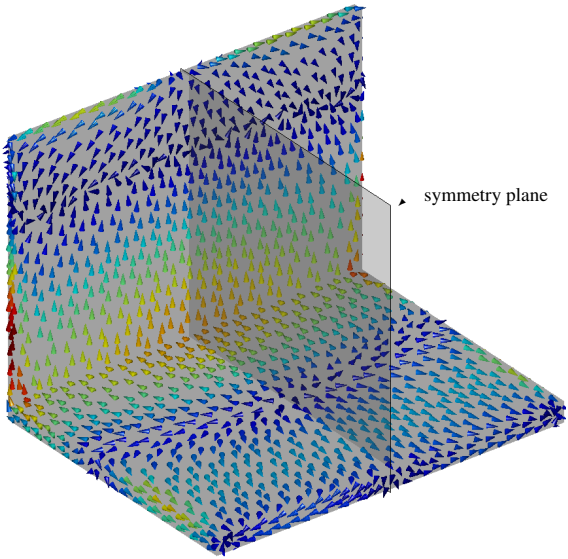

Fig. 3.20.: Vector plot of the surface current density of the 6th characteristic mode on the laptop chassis at 850 MHz.

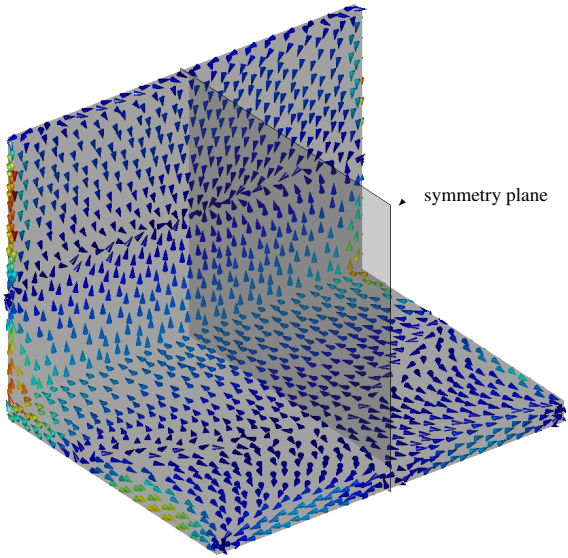

Fig. 3.21.: Vector plot of the surface current density of the 11th characteristic mode on the laptop chassis at 850 MHz.

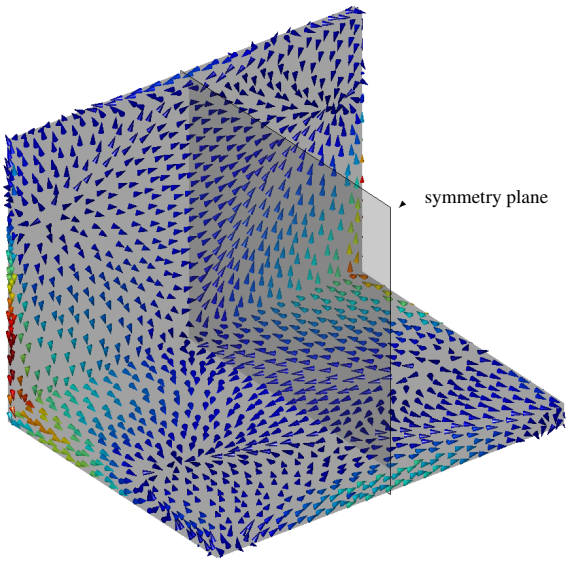

Fig. 3.22.: Vector plot of the surface current density of the 8th characteristic mode on the laptop chassis at 850 MHz.

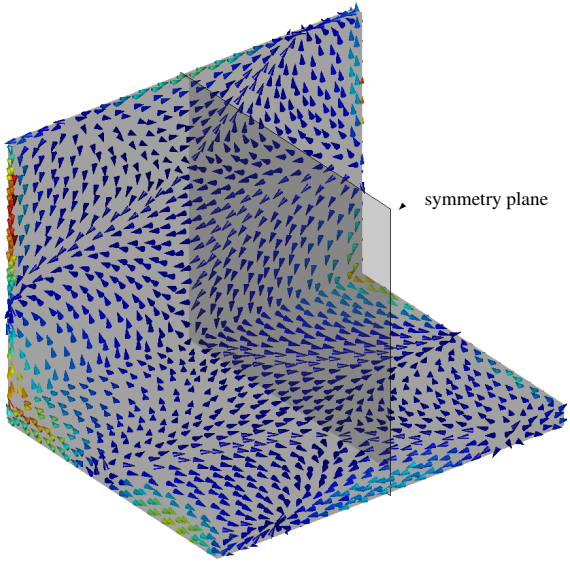

Fig. 3.23.: Vector plot of the surface current density of the 9th characteristic mode on the laptop chassis at 850 MHz.

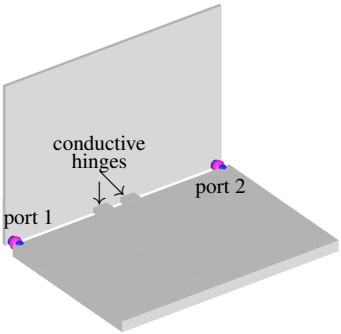

Fig. 3.24.: Simple CAD model of a laptop with locations of two conductive hinges and two ports [106].

separately excite characteristic modes of opposite symmetries an even and odd more excitation has to be provided. Simultaneous excitation of both subsets of characteristic modes can be accomplished using a 180° hybrid.

The above approach illustrates systematic construction of *radiation modes* from *characteristic modes* which are taken from mutually orthogonal subsets. Two sets of electric field expansion coefficients, computed using (3.58), corresponding to the *common mode* and the *differential mode* excitation of two couplers are disjoint (see Fig. 3.25). The common mode (Σ) is the superposition of characteristic modes marked in red, whereas the differential mode (Δ) is the superposition of characteristic modes marked in blue. The results reveal that different superposition of the characteristic modes (subsets) contribute to different radiation modes (both subsets are disjoint) which indicates that both superpositions of the characteristic modes are mutually orthogonal. Note, that in order to map radiation modes to external ports an additional 180° hybrid is required. The cumulative sum suggests that the first 15 characteristic modes contribute about $80\ \%$ of the power radiated by the antenna. Remaining higher order characteristic modes make only small contributions to the total radiated power. Moreover, the contributions to the total radiated power of the four characteristic modes, whose surface current densities are given in Figs. 3.20, 3.21, 3.22 and 3.23, are nearly equal.

The outlined solution is not the only one possible. Use of a 180° hybrid to simultaneously and independently excite both *radiation modes* is not required

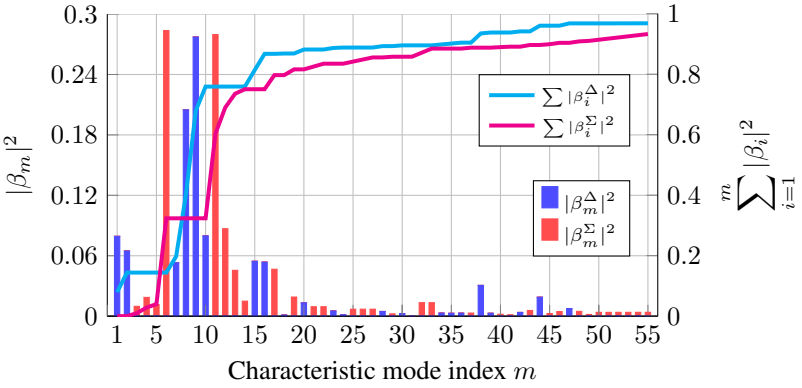

Fig. 3.25.: Squared magnitude of the electric field expansion coefficients ($|\beta_m|^2$) and its cumulative sum function over the first 55 characteristic modes at 850 MHz for the *common mode* (Σ) and *differential mode* (Δ) excitation [106].

in this design. The optimization of the position of hinges and exciters requires consideration of the power scaled electric fields $\boldsymbol{E}_{\mathrm{P},1}$ and $\boldsymbol{E}_{\mathrm{P},2}$ generated by the excitation at port 1 and port 2, respectively. These fields are linear superpositions of scaled to P_0 electric fields $\boldsymbol{E}_{\Sigma}^{'}$ and $\boldsymbol{E}_{\Delta}^{'}$ related to *radiation modes* [68], i.e. *common mode* and *differential* mode, respectively

$$\boldsymbol{E}_{\mathrm{P},1}^{'} = \alpha_{\Sigma}\boldsymbol{E}_{\Sigma}^{'} + \alpha_{\Delta}\boldsymbol{E}_{\Delta}^{'} \quad \text{and} \quad \boldsymbol{E}_{\mathrm{P},2}^{'} = \alpha_{\Sigma}\boldsymbol{E}_{\Sigma}^{'} - \alpha_{\Delta}\boldsymbol{E}_{\Delta}^{'}, \tag{3.63}$$

where α_{Σ} and α_{Δ} are coefficients. The design goal, i.e. achieving orthogonality between $\boldsymbol{E}_{\mathrm{P},1}^{'}$ and $\boldsymbol{E}_{\mathrm{P},2}^{'}$ requires

$$\langle \boldsymbol{E}_{\mathrm{P},1}^{'} | \boldsymbol{E}_{\mathrm{P},2}^{'} \rangle = 0 \quad \text{which yields} \quad |\alpha_{\Sigma}| = |\alpha_{\Delta}| = \frac{1}{\sqrt{2}}. \tag{3.64}$$

Electric field expansion coefficients, given by (3.58), were calculated in order to illustrate the design principle of operation and to show the validity of (3.64). It is apparent, from joint inspection of Fig. 3.25 and Fig. 3.26, that (3.64) is fulfilled i.e. the power delivered to each port is distributed nearly equally between radiation modes. Therefore, per port excitations excite two nearly orthogonal superpositions of radiation modes or equivalently two nearly orthogonal superpositions of characteristic modes. The latter refers to the fact that the sum of electric field expansion coefficients from both ports is approximately zero. Note that these coefficients are complex so that their phases play an important

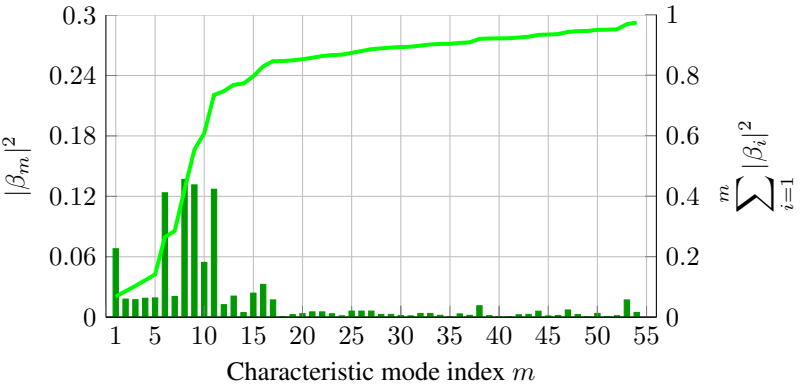

Fig. 3.26.: Squared magnitude of the electric field expansion coefficients ($|\beta_m|^2$) and its cumulative sum function over the first 55 characteristic modes at 850 MHz for per port excitation [106].

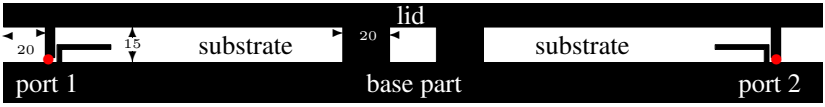

Fig. 3.27.: Detailed look at the slot between the lid and the base part of a laptop with additional L-shaped stubs [106]. All dimensions are given in mm.

role in illustration of orthogonality between two superpositions of characteristic modes.

The complete multi-band 2-port MIMO antenna system, optimized for LTE low-band and LTE mid-band and WLAN (2.4 GHz), is shown in Fig. 3.27. The per port return loss and isolation for an initial design after Fig. 3.24 which cover LTE low-band is shown in Fig. 3.28 (dashed lines). In order to obtain match in multiple bands simultaneously the L-shaped stubs were introduced. They provide additional resonance at 2.45 GHz and act as a capacitive load at around 1.75 GHz thus allowing the antenna to be matched in LTE mid-band (from 1710 MHz to 2170 MHz) and WLAN frequency bands. The antenna system features higher than 20 dB isolation between the ports and return loss within the 7 dB specification for all bands of interest (see Fig. 3.28, solid lines) which confirms that (3.64) is satisfied to a good approximation. Here, only starting considerations are made with regards to the present design. Detailed

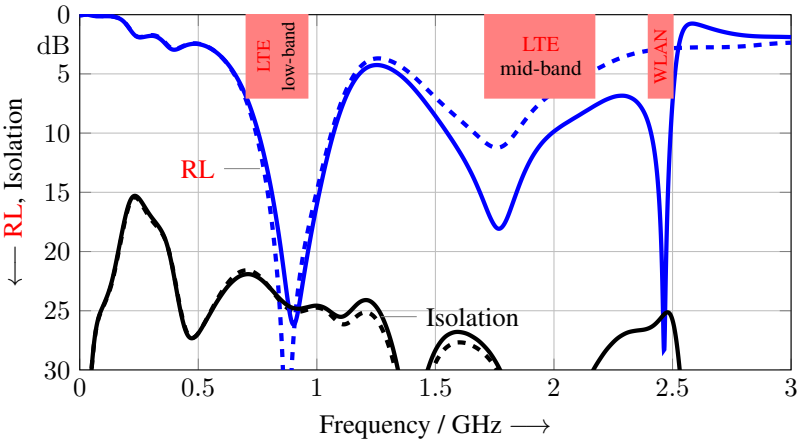

Fig. 3.28.: Per port RL and isolation versus frequency for the 2-port MIMO antenna system after Fig. 3.24a (w/o L-shaped stubs, dashed lines) and after Fig. 3.27 (with L-shaped stubs, solid lines) [106].

optimization of the design and measurements of the prototype are given in Chapter 6.

In theory, the above described design approach can be extended to realize an N-port antenna system using N *couplers* and $N-1$ *conductive hinges* which connect lid with the base part of a laptop [109]. By changing relative position of the conductive hinges and couplers along the slot between the lid and the base part it is possible to tune an N-port antenna to the desired frequency bands. However, it is necessary to note that an increasing number of couplers is accompanied by a decrease of usable TMRL bandwidth.

It is worth noting that historically also other types of mobile wireless devices feature a slot that separates two ground planes. Namely, the folder- (clamshell) and slider-type mobile phones. A broadband and multi-band single-port antenna solutions for a such platforms were the subject of extensive research in the past, e.g. [104]. Use of slots, however not practical, is frequently proposed for other types of devices e.g. a bar-type mobile phone form factor. However, due to battery placement and its significant real estate consumption these solutions have to be considered as academic exercises only.

Chapter 4

Multiport Matching Networks

The present chapter deals with multiport matching networks. In practice *characteristic modes* (see Chapter 3) often can not be directly mapped to external ports of the antenna system. Also, superpositions of *characteristic modes*, which are accessible at different ports, are in general not mutually orthogonal. Finally, impedance is of concern.

The present chapter starts from definitions of matching, decoupling and mode decomposition. Next, an overview of existing design techniques to achieve match and realize mode decomposition is given. Moreover, two newly proposed, advantageous systematic design approaches, the first for designing multiport matching networks and the second for designing Mode Decomposition Networks (MDNs) are introduced.

4.1. Definitions

The fundamental goal in design of multiport antennas is to achieve high total multiport efficiency and low modal efficiency imbalance over the desired bandwidth. In order to achieve this goal it is necessary to obtain an approximately diagonal *radiation matrix* of the antenna $\mathbf{R}$. For the purpose of a further discussion assume that the antenna is lossless and features scattering matrix $\mathbf{S}$.

The power balance relation, given for a lossless antenna by

$$\mathbf{R} = \mathbf{I} - \mathbf{S}^{\dagger}\mathbf{S} \quad (\text{if} \quad \text{lossless}) \tag{4.1}$$

(see Chapter 2 subsection 2.2.3), implies that a diagonal radiation matrix can be obtained using three different ways defined below.

Multiport match is defined as rendering all elements of the scattering matrix zero, i.e. $\mathbf{S} = \mathbf{0}$. Match leads to a diagonal *radiation matrix* which in case of a lossless antenna system implies $\mathbf{R} = \mathbf{I}$ via the power balance relation (2.23). It leads simultaneously to "per port" match and high isolation between all ports. Match defines the most general condition to be satisfied by a multiport antenna system in order to feature high modal efficiencies, high isolation between the ports and low radiation pattern overlap. The radiation matrix can become diagonal if the scattering matrix is diagonal and also in certain cases of a scattering matrix which is not diagonal. This does not mean, however, that each port is matched to the load impedance, i.e. no "per port" match. In order to obtain high isolation between the pairs of ports a specific network is required. Note that basing high isolation between pairs of ports on the notion of diagonal $\mathbf{S}^{\dagger}\mathbf{S}$, which also leads to a diagonal radiation matrix is not appropriate in general. In [33] it was shown, using a simple example, that non-diagonal matrix $\mathbf{S}$ may lead to a diagonal $\mathbf{S}^{\dagger}\mathbf{S}$. The radiation matrix can be also diagonalized using (2.21) by the unique unitary matrix $\mathbf{V}$. Simultaneously, this amounts to diagonalization of $\mathbf{S}^{\dagger}\mathbf{S}$ with an assumption that eigenvalue decomposition of $\mathbf{S}^{\dagger}\mathbf{S}$ features unique ("distinct") eigenvectors [31]. This method of achieving high isolation between pairs of ports is referred to in this dissertation as *mode decomposition* or *mapping of radiation modes to external ports*. The realization of the concept amounts to design of a specific network to map *radiation modes* of the antenna system to its external ports. The mapping is uniquely given by the unitary matrix $\mathbf{V}$.

Short summary of the above introduced definitions:

1. Match or multiport match: The scattering matrix is rendered approximately zero $\mathbf{S} \approx \mathbf{0}$.
2. High isolation between pairs of ports (referred to also as "decoupling"): The scattering matrix $\mathbf{S}$ is approximately diagonal.
3. Mode decomposition, i.e. mapping of *radiation modes* to external ports: It is a specific way of rendering radiation matrix diagonal, where the unique unitary matrix $\mathbf{V}$ after (2.21) diagonalizes both $\mathbf{R}$ and $\mathbf{S}^{\dagger}\mathbf{S}$ simultaneously.

4.2. Scattering Matrix of the Ideal Multiport Matching Network

Consider a reciprocal N-port antenna system characterized by its scattering matrix $\mathbf{S}^{\mathrm{A}}$ and let $\mathbf{S}^{\mathrm{M}}$ denote the scattering matrix of a lossless $2N$-port network (see Fig. 4.1). The scattering matrix $\mathbf{S}^{\mathrm{M}}$ of the network is related to outgoing and incoming wave quantities via the following relation

$$\begin{pmatrix} \boldsymbol{b}_1 \\ \boldsymbol{b}_2 \end{pmatrix} = \begin{pmatrix} \mathbf{S}_{11}^{\mathrm{M}} & \mathbf{S}_{12}^{\mathrm{M}} \\ \mathbf{S}_{12}^{\mathrm{M}\top} & \mathbf{S}_{22}^{\mathrm{M}} \end{pmatrix} \begin{pmatrix} \boldsymbol{a}_1 \\ \boldsymbol{a}_2 \end{pmatrix}, \tag{4.2}$$

where $\mathbf{S}^{\mathrm{M}}$ is represented using four $N \times N$ matrices. The block $\mathbf{S}_{11}^{\mathrm{M}}$ corresponds to ports $1, ..., N$ and block $\mathbf{S}_{22}^{\mathrm{M}}$ to ports $N+1, ..., 2N$. $\boldsymbol{a}_1$ and $\boldsymbol{a}_2$, $\boldsymbol{b}_1$ and $\boldsymbol{b}_2$ are incoming and outgoing wave quantities to and from the $\mathbf{S}^{\mathrm{M}}$, respectively. The outgoing from the matching network wave quantity $\boldsymbol{b}_1$ corresponds to an incoming wave quantity to the antenna. Thus, $\boldsymbol{a}_1 = \mathbf{S}^{\mathrm{A}}\boldsymbol{b}_1$. The scattering matrix of the cascade comprising antenna with matching network is defined via relation $\boldsymbol{b}_2 = \mathbf{S}^{\mathrm{P}}\boldsymbol{a}_2$. Substitution into (4.2) gives

$$\boldsymbol{b}_1 = \mathbf{S}_{11}^{\mathrm{M}}\mathbf{S}^{\mathrm{A}}\boldsymbol{b}_1 + \mathbf{S}_{12}^{\mathrm{M}}\boldsymbol{a}_2 \tag{4.3}$$

$$\mathbf{S}^{\mathrm{P}}\boldsymbol{a}_2 = \mathbf{S}_{12}^{\mathrm{M}\top}\mathbf{S}^{\mathrm{A}}\boldsymbol{b}_1 + \mathbf{S}_{22}^{\mathrm{M}}\boldsymbol{a}_2. \tag{4.4}$$

The first relation can be easily rewritten as $\boldsymbol{b}_1 = (\mathbf{I} - \mathbf{S}_{11}^{\mathrm{M}}\mathbf{S}^{\mathrm{A}})^{-1}\mathbf{S}_{12}^{\mathrm{M}}\boldsymbol{a}_2$ and substituted into the second relation resulting in

$$\mathbf{S}^{\mathrm{P}}\boldsymbol{a}_2 = \mathbf{S}_{12}^{\mathrm{M}\top}\mathbf{S}^{\mathrm{A}}(\mathbf{I} - \mathbf{S}_{11}^{\mathrm{M}}\mathbf{S}^{\mathrm{A}})^{-1}\mathbf{S}_{12}^{\mathrm{M}}\boldsymbol{a}_2 + \mathbf{S}_{22}^{\mathrm{M}}\boldsymbol{a}_2. \tag{4.5}$$

The scattering matrix of a cascade comprising the antenna with matching network is given by

$$\mathbf{S}^{\mathrm{P}} = \mathbf{S}_{12}^{\mathrm{M}\top}\mathbf{S}^{\mathrm{A}}(\mathbf{I} - \mathbf{S}_{11}^{\mathrm{M}}\mathbf{S}^{\mathrm{A}})^{-1}\mathbf{S}_{12}^{\mathrm{M}} + \mathbf{S}_{22}^{\mathrm{M}}. \tag{4.6}$$

Since the matching network is lossless $\mathbf{S}^{\mathrm{M}}\mathbf{S}^{\mathrm{M}\dagger} = \mathbf{I}$. Then, use of (4.2) leads to the set of four relations with respect to blocks of the matrix $\mathbf{S}^{\mathrm{M}}$. These relations together with (4.6) and the multiport match condition $\mathbf{S}^{\mathrm{P}} = \mathbf{0}$, allow to obtain the scattering matrix of the matching network $\mathbf{S}^{\mathrm{M}}$ which leads to vanishing scattering matrix of the cascade at a single frequency. It was shown in [33] that if the $\mathbf{S}^{\mathrm{A}}$ is the scattering matrix of the antenna and $\mathbf{R}^{\mathrm{A}}$ is the radiation matrix

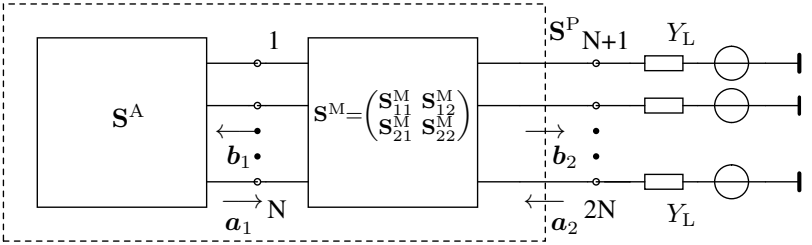

Fig. 4.1.: Schematic representation of the N-port antenna matching problem after [33].

of the antenna then the scattering matrix $\mathbf{S}^{\mathrm{M}}$ of the reciprocal and lossless network, which yields the scattering matrix of the cascade $\mathbf{S}^{\mathrm{P}} = \mathbf{0}$, is given by

$$\mathbf{S}^{\mathrm{M}} = \begin{pmatrix} \mathbf{S}^{\mathrm{A}\,\dagger} & \mathbf{R}^{\mathrm{A}\,\frac{1}{2}}\mathbf{U} \\ \mathbf{U}^{\top}\mathbf{R}^{\mathrm{A}\,\frac{1}{2}\,\top} & -\mathbf{U}^{\top}\mathbf{S}^{\mathrm{A}}\mathbf{U} \end{pmatrix}, \tag{4.7}$$

where block $\mathbf{S}^{\mathrm{M}}_{11} = \mathbf{S}^{\mathrm{A}\,\dagger}$ corresponds to ports $1, ..., N$ and block $\mathbf{S}^{\mathrm{M}}_{22} = -\mathbf{U}^{\top}\mathbf{S}^{\mathrm{A}}\mathbf{U}$ to ports $N+1, ..., 2N$ (see Fig. 4.1). $\mathbf{U}$ is, at this point of consideration, an arbitrary unitary matrix since the only function expected from $\mathbf{S}^{\mathrm{M}}$ is to provide $\mathbf{S}^{\mathrm{P}} = \mathbf{0}$ at single frequency. In [33] it is stated that $\mathbf{U}$ can provide degrees of freedom in a subsequent realization of the multiport matching network. For instance minimization of the number of branches required to realize the network or designing it with respect to a desired set of mutually orthogonal radiation patterns are possible. The second aspect is treated in [28, 29] as an optimization criterion for design of a multiport matching network for a narrowband antenna system (see subsection 4.3.4).

4.3. Implementation of Multiport Matching Networks

The present section provides an overview of the state of the art in systematic design methods for multiport matching networks. Only the most general algorithms applicable, in principle, to N-port antennas are described. Apart from those methods it is also important to note the work in [110], where a systematic design of matching networks for multiport symmetric antennas is shown.

Before actual design methods are described it is necessary to discuss how to synthesize admittance matrix and scattering matrix of the multiport matching network comprising reactive components. The details relative to this subject are given in subsection 4.3.1.

4.3.1. Construction of the admittance matrix

Consider a $2N$-port matching network for N-port antenna system. The multiport matching network is characterized by the admittance matrix $\mathbf{Y}^{\mathrm{M}}$. The matching network comprises $2N^2 + N$ branches. The general topology of the matching network is illustrated here using as an example 4-port matching network (see Fig. 4.2). The network comprises 10 branches. In specific cases (i.e. symmetric 2-port antennas) less than 10 elements may be sufficient to match the antenna. In general, if $\widetilde{G}^{\mathrm{M}}_{m}$ denotes conductance and $\widetilde{B}^{\mathrm{M}}_{m,i}$ susceptance of the branch mi then the admittance of this branch is $\widetilde{Y}^{\mathrm{M}}_{m,i} = \widetilde{G}^{\mathrm{M}}_{m,i} + \mathrm{j}\,\widetilde{B}^{\mathrm{M}}_{m,i}$, where $m, i = \{1, 2, ..., 2N\}$. The diagonal elements of the admittance matrix $\mathbf{Y}^{\mathrm{M}}$ are given by

$$Y^{\mathrm{M}}_{m,m} = \widetilde{Y}^{\mathrm{M}}_{m} + \sum_{\substack{i=1 \\ i \neq m}}^{2N} \widetilde{Y}^{\mathrm{M}}_{m,i}. \tag{4.8}$$

The off-diagonal elements of the admittance matrix are the negative values of the correspondingly indexed elements of the matching network, i.e.

$$Y^{\mathrm{M}}_{m,i} = -\widetilde{Y}^{\mathrm{M}}_{m,i}, \tag{4.9}$$

The S-parameters of the matching network itself can be represented in terms of the admittance matrix $\mathbf{Y}^{\mathrm{M}}$ using the well-known expression

$$\mathbf{S}^{\mathrm{M}} = (Y_{\mathrm{L}}\mathbf{I} - \mathbf{Y}^{\mathrm{M}})(Y_{\mathrm{L}}\mathbf{I} + \mathbf{Y}^{\mathrm{M}})^{-1}, \tag{4.10}$$

where Y_{L} is the load admittance which is assumed equal for all N output ports. The admittance of a single branch must be mapped, in general, to either a series or a shunt LC tank. Also use of a multistage network is feasible if required. The construction of an admittance based matching network featuring multiple stages may be advantageous for matching of a multiport antennas not featuring multiport symmetry. The admittance matrices of all required stages can be constructed separately. Once admittance matrices of all stages are obtained they can be converted to the corresponding scattering matrices and a

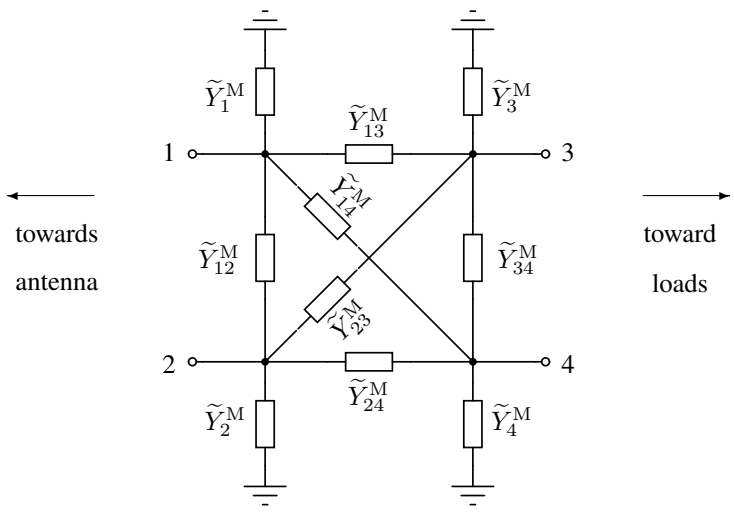

Fig. 4.2.: Admittance based representation of the 4-port matching network for 2-port antennas.

scattering matrix of the cascade can be calculated. However, it is necessary to note that both solutions, i.e. use of LC tanks or multistage matching network are not recommended since they may lead to increased number of elements and therefore increase of losses. For these reasons the admittance of the mith branch is mapped to either a single capacitance $C_{m,i}$ or a single inductance $L_{m,i}$. Formally, if lossless elements are considered ($\widetilde{G}^{\mathrm{M}}_{m,i} = 0$), the above described mapping is given by $\widetilde{Y}^{\mathrm{M}}_{m,i} = \mathrm{j}\,\omega_0 P^{\mathrm{M}}_{m,i}$ when $P^{\mathrm{M}}_{m,i} > 0$ (capacitance) and $\widetilde{Y}^{\mathrm{M}}_{m,i} = \mathrm{j}\,\frac{1}{\omega_0 P^{\mathrm{M}}_{m,i}}$ when $P^{\mathrm{M}}_{m,i} < 0$ (inductance). ω_0 denotes center radian frequency.

4.3.2. Diagonalization of admittance matrix of multiport symmetric matching networks

In case $2N$-port matching network features multiport symmetry its $2N \times 2N$ admittance matrix can be diagonalized. This diagonalization leads to a new $2N \times 2N$ block-diagonal admittance matrix. Each block of this new matrix is a 2×2 submatrix which represents a mode-specific 2-port matching network. For illustrative purposes consider the 4-port matching network after Fig. 4.2.

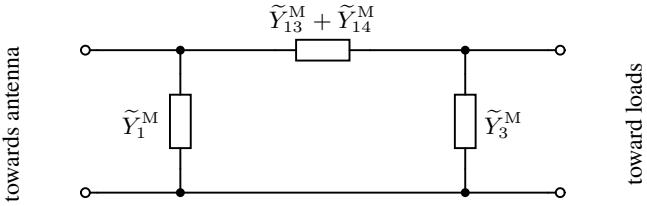

Fig. 4.3.: π-type matching network of the *common mode*.

Multiport symmetry requires that $\widetilde{Y}_1^{\mathrm{M}} = \widetilde{Y}_2^{\mathrm{M}}$, $\widetilde{Y}_3^{\mathrm{M}} = \widetilde{Y}_4^{\mathrm{M}}$, $\widetilde{Y}_{13}^{\mathrm{M}} = \widetilde{Y}_{24}^{\mathrm{M}}$, and $\widetilde{Y}_{14}^{\mathrm{M}} = \widetilde{Y}_{23}^{\mathrm{M}}$. The admittance matrix of the symmetric 4-port matching network is then

$$\begin{pmatrix} \widetilde{Y}_1^{\mathrm{M}}+\widetilde{Y}_{12}^{\mathrm{M}}+\widetilde{Y}_{13}^{\mathrm{M}}+\widetilde{Y}_{14}^{\mathrm{M}} & -\widetilde{Y}_{12}^{\mathrm{M}} & -\widetilde{Y}_{13}^{\mathrm{M}} & -\widetilde{Y}_{14}^{\mathrm{M}} \\ -\widetilde{Y}_{12}^{\mathrm{M}} & \widetilde{Y}_1^{\mathrm{M}}+\widetilde{Y}_{12}^{\mathrm{M}}+\widetilde{Y}_{13}^{\mathrm{M}}+\widetilde{Y}_{14}^{\mathrm{M}} & -\widetilde{Y}_{14}^{\mathrm{M}} & -\widetilde{Y}_{13}^{\mathrm{M}} \\ -\widetilde{Y}_{13}^{\mathrm{M}} & -\widetilde{Y}_{14}^{\mathrm{M}} & \widetilde{Y}_3^{\mathrm{M}}+\widetilde{Y}_{13}^{\mathrm{M}}+\widetilde{Y}_{14}^{\mathrm{M}}+\widetilde{Y}_{34}^{\mathrm{M}} & -\widetilde{Y}_{34}^{\mathrm{M}} \\ -\widetilde{Y}_{14}^{\mathrm{M}} & -\widetilde{Y}_{13}^{\mathrm{M}} & -\widetilde{Y}_{34}^{\mathrm{M}} & \widetilde{Y}_3^{\mathrm{M}}+\widetilde{Y}_{13}^{\mathrm{M}}+\widetilde{Y}_{14}^{\mathrm{M}}+\widetilde{Y}_{34}^{\mathrm{M}} \end{pmatrix}. \tag{4.11}$$

Diagonalization of this admittance matrix leads to a block-diagonal admittance matrix with two submatrices. The block-diagonal elements of this new matrix are referred to as *common mode* admittance matrix $\mathbf{Y}_{\Sigma}^{\mathrm{M}}$ and the *differential mode* admittance matrix $\mathbf{Y}_{\Delta}^{\mathrm{M}}$. They are given by

$$\mathbf{Y}_{\Sigma}^{\mathrm{M}} = \begin{pmatrix} \widetilde{Y}_1^{\mathrm{M}} + \widetilde{Y}_{13}^{\mathrm{M}} + \widetilde{Y}_{14}^{\mathrm{M}} & -\widetilde{Y}_{13}^{\mathrm{M}} - \widetilde{Y}_{14}^{\mathrm{M}} \\ -\widetilde{Y}_{13}^{\mathrm{M}} - \widetilde{Y}_{14}^{\mathrm{M}} & \widetilde{Y}_3^{\mathrm{M}} + \widetilde{Y}_{13}^{\mathrm{M}} + \widetilde{Y}_{14}^{\mathrm{M}} \end{pmatrix} \tag{4.12}$$

and (4.13)

$$\mathbf{Y}_{\Delta}^{\mathrm{M}} = \begin{pmatrix} \widetilde{Y}_1^{\mathrm{M}} + 2\widetilde{Y}_{12}^{\mathrm{M}} + \widetilde{Y}_{13}^{\mathrm{M}} + \widetilde{Y}_{14}^{\mathrm{M}} & -\widetilde{Y}_{13}^{\mathrm{M}} + \widetilde{Y}_{14}^{\mathrm{M}} \\ -\widetilde{Y}_{13}^{\mathrm{M}} + \widetilde{Y}_{14}^{\mathrm{M}} & \widetilde{Y}_3^{\mathrm{M}} + \widetilde{Y}_{13}^{\mathrm{M}} + \widetilde{Y}_{14}^{\mathrm{M}} + 2\widetilde{Y}_{34}^{\mathrm{M}} \end{pmatrix}, \tag{4.14}$$

respectively. Circuit representations of these matrices are shown in Fig. 4.3 and Fig. 4.4 in terms of π-type networks. It can be noticed that some entries in both matrices repeat. This leads to the relation between $\mathbf{Y}_{\Sigma}^{\mathrm{M}}$ and $\mathbf{Y}_{\Delta}^{\mathrm{M}}$, viz.

$$\mathbf{Y}_{\Delta}^{\mathrm{M}} = \mathbf{Y}_{\Sigma}^{\mathrm{M}} + 2\begin{pmatrix} \widetilde{Y}_{12}^{\mathrm{M}} & \widetilde{Y}_{14}^{\mathrm{M}} \\ \widetilde{Y}_{14}^{\mathrm{M}} & \widetilde{Y}_{34}^{\mathrm{M}} \end{pmatrix}. \tag{4.15}$$

The design of matching networks for both *radiation modes* is mutually dependent via elements $\widetilde{Y}_1^{\mathrm{M}}$, $\widetilde{Y}_{13}^{\mathrm{M}}$, $\widetilde{Y}_3^{\mathrm{M}}$. However, elements $\widetilde{Y}_{12}^{\mathrm{M}}$, $\widetilde{Y}_{34}^{\mathrm{M}}$, and $\widetilde{Y}_{14}^{\mathrm{M}}$

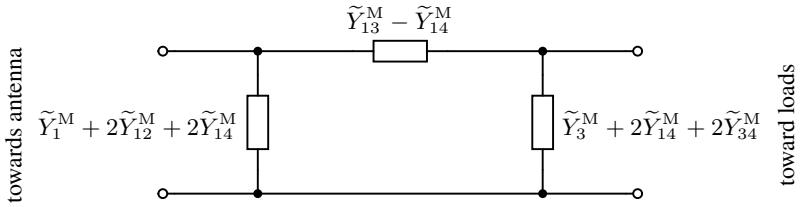

Fig. 4.4.: π-type matching network of the *differential mode*.

provide certain degree of freedom in a design of the *differential mode* matching network.

4.3.3. Design of a lossless multiport matching network at single frequency

A lossless N-port antenna can be analytically matched at a single frequency using lossless multiport matching network with the scattering matrix given by (4.7). The degrees of freedom are given by a unitary matrix $\mathbf{U}$. In general a unitary matrix $\mathbf{U}$ comprises complex entries. The values of their magnitudes can be chosen with respect to the desired set of mutually orthogonal radiation patterns. Selection of phasors in $\mathbf{U}$ amounts to different realizations of multiport matching network which, however, lead to the same set of mutually orthogonal radiation patterns.

Analytical solution for matching of symmetric 2-port antenna (I)

In order to illustrate the above stated facts it is convenient to take a recourse to a multiport matching network for a 2-port antenna. A unitary matrix $\mathbf{U}$ in this case is given by [31]

$$\mathbf{U} = \begin{pmatrix} k & \mathrm{e}^{-\mathrm{j}\phi}\sqrt{1-k^2} \\ \sqrt{1-k^2} & -k\mathrm{e}^{-\mathrm{j}\phi} \end{pmatrix}, \tag{4.16}$$

where $k \in [0, 1]$ and ϕ are real. For fixed value $\phi = 0$ the parameter k leads to a different realization of a multiport matching network supporting different sets of two mutually orthogonal radiation patterns and different return loss observed at each port. The cases when $k = 0$ and $k = \frac{1}{\sqrt{2}}$ are of importance when

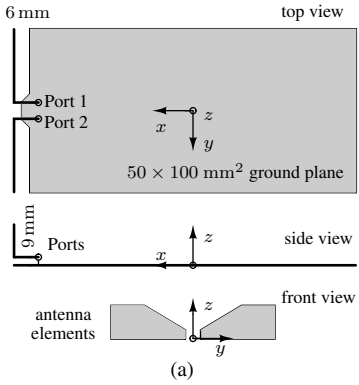

$$\mathbf{S}^{\mathrm{A}}(f_0) = \begin{pmatrix} -0.37-0.62\,\mathrm{j} & 0.093+0.13\,\mathrm{j} \\ 0.093+0.13\,\mathrm{j} & -0.37-0.62\,\mathrm{j} \end{pmatrix} \tag{4.17}$$

$$\mathbf{Y}^{\mathrm{A}}(f_0) = \begin{pmatrix} 0.116-0.305\,\mathrm{j} & 0.063+0.048\,\mathrm{j} \\ 0.063+0.048\,\mathrm{j} & 0.116-0.305\,\mathrm{j} \end{pmatrix} \tag{4.18}$$

$$\mathbf{R}^{\mathrm{A}}(f_0) = \begin{pmatrix} 0.46 & 0.23 \\ 0.23 & 0.46 \end{pmatrix} \tag{4.19}$$

Fig. 4.5.: Simplified schematic drawing of the example symmetric 2-port antenna system and its scattering matrix, admittance matrix (given in mS) and the radiation matrix at $f_0 = 1.77$ GHz.

dealing with symmetric 2-port antennas. Consider an antenna system for a handset on a $50 \times 100\ \mathrm{mm}^2$ ground plane shown in Fig. 4.5 after [111]. Two bow-tie antenna elements are placed symmetrically $6\ \mathrm{mm}$ from the shorter edge of the chassis. Each antenna element is $9\ \mathrm{mm}$ high. The S-parameters of the 2-port antenna system were obtained by FDTD simulation. The scattering matrix and the radiation matrix of the antenna at 1.77 GHz are given by (4.17) and (4.19), respectively. A lossless 4-port matching network is analytically synthesized at center frequency using (4.7) with $\mathbf{U}$ given by (4.16) for $\phi = 0$ and $k \in \{0, \frac{1}{\sqrt{2}}\}$. For $k = 0$ the matrix $\mathbf{U}$ becomes

$$\mathbf{U} = \begin{pmatrix} 0 & 1 \\ 1 & 0 \end{pmatrix}. \tag{4.20}$$

The matching network, synthesized analytically with $\mathbf{U}$ given by (4.20), is shown in Fig. 4.6. Due to symmetry of the multiport matching network $\mathrm{RL}_{33} = \mathrm{RL}_{44}$. At each port a particular superposition of the *common mode* and the *differential mode* is observed. Both superpositions are mutually orthogonal, thus the radiation patterns are mutually orthogonal (see Fig. 4.7). For $k = \frac{1}{\sqrt{2}}$ the matrix $\mathbf{U}$ becomes

$$\mathbf{U} = \mathbf{V} = \frac{1}{\sqrt{2}} \begin{pmatrix} 1 & 1 \\ 1 & -1 \end{pmatrix}. \tag{4.21}$$

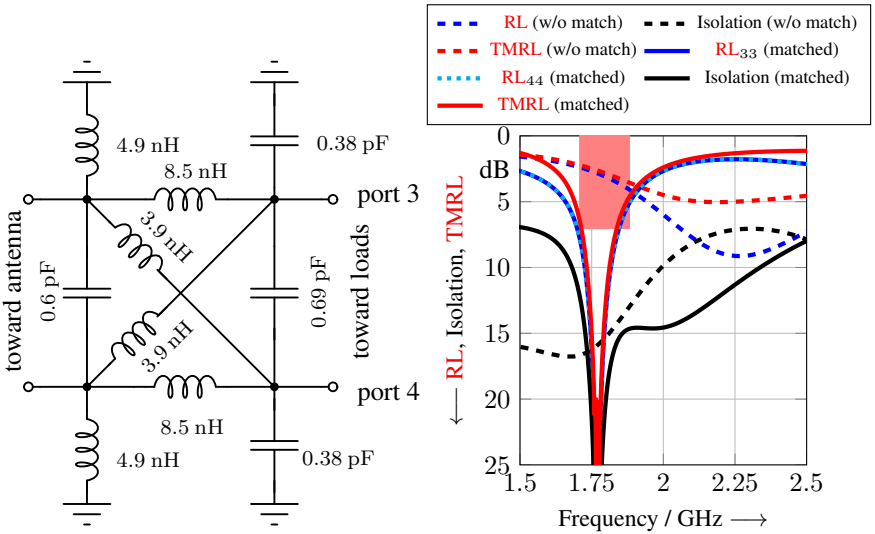

Fig. 4.6.: (a) Multiport matching network designed analytically using (4.7), where the matrix $\mathbf{U}$ is given by (4.16), with $\phi = 0$ and $k = 0$, (b) RL, isolation and TMRL of the antenna system after matching (solid) and a comparison to unmatched antenna (dashed).

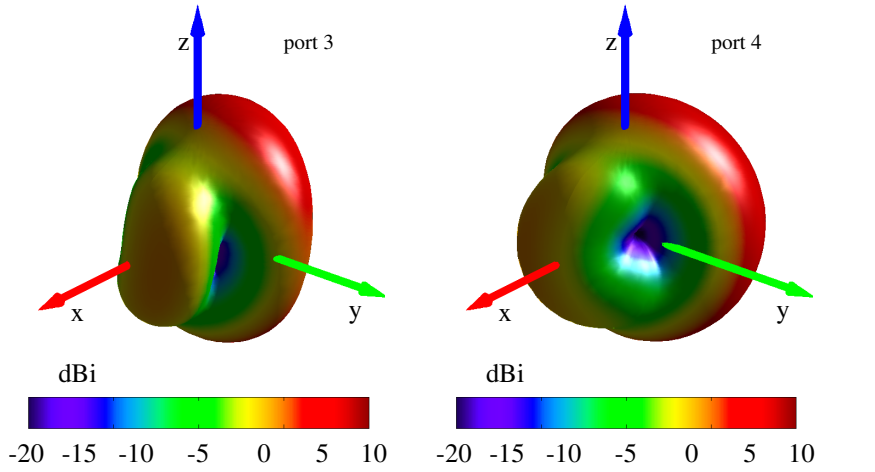

Fig. 4.7.: Total gain (both polarizations) for the port 3 (left) and port 4 (right) of the 2-port MIMO antenna after Fig. 4.5 with the matching network after Fig. 4.6 at 1.77 GHz. Gain values are given in dBi.

The matching network, synthesized analytically with $\mathbf{U} = \mathbf{V}$ given by (4.21), is shown in Fig. 4.8. Due to asymmetry of the multiport matching network $\mathrm{RL}_{33} \neq \mathrm{RL}_{44}$. Due to the fact that $\mathbf{U} = \mathbf{V}$ at the output ports the *radiation modes* of the antenna system are seen. By definition the radiation patterns associated with these modes are mutually orthogonal (see Fig. 4.9). The matching network, shown in Fig. 4.8, features $180°$ phase shift between the output ports. It is important to note that both above described solutions are narrowband.

Analytical solution for matching of symmetric 2-port antenna (II)

The unique analytical synthesis of the multiport matching network for a symmetric 2-port antennas can also be accomplished using the following discussion. Consider 2-port π-type matching networks for the *common mode* and the *differential mode* matching shown in Figs. 4.3, 4.4. Input admittance of the *common mode* Y_{Σ}^{in} and the *differential mode* Y_{Δ}^{in} seen at the the feed ports are

$$Y_{\Sigma}^{\mathrm{in}} = \widetilde{Y}_{3}^{\mathrm{M}} + \widetilde{Y}_{13}^{\mathrm{M}} + \widetilde{Y}_{14}^{\mathrm{M}} - \frac{(\widetilde{Y}_{13}^{\mathrm{M}} + \widetilde{Y}_{14}^{\mathrm{M}})^2}{\widetilde{Y}_{1}^{\mathrm{M}} + \widetilde{Y}_{13}^{\mathrm{M}} + \widetilde{Y}_{14}^{\mathrm{M}} + Y_{\Sigma}^{\mathrm{A}}} \tag{4.22}$$

and

$$Y_{\Delta}^{\mathrm{in}} = \widetilde{Y}_{3}^{\mathrm{M}} + \widetilde{Y}_{13}^{\mathrm{M}} + \widetilde{Y}_{14}^{\mathrm{M}} + 2\widetilde{Y}_{34}^{\mathrm{M}} - \frac{(\widetilde{Y}_{13}^{\mathrm{M}} - \widetilde{Y}_{14}^{\mathrm{M}})^2}{\widetilde{Y}_{1}^{\mathrm{M}} + \widetilde{Y}_{13}^{\mathrm{M}} + \widetilde{Y}_{14}^{\mathrm{M}} + 2\widetilde{Y}_{12}^{\mathrm{M}} + Y_{\Delta}^{\mathrm{A}}}, \tag{4.23}$$

respectively. Y_{Σ}^{A} and Y_{Δ}^{A} are, respectively, the common mode and the differential mode input admittances of the antenna. This linear system of 4 equations with 6 unknowns does not have a unique solution for a single frequency f_0. Many different solutions exist which minimize total multiport reflectance allowing for compromise between level of matching and bandwidth as well as complexity and values of the network elements. The number of degrees of freedom can be reduced by discarding, for example, elements $\widetilde{Y}_{12}^{\mathrm{M}}$ and $\widetilde{Y}_{14}^{\mathrm{M}}$, then relations (4.22) and (4.23) simplify to

$$Y_{\Sigma}^{\mathrm{in}} = \widetilde{Y}_{3}^{\mathrm{M}} + \widetilde{Y}_{13}^{\mathrm{M}} - \frac{\left(\widetilde{Y}_{13}^{\mathrm{M}}\right)^2}{\widetilde{Y}_{1}^{\mathrm{M}} + \widetilde{Y}_{13}^{\mathrm{M}} + Y_{\Sigma}^{\mathrm{A}}}, \tag{4.24}$$

$$Y_{\Delta}^{\mathrm{in}} = \widetilde{Y}_{3}^{\mathrm{M}} + \widetilde{Y}_{13}^{\mathrm{M}} + 2\widetilde{Y}_{34}^{\mathrm{M}} - \frac{\left(\widetilde{Y}_{13}^{\mathrm{M}}\right)^2}{\widetilde{Y}_{1}^{\mathrm{M}} + \widetilde{Y}_{13}^{\mathrm{M}} + Y_{\Delta}^{\mathrm{A}}}. \tag{4.25}$$

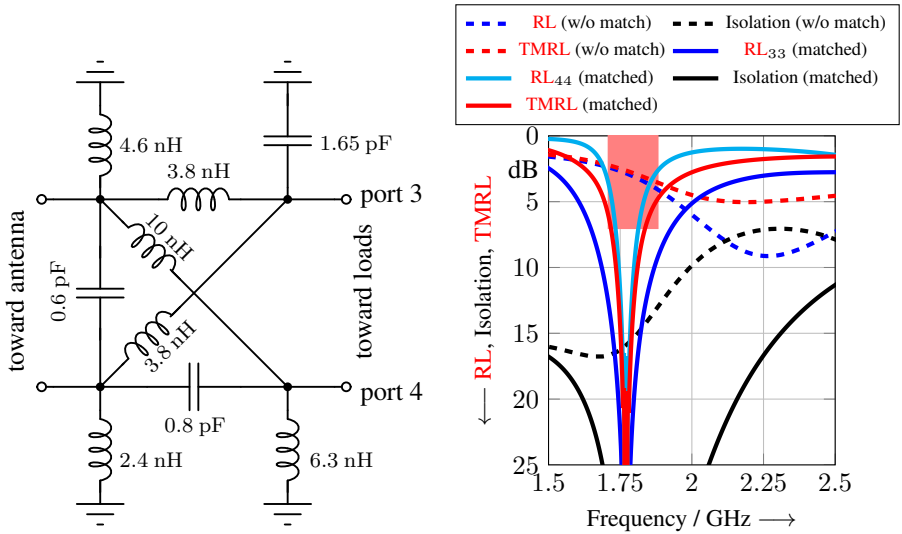

Fig. 4.8.: (a) Multiport matching network designed analytically using (4.7), where the matrix $\mathbf{U}$ is given by (4.16) with $\phi = 0$ and $k = \frac{1}{\sqrt{2}}$, (b) RL, isolation and TMRL of the antenna system after matching (solid) and a comparison to unmatched antenna (dashed).

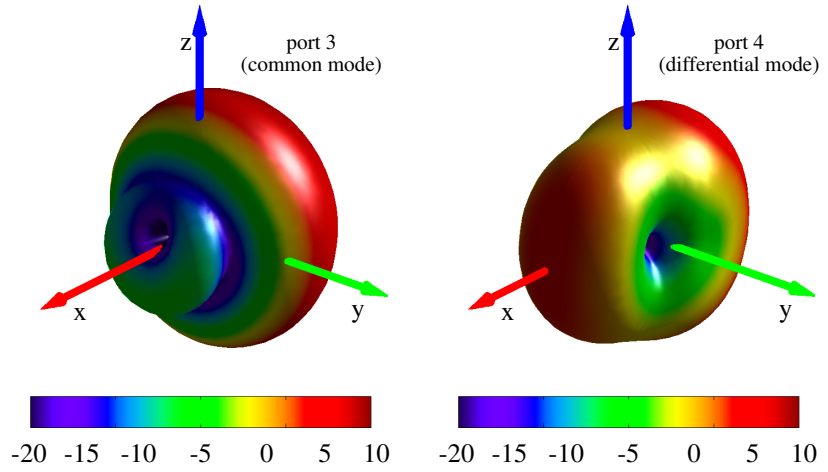

Fig. 4.9.: Total gain (both polarizations) for the port 3 (left) and port 4 (right) of the 2-port MIMO antenna after Fig. 4.5 with the matching network after Fig. 4.8 at 1.77 GHz. Gain values are given in dBi.

For matching at a single frequency f_0 (4.24) and (4.25) lead to 4 real equations with 4 unknowns which have a unique solution. This unique solution can serve as analytically obtained starting point for optimization but in many cases is already sufficient. As an example consider synthesis of a multiport matching network for symmetric 2-port antenna, shown in Fig. 4.5, at $f_0 = 1.77$ GHz. The unique solution is shown in Fig. 4.10 whereas the comparison of return loss, isolation and TMRL for the antenna without and with matching network are given in Fig. 4.11. Obviously, due to assumed symmetry of the multiport matching network $\mathrm{RL}_{33} = \mathrm{RL}_{44}$ and the descriptive quantity which determines the bandwidth is TMRL. The 7dB TMRL bandwidth is insufficient to cover PCS frequency band (from 1710 MHz to 1880 MHz). However, the values of the matching network elements remain the starting values for the proposed systematic synthesis procedure, which allows to maximize TMRL over the desired bandwidth, outlined in subsection 4.3.5.

4.3.4. Weber's systematic synthesis of multiport matching network

A systematic approach for achieving match of N-port antennas with a $2N$-port network to match the antenna system was shown in [28, 29]. Fig. 4.12 shows the schematic representation of the matching problem after [28]. A voltage transfer matrix $\mathbf{T}_\mathrm{U}$ is defined with respect to voltage vector $\boldsymbol{u}^\mathrm{A}$ at the antenna ports $1, ..., N$ and voltage vector $\boldsymbol{u}^\mathrm{P}$ at the external ports $N+1, ..., 2N$. If the antenna admittance matrix is given by $\mathbf{Y}^\mathrm{A}$ and the matching network is *lossless* then the voltage transfer function is given by

$$\mathbf{T}_\mathrm{U} = \Big(\mathcal{C}\big(\Re(\mathbf{Y}^\mathrm{A})\big)\Big)^{-1} \boldsymbol{\Psi} Y_\mathrm{L}^{\frac{1}{2}}, \tag{4.26}$$

where symbol $\mathcal{C}(\cdot)$ denotes Cholesky decomposition and Y_L is the load admittance. The unitary matrix $\boldsymbol{\Psi}$ is defined by the desired voltage transfer matrix $\mathbf{T}_{\mathrm{U,d}}$

$$\boldsymbol{\Psi} = \mathcal{C}\big((\mathbf{T}_{\mathrm{U,d}}\mathbf{T}^\dagger{}_{\mathrm{U,d}})^{-1}\big)\mathbf{T}_{\mathrm{U,d}}. \tag{4.27}$$

$\mathbf{T}_{\mathrm{U,d}}$ is arbitrary but physically constrained to the permissible set of matrices. The admittance matrix of the matching network $\mathbf{Y}^\mathrm{M}$ is a function of the voltage transfer matrix $\mathbf{T}_\mathrm{U}$ and admittance matrix of the antenna $\mathbf{Y}^\mathrm{A}$

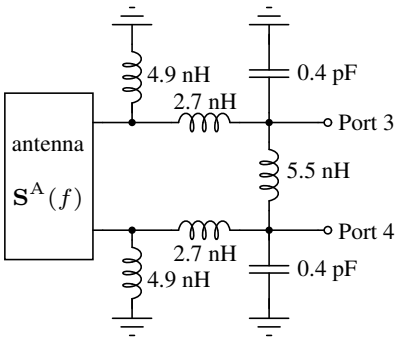

Fig. 4.10.: Matching network topology and element values for matching of the 2-port antenna system (see Fig. 4.5) at 1.77 GHz obtained analytically using (4.24) and (4.25).

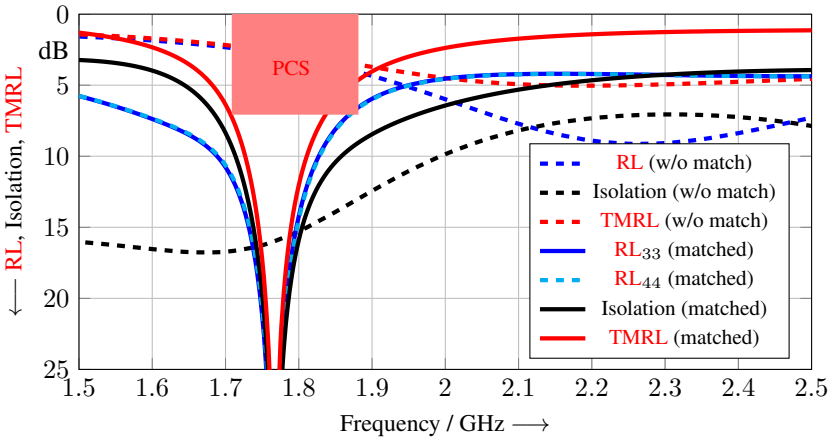

Fig. 4.11.: Per port RL, isolation and TMRL for the example of symmetric 2-port MIMO antenna after Fig. 4.5 *without* (dashed curves) and *with* (solid curves) lossless multiport matching network (see Fig. 4.10) designed analytically at 1.77 GHz using (4.24) and (4.25).

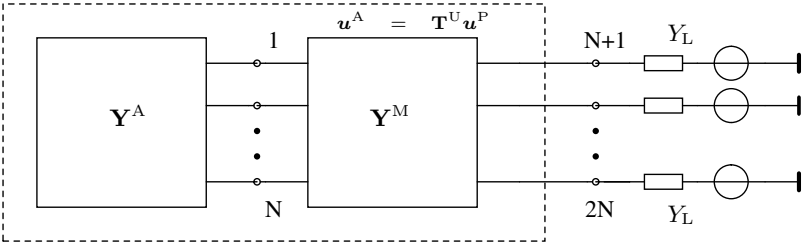

Fig. 4.12.: Simplified schematic representation of an N-port antenna matching problem as given in [28]. $\mathbf{Y}^{\mathrm{A}}$ and $\mathbf{Y}^{\mathrm{M}}$ denote admittance matrix of an antenna and a matching network, respectively. Voltages at the reference plane between the antenna and matching network $\boldsymbol{u}^{\mathrm{A}}$ are related to the voltages at the output port of the cascade $\boldsymbol{u}^{\mathrm{P}}$ are given by voltage transfer function $\mathbf{T}^{\mathrm{U}}$.

$$\mathbf{Y}^{\mathrm{M}} = \begin{pmatrix} Y_{\mathrm{L}}\left(\Im(\mathbf{T}_{\mathrm{U}})\right)^{-1}\Re(\mathbf{T}_{\mathrm{U}}) & -\Re(\mathbf{Y}^{\mathrm{A}})\Big(\Re(\mathbf{T}_{\mathrm{U}})\left(\Im(\mathbf{T}_{\mathrm{U}})\right)^{-1}\Re(\mathbf{T}_{\mathrm{U}}) + \Im(\mathbf{T}_{\mathrm{U}})\Big) \\ -Y_{\mathrm{L}}\left(\Im(\mathbf{T}_{\mathrm{U}})\right)^{-1} & \Re(\mathbf{Y}^{\mathrm{A}})\Re(\mathbf{T}_{\mathrm{U}})\left(\Im(\mathbf{T}_{\mathrm{U}})\right)^{-1} - \Im(\mathbf{Y}^{\mathrm{A}}) \end{pmatrix}, \tag{4.28}$$

which allows to calculate elements of the multiport matching network (see subsection 4.3.1). In conclusion, the approach allows to design multiport matching network for N-port antennas. Losses of the elements of the matching network can be included into the design consideration. It allows for realization of the desired set of "port patterns" as part of the design procedure. However, use of a voltage transfer function as descriptive quantity and need for specification of the desired voltage transfer function drive the complexity of the method. The design approach applies to a single frequency only. The effort of this design procedure may be justified in case of antenna systems featuring small fractional bandwidth. Therefore, the approach remains applicable to satellite communication systems. However, in case of multiport antenna design for mobile wireless communication systems the bandwidth has to be considered as an important descriptive quantity. Therefore, it is necessary to take a recourse to a numerical approach outline in the subsection 4.3.5.

4.3.5. Proposed systematic synthesis of multiport matching network (I)

Systematic design procedure for synthesis of the multiport matching network introduced by Weber in [28, 29] is appropriate for narrowband antenna system

where the goal is to design a multiport antenna with respect to a desired set of radiation patterns. However, in case of antennas for mobile wireless terminals the primary design goal is to achieve high total efficiency over the desired bandwidth. Therefore, different descriptive quantity and the optimization criterion must be used. The present subsection introduces optimization procedure, after [111], which allows to match a multiport antenna system over the desired bandwidth. Further, simple numerical example is provided in order to illustrate the usefulness of the proposed design approach.

Optimization criterion

In Chapter 2 the quantity called TMRL was introduced. It is useful to characterize a multiport antenna system with respect to mismatch. Therefore, this quantity can be successfully applied as an optimization criterion. With reference to Fig. 4.1 it is obvious that in order for the multiport antenna to be matched, ideally, $\mathbf{S}^{\mathrm{P}}$ should vanish about the design frequency f_0. A suitable measure for this is the total multiport reflectance Γ_{tot} or equivalently TMRL as defined in [38]

$$\Gamma_{\mathrm{tot}}^{\mathrm{P}} \to 0 \quad \text{or} \quad \mathrm{TMRL}^{\mathrm{P}} \to \infty. \tag{4.29}$$

Optimization procedure

Ideally, to achieve multiport match (4.29) has to be fulfilled. In practical applications it is usually required to minimize $\Gamma_{\mathrm{tot}}^{\mathrm{P}}$ over a set of frequency points $\{f_1, ..., f_k\}$ by appropriate choice of the multiport matching network topology and element values (see e.g. Fig. 4.2). The least squared error type penalty function

$$\boldsymbol{P}^{\mathrm{M,opt}} = \arg\min_{\{\boldsymbol{P}^{\mathrm{M}}\}} \sum_{k=1}^{K} \left| \Gamma_{\mathrm{tot}}^{\mathrm{P}} \left(\mathbf{S}^{\mathrm{A}}(f_k), \boldsymbol{P}^{\mathrm{M}}, f_k \right) \right|^2, \tag{4.30}$$

where $\boldsymbol{P}^{\mathrm{M}} = (P_{11}^{\mathrm{M}}, ..., P_{NN}^{\mathrm{M}})$ are circuit parameters, has to be used. $\boldsymbol{P}^{\mathrm{M,opt}} = (P_{11}^{\mathrm{M,opt}}, ..., P_{NN}^{\mathrm{M,opt}})$ are the optimum solutions. P_{ij}^{M} becomes either L_{ij} in the branch ij or C_{ij} whatever yields the smaller value of $\Gamma_{\mathrm{tot}}^{\mathrm{P}}$ (see subsection 4.3.1). Optimization is performed over a set of frequency points $\{f_1, ..., f_K\}$. Various minimization algorithms can be used for solving (4.30). A genetic algorithm is used for obtaining the type of elements and the initial element values. Then the gradient type optimization finds exact element values.

Numerical example

Consider again the example antenna system shown in Fig. 4.5 after [111]. TMRL is given for the antenna without matching and with matching network in Fig. 4.14. Without any matching the RL is lower than 4 dB over the desired PCS frequency band (from 1710 MHz to 1880 MHz). The matching network, synthesized using optimization procedure given by (4.30), is found to have a topology and element values as shown in Fig. 4.13. The element with index 12 was found to be a small value capacitance (less than 0.05 pF) and was discarded. The matched antenna features higher than 10 dB RL and isolation which correspond to better than 7 dB TMRL. The result complies with the PCS band specification at 7 dB TMRL (given by the red rectangle). Design and realization of a multiport matching network for a 2-port MIMO antenna, targeting a datacard as an intended platform, and featuring electrical switching is shown in Chapter 6.

4.4. Mapping of *Radiation Modes* to Ports: Mode Decomposition Network

In general at each external port of the antenna system a particular linear superposition of radiation modes is observed. The bandwidth of such antenna system is defined with respect to TMRL. If the desired bandwidth is smaller or equal the TMRL bandwidth then multiport antenna design is completed. However, this may not be possible for small mobile wireless devices with high aspect ratio. If the TMRL bandwidth of an antenna system is insufficient then it is necessary to exploit individual radiation mode bandwidths. Therefore, apart from multiport matching network an additional network is required to map radiation modes to external ports of the antenna system. This additional network shall be called Mode Decomposition Network (MDN) since its purpose is to map radiation modes to external port at the reference impedance level. The goal of the present section is to describe the scattering matrix of an ideal MDN and to show two possible ways of MDN's usage (see further two subsections). The scattering matrix of an MDN was given by Kahn in [30] as

$$\mathbf{S}^{\mathrm{MDN}} = \begin{pmatrix} \mathbf{0} & \mathbf{V} \\ \mathbf{V}^{\top} & \mathbf{0} \end{pmatrix}. \tag{4.31}$$

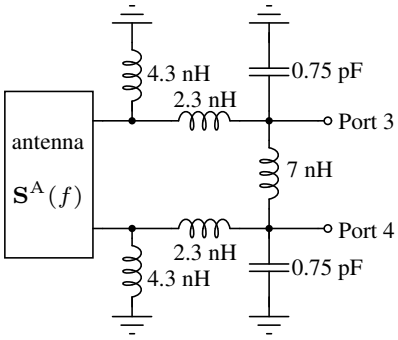

Fig. 4.13.: Matching network topology and element values for matching of the 2-port antenna system (see Fig. 4.5) within PCS frequency band (from 1.71 GHz to 1.88 GHz) obtained numerically using (4.30).

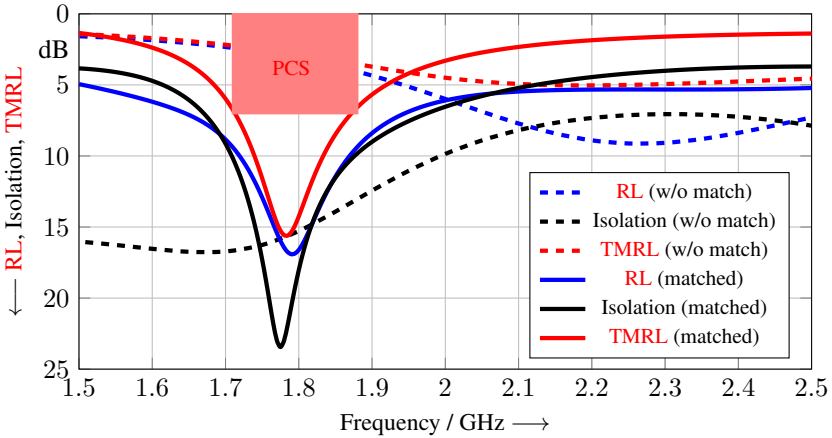

Fig. 4.14.: Per port RL, isolation and TMRL for an example of symmetric 2-port MIMO antenna after Fig. 4.5 *without* (dashed curves) and *with* (solid curves) multiport matching network after Fig. 4.13.

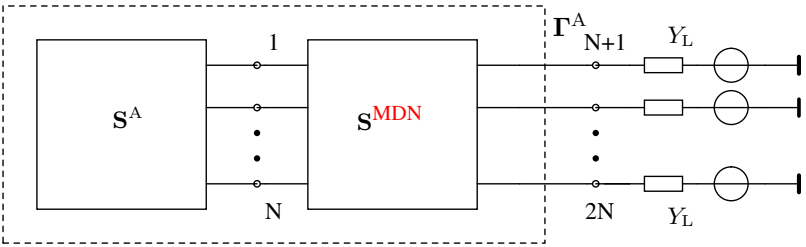

Fig. 4.15.: Simplified schematic representation of an N-port antenna with MDN.

The columns of $\mathbf{V}$ comprise the *radiation modes* of the antenna system. If an MDN is connected directly to the antenna (see Fig. 4.15) then the scattering matrix seen at the external ports of the cascade can be obtained by exploiting

$$\mathbf{S}^{\mathrm{P}} = \mathbf{S}_{21}^{\mathrm{MDN}}\mathbf{S}^{\mathrm{A}}(\mathbf{I} - \mathbf{S}_{11}^{\mathrm{MDN}}\mathbf{S}^{\mathrm{A}})^{-1}\mathbf{S}_{12}^{\mathrm{MDN}} + \mathbf{S}_{22}^{\mathrm{MDN}}, \tag{4.32}$$

where submatrices of $\mathbf{S}^{\mathrm{MDN}}$ are given by (4.31). The result is

$$\mathbf{S}^{\mathrm{P}} = \mathbf{V}^{\top}\mathbf{S}^{\mathrm{A}}(\mathbf{I} - \mathbf{0}\mathbf{S}^{\mathrm{A}})^{-1}\mathbf{V} + \mathbf{0} = \mathbf{V}^{\top}\mathbf{S}^{\mathrm{A}}\mathbf{V} = \mathbf{\Gamma}^{\mathrm{A}}, \tag{4.33}$$

where $\mathbf{\Gamma}^{\mathrm{A}}$ is the modal reflectances matrix of the antenna, which indicates that at external ports of the cascade the *radiation modes* of the antenna are directly accessible. However, it is important to note that the radiation modes at external ports remain unmatched. Also the above analysis does not take into account mismatch in the plane between multiport antenna and an MDN. The discussion on this issue is taken up in section 4.6.

Use of an MDN is of particular importance for realization of the DL-MIMO concept which is introduced in Chapter 5. In many cases an MDN provides multi-band operation of multiport antennas for MIMO application. An advantageous implementation of an MDN for 2-port antennas which not only maps radiation modes to external ports but also enables their electrical tuning is introduced in Chapter 5, after [112]. Implementation of this MDN is shown in Chapter 6 using as an example a 2-port DL-MIMO antenna for USB dongles.

4.4.1. Sequence of matching and mode decomposition

Joint inspection of (4.33) and Fig. 4.15 indicates that once *radiation modes* are mapped to external ports their *modal reflectances* can be matched to load

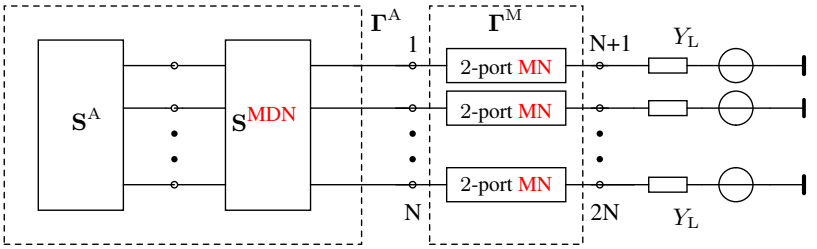

Fig. 4.16.: Schematic representation of the approach after [32] adopted by Chaudhury [15, 17, 18], Volmer [31, 33] and Lee [8, 114, 7] to map *radiation modes* to external ports and subsequently match modal reflectances using separate and independent 2-port matching networks.

impedances by means of N separate 2-port matching networks. The same sequence of mode decomposition and matching can be found from (4.7). It was shown in [33, 113] that by setting $\mathbf{U} = \mathbf{V}$ in (4.7) and subsequently using the following relations

$$\mathbf{\Gamma}^{\mathrm{A}} = \mathbf{V}^{\top}\mathbf{S}^{\mathrm{A}}\mathbf{V} \quad \text{and} \quad \mathbf{R}^{\mathrm{A}\,\frac{1}{2}} = \mathbf{V}\mathbf{C}^{\mathrm{A}\,\frac{1}{2}}\mathbf{V}^{\dagger}, \tag{4.34}$$

where $\mathbf{C}^{\mathrm{A}}$ denotes the modal efficiency matrix of the antenna, the scattering matrix of the network given by (4.7), which allows to achieve multiport match (in the sense of $\mathbf{S}^{\mathrm{P}} = \mathbf{0}$), can be represented as

$$\mathbf{S}^{\mathrm{N}} = \begin{pmatrix} \mathbf{S}^{\mathrm{A}\,\dagger} & \mathbf{V}\mathbf{C}^{\mathrm{A}\,\frac{1}{2}} \\ \mathbf{C}^{\mathrm{A}\,\frac{1}{2}}\mathbf{V}^{\top} & -\mathbf{\Gamma}^{\mathrm{A}} \end{pmatrix}. \tag{4.35}$$

The network described by (4.35) can be split into a cascade of two consecutive networks with scattering matrices given by

$$\mathbf{S}^{\mathrm{MDN}} = \begin{pmatrix} \mathbf{0} & \mathbf{V} \\ \mathbf{V}^{\top} & \mathbf{0} \end{pmatrix} \quad \text{and} \quad \mathbf{\Gamma}^{\mathrm{M}} = \begin{pmatrix} \mathbf{\Gamma}^{\mathrm{A}\,\dagger} & \mathbf{C}^{\mathrm{A}\,\frac{1}{2}} \\ \mathbf{C}^{\mathrm{A}\,\frac{1}{2}} & -\mathbf{\Gamma}^{\mathrm{A}} \end{pmatrix}, \tag{4.36}$$

where the network connected directly to the antenna is the MDN which provides mapping of *radiation modes* to external ports so that $\mathbf{S}^{\mathrm{P}} = \mathbf{\Gamma}^{\mathrm{A}}$ (see Fig. 4.16). The scattering matrix $\mathbf{\Gamma}^{\mathrm{M}}$ of the multiport matching network in (4.36) is a block-diagonal matrix comprising four diagonal submatrices. This indicates that the matching network is *not* a $2N$-port network but comprises N

separate 2-port matching networks, each responsible for matching a particular *radiation mode*. With reference to Fig. 4.16 it is easy to see that the matching condition given earlier in the present section by (4.39) for the sequence of networks given by (4.38) can be written for the sequence of networks (4.36) as

$$\mathbf{\Gamma}_{11}^{\mathrm{M}} = \mathbf{\Gamma}^{\mathrm{A}\,\dagger}, \tag{4.37}$$

which has to be fulfilled at the reference plane between MDN and 2-port matching networks.

4.4.2. Proposed sequence of matching and mode decomposition

The proposed sequence of matching and mode decomposition follows directly from inspection of (4.7). The multiport matching network with scattering parameters given by (4.7) can be split into a matching network with scattering matrix $\mathbf{S}^{\mathrm{MN}}$ and a second network with scattering matrix $\mathbf{S}^{\mathrm{D}}$, where the matching network is placed between the antenna and the second network, i.e.

$$\mathbf{S}^{\mathrm{MN}} = \begin{pmatrix} \mathbf{S}^{\mathrm{A}\,\dagger} & \mathbf{R}^{\mathrm{A}\,\frac{1}{2}} \\ \mathbf{R}^{\mathrm{A}\,\frac{1}{2}\,\top} & -\mathbf{S}^{\mathrm{A}} \end{pmatrix} \quad \text{and} \quad \mathbf{S}^{\mathrm{D}} = \begin{pmatrix} \mathbf{0} & \mathbf{U} \\ \mathbf{U}^{\top} & \mathbf{0} \end{pmatrix}. \tag{4.38}$$

It is easy to see that the matching network with the scattering matrix $\mathbf{S}^{\mathrm{MN}}$ alone is sufficient to render $\mathbf{S}^{\mathrm{P}} = \mathbf{0}$. The main condition which allows to match multiport antenna is given by [26]

$$\mathbf{S}_{11}^{\mathrm{MN}} = \mathbf{S}^{\mathrm{A}\,\dagger}. \tag{4.39}$$

The second network, given by the scattering matrix $\mathbf{S}^{\mathrm{D}}$ in (4.38), does not provide any matching capability as it represents a network featuring the reference impedance level. If this network's task is to provide mapping of *radiation modes* to external ports then $\mathbf{U} = \mathbf{V}$ which leads to $\mathbf{S}^{\mathrm{P}} = \mathbf{\Gamma}^{\mathrm{A}}$ (see Fig. 4.17). Use of an MDN is optional since at single frequency it is sufficient to use only multiport matching network with scattering matrix given by $\mathbf{S}^{\mathrm{MN}}$ in (4.38) to achieve $\mathbf{S}^{\mathrm{P}} = \mathbf{0}$. However, if broader frequency range is to be considered and the TMRL bandwidth is insufficient then use of MDN may be favorable so as to exploit modal bandwidths of all *radiation modes* individually. It is important to note that in accordance with (4.38) the multiport matching network has to be placed between the antenna and the MDN (see Fig. 4.17) [115].

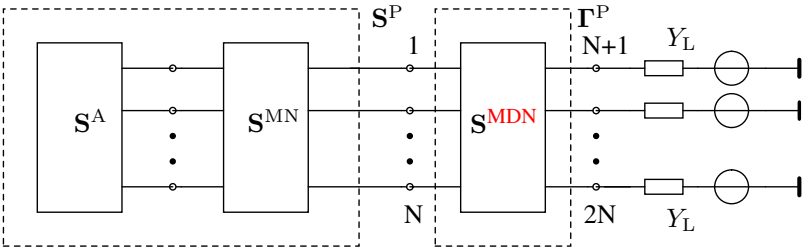

Fig. 4.17.: Schematic representation of the proper sequence of multiport matching network and MDN for an N-port antenna after [115].

This sequence of matching and mode decomposition is further motivated by the fact that it leads to minimization of losses since the MDN, which maps *radiation modes* to external ports at the reference impedance level, is applied to an already matched antenna. The systematic design approach which allows to construct both multiport matching network and MDN is outlined in section 4.7.

4.5. Mapping of *Radiation Modes* to Ports: Implementations

4.5.1. Design approach of Chaudhury, Volmer and Lee

General considerations related to a design approach for multiport antenna matching and for mapping of *radiation modes* to external ports as used by Chaudhury [15, 17, 18], Volmer [31, 33] and Lee [8, 114, 7] have been outlined in subsection 4.4.1. In [116, 18] it is shown that this design approach follows from theoretical work of Youla [32] who demonstrated that any $2N$-port matching network can be split into a cascade of three subnetworks. Two outer subnetworks are all-pass and the middle one consists of a bank of N uncoupled ideal transformers. All three networks are connected by transmission lines with arbitrary electrical lengths. Flaviis shows in [116] that the practical implementation of a network described by such cascade of three subnetworks does not require the 3rd subnetwork. Ideal transformers in a real implementation have to be replaced by 2-port matching networks. Therefore, the modified network consists of a $2N$-port network (i.e. MDN) and N 2-port matching networks

which individually match the *radiation modes* of the antenna (see Fig. 4.16). In [31, 33] the systematic design approach of an MDN is based on the concept of "radiator merging" which is applicable to synthesis of a MDN for practically relevant multiport symmetric antennas. The most general approach for synthesis of an MDN follows from [34] and is presented in section 4.7.2. The elements of lossless mode-specific 2-port matching networks can be easily obtained analytically assuming π-type matching network. The method is outlined in Chapter 5 section 5.2.

In [116] few remarks were made concerning the applicability of the design approach. For the solution to remain viable a multiport antenna must be sufficiently well-matched and losses of the MDN must be sufficiently small. Otherwise high losses may be expected because of the current path over the MDN. This is a practical limitation of the approach which tends to be ignored in the literature. An other issue it that an MDN may consume too much space to be usable in practical applications such as small mobile wireless devices. Practical implementation of multiport match and mapping of *radiation modes* to external ports which gives low losses is presented in section 4.7.

4.5.2. Geren's approach

A systematic approach to achieve multiport match was introduced in [34]. The strength of this approach is straightforward implementation, simplicity and applicability to, in general, N-port antennas. Consider the multiport antenna matching problem shown in Fig. 4.18. The impedance matrix of the antenna is denoted by $\mathbf{Z}^{\mathrm{A}}$. The matching network comprises two networks denoted by A and B which are connected via N reactances. The first step in the design algorithm is eigenvalue decomposition of the imaginary part of the antenna impedance matrix in the form

$$\mathbf{X} = \mathbf{A}^{\top} \Im(\mathbf{Z}^{\mathrm{A}}) \mathbf{A}, \tag{4.40}$$

where $\mathbf{A}$ is a real unitary matrix and $\mathbf{X} = \mathbf{diag}(X_1, X_2, ..., X_N)$ is a diagonal matrix containing the series reactances between network A and B. The topology of network A is found from a decomposition of $\mathbf{A}$ into Givens rotations

$$\mathbf{A} = \mathbf{A}_1 \mathbf{A}_2 \cdots \mathbf{A}_M, \tag{4.41}$$

with $M \leq N(N-1)/2$. The scattering matrix of the network A is given by

$$\mathbf{S}^{\mathrm{NA}} = \begin{pmatrix} \mathbf{0} & \mathbf{A} \\ \mathbf{A}^{\top} & \mathbf{0} \end{pmatrix}. \tag{4.42}$$

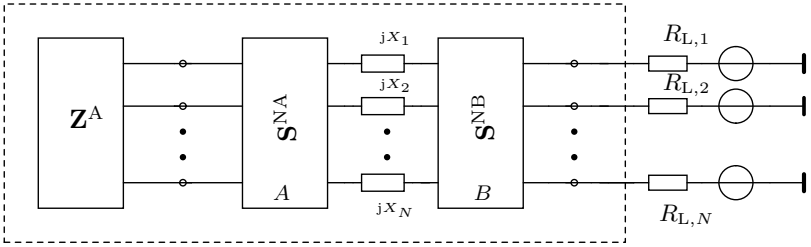

Fig. 4.18.: Schematic representation of N-port antenna system matching using multiport matching network featuring mode decomposition [34].

In order to realize network B the eigenvalue decomposition

$$\mathbf{R}_{\mathrm{L}} = \mathbf{B}^{\top}(\mathbf{A}^{\top}\Re(\mathbf{Z}^{\mathrm{A}})\mathbf{A})\mathbf{B} \tag{4.43}$$

is used. The eigenvalues of $\mathbf{A}^{\top}\Re(\mathbf{Z}^{\mathrm{A}})\mathbf{A}$ define real loads $\mathbf{R}_{\mathrm{L}} = \mathbf{diag}(R_{\mathrm{L},1}, R_{\mathrm{L},2}, ..., R_{\mathrm{L},N})$ at the output of the complete cascade. The unitary matrix $\mathbf{B}$ contains the eigenvectors. The topology of the network B is obtained from a decomposition of $\mathbf{B}$ into Givens rotations

$$\mathbf{B} = \mathbf{B}_1\mathbf{B}_2\cdots\mathbf{B}_K, \tag{4.44}$$

with $K \leq N(N-1)/2$. The scattering matrix of network B is given by

$$\mathbf{S}^{\mathrm{NB}} = \begin{pmatrix} \mathbf{0} & \mathbf{B} \\ \mathbf{B}^{\top} & \mathbf{0} \end{pmatrix}. \tag{4.45}$$

The loads at the output of the matching network are not equal and thus not adjusted to the reference impedance (typically $50\,\Omega$). As noted by the authors, an additional impedance transformation is necessary. This can be accomplished using separate and independent 2-port matching networks. The disadvantage of this design approach is a very complex circuitry, if a lumped element realization is considered. The number of 180° hybrids, featuring equal or unequal power division, used in the overall network design is high. The authors stated that no more than $N(N-1)/2$ hybrids are required to realize either network A or network B. Since the number of lumped elements required to realize a single hybrid is 14 and complete network features in addition N reactances and N 2-port matching networks with at least 2 elements then the total number of lumped elements necessary to implement Geren's approach is $14N^2 - 11N$.

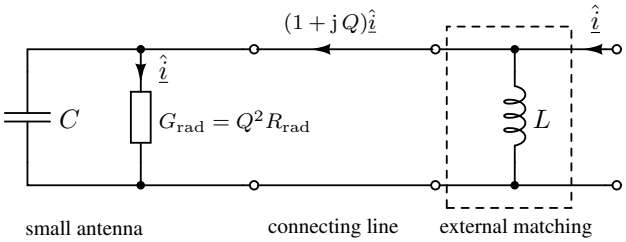

Fig. 4.19.: Illustration of losses in an electrically small antenna.

The impedance matching is performed over many elements, which is likely to increase the losses. However, the advantage of the procedure is that it allows to obtain network topology and element values in a systematic way. At the external ports the *radiation modes* of the antenna are observed. Therefore, exploitation of individual modal bandwidths is feasible with Geren's design approach.

4.6. Discussion of Low Loss Sequence of Matching and Mode Decomposition

The low loss sequence of applying multiport matching network and an MDN is of significant importance for antennas in mobile wireless terminals where high modal efficiency over the desired bandwidth is the main design goal. As indicated in [115] improper sequence of both network may result in high losses. Without loss of generality the problem is most easily illustrated for a single antenna. An electrically small dipole, which features high mismatch, may be considered as an example of antenna which can be easily associated with a single higher order *radiation mode*. A dipole antenna is capacitive below its natural resonance frequency, thus its ECM is a shunt connection of capacitance C and radiation conductance G_{rad} (see Fig. 4.19). The attached matching circuit provides the inductance required to achieve resonance at the desired frequency. The current in the resonant path of the connecting line is by a factor $\sqrt{1+Q^2}$ larger than the external feed current where Q denotes radiation quality factor of the antenna. As a result the loss resistance of the connecting line (and of further switchable or tunable elements subject to this current) is weighted with a factor of $(1+Q^2)$ compared to the case where the connecting

line would be attached behind the matching circuit. The effect is considerable since electrically small antennas feature high radiation quality factor at the order of 100...200 (see Chapter 3 section 3.3).

Reverting to multiport antennas a possible countermeasure to the problem of losses which was shown in [115] is to place the multiport matching network as close as possible to the antenna physical structure and subsequently apply an MDN, if necessary, to the already matched antenna (see Fig. 4.17). As an example consider 4-port MIMO antenna for tablet [115] (see the last section of the present chapter). Assuming that each 180° hybrid of an MDN features 1 dB insertion loss (IL) the expected maximum improvement of efficiency, compared to the design approach of Chaudhury, Volmer and Lee, is around 7 dB.

4.7. Mapping of *Radiation Modes* to Ports: Proposed Implementation

4.7.1. Proposed systematic synthesis of matching network (II)

The task of the multiport matching network here is to match the antenna without changing its *radiation mode*. In order to satisfy this condition the scattering matrix of the matched antenna $\mathbf{S}^{\mathrm{P}}$ (see Fig. 4.1) has to be diagonalizable by the same unitary matrix $\mathbf{V}$ as the scattering matrix $\mathbf{S}^{\mathrm{A}}$ of the antenna itself. The Takagi decomposition then leads to a diagonal modal reflectance matrix

$$\mathbf{\Gamma}^{\mathrm{P}} = \mathbf{V}^{\top}(\mathbf{S}_{12}^{\mathrm{M}\,\top}\mathbf{K}\mathbf{S}_{12}^{\mathrm{M}} + \mathbf{S}_{22}^{\mathrm{M}})\mathbf{V}, \tag{4.46}$$

where $\mathbf{K} = \mathbf{V}^{*}\mathbf{\Gamma}^{\mathrm{A}}(\mathbf{I} - \mathbf{\Gamma}_{11}^{\mathrm{M}}\mathbf{\Gamma}^{\mathrm{A}})^{-1}\mathbf{V}^{\dagger}$ is a complex symmetric matrix. The condition $\mathbf{\Gamma}_{11}^{\mathrm{M}} = \mathbf{\Gamma}^{\mathrm{A}\,\dagger}$, which describes multiport match between the antenna and the matching network, has to be satisfied. The matching network design procedure, described in the next subsection, by minimizing $\mathbf{S}_{12}^{\mathrm{M}\,\top}\mathbf{K}\mathbf{S}_{12}^{\mathrm{M}} + \mathbf{S}_{22}^{\mathrm{M}}$ approximates $\mathbf{\Gamma}_{11}^{\mathrm{M}} = \mathbf{\Gamma}^{\mathrm{A}\,\dagger}$ since $\mathbf{V}$ is unitary.

However, it has to be understood that at each output of the matching network still superpositions of *radiation modes* are seen. The *radiation modes* themselves are not yet directly accessible at the outputs of the multiport matching network. Nevertheless, it is possible to setup an optimization criterion and

procedure which allows to mach *modal reflectances* of the antenna over the required different frequency bands. To this end the total multiport reflectance is replaced by *modal reflectances* as the quantities to be minimized.

Optimization criterion and procedure

The matching condition for multiport antennas can be expressed in terms of minimization of *modal reflectances* or maximization of *modal return loss* over a set of frequencies $\{f_1, ..., f_N\}$. The penalty function is a weighted sum of magnitude squared modal reflectances of the form

$$\boldsymbol{P}^{\mathrm{M,opt}} = \underset{\{\boldsymbol{P}^{\mathrm{M}}\}}{\arg\min} \sum_{n=1}^{N} \sum_{k=1}^{K} |\Gamma_n^{\mathrm{P}}\Big(\mathbf{S}^{\mathrm{A}}(f_k), \boldsymbol{P}^{\mathrm{M}}, f_k\Big)|^2 \mathrm{w}_n(f_k) \tag{4.47}$$

where $\boldsymbol{P}^{\mathrm{M}} = (P_{11}^{\mathrm{M}}, ..., P_{NN}^{\mathrm{M}})$ are the parameters which yield *modal reflectances* $\Gamma_1^{\mathrm{P}}, ..., \Gamma_N^{\mathrm{P}}$ and $\boldsymbol{P}^{\mathrm{M,opt}} = (P_{11}^{\mathrm{M,opt}}, ..., P_{NN}^{\mathrm{M,opt}})$ is the optimum solution. Admittances $\widetilde{Y}_{i,j}^{\mathrm{M}}$ of the matching network are mapped to either capacitance (when $P_{i,j}^{\mathrm{M}} > 0$) or inductance (when $P_{i,j}^{\mathrm{M}} < 0$) (see Chapter 4 subsection 4.3.1). Optimization is performed over the set of frequencies $\{f_1, ..., f_K\}$ with weight terms $\mathrm{w}_1, ..., \mathrm{w}_N$ defined for all *radiation modes*.

4.7.2. Proposed systematic synthesis of MDN

The proposed systematic synthesis of an MDN follows from Geren's design procedure shown in [34] (see subsection 4.5.2). The scattering matrix of the ideal MDN is given by (4.31). The matrix $\mathbf{V}$ can be approximately factored in terms of complex Givens rotations in the form

$$\mathbf{V} \approx \mathbf{V}_1 \mathbf{V}_2 \cdots \mathbf{V}_L, \tag{4.48}$$

where $L \leq N(N-1)/2$. Each $\mathbf{V}_l$ describes a $2N$-port network with $N-2$ through connections. The complete MDN is systematically constructed, assuming approximate frequency independence of $\mathbf{V}$, by cascading L 4-port networks, each containing a hybrid with a particular power division factor k_l^2 and phase shift ϕ_l [31]

$$\begin{pmatrix} v_{ii} & v_{ji} \\ v_{ij} & v_{jj} \end{pmatrix}_l = \begin{pmatrix} k_l & \sqrt{1-k_l^2} \\ \sqrt{1-k_l^2} & -k_l \end{pmatrix} \begin{pmatrix} 1 & 0 \\ 0 & \mathrm{e}^{-\mathrm{j}\phi_l} \end{pmatrix}, \tag{4.49}$$

where v_{ij} denotes element ij of the matrix $\mathbf{V}_l$. For fully symmetric N-port antennas with respect to all port, i.e. if $s_{11} = ... = s_{NN}$ which yields explicitly known real matrix $\mathbf{V}_l$ then $k_l = \frac{1}{\sqrt{2}}$ and $\phi_l = 0°$. The first matrix on the rhs of (4.49) represents the scattering matrix of $180°$ hybrid with unequal power division factor k_l^2. The second matrix on the rhs of (4.49) represents the scattering matrix of the ideal transmission line with phase shift ϕ_l.

Examples of an MDN for multiport symmetric 2-, 3- and 4-port antennas are presented later in this subsection. Lumped element realizations of $180°$ hybrids, necessary to construct an MDN for this type of antennas, were shown in [117]. Design equations are given in appendix. D.

Examples of MDN synthesis for symmetric multiport antennas

MDN for a symmetric 2-port antenna. Design of an MDN for a symmetric 2-port antenna has been frequently considered in literature e.g. [118, 119]. The scattering matrix of this type of antennas is given by

$$\mathbf{S} = \begin{pmatrix} s_{11} & s_{12} \\ s_{12} & s_{11} \end{pmatrix}. \tag{4.50}$$

The unitary matrix

$$\mathbf{V} = \frac{1}{\sqrt{2}} \begin{pmatrix} 1 & 1 \\ 1 & -1 \end{pmatrix} \tag{4.51}$$

is real and frequency independent since the antenna is symmetric (see Chapter 2 subsection 2.3.3). The *modal reflectances* of the *common mode* and the *differential mode*, respectively are

$$\Gamma_\Sigma = s_{11} + s_{12} \tag{4.52}$$

$$\Gamma_\Delta = s_{11} - s_{12}. \tag{4.53}$$

The scattering matrix of the MDN based on (4.51) has the form

$$\mathbf{S}^{\text{MDN}} = \frac{1}{\sqrt{2}} \begin{pmatrix} 0 & 0 & 1 & 1 \\ 0 & 0 & 1 & -1 \\ 1 & 1 & 0 & 0 \\ 1 & -1 & 0 & 0 \end{pmatrix}. \tag{4.54}$$

Power delivered to port 3 splits equally between Ports 1 and 2 and both output signals are in-phase. If port 4 is excited power splits equally between ports 1

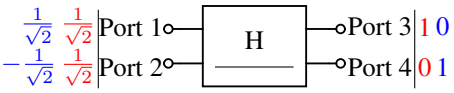

Fig. 4.20.: MDN for a symmetric 2-port antenna system comprising 180° hybrid (symbol "H"). Color coded column vectors on the left and the right side of schematic indicate excitations and their responses.

and 3 with both signals being out-of-phase. Fig. 4.20 illustrates operation of the MDN for a symmetric 2-port MIMO antenna. The MDN described by (4.54) is a 180° hybrid. The most common implementation of such a device, in the literature is a "rat-race" ring hybrid. However, other realizations of an MDN and specifically the design of an electrically tunable MDN are also possible for symmetric 2-port antennas (see Chapter 5).

MDN for a symmetric 3-port antenna. Design of an MDN for a symmetric 3-port antenna are has been considered in [120, 31, 33]. In practice, such antennas can be used in e.g. WLAN access points or LTE-enabled Customer Premises Equipment (CPE). In [31, 33] an MDN is synthesized for an arrangement of three $\lambda/4$ long and $\lambda/4$ spaced monopoles arrange along the center line of a $500 \times 500\ \mathrm{mm}^2$ ground plane. The center frequency of operation is 1 GHz. In this case the MDN features a very interesting topology and the use of a hybrid with unequal power division is necessary.

The antenna arrangement features two symmetry planes, so that $s_{11} = s_{33}$ and $s_{12} = s_{23}$. The scattering matrix then has the form

$$\mathbf{S} = \begin{pmatrix} s_{11} & s_{12} & s_{13} \\ s_{12} & s_{22} & s_{12} \\ s_{13} & s_{12} & s_{11} \end{pmatrix}. \tag{4.55}$$

Takagi decomposition of scattering matrix $\mathbf{S}$ yields the matrix $\mathbf{V}$ which can be written in the form

$$\mathbf{V} = \begin{pmatrix} \frac{k}{\sqrt{2}} & \sqrt{\frac{1-k^2}{2}} & \frac{1}{\sqrt{2}} \\ \sqrt{1-k^2} & -k & 0 \\ \frac{k}{\sqrt{2}} & \sqrt{\frac{1-k^2}{2}} & -\frac{1}{\sqrt{2}} \end{pmatrix} \tag{4.56}$$

where $k \in [0, 1]$. The value of k for *radiation modes* $\boldsymbol{V}_1$ and $\boldsymbol{V}_2$ depends on the physical structure of the antenna. The three *radiation modes* have a

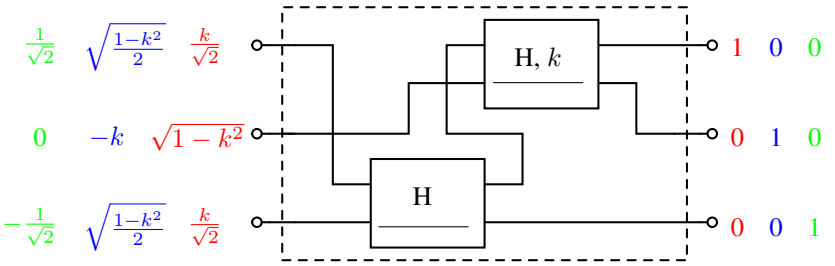

Fig. 4.21.: Schematic representation of a MDN for a symmetric 3-port antenna system with scattering matrix given by (4.55). Color coded column vectors on the left and the right side of schematic indicate excitations and their responses. The upper 180° hybrid (symbol "H") has unequal power division k.

straightforward physical interpretation. The first *radiation mode* can be viewed as an in-phase excitation of all three antenna elements. The second *radiation mode* is frequenty referred to as π-mode. Two outer elements of the antenna are feed in-phase and the center element out-of-phase. The third *radiation mode* (i.e. $\boldsymbol{V}_3 = \frac{1}{\sqrt{2}}(1, 0, -1)^\top$) can be considered as the *differential mode* of a symmetric 2-port antenna which remains when port 2 is terminated with a matched load.

The matrix $\mathbf{V}$ (4.56) can be factored using Givens rotations

$$\mathbf{V} = \begin{pmatrix} \frac{1}{\sqrt{2}} & 0 & \frac{1}{\sqrt{2}} \\ 0 & 1 & 0 \\ \frac{1}{\sqrt{2}} & 0 & -\frac{1}{\sqrt{2}} \end{pmatrix} \begin{pmatrix} k & \sqrt{1-k^2} & 0 \\ \sqrt{1-k^2} & -k & 0 \\ 0 & 0 & 1 \end{pmatrix}. \tag{4.57}$$

(4.57) indicates that construction of an MDN for a symmetric 3-port antenna system requires two 180° hybrids, one with equal and the other with unequal power division k, respectively. The fact that the power division factor k^2 of the second hybrid can be obtained directly from $\mathbf{V}$ simplifies the systematic design procedure. The MDN described by (4.57) is shown in Fig. 4.21.

MDN for a symmetric 4-port antenna. Design of a MDN for a symmetric 4-port antenna system was subject of [114, 118, 121] using geometrically symmetric arrangement of four monopole antennas on a single ground plane. More interesting, in the context of practical applications, is the work presented sequentially in [14, 15, 16, 17], where an MDN of a 4-port MIMO antenna for

a bar-type mobile phone covering WLAN was designed. The design exploits the first four *characteristic modes* on a rectangular $100 \times 40\ \mathrm{mm}^2$ chassis. The scattering matrix of a symmetric 4-port antenna has the form

$$\mathbf{S} = \begin{pmatrix} s_{11} & s_{12} & s_{13} & s_{14} \\ s_{12} & s_{11} & s_{14} & s_{13} \\ s_{13} & s_{14} & s_{11} & s_{12} \\ s_{14} & s_{13} & s_{12} & s_{11} \end{pmatrix}. \tag{4.58}$$

Due to symmetry the matrix $\mathbf{V}$ is frequency independent and explicitly given by [14]

$$\mathbf{V} = \frac{1}{2} \begin{pmatrix} 1 & 1 & 1 & 1 \\ 1 & 1 & -1 & -1 \\ 1 & -1 & 1 & -1 \\ 1 & -1 & -1 & 1 \end{pmatrix}. \tag{4.59}$$

The first *radiation mode* is a *common mode* with respect to all 4 antenna elements. All antenna elements are fed in-phase and the power is equally divided between the antenna elements. Other *radiation modes* are considered to be "differential" between different pairs of antenna elements. The second, the third and the fourth *radiation mode* can be interpreted as a *differential mode* between the two pairs of antennas located on the shorter edges of the chassis, on the diagonal of the chassis, on the longer edges of the chassis, respectively. *Modal reflectances* are related to S-parameters via relations [18]

$$\Gamma_1 = s_{11} + s_{12} + s_{13} + s_{14} \tag{4.60}$$

$$\Gamma_2 = s_{11} + s_{12} - s_{13} - s_{14} \tag{4.61}$$

$$\Gamma_3 = s_{11} - s_{12} + s_{13} - s_{14} \tag{4.62}$$

$$\Gamma_4 = s_{11} - s_{12} - s_{13} + s_{14}. \tag{4.63}$$

The matrix $\mathbf{V}$ (4.59) can be factored using Givens rotations [115]

$$\begin{pmatrix} \frac{1}{\sqrt{2}} & \frac{1}{\sqrt{2}} & 0 & 0 \\ \frac{1}{\sqrt{2}} & -\frac{1}{\sqrt{2}} & 0 & 0 \\ 0 & 0 & 1 & 0 \\ 0 & 0 & 0 & 1 \end{pmatrix} \cdot \begin{pmatrix} 1 & 0 & 0 & 0 \\ 0 & 1 & 0 & 0 \\ 0 & 0 & \frac{1}{\sqrt{2}} & \frac{1}{\sqrt{2}} \\ 0 & 0 & \frac{1}{\sqrt{2}} & -\frac{1}{\sqrt{2}} \end{pmatrix} \cdot \begin{pmatrix} \frac{1}{\sqrt{2}} & 0 & \frac{1}{\sqrt{2}} & 0 \\ 0 & 1 & 0 & 0 \\ \frac{1}{\sqrt{2}} & 0 & -\frac{1}{\sqrt{2}} & 0 \\ 0 & 0 & 0 & 1 \end{pmatrix} \cdot \begin{pmatrix} 1 & 0 & 0 & 0 \\ 0 & \frac{1}{\sqrt{2}} & 0 & \frac{1}{\sqrt{2}} \\ 0 & 0 & 1 & 0 \\ 0 & \frac{1}{\sqrt{2}} & 0 & -\frac{1}{\sqrt{2}} \end{pmatrix}. \tag{4.64}$$

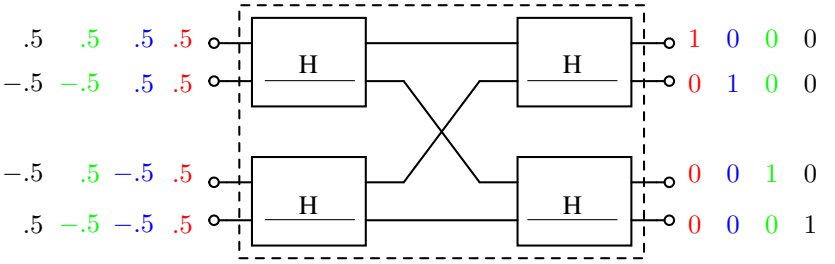

Fig. 4.22.: Schematic representation of a MDN for symmetric 4-port antenna system after e.g. [114] with scattering matrix given by (4.58). Color coded column vectors on the left and the right side of schematic indicate excitations and their responses. Symbol "H" denotes 180° hybrid.

Each matrix corresponds to a 180° hybrid with equal power division. The ones on the diagonal of each matrix indicate the bypass connections between the hybrids. The result given by (4.64) allows to construct a unique MDN which provides excitation of all four *radiation modes* of the antenna system (see Fig. 4.22). It comprises four identical 180° hybrids two in each of the two stages of the network. The network depicted in Fig. 4.22 can be used to realize a 4-port MIMO antenna as was shown in [115] and in the next subsection.

4.7.3. Example antenna design

Construction of *radiation modes* from *characteristic modes*

As an example of application of the systematic design procedures outlined in Chapters 3 and 4 consider design of a multiport antenna system for a 176×230 mm^2 tablet computer. Characteristic modes were obtained on the surface corresponding to the ground plane of the tablet using (3.12). Four capacitive characteristic modes, with surface current densities given in Fig. 4.23, were identified to feature small magnitude eigenvalues in the LTE low-band (from 704 MHz to 960 MHz). In order to strongly excite these four capacitive characteristic modes four low-profile ($\mathrm{h} = 5$ mm) capacitive couplers located at the corners of the device were proposed [115] (see Fig. 4.24). The placement of couplers in the four corners is the same as that reported in [17] for a Wireless Local Area Network (WLAN) frequency band 4-port MIMO antenna. Such placement of capacitive couplers maximizes the reaction integral which means

that the desired four characteristic modes are strongly excited (see Chapter 3). However, as opposed to [17] the present example does not require a slot in the ground plane. In a simplified picture four couplers excite four superpositions of characteristic modes. These superpositions are not yet mutually orthogonal. A multiport matching network which preserves the original *radiation modes* of the antenna structure, designed with respect to the procedure given by (4.47), is necessary in order to match the antenna over the desired E-UTRA BCs in the LTE low-band. Further, mapping of *characteristic modes* to external ports of the antenna system using an MDN described by (4.64) (see Fig. 4.22) is required in order for these modes to correspond to four *radiation modes* of the antenna system defined by multiport symmetry. The design aspects of both networks for the example antenna are outlined in the next subsubsection.

Systematic design of multiport matching network and MDN

The design goal of the multiport matching network was to cover E-UTRA band class (BC) 17 with all four ports and as many as possible remaining BCs in the LTE low-band with at least single port. For illustrative purposes ideal lossless reactive elements were assumed in synthesis of the multiport matching network. The result of the optimization procedure, given by (4.47), is shown in Fig. 4.25. The multiport matching network features 20 lumped elements. This particular solution was chosen out of many others because this network comprises inductances with the smallest nominal values. Therefore, subsequent realization of the network using lossy inductances will lead to a solution with small losses. Four linear superpositions of *radiation modes* are seen at the output of the cascade, comprising the antenna and the multiport matching network. These superpositions are mutually orthogonal within bandwidth given by TMRL. The 7dB TMRL bandwidth is sufficient to cover DL portions of BC 17 and BC 13 but insufficient to cover the Uplink (UL) portions of these bandclasses. In order to exploit bandwidths of *radiation modes* individually the modes are mapped to external ports using MDN. Schematic representation of the complete network comprising multiport matching network and MDN is illustrated in Fig. 4.26. Design of MDN is based on the systematic procedure outlined in section 4.7.2. Due to multiport symmetry of the antenna system the resulting MDN comprises four 180° hybrids. For illustrative purposes it is assumed that all hybrids are ideal and lossless. Therefore, at the external ports of the antenna system reflectances of the four *radiation modes* are seen (see Fig. 4.28).

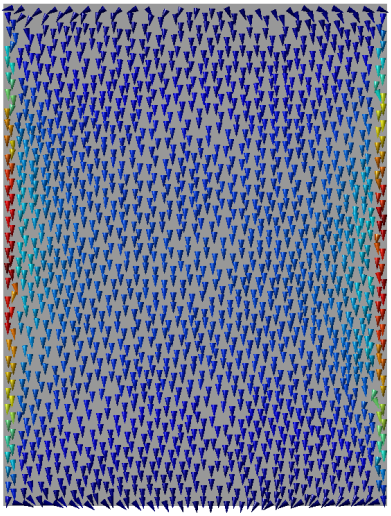

(a) 1st mode 625 MHz

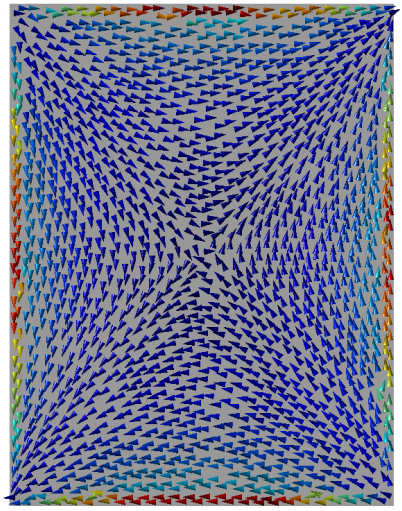

(b) 2nd mode 960 MHz

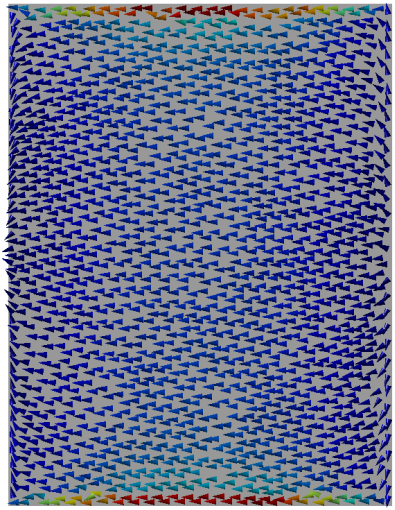

(c) 3rd mode 1157 MHz

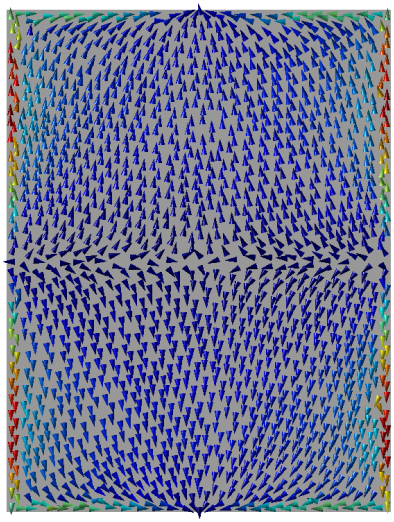

(d) 4th mode 1527 MHz

Fig. 4.23.: Vector plot of the surface current density on the 176 mm $\times$230 mm surface for the first four capacitive characteristic modes at 800 MHz.

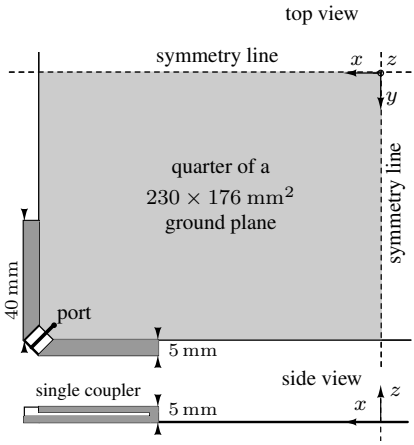

Fig. 4.24.: Simplified schematic drawing of a small single capacitive coupler used in 4-port MIMO antenna system for tablet [115].

Numerical results

As stated before the TMRL 7 dB bandwidth observed at the output of the multiport matching network was found insufficient to match the antenna in both the UL and the DL portions of a band simultaneously (e.g. Evolved Universal Terrestrial Radio Access (E-UTRA) band class (BC) 17, see Fig. 4.28). However, application of the DL-MIMO concept (see further description in Chapter 5) using the cascade comprising multiport matching network depicted in detail in Fig. 4.25 and an ideal MDN (see Fig. 4.26) leads to the *modal return loss* seen at the external ports as shown in Fig. 4.28. The result indicates that this example antenna system is capable of providing single antenna operation in UL combined with DL-MIMO operation using four *radiation modes* (mapped to the external ports) in E-UTRA BC 17 (704 MHz to 746 MHz). In addition MIMO operation in both UL and DL is provided with two *radiation modes* in BC 13 (746 MHz to 787 MHz). Moreover, single antenna operation in both UL and DL is supported for BC 5 (824 MHz to 894 MHz).

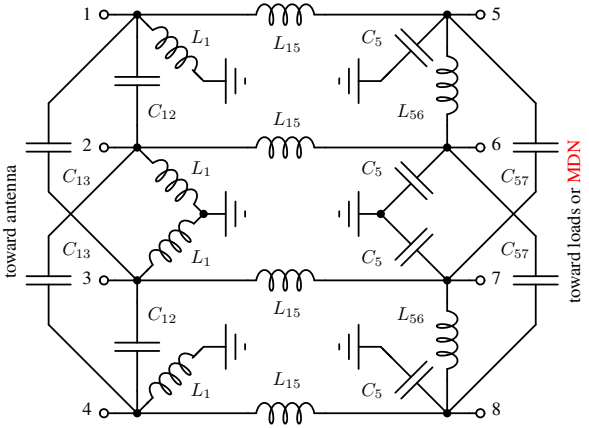

L_1	C_{12}	C_{13}	L_{15}	C_5	L_{56}	C_{57}
3.1 nH	5.1 pF	8.6 pF	4.3 nH	13 pF	9.7 nH	5.1 pF

Fig. 4.25.: Schematic of the multiport matching network for the symmetric 4-port MIMO antenna for tablet [115] after Fig. 4.24.

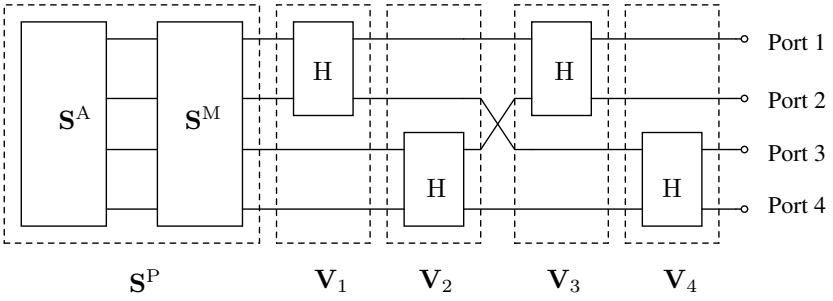

Fig. 4.26.: Schematic representation of the sequence of matching network (depicted in detail in Fig. 4.25) and MDN for the symmetric 4-port MIMO antenna for tablet [115].

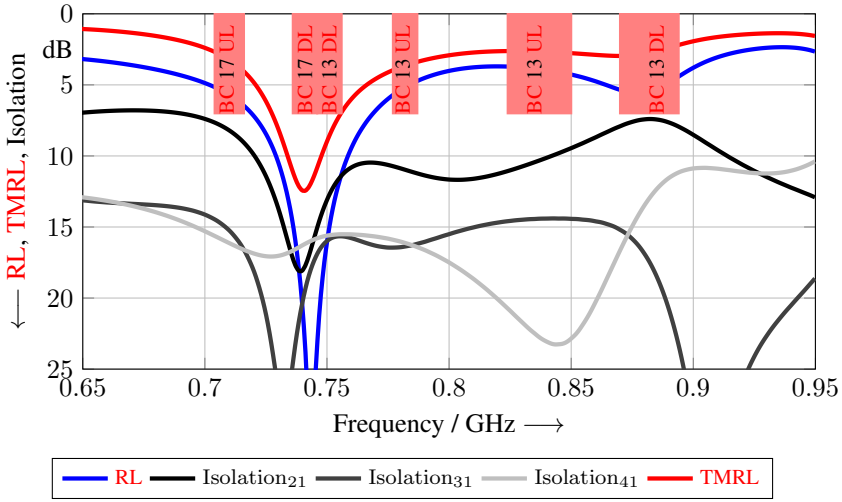

Fig. 4.27.: Per port RL, isolation between pairs of ports and TMRL for an example 4-port MIMO antenna for tablet (see Fig. 4.24) with multiport matching network after Fig. 4.25. No additional MDN is employed.

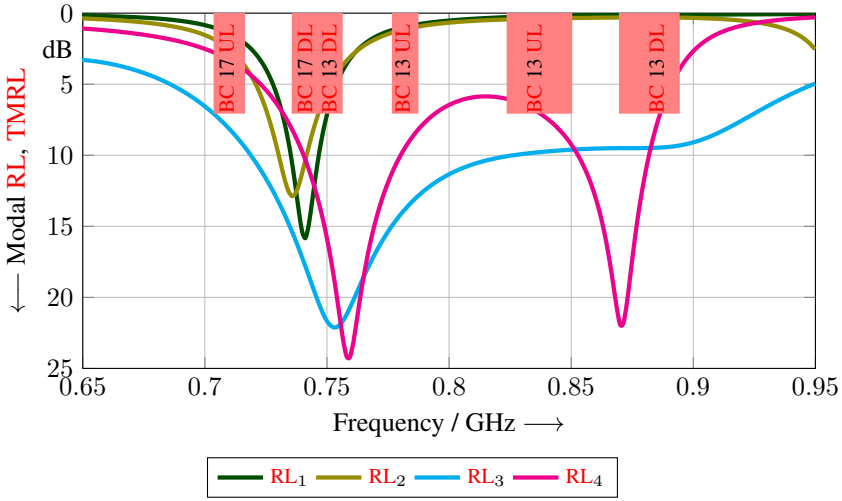

Fig. 4.28.: Modal RL of the four *radiation modes* for the 4-port MIMO antenna for tablet [115] with multiport matching network and MDN.

Chapter 5

Multiport Antennas for Small Terminals

The present chapter focuses in particular aspects of antenna design for small mobile wireless terminals. The most important descriptive quantities when discussing properties of electrically small antennas remain the radiation quality factor and total efficiency. Overview of analytical expressions for radiation quality factor which do not require prior knowledge of antenna input impedance is provided. These expressions set fundamental limits on the maximum attainable bandwidth which can be achieved in a given volume. If the antenna input impedance is known it is possible to obtain its bandwidth directly without taking recourse to the notion of radiation quality factor. Estimation of the total efficiency of electrically small antennas is also of significant practical interest. In this chapter two independent approaches which allow to do this numerically are shown.

If the instantaneous bandwidth of an antenna is too small to cover the desired frequency bands, electrical switching is required. Electrical switching, in general, introduces additional dissipation. In order to maintain high total efficiency a new concept where electrical reconfiguration of the antenna is divided into coarse electrical switching in the antenna physical structure and fine electrical tuning in the external matching network is introduced to reduce losses.

The above summarized aspects, pertinent to design of electrically small antennas, are equally relevant in the context of multiport antennas for small mobile

wireless terminals. A practically relevant method to cope with bandwidth restrictions of multiport antennas for MIMO application in mobile wireless terminals is presented by the DL-MIMO concept. Application of this concept is shown for USB dongle antennas. Further, basic aspects relative to subsequent systematic design of an electrically switchable and electrically tunable 2-port DL-MIMO antennas for small USB dongles covering multiple frequency bands are discussed in the present chapter.

5.1. Fundamental Limits on Radiation Quality Factor

5.1.1. Fundamental analytical expressions

Estimation of bandwidth and fundamental limits for the bandwidth of electrically small antennas have been subject of intensive studies. It is known that the inverse of the radiation quality factor is a good approximation of bandwidth for electrically small antennas. Therefore, it is useful to recall the basic analytical expressions for the radiation quality factor which depend on the volume occupied by the antenna. Analytical expressions which allow to obtain radiation quality factor without prior knowledge of the antenna input impedance are of interest. Fundamental research relative to the estimation of the radiation quality factor was conducted, to the most part, assuming sphere as a volume circumscribing the antenna. In [122] Wheeler proposed that electrically small antennas be defined as those with $ka < 0.5$, where $ka = \frac{2\pi}{\lambda}a$. λ denotes wavelength and a is the minimum radius of a sphere (often referred to as *Chu sphere*) in which the antenna is enclosed. Bounds on the radiation quality factor for lossless linearly polarized antenna, discussed in the present section, are valid for $ka < 0.5$.

Historically, for the first time a bound on the radiation quality factor (applicable to lossless linearly polarized antennas) was given by Chu in [75] as

$$Q_{\mathrm{rad,C}} = \frac{1}{(ka)^3} + \frac{1}{ka} \quad \text{for} \quad (\mathrm{TM}_{10} \text{ or } \mathrm{TE}_{10} \text{ mode}). \tag{5.1}$$

It is known that Chu's expression gives the lowest bound on the radiation quality factor assuming that the antenna "fills" the *Chu sphere* in an "optimum" fashion. However, it is important to note that in his derivation Chu did not consider reactive energy stored inside the sphere circumscribing the antenna. Thal

consider also the energy stored inside the *Chu sphere* [123, 124, 99] which led to the following estimates of the radiation quality factor

$$Q_{\mathrm{rad,T,TM_{10}}} = \frac{1.5}{(ka)^3} \quad \text{for} \quad (\mathrm{TM_{10}\ mode}) \tag{5.2}$$

and

$$Q_{\mathrm{rad,T,TE_{10}}} = \frac{3}{(ka)^3} \quad \text{for} \quad (\mathrm{TE_{10}\ mode}). \tag{5.3}$$

Thal's approximation of the radiation quality factor for the $\mathrm{TM_{10}}$ mode is about 1.5 times higher than that given by Chu (5.1). The practical realization of a single-polarized folded spherical helix which approaches Thal's analytical expression was shown by Best in [125].

Recent work on lower bounds for the radiation quality factor was conducted for antennas circumscribed by certain, typically considered in engineering practice, volumes featuring different aspect ratios. More realistic bounds on the radiation quality factor for many types of antenna commonly used antennas were given. Work which led to analytical expressions for the lower bound on the radiation quality for many practical antennas was conducted by Gustafsson [100]. The resulting analytical expression has the form

$$Q_{\mathrm{rad,G}} = \frac{1.5}{(ka)^3 \gamma_1^{\mathrm{norm}}}, \tag{5.4}$$

where γ_1^{norm} is a coefficient which depends on the geometry of the considered volume. For a cylindrical volume with $d/\ell = 10^{-3}$, where $\ell = 2a$ and d is the diameter of a cylinder, $\gamma_1^{\mathrm{norm}} = 0.05$. For a sphere with radius a, $\gamma_1^{\mathrm{norm}} = 1$. In this case Gustafsson's analytical expression (5.4) is identical to Thal's analytical expression (5.2) for a single $\mathrm{TM_{10}}$ spherical mode.

5.1.2. Lower bound on the radiation quality factor of antenna circumscribed by cylindrical region

Gustafsson's analytical expression for the lower bound on radiation quality factor of electrically small linearly polarized antennas after (5.4) [102] is of significant practical importance since it is applicable to antennas enclosed by regions other than a sphere. In the present section the lower bound on the radiation quality factor, which can be achieved by antenna confined to a cylindrical

region, is evaluated. Fig. 5.1 shows comparison between analytical expression given by Gustafsson for a cylindrical region with two different aspect ratios $\ell/d = 60$ and $\ell/d = 6$ where d is the diameter of the cylinder and ℓ is its length (note that $\ell = 2a$). The results show that the bound strongly depends on the aspect ratio ℓ/d of a cylindrical region. A cylindrical region with low aspect ratio results in a low radiation quality factor.

A further aspect of interest is design of the optimum radiator within a given region of space, i.e. one which features radiation quality factor close to Gustafsson's analytical expression. In [126] Wheeler discussed the radiation quality factor of antennas which are circumscribed by a cylindrical region. According to [127] the conical dipole and helix with discs feature larger "sphere of influence" than a straight dipole. The largest "sphere of influence" in a cylindrical volume features helix with discs. These observations of Wheeler are used further in the present work to design a symmetric 2-port DL-MIMO antenna for USB dongles featuring high total efficiencies of both *radiation modes* (see Chapter 6). The antenna physical structure comprises a helix with capacitive plates at its ends which approaches Wheeler's helix with discs [127].

5.1.3. Radiation quality factor of electrically small dipole

For a lossless electrically small dipole analytical expression for radiation quality factor exist. The input impedance of a short dipole is explicitly known. It depends on dipole's electrical length ℓ/λ and its diameter d. Therefore, the radiation quality factor can be obtained using the expression given by Yaghjian in [71]. The analytical approximation for the *radiation resistance* of an electrically small dipole ($\ell \ll \lambda$) is given by Balanis [128] as

$$R_{\text{rad}} \approx \eta_0 \frac{\pi}{6} \left(\frac{\ell}{\lambda}\right)^2 \quad (\text{for} \quad \ell \ll \lambda), \tag{5.5}$$

where η_0 is the impedance of the free space ($\eta_0 \approx 377\ \Omega$) and λ is the wavelength. A short dipole is capacitive. It is possible to approximate its reactance by [128]

$$X \approx -\frac{\eta_0}{\pi} \frac{\ln\left(\frac{\ell}{d} - 1\right)}{\tan\left(\pi \frac{\ell}{\lambda}\right)} \quad (\text{for} \quad \ell \ll \lambda), \tag{5.6}$$

where d is the diameter of the wire. The radiation quality factor of an electrically small dipole can approximately be found from the above approxima-

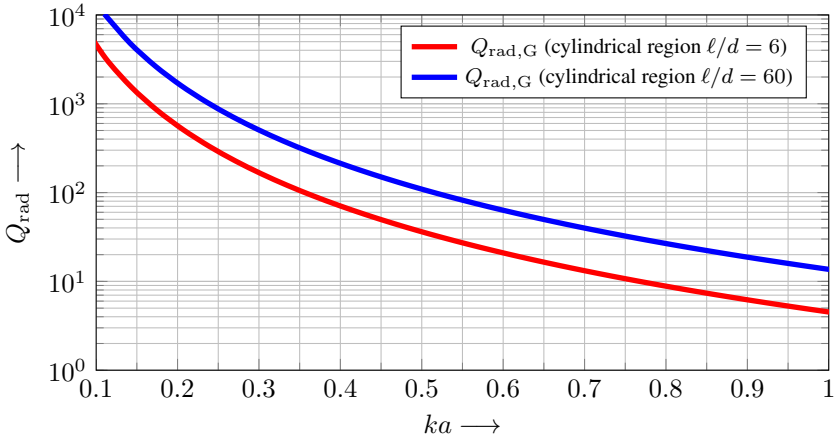

Fig. 5.1.: Radiation quality factor Q_{rad} versus ka after Gustafsson's analytical expression [102] for two antennas which are circumscribed by cylindrical regions with different aspect ratios.

tions of the radiation resistance and reactance. The analytical expression for radiation quality factor given by Gustafsson for $\ell/d = 60$ (see Fig. 5.1) and its analytical approximation calculated using Yaghjian's expression [71] with (5.5) and (5.6) are in good agreement.

5.2. Evaluation of Bandwidth

Evaluation of bandwidth for multiport antennas can be accomplished using multiport matching network (see Chapter 4 subsection 4.3.1). Given the scattering matrix of the antenna and the scattering matrix $\mathbf{S}^{\mathrm{A}}$ of the matching network $\mathbf{S}^{\mathrm{M}}$ it is easy to obtain the scattering matrix of the cascade $\mathbf{S}^{\mathrm{P}}$, using (4.6), which allows to observe the bandwidth. In practice, there are typically only few modes which are critical and one can specifically investigate the bandwidth of these modes separately. This is equivalent to analysis of a single feed antenna. The present section shows two methods which allows to numerically obtain bandwidth of a single feed antenna.

5.2.1. Using explicitly known elements of the ideal matching network at single frequency

The scattering matrix of the ideal lossless 2-port matching network for matching a lossless single feed antenna ($N = 1$), featuring reflectance Γ^{A}, at single frequency can be obtained from (4.7) (see Chapter 4 section 4.2). It is given by

$$\mathbf{S}^{\mathrm{M}} = \begin{pmatrix} \Gamma^{\mathrm{A}\,*} & u\sqrt{1-\left|\Gamma^{\mathrm{A}}\right|^2} \\ u\sqrt{1-\left|\Gamma^{\mathrm{A}}\right|^2} & -u^2\Gamma^{\mathrm{A}} \end{pmatrix}, \tag{5.7}$$

where u is an arbitrary unit phasor (i.e., $u = \mathrm{e}^{\mathrm{j}\,\phi}$ with real ϕ). This implies that for a given reflectance Γ^{A} an infinite set of impedance matching networks exists. From this infinite set a particular realization which maximizes total efficiency of an antenna in a subsequent practical realization of the network can be selected. For the purpose of further discussion assume that $\phi = 0$. The admittance matrix of the matching network can be explicitly obtained and its elements mapped to circuit elements of the π-type matching network shown in Fig. 5.2. At single frequency the admittances of this matching network are given by

$$\widetilde{Y}_1^{\mathrm{M}} = \mathrm{j}\,Y_{\mathrm{L}}\frac{1-\Re(\Gamma^{\mathrm{A}})-\sqrt{1-\left|\Gamma^{\mathrm{A}}\right|^2}}{\Im(\Gamma^{\mathrm{A}})} \tag{5.8}$$

$$\widetilde{Y}_2^{\mathrm{M}} = \mathrm{j}\,Y_{\mathrm{L}}\frac{\sqrt{1-\left|\Gamma^{\mathrm{A}}\right|^2}}{\Im(\Gamma^{\mathrm{A}})} \tag{5.9}$$

$$\widetilde{Y}_3^{\mathrm{M}} = \mathrm{j}\,Y_{\mathrm{L}}\frac{1+\Re(\Gamma^{\mathrm{A}})-\sqrt{1-\left|\Gamma^{\mathrm{A}}\right|^2}}{\Im(\Gamma^{\mathrm{A}})}, \tag{5.10}$$

where Y_{L} is the load admittance. Depending on the value of Γ^{A} at a single frequency the admittance $\widetilde{Y}_i^{\mathrm{M}}$, where $i = \{1, 2, 3\}$, is mapped to either capacitance C_i or inductance L_i (see Chapter 4 subsection 4.3.1). Once the reflectance Γ^{P} at the output of the cascade comprising the antenna with the matching network is obtained over frequency range it is possible to calculate the fractional x dB bandwidth of a lossless single feed antenna featuring single resonance using (2.38).

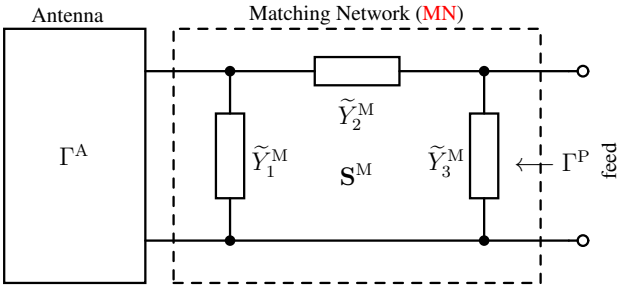

Fig. 5.2.: Schematic of a cascade comprising antenna and the π-type Matching Network (MN) comprising three components with admittances Y_1^{M}, Y_2^{M} and Y_3^{M}.

5.2.2. Matching network synthesis by minimization of reflectance at single frequency

The problem of finding the bandwidth of a single resonant antenna can also be solved numerically. The advantage of this method is that the matching network can be lossy. Thus, the bandwidth of a lossy antenna can be found assuming that dissipation occurs predominantly in the elements of the matching network and the dissipation in the antenna is small. The simulation setup comprises a cascade of antenna and a π-type matching network (see Fig. 5.2). Minimization of the reflectance or alternatively maximization of the return loss at the prescribed center frequency at the output of the cascade is the goal of the optimization procedure. To simplify notation the least squared error type penalty function, used to minimize the Γ^{P} seen at the output of the cascade, is given with respect to a single center frequency f_0

$$\boldsymbol{P}^{\mathrm{M,opt}} = \underset{\{\boldsymbol{P}^{\mathrm{M}}\}}{\arg\min} \left| \Gamma^{\mathrm{P}} \left(\Gamma^{\mathrm{A}}(f_0), \boldsymbol{P}^{\mathrm{M}}, f_0 \right) \right|^2, \tag{5.11}$$

where $\boldsymbol{P}^{\mathrm{M}} = (P_1^{\mathrm{M}}, P_2^{\mathrm{M}}, P_3^{\mathrm{M}})$ are the parameters of the π-type matching network which yield Γ^{P} and $\boldsymbol{P}^{\mathrm{M,opt}} = (P_1^{\mathrm{M,opt}}, P_2^{\mathrm{M,opt}}, P_3^{\mathrm{M,opt}})$ are the optimum solutions. Optimization is performed at a center frequency f_0. The admittance $\widetilde{Y}_i^{\mathrm{M}}$, where $i = \{1, 2, 3\}$, is mapped to either capacitance (when $P_i^{\mathrm{M}} > 0$) or inductance (when $P_i^{\mathrm{M}} < 0$) (see Chapter 4 subsection 4.3.1). Various minimization algorithms can be used for solving (5.11). A genetic algorithm is used for obtaining the type of elements and the initial element values. Then the gradient type optimization finds exact element values. The quantity

$\Gamma^{\mathrm{P}}(\boldsymbol{P}^{\mathrm{M,opt}}, f_0)$ is the reflectance over frequency of the cascade matched at the center frequency f_0. It allows for simple evaluation of the fractional x dB bandwidth using (2.38).

5.3. Efficiency degradation due to matching network

A general expression for the total efficiency of a matched antenna at resonance was given in [129]. It is based on the following discussion of losses in the antenna system comprising antenna with a lossy matching network. Consider the antenna with radiation efficiency η_{rad} featuring reactance type radiation quality factor Q_{A} which is defined as a ratio of rectance to the radiation resistance of the antenna (i.e. $X_{\mathrm{A}}/R_{\mathrm{A}}$). The antenna is matched using elements of the opposite type of the antenna equivalent circuit reactance. Let Q_{M} denote the lowest quality factor among all components comprising matching network. The upper bound on the total efficiency of matched antenna is then expressed as in [129] by

$$\eta_{\mathrm{tot}} \leq \eta_{\mathrm{rad}}\eta_{\mathrm{M}} = \eta_{\mathrm{rad}}\frac{1}{1+\frac{Q_{\mathrm{A}}}{Q_{\mathrm{M}}}} \quad (\text{if matched}), \tag{5.12}$$

where η_{M} denotes efficiency of the matching network. Inspection of the above relation reveals that if the values of radiation quality factors of the antenna itself and the matching network are of similar magnitude then the total efficiency is about one half of the radiation efficiency of the antenna itself. If the reactance type radiation quality factor of the antenna is much higher than the Q-factor of the largest reactive component in the matching network (i.e. $Q_{\mathrm{M}} \ll Q_{\mathrm{A}}$) then the total efficiency of matched antenna much smaller than the radiation efficiency ($\eta_{\mathrm{tot}} \ll \eta_{\mathrm{rad}}$). Typically, the elements with lowest Q-factor are the inductors. Inductor loss (given by Equivalent series resistance (ESR)) is proportional to inductance value. The efficiency therefore depends also on required inductor values to match the input impedance of the antenna. This question is examined numerically in detail in the section 5.4 for a simple inductive L-type matching network.

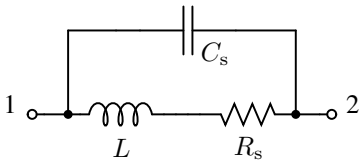

Fig. 5.3.: Equivalent circuit model of a wirewound inductor.

5.4. Numerical Evaluation of Total Efficiency

5.4.1. Losses of wirewound inductors

It was shown in [129] (see section 5.3) that losses in the antenna system are due to the finite Q-factor of inductors used in the matching network. The general statement given by (5.12) can also be expressed by comparing antenna radiation resistance $R_\mathrm{rad}(\omega)$ and ESR of the inductor, here given by $R_\mathrm{loss}(\omega)$, at a given radian frequency ω. However, the ESR is often given in the datasheets at DC only. The goal of the present subsection is to provide an expression to obtain ESR of a wirewound inductor at any frequency below the self-resonance frequency in order to use it further to estimate total efficiency of the antenna at single frequency. The loss resistance R_loss can be estimated based on an equivalent circuit model (see Fig. 5.3) comprising series connection of nominal inductance L and resistance of a wire R_s with shunt capacitance C_s which represents capacitance between windings. The datasheet provided by the manufacturer often in addition to nominal L includes also Q-factor and self-resonance frequency f_SFR. This data allows to calculate capacitance C_s and resistance R_s using

$$C_\mathrm{s} = \frac{1}{4\pi^2 f_\mathrm{SFR}^2 L} \quad \text{and} \quad R_\mathrm{s} = \frac{2\pi f L}{Q}, \tag{5.13}$$

where Q and L are taken at the frequency of interest f. The real part of the impedance of the equivalent circuit model is the loss resistance of the wirewound inductor

$$R_\mathrm{loss}(\omega) = \Re\Big(Z(\omega)\Big) = \Re\left(\frac{1}{\mathrm{j}\omega C_\mathrm{s} + \frac{1}{R_\mathrm{s}+\mathrm{j}\omega L}}\right). \tag{5.14}$$

Note that the impact of C_s on the loss resistance is small when $f \ll f_\mathrm{SFR}$ and but increases rapidly with frequency when approaching self-resonance frequency. Typically, the loss resistance increases proportionally with logarithm

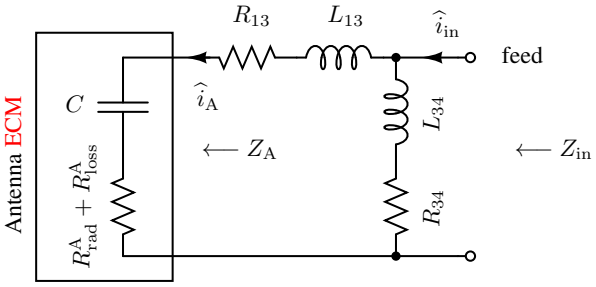

Fig. 5.4.: Schematic representation of the antenna matching using lossy L-type matching network.

of frequency and the value of nominal inductance. In order to minimize losses it is imperative to use in the matching network inductors with small nominal values.

5.4.2. Proposed simple approach

The total efficiency of a lossy antenna matched at a single frequency using an external lossy L-type matching network can be numerically evaluated based on the following discussion. Consider an electrically small dipole whose input impedance can be represented using ECM comprising series connection of a resistor and a capacitor (see Fig. 5.4). The resistor models radiation resistance and loss resistance of the antenna $R^{\rm A}_{\rm rad} + R^{\rm A}_{\rm loss}$. Its change over frequency is typically small for electrically small antennas. The reactance of an electrically small dipole changes rapidly over frequency. It is modeled by the capacitance C. The input impedance $Z_{\rm in}$ of an arrangement comprising ECM of the antenna and a simple L-type passive matching network after Fig. 5.4 featuring two lossy inductors with impedances Z_{13} and Z_{34} is found to be

$$Z_{\rm in} = \frac{1}{\frac{1}{Z_{34}} + \frac{1}{Z_{13}+Z_{\rm A}}}, \tag{5.15}$$

where $Z_{\rm A}$ is the impedance of the antenna. The available power $P_{\rm av}$ and the power radiated by the antenna $P_{\rm rad}$ can be expressed as

$$P_{\rm av} = \frac{|\widehat{i}_{\rm in}|^2}{2}\Re\Big(Z_{\rm in}\Big) \quad \text{and} \quad P_{\rm rad} = \frac{|\widehat{i}_{\rm A}|^2}{2}R^{\rm A}_{\rm rad}, \tag{5.16}$$

respectively. The total efficiency of an arrangement comprising antenna and matching network, where the antenna is matched at a single frequency, is given by

$$\eta_{\mathrm{tot}}(\omega_0) = \eta_{\mathrm{rad}}^{\mathrm{A}} \frac{P_{\mathrm{rad}}}{P_{\mathrm{av}}} = \eta_{\mathrm{rad}}^{\mathrm{A}} \frac{R_{\mathrm{rad}}^{\mathrm{A}}}{\Re\left(Z_{\mathrm{in}}\right)} \frac{|\widehat{i}_{\mathrm{A}}|^2}{|\widehat{i}_{\mathrm{in}}|^2}, \tag{5.17}$$

where $\eta_{\mathrm{rad}}^{\mathrm{A}}$ is the radiation efficiency of the antenna. Kirchhoff's circuit laws allow to obtain the ratio of the RF current flowing through the antenna only and the input RF current

$$\frac{|\widehat{i}_{\mathrm{A}}|}{|\widehat{i}_{\mathrm{in}}|} = \frac{1}{1 + \frac{Z_{\mathrm{A}} + Z_{13}}{Z_{34}}}. \tag{5.18}$$

The total efficiency of matched antenna at a single frequency is then given by

$$\eta_{\mathrm{tot}}(\omega_0) = \eta_{\mathrm{rad}}^{\mathrm{A}} \cdot \frac{R_{\mathrm{rad}}^{\mathrm{A}}}{\Re\left(Z_{\mathrm{in}}\right)} \left| \frac{1}{1 + \frac{Z_{\mathrm{A}} + R_{13} + \mathrm{j}\omega L_{13}}{R_{34} + \mathrm{j}\omega L_{34}}} \right|^2. \tag{5.19}$$

The above described method of estimating total efficiency is applied to evaluate the total efficiency of the antenna for USB dongles (see subsection 5.7.3).

5.4.3. The approach where antenna input impedance is represented as a 2-port network

In engineering practice frequently a simulation setup is desired which allows to calculate total efficiency of an antenna with a lossy matching network using S-parameters of commercially available devices. Such a setup is shown in Fig. 5.5 after [130]. It consists of a 2-port ECM of an antenna which comprises series reactance X^{A}, series loss resistance $R_{\mathrm{loss}}^{\mathrm{A}}$ and a transformer with $\sqrt{\frac{R_{\mathrm{rad}}^{\mathrm{A}}}{Z_{\mathrm{L}}}} : 1$ transformation ratio, where $Z_{\mathrm{L}} = 50\ \Omega$ and $R_{\mathrm{rad}}^{\mathrm{A}}$ denotes radiation resistance, and a matching network. The setup allows to calculate either total efficiency of matched antenna assuming known $R_{\mathrm{loss}}^{\mathrm{A}}$ or efficiency of a lossy matching network with lossless antenna when $R_{\mathrm{loss}}^{\mathrm{A}}$ is unknown (i.e. $R_{\mathrm{loss}}^{\mathrm{A}}$ is assumed to be zero), respectively, via evaluation of $|s_{21}|^2$. This method of numerical evaluation of total efficiency was used to obtain electrical tuning capabilities of an electrically tunable MDN for 2-port MIMO antennas in [112] (see Appendix E).

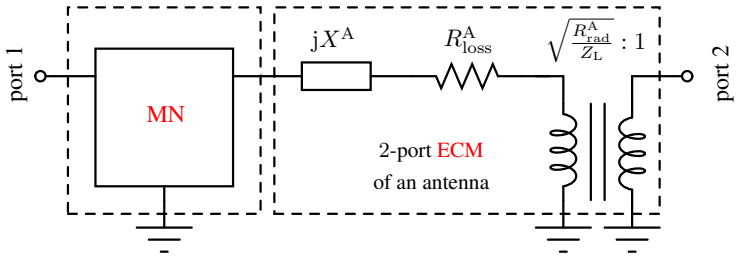

Fig. 5.5.: Simplified schematic representation of the simulation setup after [130] which can be used to evaluate total efficiency of the antenna with MNs in terms of $|s_{21}|^2$.

5.5. Combining Electrical Switching and Electrical Tuning

5.5.1. Antenna reconfiguration and tunable matching circuits

Antennas for mobile wireless terminals must cover a wide range of frequencies and often allow for multi-band operation. This is in contrast to what can be typically achieved with electrically small antennas. They feature narrow bandwidth and small efficiency. Therefore, providing some mechanism to cover the desired wide bandwidth with at least acceptable efficiency is mandatory. The best candidate for realization of antenna reconfigurability in small mobile wireless terminals is a combination of coarse electrical switching with fine electrical tuning. The idea follows from the realization that at its feed, when matched, an electrically small antenna features rapidly changing input impedance with frequency (see e.g. Fig. 5.6). Also the magnitude of the current is the maximum at the feed. Therefore, electrical tuning of an electrically small antennas at the feed is not advisable due to high losses and insufficient tuning range over frequency. For these reasons at least coarse electrical switching within the antenna physical structure itself is preferable. It allows to place switching elements in locations where current (or voltage, respectively) is not at maximum to reduce losses (see e.g. Fig. 5.7). Afterwards, additional fine electrical tuning can then be performed within a tuning module placed behind the antenna physical structure on the printed circuit board (PCB) of a terminal. This approach is also considered preferable from a design point of view, because

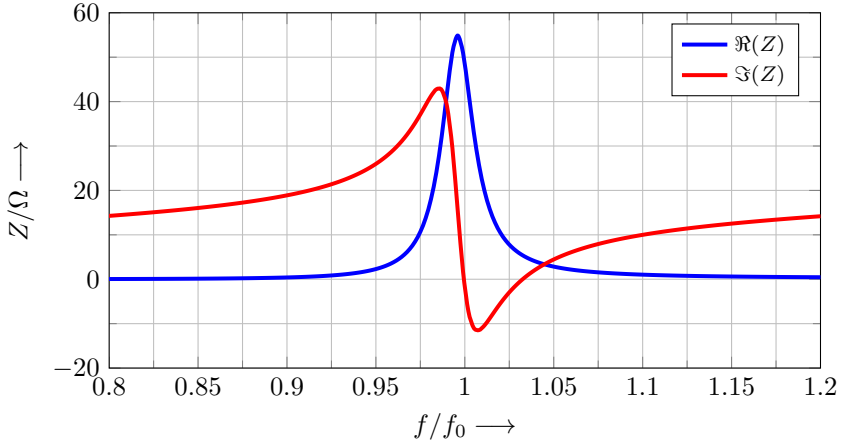

Fig. 5.6.: Impedance versus normalized frequency of matched electrically small linear dipole ($\ell/\lambda = 0.2$).

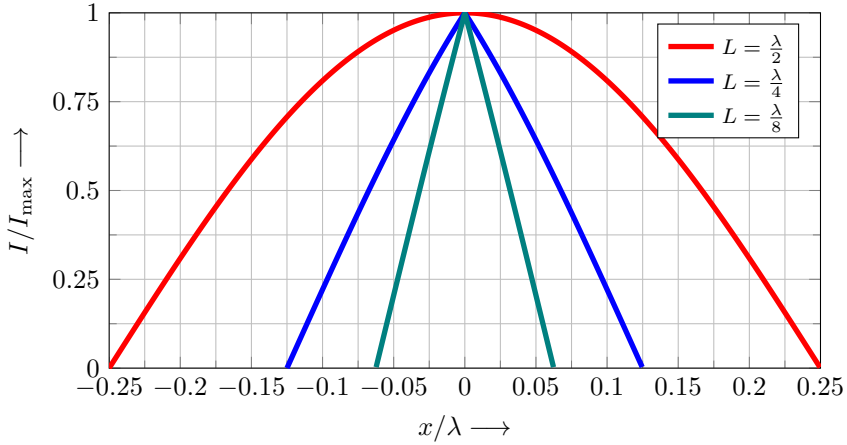

Fig. 5.7.: Normalized currents $I/I_{\max}$ versus electric length of the dipole x/λ, where $-L/2 \leq x \leq L/2$, for different dipole lengths $L \in \{\lambda/2, \lambda/4, \lambda/8\}$ after analytical expressions given in [128].

it allows to separate design and optimization of the antenna physical structure itself from that of a tuning module. The idea leads to the definition of a "soft" specification of the interface between the antenna and the tuning module. The antenna will be required only to be electrically switched to an extent which assures that its impedance stays within a specified region of the Smith chart. The module with additional electrical tuning capabilities will be required only to map this region of the Smith chart to the desired load impedance.

In order to realize the outlined concept it is necessary to first discuss which RF components are suitable to implement coarse electrical switching and which are more appropriate for realization of fine electrical tuning. At this point of considerations it should be apparent that integration of the highly complex components featuring digital control interfaces into the antenna physical structure may not be feasible. This means that all highly integrated RF components such as e.g. Digitally Tunable Capacitors (DTCs) are more suitable for a tuning module placed on the PCB of a device. Use of varactor diodes is often reported, however in general their use in design of electrically small antennas remains problematic due to their nonlinear behavior in the transmit mode of operation. RF-MEMS Single Pole, Single Throw (SPST) switches and RF-PIN diodes are identified as the components which can be used for coarse electrical switching in the antenna physical structure. Application of all above mentioned devices in realization of electrical switching and tuning is discussed in the the present section.

5.5.2. Realization of coarse electrical switching

The present section provides an overview of advantages and disadvantages of RF-MEMS SPST switches and RF-PIN diodes in application to electrical coarse switching in the antenna physical structure. For an example of switching applied in the antenna physical structure consider an electrically small dipole. It can be realized using some form of a meander line or a helix with capacitive plates at both ends. Switching can be accomplished by providing electrical short between meander lines or windings of a helix (see e.g. Fig. 5.8). Detailed design and measurement of the prototype of an electrically switchable 2-port DL-MIMO antenna covering four BC in the LTE low-band (from 704 MHz to 960 MHz) is shown in Chapter 6 section 6.1.3.

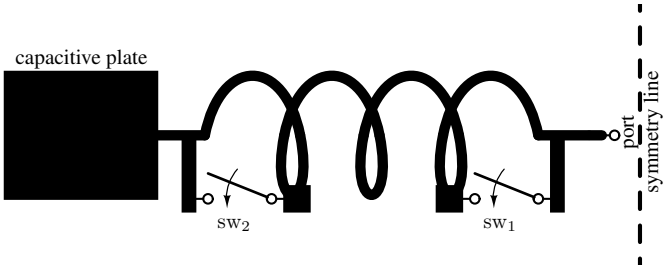

Fig. 5.8.: Simplified illustration of switching in a single arm of an example electrically small antenna. Two switches with open and close states allow to switch the antenna between four frequency bands.

MEMS SPST switches

The name RF-MEMS refers to a variety of electronic components of which mechanically moving sub-millimeter-sized parts provide RF functionality. Capacitive RF-MEMS switches employ the movement of a mechanical component to place a variable capacitance in the path of a RF transmission line, thereby either blocking or enabling transmission of an RF signal along that line. MEMS SPST switches offer high isolation in the open state and low insertion loss in the conducting state in a system which is at reference impedance level. For instance the S-parameters of a single RF-MEMS SPST for both ON and OFF states for a switch from DelfMEMS allow to extract the ECM of the switch. In a $50\ \Omega$ RF system the isolation in the OFF state is higher than 60 dB and insertion loss lower than 0.15 dB. In the ON state return loss is higher than 30 dB and insertion loss is at around 0.2 dB. In the LTE low-band frequency range (from 704 MHz to 960 MHz) the ECM in the OFF state comprises parallel $R_{\text{off}}C_{\text{off}}$ with $R_{\text{off}} = 1\ \text{M}\Omega$ and $C_{\text{off}} = 1.2$ fF and in the ON state comprises series $R_{\text{on}}L_{\text{on}}$ with $R_{\text{on}} = 1.6\ \Omega$ and $L_{\text{on}} = 0.8$ nH. The product $R_{\text{on}}C_{\text{off}}$ is a figure of merit. For the present example its value is 1.92 fs. The linearity, power handling and Q-factor are excellent, but RF-MEMS SPST switches require high control voltage of up to 120 V.

RF-MEMS SPST switch biasing

Electrostatic biasing implies no current flow, allowing high-resistivity biasing lines to be used instead of RF choke inductors (see Fig. 5.9). An advantage

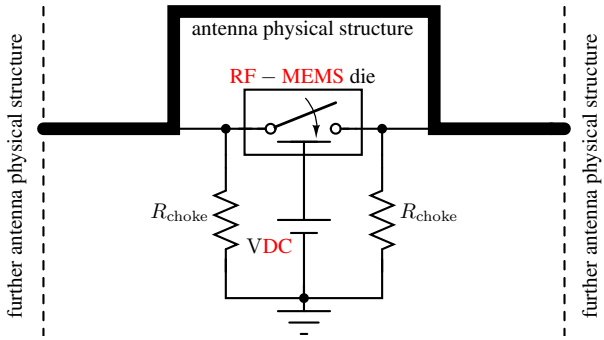

Fig. 5.9.: Simplified illustration of biasing network for RF-MEMS SPST used to electrically shorten the antenna physical structure.

over the use of PIN diodes is clear since the biasing lines do not require high value RF choke inductors. Typical values of R_{choke} given in the datasheets are in the interval from $40\ \text{k}\Omega$ to $100\ \text{k}\Omega$.

RF-PIN diodes

The PIN diodes are versatile semiconductor devices used in a variety of applications. The goal of the present short overview is to provide basic statements related to use of RF-PIN diodes as switches. RF-PIN diodes feature small size and high reliability. The power handling capability of the RF-PIN diode (PIN) diode is limited by either the diode's breakdown voltage or its power dissipation. For example, for the series connection and a diode with a low and high resistance state of $1\ \Omega$ and $10\ \text{k}\Omega$, respectively, approximately $2\ \%$ (CW Power Multiplier = 50) of the input power dissipates in the diode in either the "ON" or the "OFF" state. This means that the diode with $P_{\text{diss}} = 250\ \text{mW}$ can handle $12.5\ \text{W}$ of input power. An other important quantity to consider is the *carrier lifetime*. As a rule of thumb it is accepted that a RF-PIN diode should be operated at frequencies considerably higher than the minimum frequency of operation given by [131] (pp. 98)

$$f_{\min} \geq \frac{10}{\tau}, \tag{5.20}$$

where τ is the *carrier lifetime*. Use of a RF-PIN diode above this frequency avoids significant harmonic effects by preventing modulation of the charge car-

Tab. 5.1.: Comparison of descriptive quantities for BA 592 and BAR 90 from Infineon [132]. C_T refers to diode capacitance, R_P is parallel resistance and r_f is forward resistance.

parameter	unit	BA 592	BAR 90	notes
package		SC79	TSLP-2-7	
C_T	pF	1	0.3	$V_R = 0$ V, $f = 100$ MHz
R_p	kΩ	100	35	$V_R = 0$ V, $f = 100$ MHz
r_f	Ω	0.4	0.8	$I_F = 10$ mA, $f = 100$ MHz
τ_{rr}	ns	120	750	carrier life time
W_I	μm	3	20	I-region width
IL	dB	0.4	0.08	$I_F = 10$ mA, $f = 1.8$ GHz
isolation	dB	5.5	18	$V_R = 0$ V, $f = 1$ GHz
V_R	V	35	80	reverse voltage

rier concentration. Below this frequency the diode behaves like a varactor. For τ from around 500 ns to 1000 ns the minimum operating frequency is between 20 MHz to 10 MHz. If the intended frequency range of antenna operation is above these frequencies the RF-PIN diode behaves like a switch. In the conducting state of the diode the product of DC current and series RF resistance is a constant, dependent on the design of a PIN diode [131]

$$R_s^{RF} I_F^{DC} = \text{const.} \tag{5.21}$$

The value of the constant depends on the width of the I-region of semiconductor, carrier lifetime and mobilities of electrons and holes. Achievable resistance values are between 0.1 Ω and 10 kΩ. For switching applications, especially when dealing with electrically small antennas, the RF resistance has to be minimized so as to maximize total efficiency. This clearly requires high DC current to be delivered. In engineering practice, often a trade-off between the current consumption and low RF resistance of the diode has to be made. Parameters of two different RF-PIN diodes are given in Tab. 5.1. These two diodes are used in the electrically switchable antennas described in Chapter 6.

RF-PIN diode biasing considerations

An important issue when using RF-PIN diodes is design of a proper biasing circuit. The basic biasing circuit for an RF-PIN diode is shown in Fig. 5.10. The major challenge in design of a biasing circuit for RF-PIN diodes is DC-RF isolation. The ratio of RF current I_L flowing through the choke inductor L_{choke}, located in the vicinity of the diode, to RF current I_D flowing through

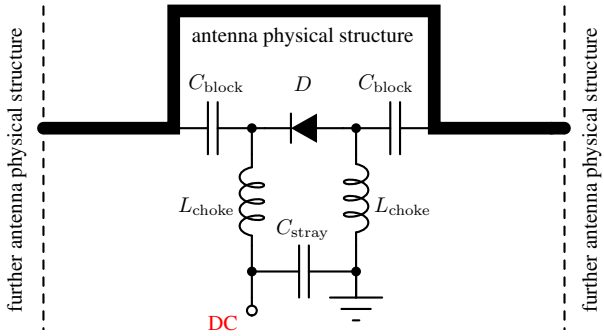

Fig. 5.10.: Simplified illustration of biasing network for RF-PIN diode used to electrically shorten part of the antenna physical structure.

RF-PIN diode must be minimized. Parasitic resonances, caused by current loops created by biasing lines and the antenna physical structure, must be prevented. The first task in the design process of biasing lines is to select appropriate size of SMD components and to identify the required value of choke inductance L_{choke}. The trade-off between the nominal value of inductance and the series loss resistance has to be exploited. The size of the choke inductors has to be maintained small as larger choke inductors interact strongly with the electromagnetic field generated by the antenna physical structure. Larger size of the choke inductors would also be impractical for mobile wireless devices due to real estate limitation for additional component placement. Moreover, larger components require including them into the CAD model of the antenna as physical components which yields to cumbersome and time consuming simulations. In order to bypass the requirement for choke inductors to feature high nominal values they can be replaced by a series connection of a few inductors with smaller nominal values. Practical utilization of RF-PIN diodes for electrical switching in the antenna physical structure is shown in Chapter 6.

5.5.3. Realization of fine electrical tuning

Fig. 5.11 shows schematic of the π-type electrically switchable matching network [133]. The inductors, denoted by L_1, L_2 and L_3 have fixed values, whereas capacitors C_1, C_2 and C_3 are tunable. These electrically tunable components shall feature continuous tuning capabilities (varactors) or a discrete tuning capabilities with small step (e.g. DTCs). Advantages and disadvantages

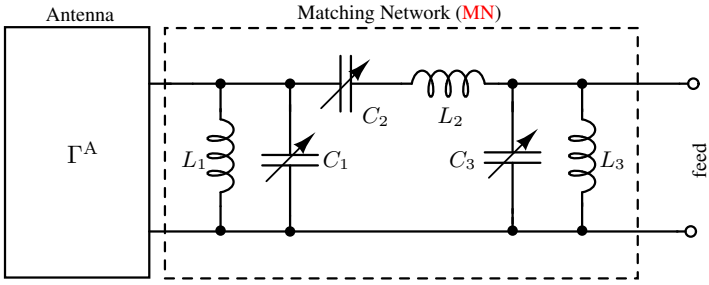

Fig. 5.11.: Schematic of an electrically tunable Matching Network (MN) comprising three independently tuned components C_1, C_2 and C_3.

of varactor diodes versus DTCs in an electrically tunable matching network are discussed in this subsection. A tuning ratio, defined as the ratio of the maximum capacitance, to the minimum capacitance of about 5 was found to be sufficient to match antenna input impedances over a wide range of frequencies [112]. If the tuning range of is known complete matching network can be systematically synthesized [112] (see Appendix E).

Varactor diode

Varactor diodes are well suited for realization of electrical tuning in receive only applications such as e.g. digital video broadcasting – terrestrial (DVB-T) [134]. As long as the RF voltage over the varactor diode is small, non-linearity is *not* a problem. This is generally not the case for concurrent receive and transmit operation because of high RF voltages. The capacitance – voltage relation of a varactor diode may be approximated by

$$C(V) = C_0 \left(1 + \frac{V}{V_0}\right)^{-\gamma} \tag{5.22}$$

where V denotes reverse voltage, V_0 the built in potential ($\sim 0.7\,\mathrm{V}$ for Si and $1.2 \ldots 1.3\,\mathrm{V}$ for GaAs devices). The exponent γ is typically 0.47 for Si varactors with abrupt doping profile and 0.50 for some GaAs abrupt junction varactors. Varactors with hyperabrupt doping profiles are available with γ values of e.g. 0.75, 1.0, 1.25 and 1.50. Low-voltage types require a control voltage in the range $1 \ldots 3\,\mathrm{V}$ or $1 \ldots 4.5\,\mathrm{V}$, high-voltage types typically up to $25\,\mathrm{V}$ or $28\,\mathrm{V}$. Varactors offer the following advantages:

1. high-impedance control lines permit placement in “hot” regions of an antenna structure,
2. negligible current consumption,
3. continuous tuning which allows for e.g. factory corrections using (look-up table) to e.g. adapt to different operating environments of a terminal or to compensate for manufacturing tolerances.

Limitations result from the non-linearity of the $C(V)$ relation (5.22). The RF voltage drop over the varactor must be limited to a small fraction of the DC tuning voltage. A fixed series capacitance may therefore be mandatory. This restricts the attainable frequency tuning ratio. With high voltage varactor diodes it is expected that frequency can be tuned by about $5\ \%$ which is insufficient to e.g. cover the whole LTE low-band. In summary the disadvantages are

1. requirement for a digital to analog converter (DAC) whose output covers the voltage range,
2. restricted tuning range because a trade-off between tuning range and linearity must be made.

Digitally Tunable Capacitors (DTCs)

A digitally tuned capacitors, contains a bank of switches and capacitors. In Silicon-On-Insulator (SOI)/Silicon-On-Silicon (SOS) devices Field-effect transistor (FET) switches and Metal-Insulator-Metal (MIM) capacitors with binary-weighted values are used. SOI/SOS switches feature high linearly and are well suited to low power applications. High voltage endurance requires multiple FET devices in series which adds series resistance and lowers the quality factor. The major advantage of DTCs is that they are controlled directly using a digital interface (e.g. SPI). For further discussion a PE64904 devices from Peregrine are considered. They were designed for the frequency range from $100\ \mathrm{MHz}$ to $3000\ \mathrm{MHz}$. Therefore, they covers the majority of E-UTRA BCs. The tuning range is from $0.7\ \mathrm{pF}$ to $4.6\ \mathrm{pF}$ (series configuration) which gives a tuning ratio of about 5. The tuning step is only $131\ \mathrm{fF}$. Other advantageous properties of DTCs include high power handling capability (up to $38\ \mathrm{dBm}$), high linearity and low power consumption. The ESR is approximately $1.4\ \Omega$. Realistic equivalent circuit models of Peregrine’s DTCs, which include losses, are used in the numerical evaluation of tuning capabilities of an electrically tunable MDN for 2-port MIMO antennas (see subsection 5.7.4 and Appendix E).

5.6. Downlink (DL)-MIMO Concept

Due to the fact that mobile traffic is typically asymmetric and for reasons of battery time and cost most presently available mobile wireless devices feature multiple receivers but only a single transmitter for a given band. The LTE standard currently requires antenna systems which support Single User (SU)-MIMO in the DL but not necessarily in the UL. An antenna system for Frequency Division Duplex (FDD) which supports MIMO in the DL but not in the UL is referred to as a DL-MIMO antenna. The concept is general and applicable whenever $N_{\mathrm{RX}} > N_{\mathrm{TX}} > 1$, where N_{RX} is the number of receivers and N_{TX} is the number of transmitters.

Multiport antennas on small mobile platforms exhibit significant difference in radiation properties of both *radiation modes* [1] and *characteristic modes* [10]. The modal radiation quality factor increases (modal bandwidth decreases) with modal index (see Chapter 3). The frequency range over which all *radiation modes* can be matched simultaneously to the desired level of TMRL [38] is dominated by the smallest modal bandwidth. In small mobile wireless devices, such as datacards, USB dongles and various handset form factors this bandwidth may be insufficient to cover both the UL and the DL portion of a given BC simultaneously. Instead of compromising on TMRL the available bandwidth of each of e.g. two *radiation modes* can then be exploited by matching the *radiation mode* with lower radiation quality factor over the UL and DL portion of the band simultaneously but the other only over the DL portion. For an N-port antenna ($N > 2$) the DL-MIMO concept means in general assigning a first subset of *radiation modes* to the DL frequency band and use for DL reception and assigning a second subset to both UL and DL frequency bands.

To illustrate the DL-MIMO concept it is convenient to revert to a very simple model which nevertheless reproduces the situation under study in section 5.7 quantitatively quite well. Consider two collinear half-wavelength dipoles operating at 750 MHz and separated by the distance ℓ. Fig. 5.12 shows the fractional 7 dB bandwidth of the common mode ($b_{\Sigma}^{7\mathrm{dB}}$) and the differential mode ($b_{\Delta}^{7\mathrm{dB}}$) and in addition the fractional 7 dB TMRL bandwidth ($b_{\mathrm{tot}}^{7\mathrm{dB}}$), which could be achieved using a multiport matching network [111], as function of electrical distance ℓ/λ between the dipoles. If the fractional bandwidth required to cover the UL and DL portions simultaneously is smaller than the TMRL bandwidth (olive curve), the DL-MIMO antenna system is *not* required. If not, but if the fractional bandwidth of the DL portion of a band alone is smaller than the bandwidth of the *differential mode* (red curve) then mapping

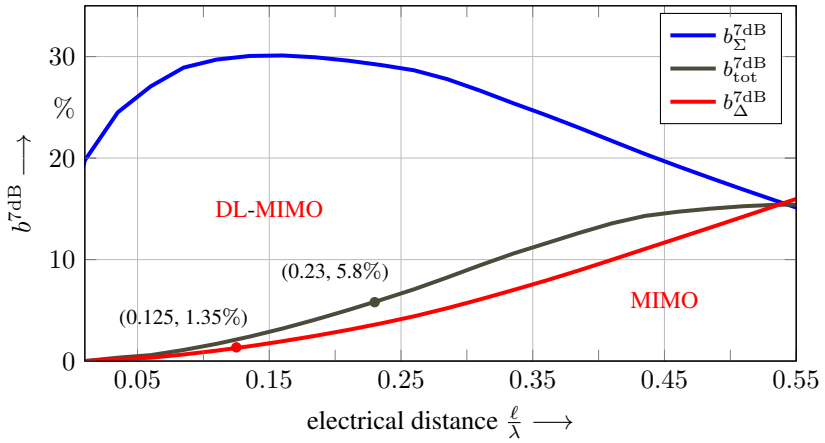

Fig. 5.12.: Fractional 7 dB bandwidth of the *common mode* ($b_\Sigma^{7\mathrm{dB}}$, blue curve), the *differential mode* ($b_\Delta^{7\mathrm{dB}}$, red curve) and the fractional 7 dB bandwidth with respect to *total multiport reflectance* [38] ($b_{\mathrm{tot}}^{7\mathrm{dB}}$, olive curve) over separation ℓ/λ of a pair of collinear dipoles.

of *radiation modes* to external ports and hence DL-MIMO operation is a viable solution. As a specific example consider E-UTRA BC 17 which requires a fractional instantaneous bandwidth of 5.8 % to cover both UL and DL simultaneously. The common mode of the arrangement obviously has sufficient bandwidth. However, the bandwidth of the differential mode is smaller and dominates total multiport reflectance bandwidth if both radiation modes are to be matched simultaneously over the whole band. According to Fig. 5.12 a separation of 0.23λ (roughly 95 mm) would be required to achieve 7 dB TMRL over both the UL and DL portions of the band simultaneously. The 10 MHz DL portion alone, on the other hand, corresponds to a fractional bandwidth of only 1.35 % which is covered by the differential mode at a separation of only 0.125λ (roughly 50 mm).

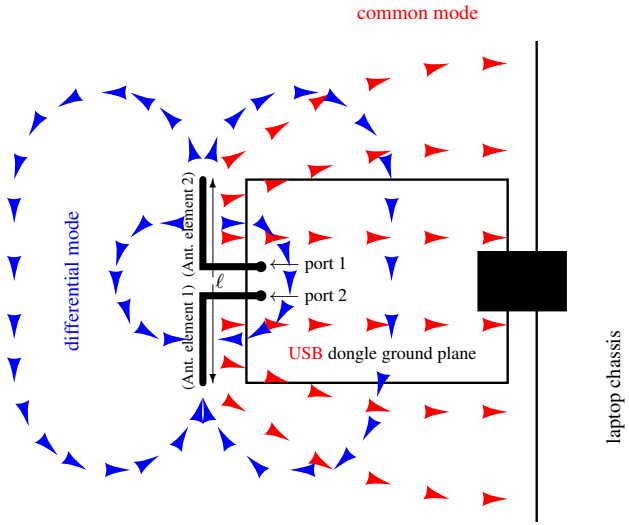

Fig. 5.13.: Illustrative representation of principle of operation of a symmetric 2-port antenna for USB dongles comprising two elements. The graphics shows schematically capacitive coupling of the antenna to the laptop chassis (*common mode*, red) and small dipole operation (*differential mode*, blue).

5.7. Multiport Antennas for USB dongles

5.7.1. Design approach using *radiation modes*

The chassis of a laptop acts as a radiator which can be used in the subsequent antenna design. The radiation characteristic of the laptop chassis can be described in terms of *characteristic modes* [10]. In [106] it was shown that a significant number of characteristic modes featuring low radiation quality factors can be excited on the laptop chassis in the LTE low-band frequency range. It was verified in [107] that excitation of two orthogonal superpositions of characteristic modes on the laptop chassis using extremely small couplers allows for a broadband 2-port MIMO antenna featuring high total per port efficiencies.

Fig. 5.13 refers to an USB dongle plugged into a laptop. A coupler, placed along the short edge of a USB dongle ground plane, comprises two symmetric antenna elements. An advantage from excitation of surface current density on the laptop chassis can be drawn for only one of the *radiation modes* only. This

surface current density, which corresponds to a certain superposition of characteristic modes on the laptop chassis featuring low radiation quality factors, can be associated with the *common mode*. In the *common mode* the antenna is operated as a capacitive coupler against the chassis of a laptop. In the *common mode* an electric field normal to the edge of the laptop is observed (see Fig. 5.13, red arrows). Typically, the bandwidth of this radiation mode is sufficient to cover any E-UTRA BC in the LTE low-band ($Q_\Sigma \approx 5...15$). However, excitation of an appreciable second, orthogonal surface current density on the laptop chassis turns out to be impracticable given small size of USB dongles. Therefore, in the differential mode the antenna is operated as an electrically small dipole ($Q_\Delta \approx 100...200$ for $\ell = 30\,\mathrm{mm}$). The electric field of this *radiation mode* is tangential to the edge of the laptop (see Fig. 5.13, blue arrows). The most critical, with respect to attainable bandwidth and total efficiency, is the *differential mode*. Therefore, all considerations in this section apply to the *differential mode* only.

5.7.2. Estimate on attainable bandwidth of the *differential mode*

Under free space conditions the fractional 7 dB bandwidth of the *differential mode* can be found approximately as an the inverse of the radiation quality factor after Gustafsson's analytical expression (5.4) [102] for given aspect ratio ℓ/d of a cylindrical shape (see subsection 5.1.2). In the present subsection the maximum attainable bandwidth of the *differential mode* is also numerically evaluated taking into account the dipole's proximity to the ground plane of the USB dongle and the chassis of a laptop. For the purpose of the numerical analysis the antenna physical structure is simplified to a bow-tie dipole with capacitive plates at its ends. This model serves as basis for further design decisions. It is not, however, the final design. The maximum attainable bandwidth of *the differential mode* was obtained using FDTD simulations of the antenna physical structure comprising two $\ell \times 10\ \mathrm{mm}^2$ bow-tie elements with $10 \times 15\ \mathrm{mm}^2$ capacitive plates at their ends. The length $\ell \in \{30, 45, 60, 75\}\ \mathrm{mm}$ of a bow-tie dipole was a parameter in the present analysis. It was placed symmetrically at a distance of $80\ \mathrm{mm}$ from the model of $320 \times 220 \times 10\ \mathrm{mm}^3$ laptop chassis. For a given ℓ an FDTD simulation was performed over the frequency range from 700 MHz to 1000 MHz and the 7 dB bandwidth of the *differential mode* was obtained. The results, depicted in Fig. 5.14, clearly show that the width of a USB dongle for antenna placement has to be at least $60\ \mathrm{mm}$.

With this size the DLs portions of all considered BCs in the LTE low-band can be covered. Critical still remains BC 20. The same type of analysis was performed for the *common mode* with the same size of the laptop chassis. It was found that the *common mode*, with bow-tie elements commonly used as a capacitive coupler against the chassis, features always bandwidth of at least 100 MHz for any ℓ from 30 mm to 75 mm. The *common mode* is therefore not critical with respect to bandwidth.

5.7.3. Estimate on the total efficiency of the *differential mode*

For the purpose of numerical evaluation of the total efficiency of the *differential mode* the complete simulation setup and the antenna physical structure remain the same as used in the previous subsection. Approach I, outlined in section 5.4, is used to numerically obtain the total efficiency of the *differential mode* at three center frequencies f_0 for different lengths ℓ. It was assumed that the inductors L_{13} and L_{34} (see Fig. 5.4) feature quality factor of approximately 200 (achievable with "air core" inductances) and have the most significant contribution to the overall losses of the *differential mode*. The radiation efficiency of the *differential mode* is 95 %. Fig. 5.15 shows total efficiency over the antenna length and for three different center frequencies. The total efficiency increases with antenna length and frequency. The analysis also shows significant decrease of the total efficiency due to loss of inductors in the lower part of the LTE low-band. The results suggest that inductors should be placed in the antenna physical structure. For $\ell = 30$ mm the efficiency of the *differential mode* is close to that reported in e.g. [53] (below -5.5 dB) for 66×25 mm^2 USB dongle. $\ell = 60$ mm is required to achieve total efficiency of the *differential mode* of about -3 dB.

5.7.4. Proposed realization of an MDN

For a symmetric 2-port MIMO antenna an electrically tunable MDN can be embedded into the antenna physical structure. A patented approach (see Fig. 1.6) [49] exists, where the monopole and dipole antennas are physically separated [50]. Similar approach, where separate monopole and magnetic dipole (loop antenna) were used, was outlined in [51]. Both are straightforward and simple to implement but require additional volume for separation

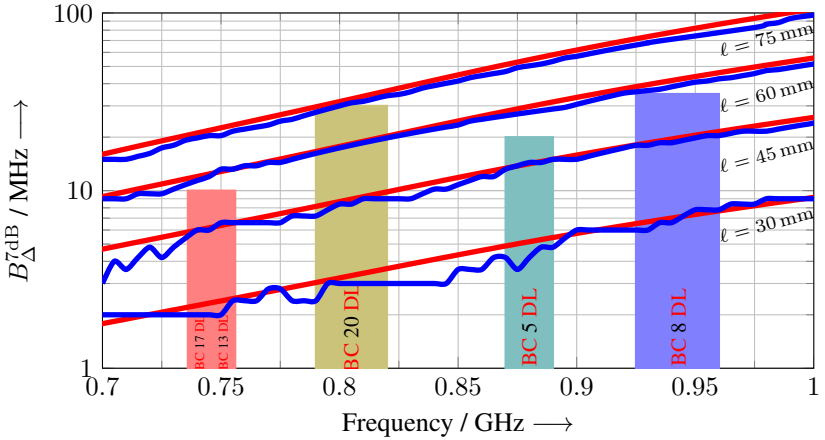

Fig. 5.14.: 7 dB bandwidth of the *differential mode* of a bow-tie antenna for $\ell \in \{30, 45, 60, 75\}$ mm and $d = 10$ mm. The $80 \times 30\,\mathrm{mm}^2$ ground plane of the USB dongle and $320 \times 220 \times 15\,\mathrm{mm}^3$ chassis of the laptop were included in the FDTD simulation. Red curves refer to the 7 dB bandwidth calculated using (2.42) and (2.39). Blue curves refer to numerical results assuming lossless L-type matching network comprising a single inductor and a single capacitor, respectively. The rectangles indicate DL portions of BCs 17, 13, 20, 5 and 8.

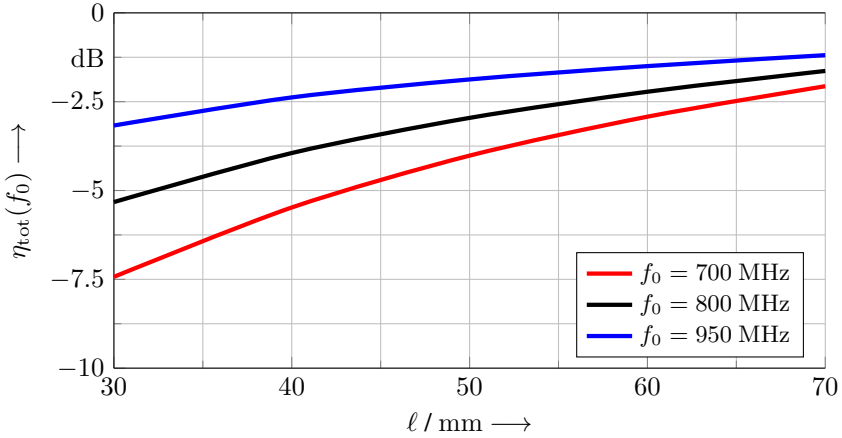

Fig. 5.15.: Estimated total efficiency of the *differential mode* $\eta_{\mathrm{tot}}(f_0)$ versus antenna length ℓ for three different center frequencies f_0.

of antennas and their placement. An advantageous approach, where both *radiation modes* can be excited using the same antenna physical structure, is given in the present section.

In chapter 4 it was shown that MDN featuring reference impedance level for matched 2-port MIMO antennas comprises a 180° hybrid (see general schematic in Fig. 4.17). It provides a valid staring point from which a straightforward extension of the MDN toward electrical tuning is possible. Fig. 5.16 shows the proposed electrically tunable MDN for symmetric 2-port MIMO antennas [112]. It represents a specific embodiment of a solution shown in [135], where a 180° hybrid was converted into an in-phase line and a balun. The center-tapped reactance $2X_{12}$ maps *radiation modes* to external ports Σ and Δ via separate mode-specific matching networks ΣMN and ΔMN. Either a balun transformer or a common mode choke can be used to suppress the *common mode* signal in the *differential mode* branch. If the *differential mode* of an antenna has radiation properties similar to an electrically small dipole, the center-tapped reactance becomes inductance $2L_{12}$. Further, it must be a part of the antenna physical structure and feature small value (e.g. 3.9 nH) so as to maintain high efficiency of the *differential mode*. Application of this embodiment of MDN to 2-port MIMO antennas for USB dongles is given in Chapter 6. In other applications, the center-tapped inductance $2L_{12}$ can be a part of a separate tuning module placed on e.g. separate from the antenna external PCB. This assumes that the losses of the cables connecting the module to the antenna are sufficiently small. In the present approach matching networks are separate and thus independent. The topologies of ΣMN and ΔMN are not mutually constrained as in case of a multiport matching network [28, 111]. This allows for larger tuning range as compared to an electrically tunable multiport matching network reported [137]. The tuning range of the present solution (see Fig. E.1) was numerically evaluated assuming realistic lossy components [112] (see Appendix E).

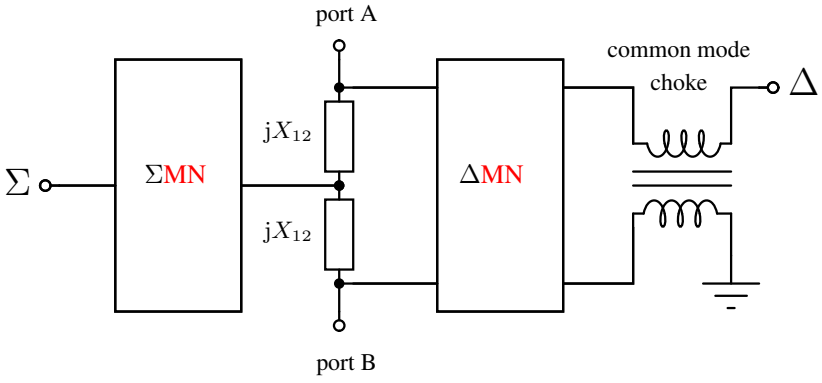

(a)

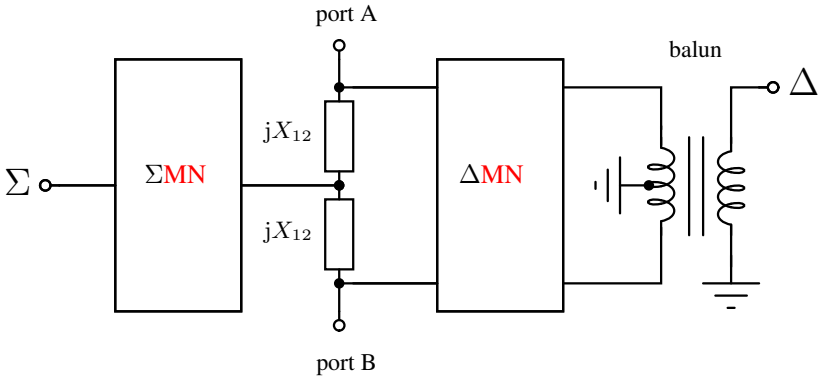

(b)

Fig. 5.16.: Electrically tunable MDN for a symmetric 2-port MIMO antenna comprising separate ΣMN and ΔMN. MDN uses center-tapped reactance $2X_{12}$ as an in-phase line and either (a) common mode choke [112, 136] or (b) a balun as an out-of-phase line to obtain 180° phase shift.

Chapter 6

Prototypes: Design, Fabrication and Measurements

The present chapter describes design procedure, fabrication process and characterization of the antenna prototypes which were referred to in the previous chapters. The most important descriptive quantities such as TMRL, modal RL, isolation, total per port and modal efficiencies were measured for all prototypes. Comparison between measured and simulated data is shown where applicable. Two prototypes featuring electrical switching using high performance RF-PIN diodes, one a 2-port MIMO antenna for datacards and the other 2-port DL-MIMO antenna for USB dongles, were designed, fabricated and measured. In order to validate fabrication method before fabrication of the electrically switchable antenna for USB dongles its fixed frequency version was built and measured. The fourth prototype is a wideband 2-port MIMO antenna for monocoque laptops. Due to broadband frequency response neither electrical switching nor electrical tuning was implemented in this prototype.

6.1. Design of the Prototypes

6.1.1. Prototype I: Electrically switchable 2-port MIMO antenna for datacards

Antenna physical structure

Based on the extensive numerical evaluations using *modal analysis*, shown in the previous chapters, the length of the bow-tie shaped antenna elements were chosen to be $\ell = 90$ mm. The area of capacitive plates was selected to be $A = 10 \times 15$ mm^2 (see details in Fig. 6.1 and Fig. 6.2). In the *common mode* the antenna is operated as a capacitive coupler against the chassis of a device. A relatively large *common mode* bandwidth can be achieved, since the electrical size of the radiator is substantially larger in *common mode* because the ground plane of the laptop forms a large counterpoise. The *differential mode* features radiation properties of a $\lambda/4$ dipole at about 850 MHz. In the *differential mode* the antenna is operated as a dipole. The design goal was to achieve sufficient bandwidth so as to cover both UL and DL portions of a band of any single BC in the LTE low-band simultaneously with higher than 7 dB TMRL. A multiport matching network is designed and further extended toward electrical switching between BC 20 and BC 8. Note that the antenna physical structure is not optimized. It is used here only to illustrate switching capabilities of an electrically switchable multiport matching network.

Electrically switchable multiport matching network

The initial topology and element values of the multiport matching network were found via maximization of TMRL using algorithm outlined in chapter 4. An electrically switchable multiport matching network was designed to cover BC 20 and BC 8 of the LTE low band (Europe) frequency bands. It was optimized and simplified so that the *differential mode* is switched without causing much impact on the *common mode* which is matched over a broad frequency range (Table. 6.1 and Fig. 6.1). Element L_{12} of the multiport matching network is split into three inductances with smaller values L_{11}, L_{22} and L_{11}, respectively. The center inductance L_{22} can be shunted by the RF-PIN diode so that for diode in the open state $L_{12} \approx 2L_{11} + L_{22}$ and in the closed state $L_{12} \approx 2L_{11}$. By performing only a few Method of Moments (MoM) simulations the optimum values for L_{11} and L_{22} so as to cover the desired BCs were

Tab. 6.1.: Nominal values of SMD components used for the electrically switchable multiport matching network after Fig. 6.1 and Fig. 6.2. Units used are nH and pF.

element	L_1	L_{11}	L_{22}	L_{13}	L_{34}	L	C
value	12	6.8	12	6.8	18	270	82

found. The circuit level model of the multiport matching network is shown in Fig. 6.1). In the open state of the RF-PIN diode the antenna covers BC 20 and in the conducting state BC 8. The RF PIN diode BA 592 from Infineon was selected as a switch. It features very low forward resistance of about $0.45\ \Omega$ for a forward current of $3\ \mathrm{mA}$. This is sufficiently low as compared to the loss resistance of SMD wirewound inductors. Therefore, the diode contributes less to loss than a SMD wirewound inductance. The reverse voltage of $35\ \mathrm{V}$ is sufficient given the diode's position in the matching network. The RF voltage in the center of the physical structure of the antenna operated in the *differential mode* is ideally zero. In the common mode of operation the RF voltage is near the maximum. Given the fact that looking at the antenna feeds per port a particular orthogonal superposition of both *radiation modes* is seen the value of RF voltage across the PIN diode is expected to be one half of the maximum value for the *common mode* of operation. For the available RF power at one of the ports of $1\ \mathrm{W}$ the RF power at $900\ \mathrm{MHz}$ dissipated over RF-PIN diode in the conducting state was found to be $100\ \mathrm{mW}$. In the open state the diode RF voltage across at $825\ \mathrm{MHz}$ is about $10\ \mathrm{V}$. It is sufficiently low as compared to reverse voltage of the BA592 RF-PIN diode which is $35\ \mathrm{V}$. Standard biasing technique was employed. Two $82\ \mathrm{pF}$ capacitors serve as DC blocks. The RF chokes are wirewound $270\ \mathrm{nH}$ SMD inductors. The layout of the simulation model is shown in Fig. 6.2. S-parameter models of all components were included in the simulation. The results of the MoM simulation and comparison against measured data are given in the next section of the present chapter.

6.1.2. Prototype II: Fixed frequency 2-port DL-MIMO antenna for USB dongles

Operating principle

The design of a small 2-port DL-MIMO antenna with separate and independent mode-specific matching networks was outlined in the previous chapter (see Fig. 5.16). The solution, depicted schematically in Fig. 6.3, comprises

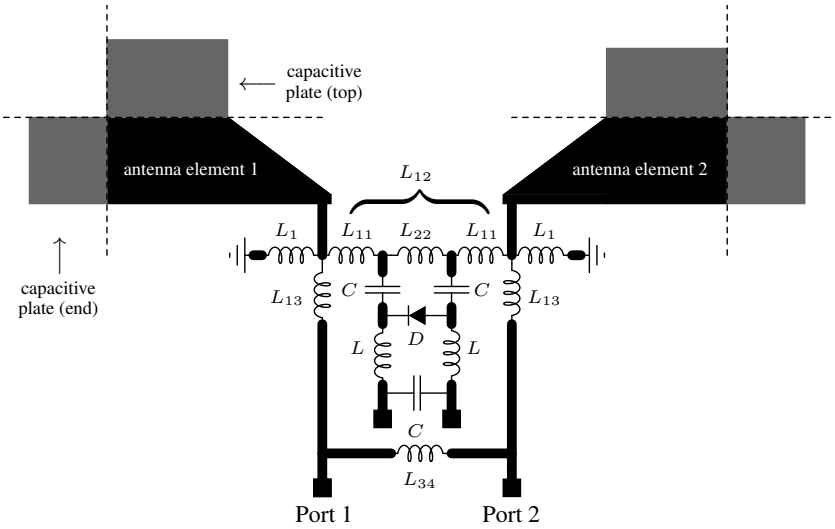

Fig. 6.1.: Schematic representation of an electrically switchable 2-port MIMO antenna for Datacards.

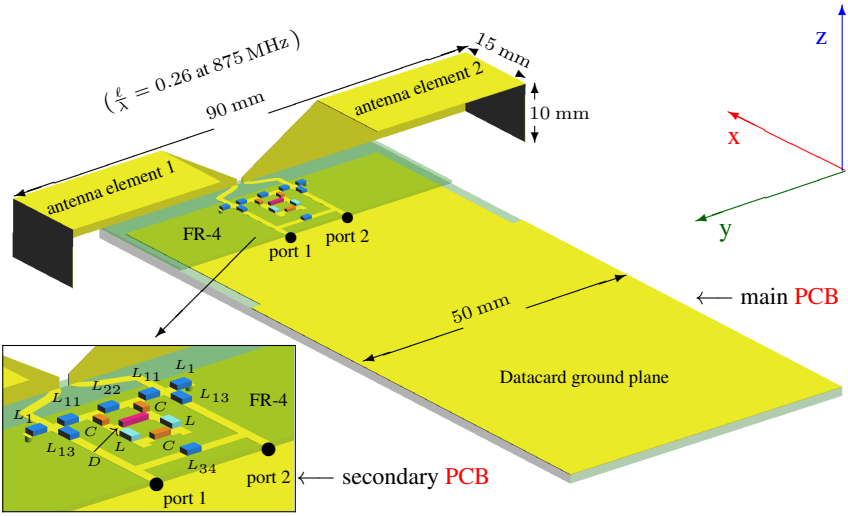

Fig. 6.2.: CAD model of the electrically switchable 2-port MIMO antenna for 100 mm long and 54 mm wide datacardr [138] after Fig. 6.1.

two inductors L_{12} incorporated into the physical structure of the antenna. A center-tap provides *common mode* output (Σ) and two off-center connections the *differential mode* output (Δ). A common mode choke is used in order to suppress the *common mode* in the *differential mode* branch. In the *common mode* the antenna is operated as a capacitive coupler against the chassis of the device. A relatively large *common mode* bandwidth can be achieved, since the electrical size of the radiator is substantially larger in *common mode* because the ground plane of the laptop forms a large counterpoise. The *differential mode* features radiation properties of an electrically small dipole (see chapter 5).

The above method of mapping *radiation modes* to external ports of the antenna is an essential part of the present solution. It represents a specific realization of an MDN shown in [135], where a 180° hybrid was converted into an in-phase line and a balun. It allows to map radiation modes to external ports at the reference impedance level. The present solution is advantageous as, in addition to mapping *radiation modes*, it also allows to match *radiation modes* using separate and independent mode-specific MNs. The solution allows to achieve relative high *modal efficiencies*.

To exploit the maximum attainable bandwidth of the *differential mode* in the LTE low-band (from $704\,\mathrm{MHz}$ to $960\,\mathrm{MHz}$), within the available $60 \times 15 \times 10$ mm^3 volume antenna, elements each comprising a helix and capacitive plate are used [127] (see chapter 5). Therefore, the physical structure of the antenna is a capacitively and inductively loaded electrical dipole. For the *common mode*, as stated earlier, the antenna operates like a monopole against the chassis.

Design details

The simulation model of the antenna is depicted in Fig. 6.4. The maximum width of the USB-dongle at its tip is $w = 60\,\mathrm{mm}$. The majority of the SMD components, including the TCN1-10 common mode choke from MiniCircuits, were modeled using their S-parameters in order to precisely account for their impact on the performance of both *radiation modes*. The device is specified with an IL of $0.85\,\mathrm{dB}$ and a maximum phase imbalance of 6° in the LTE low-band. However, since the reference ground is not present under elements L_{12}, these components were modeled using ECMs comprising series connection of a $3.9\,\mathrm{nH}$ inductance and a loss resistance of $1\,\Omega$. Table 6.2 shows the nominal values of the SMD components. Furthermore, the simulation model comprises

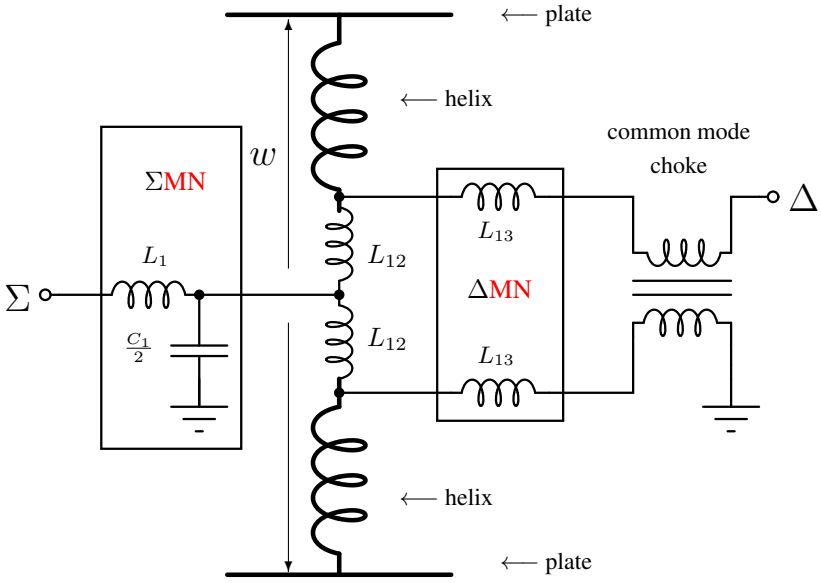

Fig. 6.3.: Schematic representation of the 2-port DL-MIMO antenna for USB dongles with center-tapped inductance $2L_{12}$ and a common mode choke [136]. Δ and Σ denote the *differential mode* and the *common mode* ports, respectively. Antenna physical structure is a helix with capacitive plates at its ends.

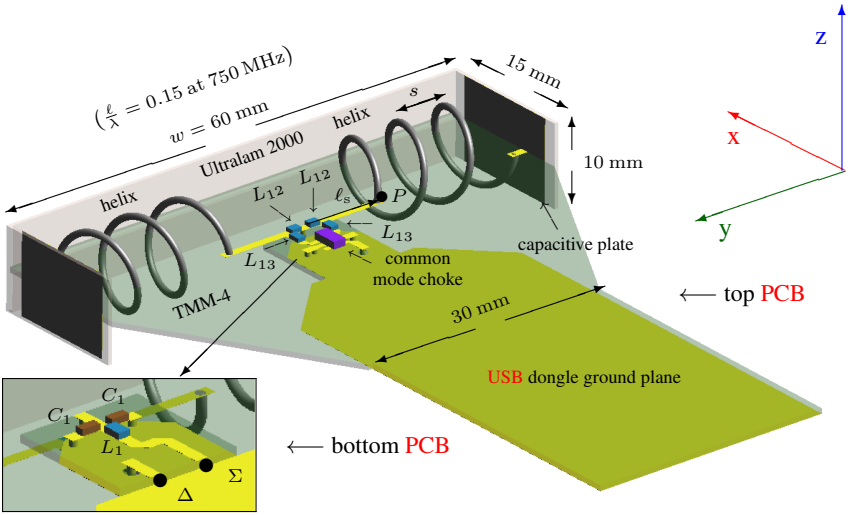

Fig. 6.4.: Simulation model of the 2-port DL-MIMO antenna for 80 mm long USB dongle [138] after [136].

Tab. 6.2.: Nominal values of the 0603 SMD components in Fig. 6.4 [136].

center-tapped inductance	ΔMN	ΣMN	
$2L_{12}$	L_{13}	C_1	L_1
7.8 nH	3.9 nH	1 pF	15 nH

Tab. 6.3.: Resonance frequency of the *differential mode* versus length ℓ_s obtained using FDTD simulation [136].

ℓ_s / mm	4	6	8	10	12
$f_{\Delta,\mathrm{res}}$ / GHz	0.762	0.758	0.752	0.747	0.741

the base part of a $320 \times 220 \times 15$ mm^3 laptop chassis. The *differential mode* matching network (ΔMN) consists of only two series inductors L_{13} in order to avoid losses. For the *common mode* matching network (ΣMN) an L-type topology, with shunt $C_1/2$ and series L_1 is acceptable because the radiation quality factor of this *radiation mode* is low. A low loss replacement of FR 4 (0.64 mm thick Rogers TMM 4 with $\tan\delta = 0.002$) was used for the PCB of the USB dongle. The capacitive plates are realized on 0.51 mm thick Ultralam 2000 ($\tan\delta = 0.0019$). The width and height of the capacitive plates are given in Fig. 6.4. The number of turns of the helix was fixed to $N = 3$ which was found sufficient to obtain resonance near 746 MHz with a helix diameter of $2r = 9$ mm. The helix was realized using 0.8 mm diameter silver plated wire.

Tuning of the *differential mode*

The choice of value for L_{12} was dictated by how much of the total inductance of the helix L_{helix} can be realized in the antenna physical structure so as to achieve resonance and the desired level of input impedance at around 750 MHz. The resonance frequency is proportional to $L_{\mathrm{helix}} + L_{12}$ whereas the impedance level is proportional to $L_{12}/(L_{\mathrm{helix}} + L_{12})$. The "fine" tuning of the resonance of the *differential mode* is simple since only a single parameter is to be considered, i.e. the position of the point P on the y axis which is given by the distance ℓ_s from the symmetry plane (see Fig. 6.4). This parameter defines the pitch s of the helix. The resonance frequency of the *differential mode* decreases with increasing ℓ_s (see Table 6.3). In order to obtain resonance at nearly 746 MHz $\ell_s = 10$ mm was selected. Moreover, during the fabrication process the total length of the helix was adjusted to slightly tune the resonance of the differential mode to the desired frequency in order to compensate for manufacturing inaccuracies.

6.1.3. Prototype III: Electrically switchable 2-port DL-MIMO antenna for USB dongles

General description

Fig. 6.5 shows an extension of the above approach which allows for electrical switching of the *differential mode* of the antenna between different DL portions of four different BCs in the LTE low-band. The solution makes use of the MDN after [135, 112, 136] shown in Chapter 5 (see Fig. 5.16a). L_{12} is a part of the antenna physical structure. Separate electrically tunable MNs for an independent fine tuning of both *radiation modes* can be added. The design approaches the optimum radiator [127, 136]. Electrical switching between four BCs in the LTE low-band is achieved by electrical shorting of two windings per arm of the helix using two RF-PIN diodes. The relative fractions of the helix inductance which are electrically shorted follow from the desired switching steps. The topology shown in Fig. 6.5 and in particular placement of RF-PIN diodes also follows from the goal to minimize the interaction between the antenna physical structure and and the unavoidable biasing circuitry. The number of biasing lines is minimized by using common Direct Current (DC) ground return line for RF-PIN diodes D_1 and D_2 and a single biasing line for the pair of diodes labeled D_1. The solution features the minimum number of the SMD components and DC lines for biasing. All elements labeled L, L_{11}, L_{22} are chokes. All elements labeled C are DC blocks. With area of capacitive plates fixed to the maximum allowed 15×10 mm^2 the only parameter to adjust the design for the lowest frequency of operation of the *differential mode* (diode state 00) is the total inductance. It comprises the inductance of two helices, $2L_{12}$ and the inductance of the straight strips connecting both pairs of elements. The values $N = 3$ (number of turns of the helix), $L_{12} = 3.9$ nH and $\ell_s = 10$ mm were found to be sufficient to obtain resonance near 746 MHz (the lowest required frequency of operation for *differential mode*). The diameter of the helix is $2r = 9$ mm. The straight strips, connecting L_{12} with a helix, were introduced to provide straight RF current flow about the feed in order to minimize losses. The higher frequency switching states are achieved by electrically shunting parts of the helix (diode states 01, 10, 11).

CAD model description

The CAD model of the antenna structure is shown in Fig. 6.6. 0.64 mm thick Rogers TMM 4 with $\tan\delta = 0.002$ was used for PCB of the USB dongle as a

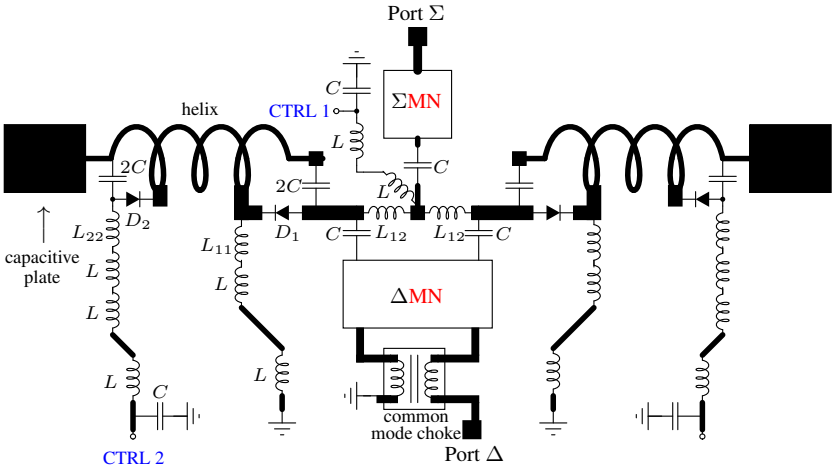

Fig. 6.5.: Schematic representation of electrically switchable 2-port DL-MIMO antenna for USB-dongles. Two RF-PIN diodes per arm of the antenna (D_1 and D_2) realize four possible switching states of the *differential mode* covering DLs of BC 17, BC 13, BC 20, BC 5 and BC 8.

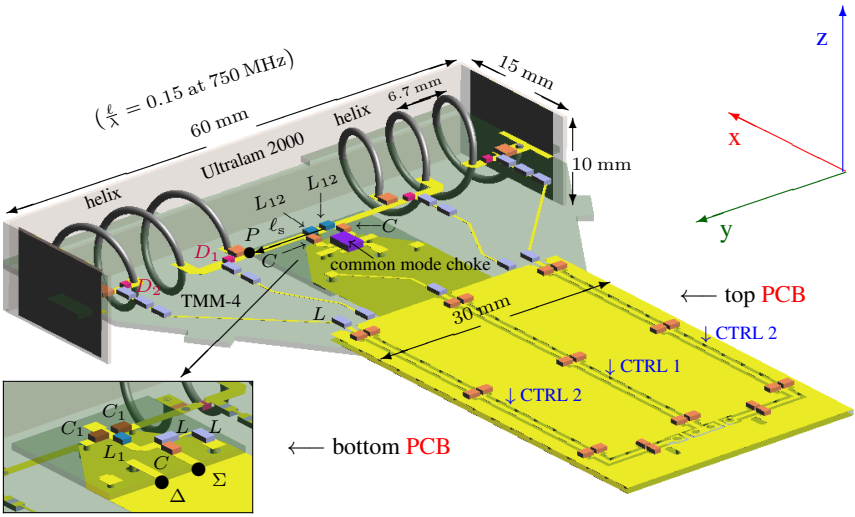

Fig. 6.6.: CAD model of the electrically switchable 2-port DL-MIMO antenna for 80 mm long USB-dongle form factor [138]. Each set of the same SMD components are marked by a unique color. ΣMN comprises shunt $C_1 = 1$ pF and series inductance $L_1 = 15$ nH.

low-loss substitution of the standard FR 4. Capacitive plates are made of 0.51 mm thick Ultralam 2000 ($\tan\delta = 0.0019$). A TCN1-10 "balun" from Mini-Circuits was selected for the common mode choke. It features average 0.85 dB insertion loss (IL) over the LTE low-band and maximum phase imbalance of $6°$. High quality factor 0603 SMD components from Johansontechnology were used for most of inductors and capacitors and DC blocks ($C = 82$ pF). For the $L = L_{11} = L_{22} = 270$ nH RF chokes components from CoilCraft were selected. Components with no reference ground were modeled using ECMs. The pith of the helix is $s = 6.7$ mm.

Electrical switching

Due to tough requirements anticipated from the RF-PIN diodes in the present design with respect to the reverse voltage and losses a silicon deep trench diode BAR 90 from Infineon was selected for the present design. The ECM of this diode is given by a parallel RC tank with $R_{\mathrm{D}} = 5$ kΩ, $C_{\mathrm{D}} = 0.2$ pF and as series RL tank ($R_{\mathrm{D}} = 1.3$ Ω, $L_{\mathrm{D}} = 0.4$ nH) in the open state and conducting state, respectively. It features very low "off" capacitance and small "on" resistance. The reverse voltage of the diode is $V_{\mathrm{R}} = 80$ V. The peak-to-peak RF voltage across diodes D_1 and D_2 were found to be 34 V and 54 V, respectively (see Fig. 6.5). This indicates that for input RF power of 1 W, the useful RF signal will not be clipped if the RF-PIN diodes are biased at 40 V. The challenge in design of biasing network is to achieve sufficiently low losses the low ratio of RF current flowing through L_{11} and L_{22} (see Fig. 6.5) to the RF current flowing through RF-PIN diode has to be minimized. Further, minimization of this ratio leads also to decrease of parasitic resonances, related to current loops created by biasing lines and the helix. Ultimately it increases the total efficiency of both *radiation modes* of the antenna.

Design of biasing circuitry

Biasing lines were routed at right angle relative to the electric field lines in the near field of the *differential mode* in order to minimize interaction. Further task in the design of biasing lines was to select an appropriate size and the value of choke inductors. The trade-off between the nominal value of inductance and the series (loss) resistance was considered. The limiting parameter is the Self-resonant frequency (SRF) of a choke. The size of the choke inductors has to be maintained small to avoid interaction with the electromagnetic

field of the antenna. Large choke inductors must be included into the CAD model of the antenna as physical components which yields to cumbersome and time consuming full-wave simulations. Choke inductors are realized as series connections of a few inductors with smaller values featuring high SRF. These choke inductors have to be distributed over the length of the biasing lines. It was found that the choke inductance has to be at least $1\ \mu\mathrm{H}$. Several attempts have been made in order to find the number and the best placement of $270\ \mathrm{nH}$ 0603 size inductors (CoilCraft) along the biasing lines so as to minimize interaction between antenna physical structure and biasing circuitry. It was found that the RF current through choke L_{11} is about $25\ \mathrm{dB}$ smaller than the RF current through diode D_1 in the conducting state. The RF current through choke L_{22} is about $45\ \mathrm{dB}$ smaller than the RF current flowing through the D_2 diode in the conducting state. The rule of thumb is to place multiple inductors in the immediate vicinity of RF-PIN diodes. A single choke per biasing line at the ground plane is sufficient (see Fig. 6.6).

6.1.4. Prototype IV: 2-port MIMO antenna for laptops

Theoretical foundations for the design of a broadband 2-port MIMO antenna for laptops were given in Chapter 3 using *theory of characteristic modes* and *modal analysis* based on the spectrum of *radiation matrix*. In the present section the design details are shown and discussed. The simulation model of the antenna is given in Fig. 6.7. A 13" laptop is considered. The couplers comprise a $20\times15\times5.5\ \mathrm{mm}^3$ opening ("box") at the back of the laptop's base part. Each "box" has at its top a $0.5\ \mathrm{mm}$ thick FR-4 PCB with $50\ \Omega$ microstrip line which widens at the open end of the "box" and connects to the lid part of the laptop. Flexible PCB would be used in a real product. The width of the conductive hinges is $20\ \mathrm{mm}$. The width of the slot between the lid and the base part has significant impact on the TMRL bandwidth. The wider the slot the wider the bandwidth. For narrower width of the slot the bandwidth decreases since more electromagnetic energy is stored in the near-field. A $15\ \mathrm{mm}$ wide slot was selected during the optimization process as a trade-off between the maximum bandwidth in the LTE low-band and maximum width acceptable in a product. The distance of the conductive hinges and *couplers* from the symmetry plane is denoted by $|y_1|$ and $|y_2|$, respectively (Fig. 6.7). For fixed $|y_2|$ and increasing $|y_1|$ the $7\ \mathrm{dB}$ TMRL bandwidth increases and the resonance frequency also increases (Fig. 6.8). Two independent parameter sweeps over $|y_1|$ and $|y_2|$ allowed to find the optimum positions of the conductive hinges and the *couplers*

so as to cover LTE low-band and LTE mid-band with higher than 7 dB TMRL. They are given by $|y_1| = 20$ mm and $|y_2| = 145$ mm. The results shown in Fig. 6.8 allow to "fine" tune the design to the desired frequency bands. The results of the FDTD simulation for the CAD model given in Fig. 6.7 are shown in the next section together with measured results for the prototype.

6.2. Measurement Results

6.2.1. Prototype I: Electrically switchable 2-port MIMO antenna for datacards

Fig. 6.9a depicts the antenna prototype without matching network. In Fig. 6.9b the antenna prototype with electrically switchable matching network is shown. 1.5 mm thick FR-4 substrate was used for the main PCB. 0.5 mm thick FR-4 was used for the replaceable networks. The antenna structure, comprising two bow-tie shaped fins, was fabricated from 0.1 mm thick copper foil. 0603 SMD components were used for the multiport matching network. Solder pads for placement of BA 592 RF-PIN diode and the remaining SMD components were included in the layout.

Measurements were performed with the datacard plugged into a commercially available 15" laptop with a 54 mm datacard slot. Comparison between simulated and measured *modal impedances* the antenna without electrically switchable multiport matching network are given in Fig. 6.10. The modal modal impedance, derived from measured S-parameters, are in an acceptable agreement with data obtained using MoM simulator. The S-parameters of the prototype with matching network for the two different switching states of the RF-PIN diode were measured using Rhode&Schwarz ZVB-20 Vector Network Analyzer (VNA) over the frequency range from 750 MHz to 1000 MHz. The results are given in Fig. 6.11. Fig. 6.11a refers to the diode in the open state in which case the antenna should cover BC 20. The measured and simulated TMRL are in a good agreement. The prototype provides at least 7 dB TMRL over BC 20. In the conducting state of the RF-PIN diode the antenna was designed to cover BC 8 (see Fig. 6.11b). The measured and simulated maxima of isolation are about 50 MHz apart. However, the measured TMRL still complies with the requirement. In both cases the differences between measured and simulated results can be contributed to crude fabrication technique and relatively high tolerances (about ± 5 %) of SMD components.

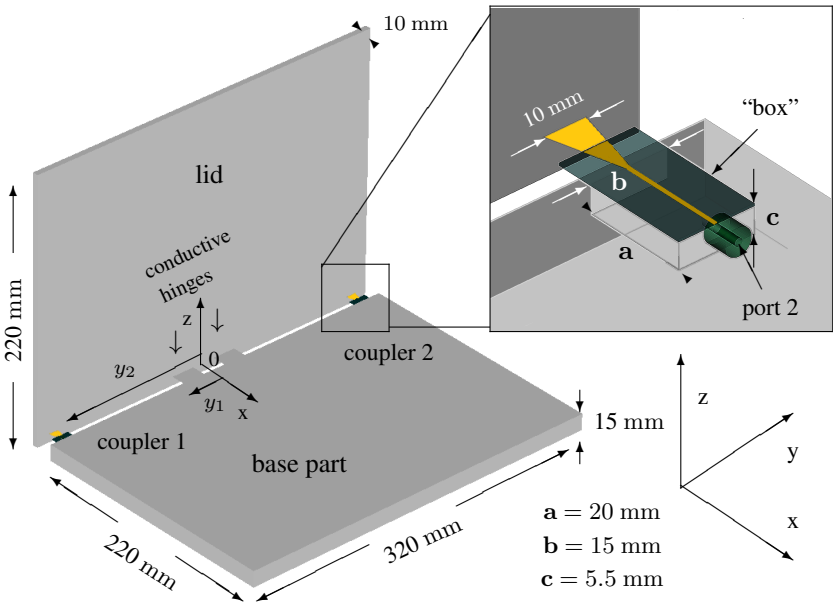

Fig. 6.7.: CAD model of a 13" laptop where $|y_1|$ denotes locations of two conductive hinges and $|y_2|$ indicates the positions of two *couplers* relative the symmetry plane xz [107]. The width of the slot between the lid and the base part is 15 mm.

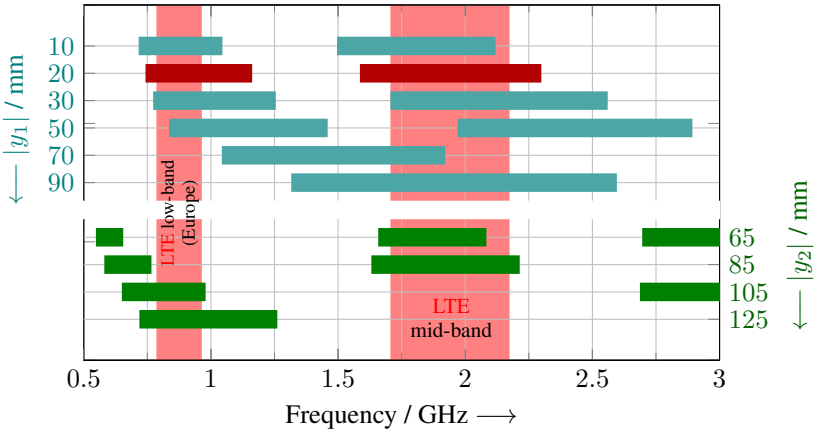

Fig. 6.8.: The 7 dB TMRL bandwidth for two independent parameter sweeps over $|y_1|$ for fixed $|y_2| = 145$ mm and $|y_2|$ for fixed $|y_1| = 20$ mm for a monocoque laptop model after Fig. 6.7 [107]. The design goal is marked with rose rectangles and includes LTE low-band (Europe) and LTE mid-band. Red rectangles indicates the design which fulfills the above stated goal.

The total efficiencies were measured for the RF-PIN diode in the open state. The maximum of total efficiency relative to port 1 and port 2 was measured to be 75 % and 82 %, respectively. It is not lower than 50 % at the lower edge of BC 20. The radiation pattern overlap calculated from measured radiation patterns was found to be below 0.1 within BC 20 with the minimum value of 0.015.

6.2.2. Prototypes II and III: Fixed frequency and electrically switchable 2-port DL-MIMO antenna for USB dongles

In order to verify the design of the fixed frequency and electrically switchable 2-port DL-MIMO antennas for USB dongles both prototypes were fabricated (Figs. 6.12 and 6.13). High accuracy required for the layout was achieved by employing the milling process using ProtoMat S100 from LPKF. The system allows for the minimum drill diameter of 0.25 mm. To electrically connect top and bottom ground of two PCBs a high conductivity solder paste CR 44 from EDSYN was used. The via holes between the uppermost layer of the top PCB with the bottommost layer of the bottom PCB were realized using 0.6 mm diameter silver plated wires. Via holes connecting two metal layers on the opposite sides of the same substrate were realized using LPKF ProConduct. The helix was fabricated using 0.8 mm diameter silver plated wire.

All measurements were performed with a laptop chassis mockup in a form of a 320×220 mm^2 ground plane. The USB-dongle was attached to the laptop chassis in the center of one of the short edges of the laptop. The S-parameters were measured using Rhode&Schwarz ZVB 20 VNA. Measurements of the radiation patterns were performed in an anechoic chamber. The center of rotation, the same as in the simulations, is the geometric center of the bounding box containing USB dongle plugged into the laptop chassis. High quality tunable reference dipole (Schwarzbeck UHAP, 300 MHz - 1000 MHz) was used to calibrate the measurement. Angular resolution in elevation was $\Delta\vartheta = 5°$ while in azimuth the number of sampling points was reduced in proportion to $\sin\vartheta$ so that $\Delta\varphi \approx 5°/\sin\vartheta$. Total efficiency was calculated by radiation pattern integration over all 1830 angular positions.

Tab. 6.4.: Maximum measured and simulated per port gain at 746 MHz of the fixed frequency 2-port DL-MIMO antenna for USB dongles after Fig. 6.12.

G_{max} (dBi) at 746 MHz		
	simulated	measured
Σ	3.9	2.8
Δ	3.8	4.1

Fixed frequency prototype

Fig. 6.14 shows comparison between measured and simulated S-parameters of the antenna. Measured per port return loss and isolation are in fairly good agreement with those obtained using FDTD electromagnetic simulation. The differential mode RL is higher than 7 dB in DL portions of BC 17 and BC 13. The common mode RL is above 10 dB from about 700 MHz to 825 MHz. The measured isolation is higher than 17 dB in the desired frequency range. Probable cause of the maximum of 5 dB deviation from simulation result is worst performance of the TCN1-10 common mode choke than that given by S-parameters provided by the manufacturer.

Pattern were measured in the frequency range from 700 MHz to 800 MHz with 2.5 MHz step. The total efficiency is higher than -3 dB over the DL portion of BC 13 and BC 17 for both *radiation modes* (maximum value for the *differential mode* is -1.5 dB) and better than -3 dB over the UL portion of BC 13 and BC 17 for the *common mode* (see Fig. 6.15). The difference between measured and simulated values of total efficiency for the common mode can be attributed to higher, than assumed in the simulation, losses of the inductor in the *common mode* matching network. Simulated radiation patterns of the antenna are given in Fig. 6.16. Measured patterns (see Fig. 6.17) as well as maximum gain (see Tab. 6.5) are in good agreement with simulated maximum gain and patterns, respectively.

Electrically switchable prototype

Simulated and measured RL of the *differential mode* for all four states of the RF-PIN diodes are shown in Fig. 6.18. The differential mode RL is always higher than 7 dB for all four switching states of the antenna. The attained bandwidth is sufficient to potentially cover all four DL portions of the desired BCs. Small deviation from the desired frequency ranges can be resolved by final optimization of the design i.e. changing diameter of each winding of

the helix. The isolation between ports Σ and Δ is always higher than 15 dB (see Fig. 6.19). It is the lowest at the edges of the LTE low-band where the amplitude unbalance of TCN1-10 common mode choke is relatively high, i.e. 0.6 dB. Fig. 6.20 shows measured total efficiency of the *differential mode*. It is not lower than 50 % for BC 17, 13, 5 and 8. The total efficiency of the *differential mode* for both pairs of diodes in the state 00 is about -1 dB and is the highest among all remaining switching states. In the remaining states the maximum values of total efficiency of the *differential mode* are about -3 dB. The total efficiency of the *common mode* (see Fig. 6.21) is higher than 25 % across all considered BCs which is still high considering that fixed ΣMN was used.

6.2.3. Prototype IV: 2-port MIMO antenna for 13" laptop

The prototype of the 2-port MIMO antenna on a 13" monocoque laptop was fabricated using dimensions given in the previous chapter (see Fig. 6.22). The prototype was fabricated using 1 mm thick aluminium sheets and U-shaped profiles. 0.5 mm thick FR-4 was used in construction of the for the couplers. The coax lines which connect couplers to external ports were routed inside the prototype.

The per port return loss and isolation were measured using ZVB 20 VNA over the 10 MHz to 3 GHz frequency range. The results shown in Fig. 6.23 are in good agreement with those obtained using electromagnetic field simulator. The deviation from the simulated results observed in the LTE mid-band (from 1710 MHz to 2170 MHz) is due to fabrication inaccuracies. Still, the per port RL and TMRL are higher than 7 dB for all bands of interest. The isolation is higher than 17 dB over the whole frequency range of the measurement. Therefore, the modal return loss of both radiation modes is nearly equal to TMRL.

Radiation pattern measurements were performed in the anechoic chamber. Per port radiation patterns at 900 MHz (see Fig. 6.24) are orthogonal due to $90°$ phase difference between their respective ϑ and φ components. Measured gain has maxima at $\vartheta = 45°$, $\varphi = 6°$ for port 1 and at $\vartheta = 40°$, $\varphi = 354°$ for port 2, respectively (see Tab. 6.5). It is only 0.28 dB lower than maximum gain obtained using FDTD simulation. In order to directly measure modal radiation patterns a $180°$ hybrid is required. To circumvent this requirement it is also possible to calculate these radiation patterns from measurements. Fig. 6.25

Tab. 6.5.: Maximum measured per port gain at 900 MHz, 2000 MHz and a comparison to gain obtained using FDTD simulation of 2-port MIMO antenna for laptops after Fig. 6.22.

G_{max} (dBi) at 900 MHz		
port 1	port 2	simulated
8.18	7.96	8.35

G_{max} (dBi) at 2000 MHz		
port 1	port 2	simulated
7.85	7.89	10.9

shown modal radiation patterns. The per port patterns measured at 2000 MHz are shown in Fig. 6.26. They are more uniform (omnidirectional) because a larger number of characteristic modes is excited on the laptop chassis in this frequency range as compared to the LTE low-band. Measured maximum gain (Table 6.5) is about 3 dB lower than that predicted by the FDTD simulation. This is due to insufficient accuracy of the manufacturing process. Modal radiation patterns are shown in Fig. 6.27. The total per port efficiencies were calculated (via radiation pattern integration) to be 95 % and 82 % at 900 MHz and 2000 MHz, respectively. It is easy to see from the high isolation between the antenna ports that radiation patterns are approximately orthogonal. The radiation pattern overlap is 0.05 at 900 MHz and 0.02 at 2 GHz.

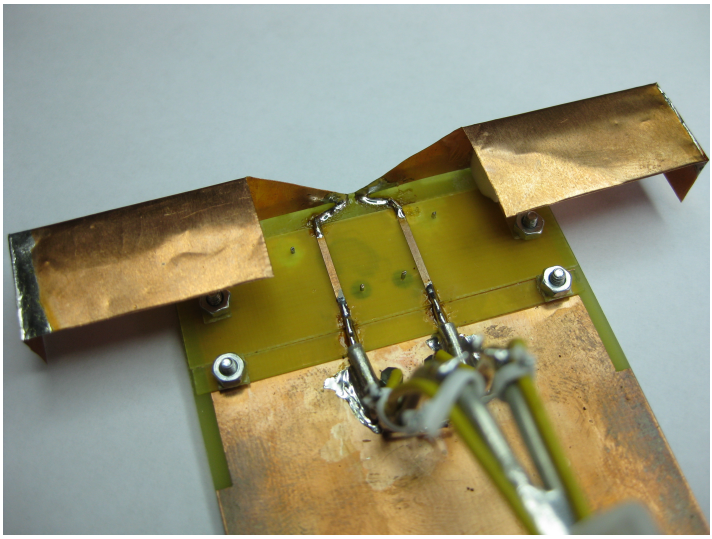

(a) without multiport matching network

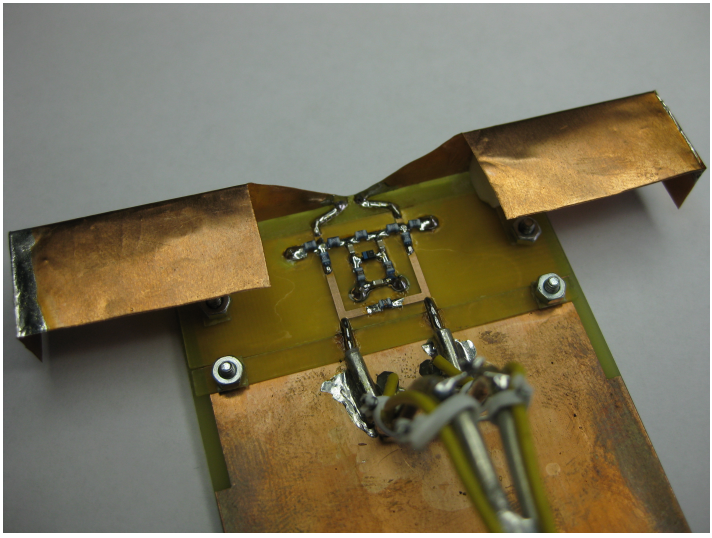

(b) with switchable multiport matching network

Fig. 6.9.: 2-port MIMO antenna prototype for datacards (a) without matching network, (b) with switchable matching network.

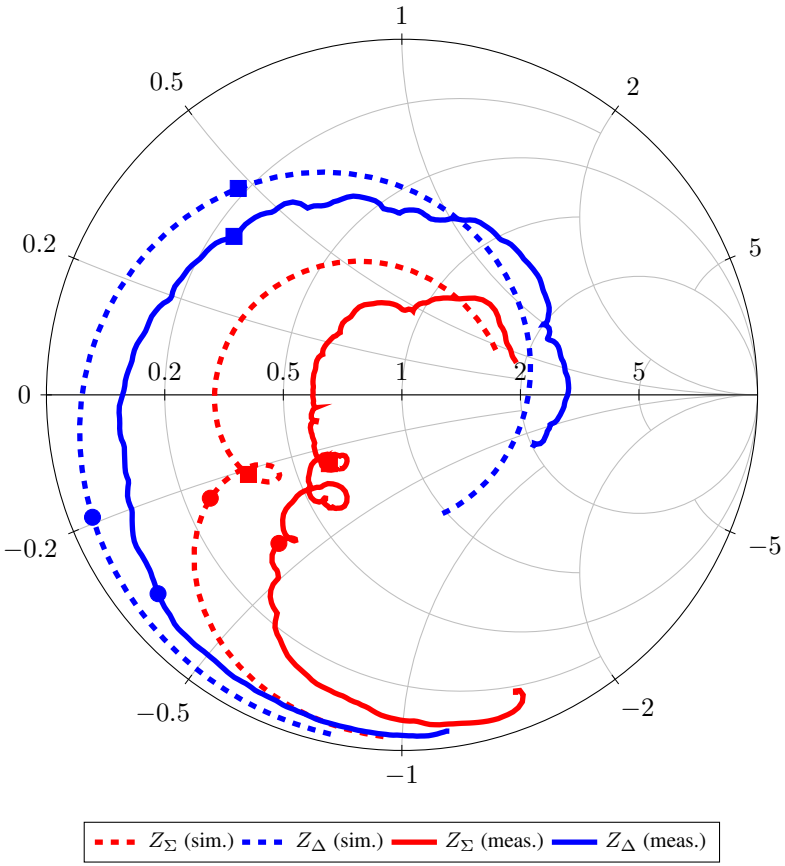

Fig. 6.10.: Simulated (dashed curves) and measured (solid curves) modal impedances of the unmatched antenna (without multi-port matching network) after Fig. 6.9a from 500 MHz to 1500 MHz. Solid circles and solid squares refer to modal impedance at 750 MHz and at 1000 MHz, respectively.

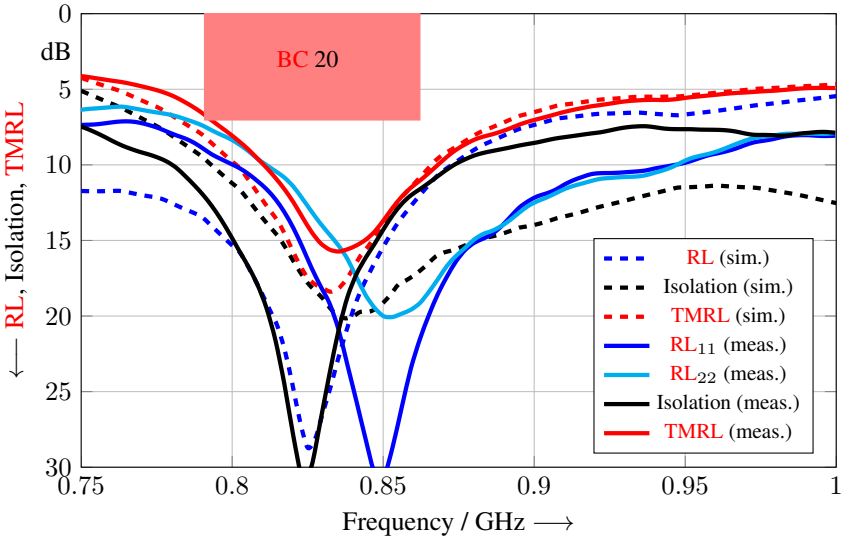

(a) RF-PIN diode in open state

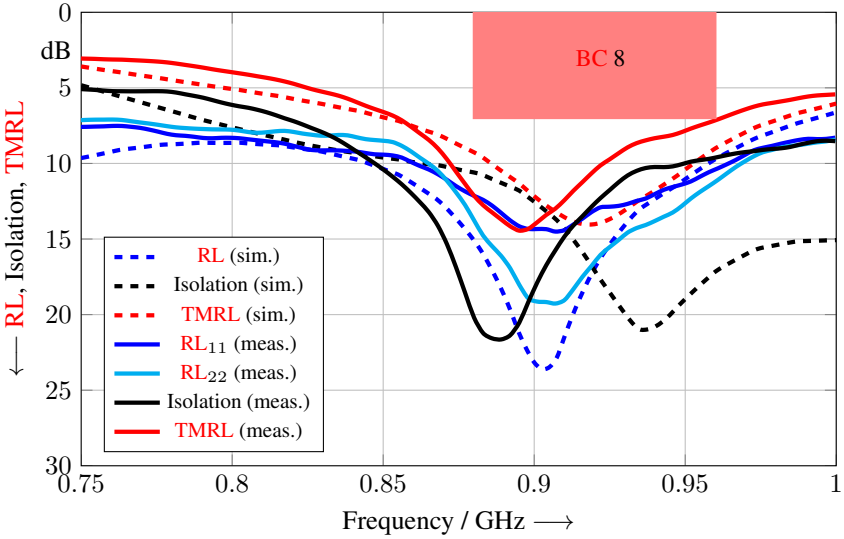

(b) RF-PIN diode in conducting state

Fig. 6.11.: Simulated (dashed curves) and measured (solid curves) per port RL, isolation and TMRL for the antenna prototype after Fig. 6.9 and RF-PIN diode in (a) open state and (b) conducting state.

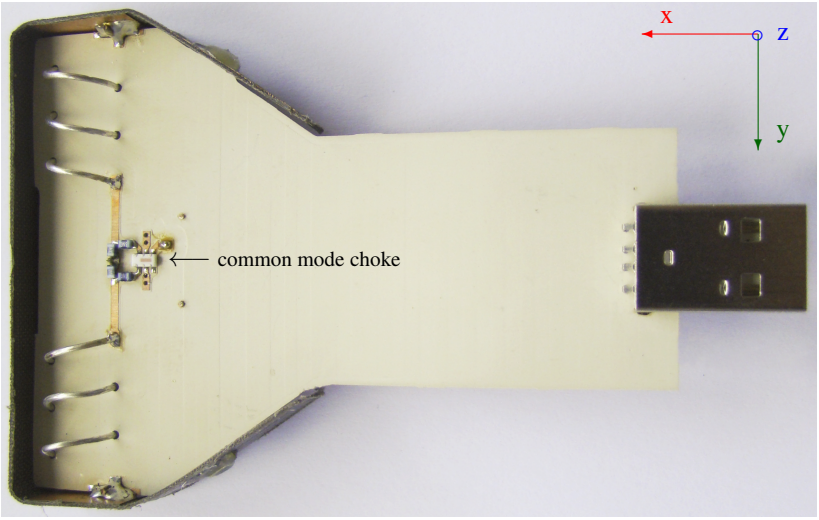

Fig. 6.12.: Fixed frequency 2-port DL-MIMO antenna prototype for USB dongles. Top view on the top PCB of the USB dongle [136].

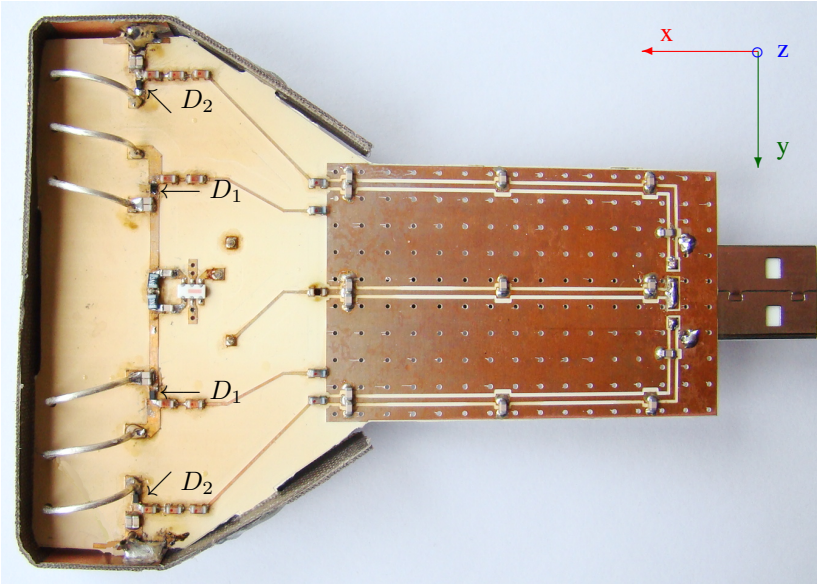

Fig. 6.13.: Electrically switchable 2-port DL-MIMO antenna prototype for USB dongles. Top view on the top PCB of the USB dongle.

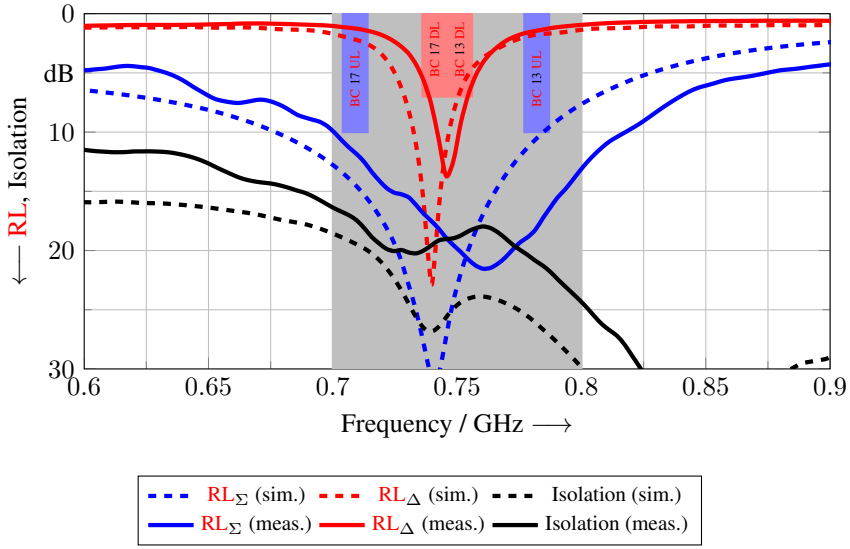

Fig. 6.14.: Simulated (dashed curves) and measured (solid curves) return loss and isolation of the antenna system after Fig. 6.4 and after Fig. 6.12, respectively [136]. Gray rectangle denotes frequency range of total efficiency measurement shown in Fig. 6.15.

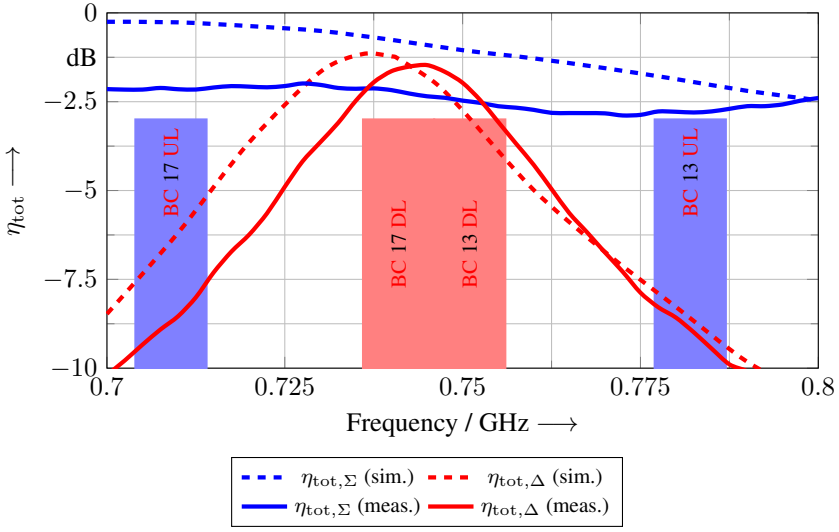

Fig. 6.15.: Simulated (dashed curves) and measured (solid curves) total efficiency of the *common mode* $\eta_{\text{tot},\Sigma}$ and the *differential mode* $\eta_{\text{tot},\Delta}$ of the antenna system after Fig. 6.12 (attached to a laptop chassis) [136].

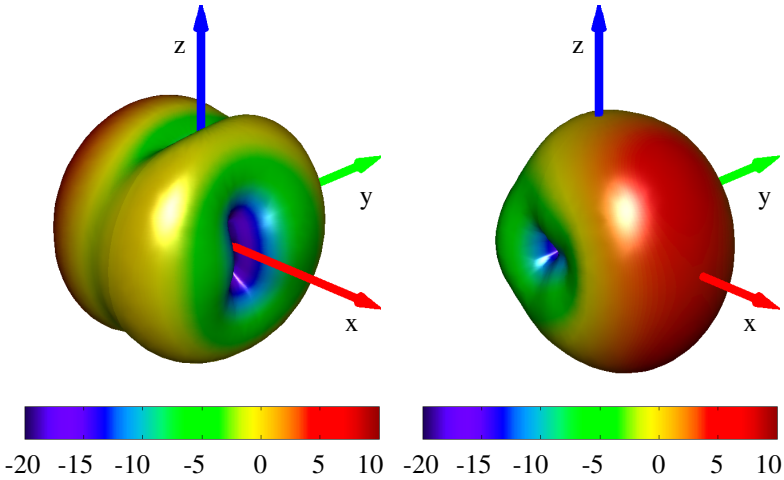

Fig. 6.16.: Simulated total gain (both polarizations) for the *common mode* (left) and the *differential mode* (right) of the antenna system after Fig. 6.4 at 746 MHz [136]. Gain values are given in dBi.

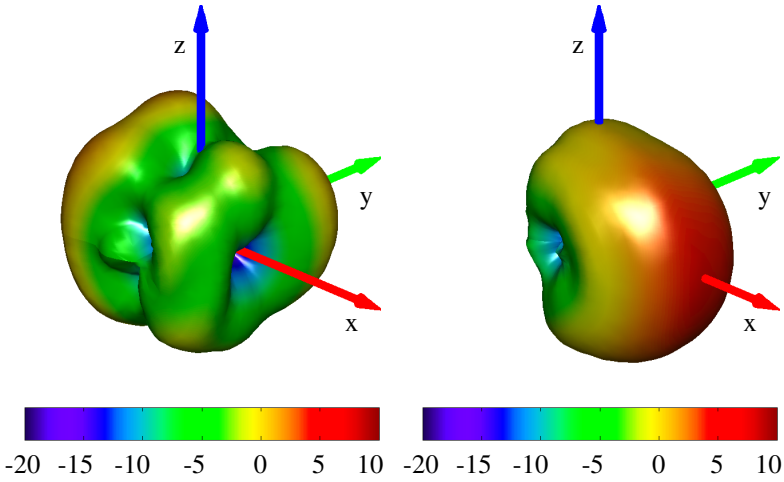

Fig. 6.17.: Measured total gain (both polarizations) for the *common mode* (left) and the *differential mode* (right) of the antenna system after Fig. 6.12 at 746 MHz [136]. Gain values are given in dBi.

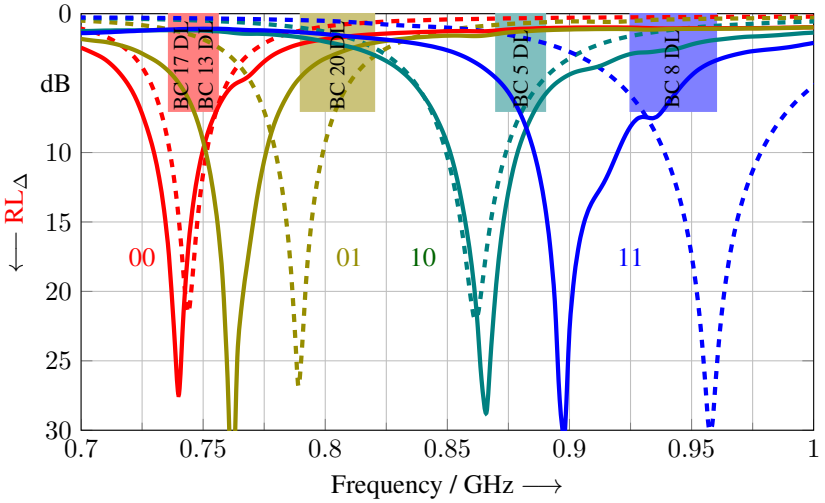

Fig. 6.18.: Simulated (dashed curves) and measured (solid curves) return loss of the *differential mode* (RL_Δ) of the electrically switchable antenna system after Fig. 6.6 and Fig. 6.13, respectively. Switching states of the RF-PIN diodes D_1 and D_2 are given by 0 (denotes open state) and 1 (denotes conducting state). The rectangles indicate DL portions of BCs 17, 13, 20, 5 and 8.

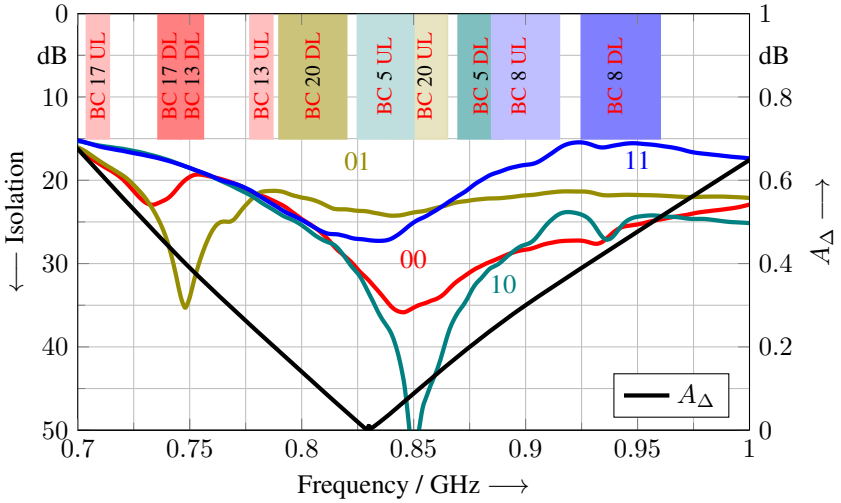

Fig. 6.19.: Measured isolation of the electrically switchable antenna system after Fig. 6.13. Switching states of the RF-PIN diodes D_1 and D_2 are given by 0 (denotes open state) and 1 (denotes conducting state). Black curve denotes amplitude unbalance A_Δ of TCN1-10 common mode choke.

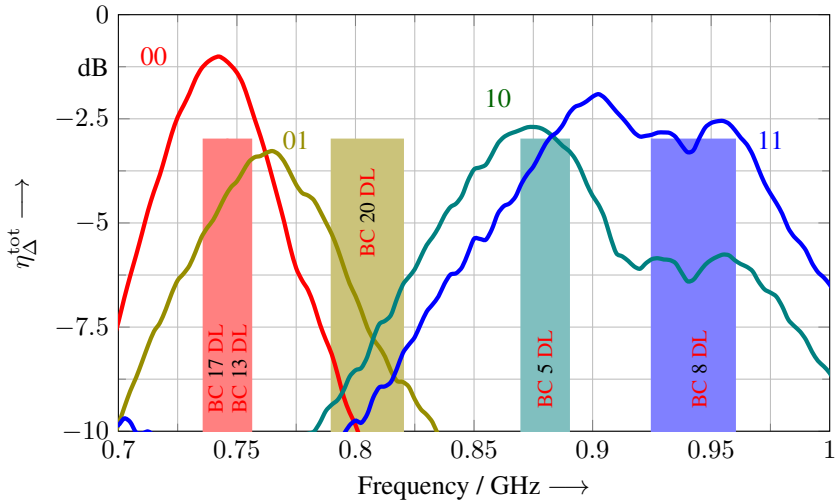

Fig. 6.20.: Measured total efficiency of the *differential mode* ($\eta_\Delta^{\mathrm{tot}}$) of the antenna system after Fig. 6.13. Switching states of the RF-PIN diodes D_1 and D_2 are given by 0 (denotes open state) and 1 (denotes conducting state). The rectangles indicate DL portions of BCs 17, 13, 20, 5 and 8 with total efficiency lower than -3 dB.

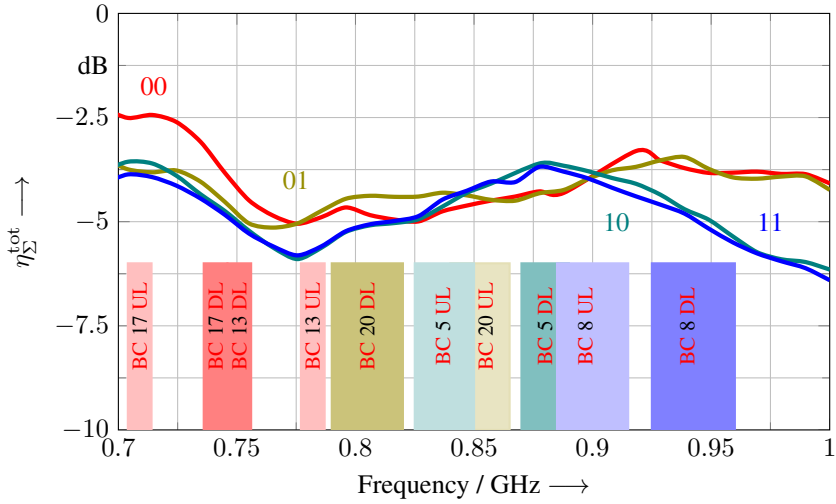

Fig. 6.21.: Measured total efficiency of the *common mode* ($\eta_\Sigma^{\mathrm{tot}}$) of the antenna system after Fig. 6.13. Switching states of the RF-PIN diodes D_1 and D_2 are given by 0 (denotes open state) and 1 (denotes conducting state). The rectangles indicate DL portions of BCs 17, 13, 20, 5 and 8 with total efficiency lower than -6 dB.

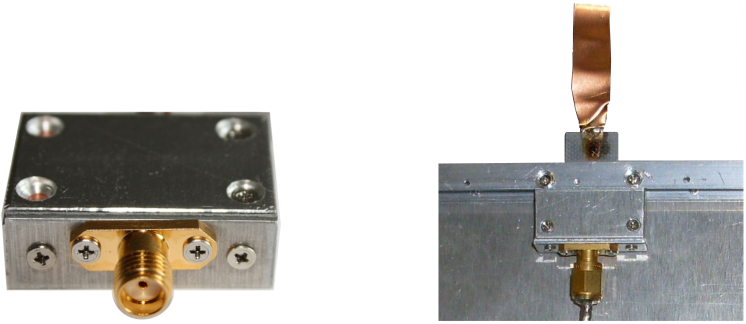

(a) “box” and coupler

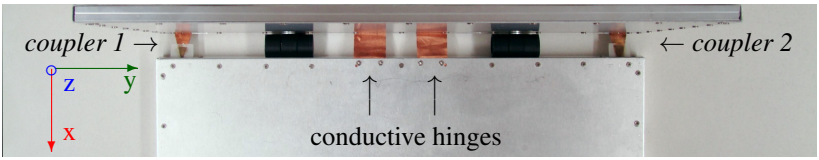

(b) top view

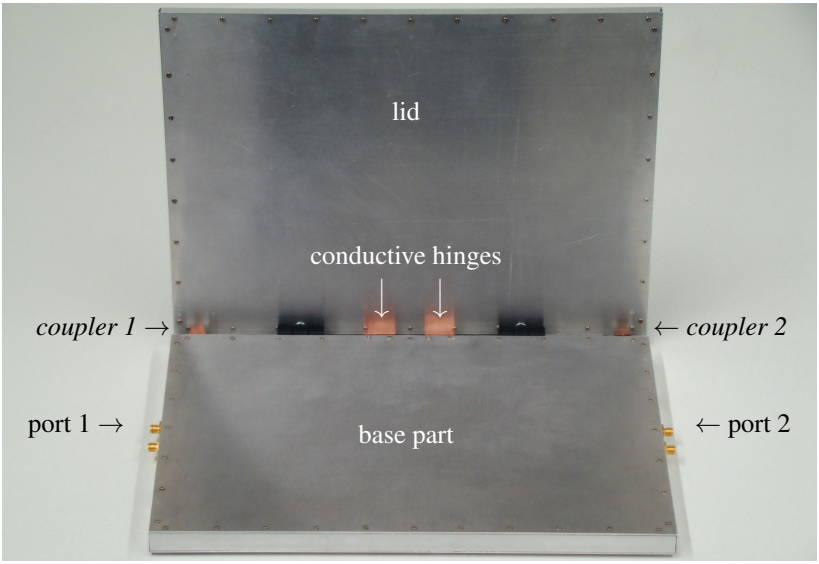

(c) front view

Fig. 6.22.: 2-port MIMO antenna prototype for LTE-enabled 13” monocoque laptop covering LTE low-band and LTE mid-band [107].

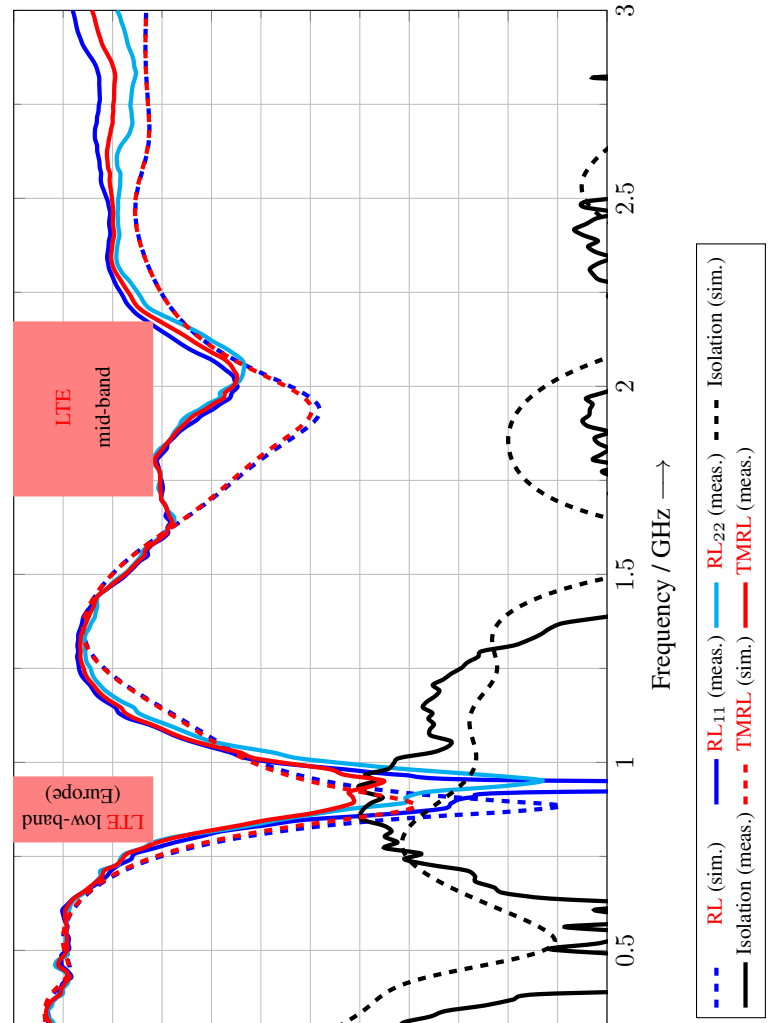

Fig. 6.23.: Simulated (dashed lines) and measured (solid lines) per port return loss and isolation of the 2-port antenna for LTE low-band (Europe) and mid-band antenna for 13" monocoque laptop after Fig. 6.22 [107].

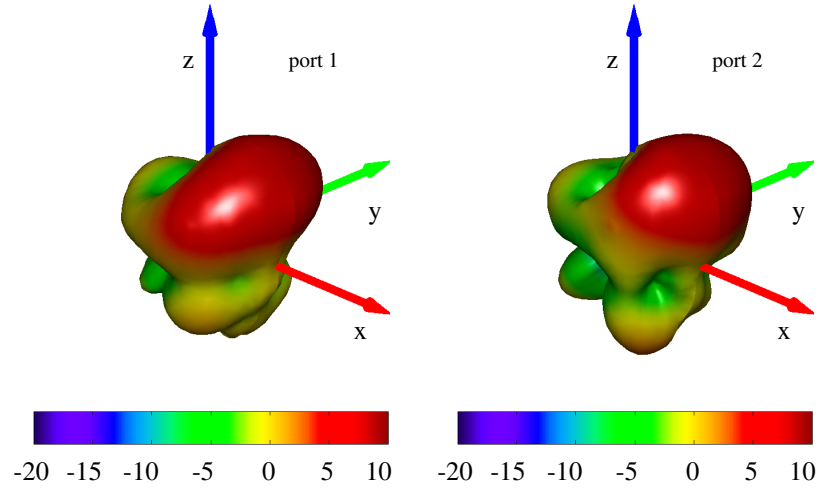

Fig. 6.24.: Total gain (both polarizations) for the port 1 (left) and port 2 (right) of the 2-port MIMO antenna for monocoque laptop prototype after Fig. 6.22 at 900 MHz. Gain values are given in dBi.

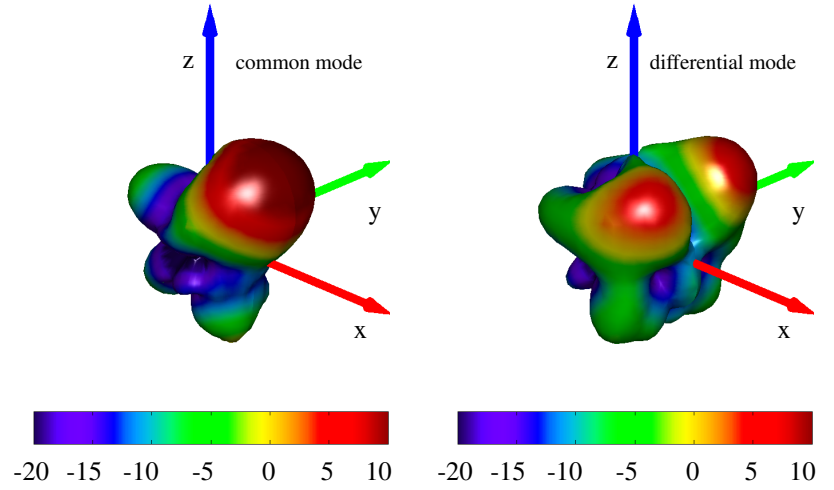

Fig. 6.25.: Total gain (both polarizations) for the *common mode* (left) and *differential mode* (right) of the 2-port MIMO antenna for monocoque laptop prototype after Fig. 6.22 at 900 MHz. Gain values are given in dBi.

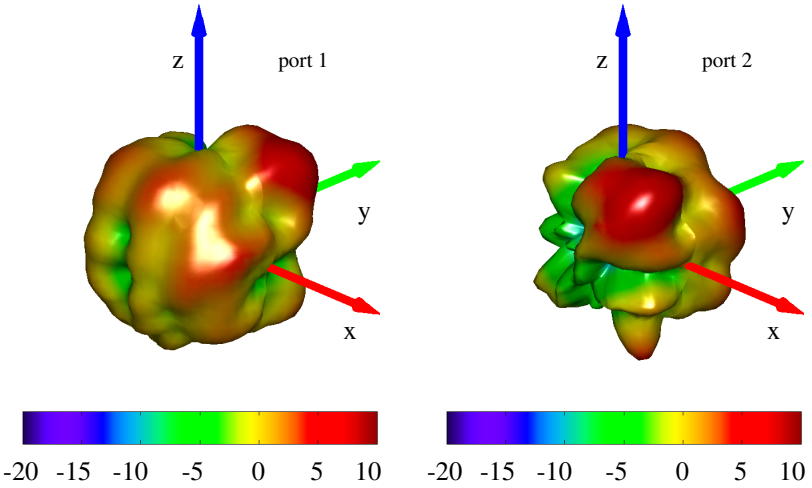

Fig. 6.26.: Total gain (both polarizations) for the port 1 (left) and port 2 (right) of the 2-port MIMO antenna for monocoque laptop after Fig. 6.22 at 2000 MHz. Gain values are given in dBi.

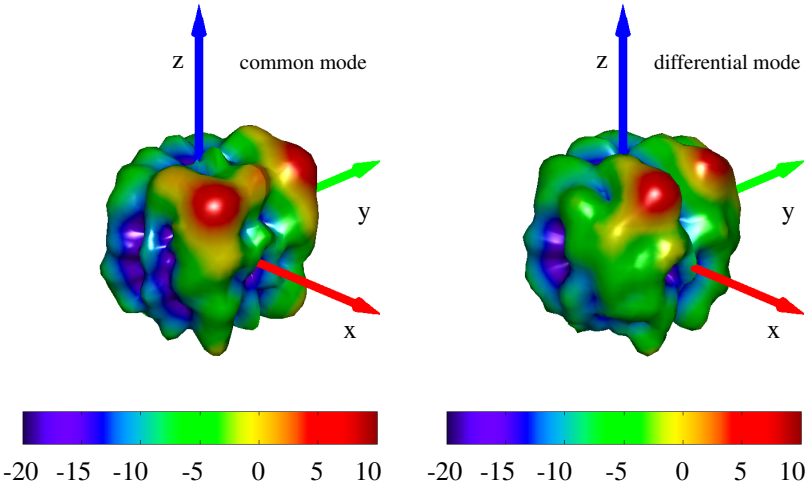

Fig. 6.27.: Total gain (both polarizations) for the *common mode* (left) and *differential mode* (right) of the 2-port MIMO antenna for monocoque laptop after Fig. 6.22 at 2000 MHz. Gain values are given in dBi.

Chapter 7

Conclusions

Mobile wireless communication systems have undergone a tremendous development in the past decade. One of the major advancements is the widespread use of MIMO transmission schemes beginning with the introduction of the 3rd Generation Partnership Project (3GPP) standard LTE and being extended in LTE Advanced. So as to support MIMO transmission schemes mobile terminals must be equipped with multiport antenna systems. The term refers to an arrangement of two or more antenna elements operating in the same frequency range and mounted on the same mobile wireless platform. Reduced volume per antenna element and strong interaction between all antenna elements are major design challenges and require for new systematic design approaches beyond classical single antenna design. The ongoing miniaturization of mobile terminals, the extension of the mobile spectrum and in particular the opening of new mobile communication bands at the lower end of the spectrum exacerbate these challenges. Design and characterization of multiport antennas have therefore become subject of high interest and of numerous research projects in both academia and industry.

This dissertation contributes to the development of systematic design procedures for multiport antennas with emphasis on accounting for the restrictions and side conditions which apply when designing multiport antennas for actual consumer equipment. The dissertation has developed along an industry funded research project, with a focus on electrically small devices where antenna design is constantly faced with fundamental physical limits.

Chapter 1 gives an overview of the state of the art in antenna characterization and design techniques applicable to multiport antennas for MIMO.

Chapter 2 introduces into the analysis of multiport antennas in terms of their *radiation modes*. *Modal analysis*, based on spectrum of the *radiation matrix*, allows for unambiguous characterization of a multiport antenna by means of invariant properties. Modal descriptive quantities are defined which are basic to the design approach followed in this dissertation.

Analyzing a multiport antenna with respect to its *radiation modes* is possible only after a design concept has been conceived. More fundamental from a design point of view is the question for the space of feasible radiation modes and their realization under the constraint of a given chassis form factor. Chapter 3 addresses this question based on the *theory of characteristic modes* for conducting bodies. The relevant properties of characteristic modes on the chassis of mobile terminals are reviewed. The excitation of characteristic modes by means of capacitive and inductive coupling elements is investigated in detail. Finally, a systematic design approach for multiport antennas is presented in which the antenna's *radiation modes* are constructively derived from the usable characteristic chassis modes.

Chapter 4 deals with design of matching networks for N-port antennas. Starting from the general expression for the scattering matrix of an ideal $2N$-port matching network different topologies and alternative implementations are discussed. As a solution of particular interest in cases where some *radiation modes* feature insufficient bandwidths, special attention is given to systematic design of MDN which maps *radiation modes* to external ports of the antenna system.

Chapter 5 focuses on the particular problems encountered in the design of antenna systems for extremely small mobile wireless terminals. After a review of applicable fundamental limits bandwidth estimation and approaches to maintain a decent total efficiency are discussed. The combination of electrical switching in the antenna structure with electrical tuning in an external matching network is suggested in this context. The DL-MIMO concept is introduced as a system level measure to cope with insufficient bandwidth. The different aspects are exemplified with the design of a 2-port MIMO antenna for a USB dongle.

Chapter 6 describes in detail design, fabrication and measurement of four antenna prototypes. The validity of the design approach described in the previous chapters is confirmed.

In conclusion, a systematic design approach, which combines the theory of characteristic chassis modes for conducting bodies with modal analysis of a multiport antenna, i.e. considers the spectrum of its *radiation matrix* is presented. The approach is successfully applied to a number of practically relevant design problems. The design technique permits identification of near optimum antenna solutions which approach the fundamental limits of attainable bandwidth and total efficiency.

Kapitel 8

Zusammenfassung

Die Mobilkommunikation hat in den letzten Jahren eine enorme Entwicklung durchlaufen. Eine der wesentlichen technischen Weiterentwicklungen ist der Übergang zu MIMO Übertragungsverfahren, in großem Maßstab beginnend mit der Einführung des 3GPP Standards LTE und in größerem Umfang noch im zukünftigen LTE-Advanced. Mobile Endgeräte müssen dazu mit Mehrtorantennen ausgestattet sein. Der Begriff *Mehrtorantenne* bezeichnet eine Anordnung von zwei oder mehr Antennenelementen, die im gleichen Fequenzbereich betrieben werden und auf einer gemeinsamen Plattform angeordnet sind. Die Verringerung des je Antennenelement zur Verfügung stehenden Volumens und die starke Kopplung zwischen den Antennenelementen führen auf neue Herausforderungen für den Entwurf. Neue, systematische Entwurfsmethoden jenseits der klassischen Methoden für den Entwurf von Einzelantennen sind gefordert. Die fortschreitende Miniaturisierung mobiler Endgeräte, die Erweiterung des für den Mobilfunk genutzten Spektrums und insbesondere die Öffnung neuer Bander am unteren Ende des Spektrums für den Mobilfunk verschärfen die Anforderung an die Entwurfsmethodik. Entwurf und Charakterisierung von Mehrtorantennen sind deswegen heute Themen von großem Interesse und Gegenstand zahlreicher industrieller und akademischer Forschungsprojekte.

Die vorliegende Dissertation liefert einen Beitrag zur Entwicklung systematischer Entwurfsverfahren für Mehrtorantennen unter besonderer Berücksichtigung der Einschränkungen und Randbedingungen die beim Entwurf von kommerziellen Endgeräten vorliegen. Zahlreiche Fragestellungen ergaben sich aus einem vom Verfasser bearbeiteten industriellen Forschungs-

und Entwicklungsprojekt mit Schwerpunkt auf elektrisch kleinen Endgeräten, bei denen der Entwurf stets mit fundamentalen physikalischen Schranken konfrontiert ist.

Kapitel 1 gibt einen Überblick über den Stand der Technik auf dem Gebiet des Entwurfs und der Charakterisierung von Mehrtorantennen für MIMO Anwendungen.

Kapitel 2 führt in die Analyse von Mehrtorantennen mit Hilfe ihrer Strahlungsmoden ein. Die modale Betrachtung auf Grundlage des Spektrums der Strahlungsmatrix gestattet es, Mehtorantennen mit Hilfe ihrer invarianten Eigenschaften eindeutig zu charakterisieren. Es werden die modalen Beschreibungsgrößen definiert auf denen der in dieser Arbeit verfolgte Entwurfsansatz basiert.

Die Strahlungsmoden einer Mehtorantenne können jedoch erst betrachtet werden, wenn ein Entwurf bereits vorliegt. Die vom Standpunkt der Entwurfsmethodik wichtigere Frage ist die nach Raum der unter den Einschränkungen eines gegebenen Geräte-Formfaktors realisierbaren Strahlungsmoden. Sie wird in Kapitel 3 auf Grundlage der Theorie Charakteristischer Moden leitender Körper behandelt. Die relevanten Eigenschaften charakteristischer Moden auf dem Gehäuse elektrisch kleiner mobiler Endgeräte werden betrachtet. Die Anregung charakteristischer Moden mit Hilfe von kapazitiven und induktiven Koppelelementen wird ausführlich untersucht. Abschließend wird ein Entwurfsansatz für Mehtorantennen beschrieben, in welchem die Strahlungsmoden der Antenne konstruktiv aus den nutzbaren charakteristischen Moden des Gehäuses abgeleitet werden.

In Kapitel 4 werden Anpassnetzwerke für N-Tor Antennen behandelt. Ausgehend von der allgemeinen Formulierung für die Streumatrix des benötigten $2N$-Tor Netzwerkes werden verschiedene Topologien und Realisierungsalternativen diskutiert. Gesondert betrachtet werden noch einmal MDNs, welche die Strahlungsmoden einer Mehtorantenne unmittelbar auf die Speisetore abbilden, da sie in Falle unzureichender modaler Bandbreiten, von besonderem Interesse sind.

Kapitel 5 fokussiert auf die besonderen Probleme bei beim Entwurf extrem kleiner Antennensysteme. Nach Betrachtung in die maßgeblichen physikalischen Beschränkungen werden die Abschätzung erreichbarer Bandbreiten und Maßnahmen zur Sicherstellung eines akzeptablen Wirkungsgrades diskutiert. Vorgeschlagen wird in diesem Zusammenhang die Kombination von elektrisch rekonfigurierbaren Antennenstrukturen mit elektrisch abstimmbaren Anpass-

netzwerken. Die verschiedenen Aspekte werden am Beispiel des Entwurfs eines 2-Tor MIMO Antennensystems für einen USB Dongle erläutert.

Kapitel 6 beschreibt im Detail den Entwurf, die Herstellung und die messtechnische Charakterisierung vier unterschiedlicher Prototypen von Mehrtorantennen. Anhand der Beispiele wird der in den vorherigen Kapiteln entwickelte Entwurfsansatz validiert.

Insgesamt wird mit dieser Arbeit ein systematischer Entwurfsansatz vorgeschlagen, der auf der Kombination der Theorie charakteristische Moden leitender Körper mit der modalen Analyse von Mehrtorantennen, d.h. der Betrachtung des Spektrums der Strahlungsmatrix aufbaut. Der Ansatz wird erfolgreich auf eine Reihe praktisch relevanter Entwurfsaufgaben angewandt. Er führt auf ein systematisches Entwurfsverfahren, das es gestattet, Lösungen in der Nähe der physikalischen Grenzen für die erreichbare Bandbreite und den Wirkungsgrad aufzufinden.

Appendix A

Bandwidth and radiation quality factor

Voltage Standing Wave Ratio (VSWR) bandwidth

With regards to Fig A.1 the input impedance of the arrangement comprising the antenna and the matching network is

$$Z_{\mathrm{in}}(\omega) = R_{\mathrm{A}}(\omega) + \mathrm{j}\left(X_{\mathrm{A}}(\omega) + X_{\mathrm{M}}(\omega)\right) = R_{\mathrm{A}}(\omega) + \mathrm{j}\, X_{\mathrm{in}}(\omega), \qquad \text{(A.1)}$$

where $X_{\mathrm{A}}(\omega)$ and $X_{\mathrm{M}}(\omega)$ are the reactance of the antenna and that of the matching impedance, respectively. $R_{\mathrm{A}}(\omega)$ denotes the radiation resistance of the antenna. The series reactance used to compensate antenna reactance $X_{\mathrm{A}}(\omega_0)$) after Fig. A.1 is

$$X_{\mathrm{M}}(\omega) = \begin{cases} \omega L_{\mathrm{M}} & \text{for} \quad X_{\mathrm{A}}(\omega_0) < 0 \\ -\frac{1}{\omega C_{\mathrm{M}}} & \text{for} \quad X_{\mathrm{A}}(\omega_0) > 0 \end{cases} \qquad \text{(A.2)}$$

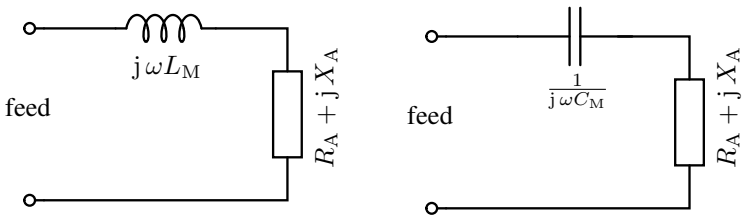

Fig. A.1.: Equivalent circuit models representing matching problem of an antenna. The antenna impedance $Z_\mathrm{A} = R_\mathrm{A} + \mathrm{j}\,X_\mathrm{A}$ has an equivalent circuit model of a series RLC.

At resonance ($\omega = \omega_0$) the input reactance is zero. The frequency derivative of the input reactance can be written in terms of the antenna reactance as

$$\frac{\mathrm{d}X_\mathrm{in}(\omega)}{\mathrm{d}\omega} = \frac{\mathrm{d}X_\mathrm{A}(\omega)}{\mathrm{d}\omega} + \frac{|X_\mathrm{A}(\omega)|}{\omega}. \tag{A.3}$$

The second term on the rhs takes into account the presence of the matching network [71]. The magnitude squared of the reflection coefficient for load impedance $Z_\mathrm{L} = R_\mathrm{A}(\omega_0)$ is

$$|\Gamma(\omega)|^2 = \frac{X_\mathrm{in}^2(\omega) + \big(R_\mathrm{A}(\omega) - R_\mathrm{A}(\omega_0)\big)^2}{X_\mathrm{in}^2(\omega) + \big(R_\mathrm{A}(\omega) + R_\mathrm{A}(\omega_0)\big)^2}. \tag{A.4}$$

It is convenient to define a real parameter

$$\beta = \frac{|\Gamma_\mathrm{max}|^2}{1 - |\Gamma_\mathrm{max}|^2} = \frac{(s-1)^2}{4s}, \tag{A.5}$$

where $|\Gamma_\mathrm{max}|$ is the maximum permissible magnitude of the reflection coefficient at the band edges and s denotes the corresponding VSWR. This allows to rewrite (A.4) in the form

$$X_\mathrm{in}^2(\omega_\pm) + \big(R_\mathrm{A}(\omega_\pm) - R_\mathrm{A}(\omega_0)\big)^2 = 4\beta R_\mathrm{A}(\omega_0) R_\mathrm{A}(\omega_\pm). \tag{A.6}$$

Taylor series expansion of the lhs of (A.6) about the resonance, i.e. $\omega = \omega_0$, under the assumption that the higher order terms are negligible ($O(\Delta\omega_\pm)^3$) leads to

$$\left|\frac{\mathrm{d}Z_\mathrm{in}(\omega)}{\mathrm{d}\omega}\right|_{\omega_0}^2 (\Delta\omega_\pm)^2 \approx 4\beta R_\mathrm{A}^2(\omega_0). \tag{A.7}$$

The approximation is valid if the variation of antenna radiation resistance is small about the resonance frequency, i.e. $R_{\mathrm{A}}(\omega_0) \approx R_{\mathrm{A}}(\omega_\pm)$. The fractional bandwidth is then

$$b(\omega_0) = \frac{\omega_+ - \omega_-}{\omega_0} = \frac{2\Delta\omega_\pm}{\omega_0} \approx \frac{4\sqrt{\beta}R_{\mathrm{A}}(\omega_0)}{\omega_0 \left|\frac{\mathrm{d}Z_{\mathrm{in}}(\omega)}{\mathrm{d}\omega}\right|_{\omega_0}}. \tag{A.8}$$

Radiation quality factor evaluation using Maxwell's equations

Starting from the definition of the radiation quality factor and using Maxwell's equations, their derivatives and with $P_{\mathrm{rad}} = \frac{1}{2}R_{\mathrm{A}}\left|I_{\mathrm{in}}\right|^2$ it was shown in [71] that

$$Q(\omega_0) = \frac{2\omega \max\left(\langle W_{\mathrm{M}}\rangle, \langle W_{\mathrm{E}}\rangle\right)}{P_{\mathrm{rad}}} = \frac{\omega_0}{2R_{\mathrm{A}}(\omega_0)}\left(\left.\frac{\mathrm{d}X_{\mathrm{in}}(\omega)}{\mathrm{d}\omega}\right|_{\omega_0} - \frac{4}{I_{\mathrm{in}}^2}W_{\mathrm{D}}(\omega_0)\right) \tag{A.9}$$

The second term in the parentheses on the rhs of (A.9) contains dispersive energy contribution W_{D} to the Q-factor. This term is missing in the derivation shown by Geyi [74] which was criticized by Andersen in [139]. Fante [140] argued that the term is negligible for some types of antennas, e.g. linear radiators with symmetric current distribution and electrically small antennas. The omission of the term was fixed by Yaghjian [71] by considering both series and shunt RLC equivalent circuit models of the antenna. The approach leads to the equation

$$\left.\frac{\mathrm{d}X_{\mathrm{in}}(\omega)}{\mathrm{d}\omega}\right|_{\omega_0} - \frac{4}{I_{\mathrm{in}}^2}W_{\mathrm{D}}(\omega_0) = \sqrt{\left(\left.\frac{\mathrm{d}X_{\mathrm{in}}(\omega)}{\mathrm{d}\omega}\right|_{\omega_0}\right)^2 + \left(\left.\frac{\mathrm{d}R_{\mathrm{A}}(\omega)}{\mathrm{d}\omega}\right|_{\omega_0}\right)^2}. \tag{A.10}$$

Thus, the radiation quality factor is given by

$$Q(\omega_0) = \frac{\omega_0}{2R_{\mathrm{A}}(\omega_0)}\left|\frac{\mathrm{d}Z_{\mathrm{in}}(\omega)}{\mathrm{d}\omega}\right|_{\omega_0}. \tag{A.11}$$

The full expression on the radiation quality factor, given in [71], in terms of the radiation resistance of the antenna and its reactance has a form

$$Q(\omega_0) = \frac{\omega_0}{2R_\mathrm{A}(\omega_0)} \sqrt{\left(\left.\frac{\mathrm{d}R_\mathrm{A}(\omega)}{\mathrm{d}\omega}\right|_{\omega_0} \right)^2 + \left(\left.\frac{\mathrm{d}X_\mathrm{A}(\omega)}{\mathrm{d}\omega}\right|_{\omega_0} + \frac{|X_\mathrm{A}(\omega_0)|}{\omega_0} \right)^2}, \tag{A.12}$$

If the variation of antenna radiation resistance over frequency is small then the form [74]

$$Q(\omega_0) = \frac{\omega_0}{2R_\mathrm{A}(\omega_0)} \left| \left.\frac{\mathrm{d}X_\mathrm{A}(\omega)}{\mathrm{d}\omega}\right|_{\omega_0} + \frac{|X_\mathrm{A}(\omega_0)|}{\omega_0} \right|. \tag{A.13}$$

is recovered.

Relation between VSWR bandwidth and radiation quality factor

Comparison of (A.8) and (6.2.3) yields an approximate relation between the radiation quality factor and the bandwidth for a given $s = \mathrm{VSWR}$, viz.

$$Q(\omega_0) \approx \frac{2\sqrt{\beta}}{b(\omega_0)} = \frac{1}{b(\omega_0)} \frac{s-1}{\sqrt{s}}. \tag{A.14}$$

Simple-minded derivation of the above expression, assuming series RLC as the antenna ECM and further that the radiation resistance is constant with frequency, the loss resistance is negligible, was given in [141]. The normalized to radiation resistance impedance is $z = 1 + \mathrm{j}\, Q\nu$, where $\nu = b = (\frac{\omega}{\omega_0} - \frac{\omega_0}{\omega})$. The maximum allowed magnitude of the reflection coefficient within the bandwidth b leads to a relation between $s = \mathrm{VSWR}$ and the product bQ

$$\left(\frac{s-1}{s+1}\right)^2 = |\Gamma_\mathrm{max}|^2 = \left|\frac{1+\mathrm{j}\, Qb - 1}{1+\mathrm{j}\, Qb + 1}\right|^2 = \frac{(Qb)^2}{4+(Qb)^2}. \tag{A.15}$$

Expressing equality by bringing bQ on the lhs of the expression yields the same result as (A.14), i.e.

$$bQ = \frac{s-1}{\sqrt{s}}. \tag{A.16}$$

Tab. A.1.: The coefficients α_n and β_n, for number of matching network stages n, used in (A.17).

n	α_n	β_n
1	1	1
2	2	1
...	...	...
∞	π	0

According to [71] the relation remains a good approximation for $Q > 4$. Frequently in engineering practice the fractional 7 dB bandwidth is of interest. For this level of RL the VSWR $= 2.63$ and subsequently $\sqrt{\beta} \approx 0.5$. The analytical expression which binds fractional bandwidth b_n for a certain number n of matching network stages and a particular level of the maximum reflectance $|\Gamma_{\max}|$ and radiation quality factor Q introduced by Bode and Fano in [142, 143] and later reevaluated in [127, 144] has a form

$$b_n Q = \frac{1}{\beta_n \sinh\left(\frac{1}{\alpha_n} \ln\left(\frac{1}{|\Gamma_{\max}|}\right)\right) + \frac{(1-\beta_n)}{\alpha_n} \ln\left(\frac{1}{|\Gamma_{\max}|}\right)}, \tag{A.17}$$

where α_n and β_n are real coefficients given in Tab. A.1 [144]. For $n = 1$ (A.17) corresponds well to (A.14) for $20 \log_{10} |\Gamma_{\max}| < -7$dB (see Fig. A.2). According to (A.17) increase of number of matching network stages to $n = 2$ increases $b_n Q$ product about 2.5 times for $20 \log_{10} |\Gamma_{\max}| \approx -7$dB in comparison to $n = 1$. Further increase of n does not significantly increase the bQ product. In practice, it is difficult to approach the limit for $b_\infty Q$. Several strategies to approach it using Chebychev matching network were outlined in [143]. The disadvantage of this solutions are that they require multiple elements including transformers which results in high losses. This is the reason why in engineering practice frequently only a simple L-type, T-type and π-type matching networks with minimum number of elements are used, especially when matching antennas for small mobile wireless devices. Use of these simple solutions is of significant practical importance when dealing with multi-port antennas where even the first few higher order radiation modes feature high modal radiation quality factors.

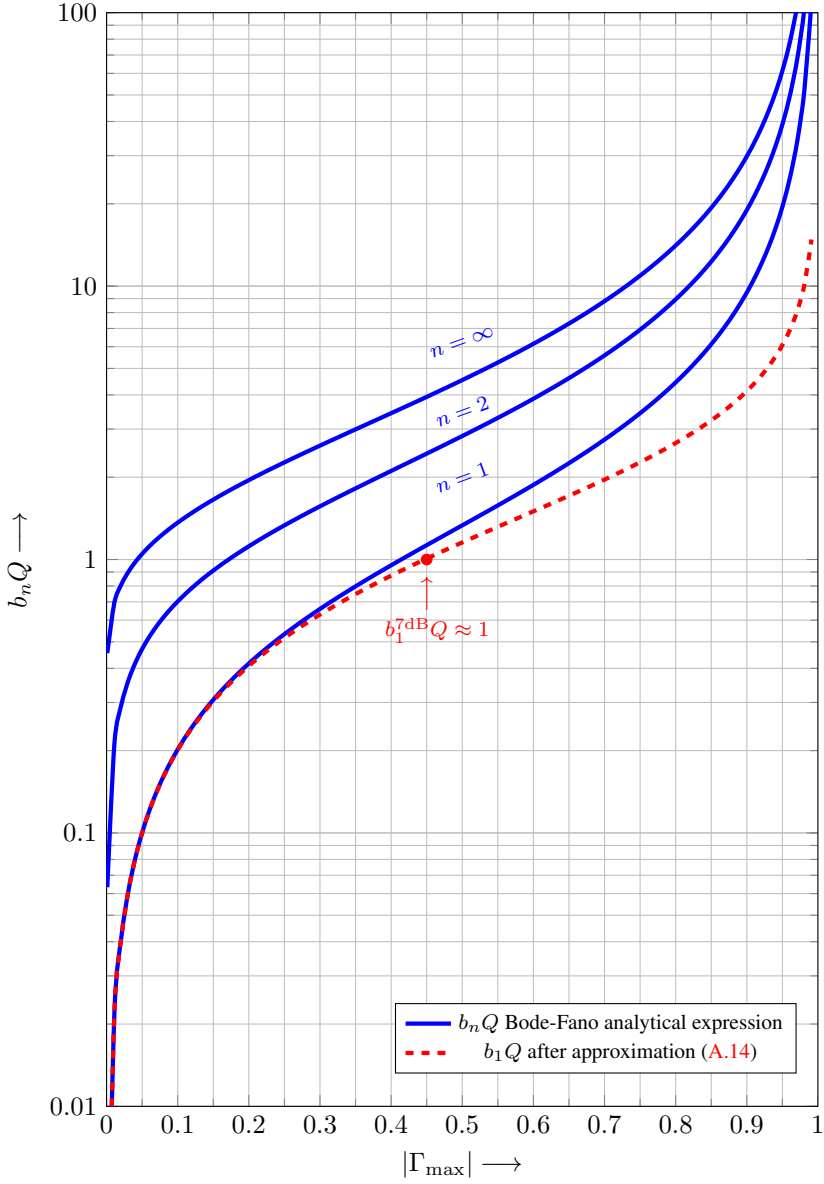

Fig. A.2.: b_nQ product after analytical expression given by Bode-Fano [142, 143] for different numbers of matching network stages n [127, 144] (solid blue) and b_nQ product after approximation (A.14) for comparison (dashed red).

Appendix B

Upper bound on radiation pattern overlap

In order to derive an upper bound on radiation pattern overlap consider an N-port antenna system and assume that only port m and port n are fed. All other ports are terminated with the reference impedance. This reduces the problem of finding an upper bound on pattern overlap for an N-port antenna to that of a 2-port antenna. The modal efficiencies η_m and η_n are bounded below by $\eta_{\min}$ and above by $\eta_{\max}$, respectively which are the minimum and maximum of the modal efficiencies of the N-port antenna system. The radiation matrix of the remaining 2-port antenna is of the form

$$\begin{pmatrix} R_{mm} & R_{mn} \\ R_{nm} & R_{nn} \end{pmatrix} = \begin{pmatrix} c & -s \\ s & c \end{pmatrix} \begin{pmatrix} \eta_{\max} & 0 \\ 0 & \eta_{\min} \end{pmatrix} \begin{pmatrix} c & -s \\ s & c \end{pmatrix}^{\dagger}, \tag{B.1}$$

where c and s are the elements of the unitary matrix $\mathbf{V}$ and hence satisfy $|c|^2 + |s|^2 = 1$ and $sc^* = s^*c$. The complex pattern overlap (2.14) can be expressed using (B.1) as

$$\rho_{mn} = \frac{\eta_{\max} s^* c - \eta_{\min} c^* s}{\sqrt{(\eta_{\max} |c|^2 + \eta_{\min} |s|^2)(\eta_{\max} |s|^2 + \eta_{\min} |c|^2)}}. \tag{B.2}$$

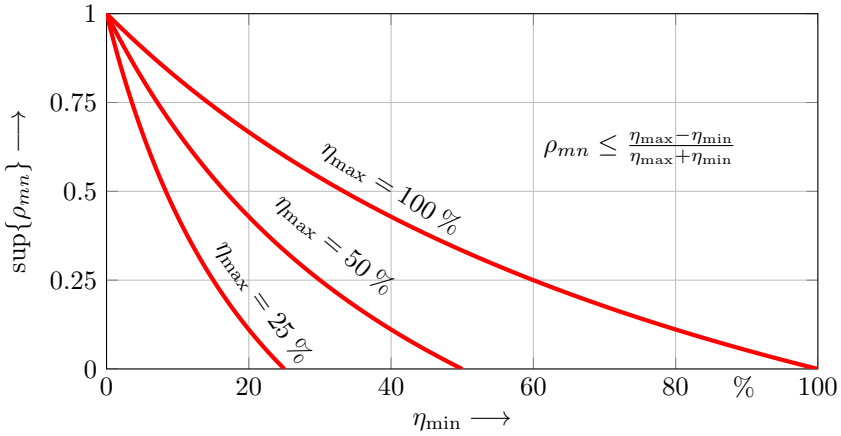

Fig. B.1.: Upper bound on radiation pattern overlap versus the minimum modal efficiency for an N-port antenna according to (B.4) for different values of the maximum modal efficiency.

Making use of $sc^* = s^*c$ in the nominator it is easy to simplify the above relation to

$$\rho_{mn} = \frac{(\eta_{\max} - \eta_{\min})c^* s}{\sqrt{|c|^2 |s|^2 (\eta_{\max}^2 + \eta_{\min}^2) + \eta_{\max}\eta_{\min}(|c|^4 + |s|^4)}}. \tag{B.3}$$

Since (B.3) is symmetric in $|c|$ and $|s|$ it can attain an extremum only for $|c| = |s|$. It is easily verified that ρ_{mn} attains its maximum for $|c| = |s| = \frac{1}{\sqrt{2}}$. By substitution of this value into (B.3) one obtains

$$|\rho_{mn}| \leq \frac{\eta_{\max} - \eta_{\min}}{\eta_{\max} + \eta_{\min}}. \tag{B.4}$$

(B.4) represents an upper bound on radiation pattern overlap for an arbitrary N-port antenna. The relation is depicted graphically for different values of $\eta_{\max}$ in Fig. B.1. Large values of $\eta_{\max}$ and $\eta_{\min}$ and small *modal efficiency imbalance* [61] or small condition number $\eta_{\max}/\eta_{\min}$ corresponds to a small bound on pattern overlap. With reference to (B.1) it is easy to see that (B.4) is a bound, but smaller values than ρ_{mn} can be obtained if $c = 1$ and $s = 0$ which corresponds to mapping *radiation modes* to external ports.

If $\eta_{\max}$ is unknown the upper bound (B.4) can be replaced by the coarser bound

$$|\rho_{mn}| \leq \frac{1-\eta_{\min}}{1+\eta_{\min}}. \tag{B.5}$$

The upper bounds on pattern overlap after (B.4) and (B.5) are tighter than an earlier expression given in [80], viz.

$$|\rho_{mn}| \leq \frac{1-\eta_{\min}^{\text{port}}}{\eta_{\min}^{\text{port}}}, \tag{B.6}$$

where $\eta_{\min}^{\text{port}}$ is the minimum *per port efficiency*. This is due to $\eta_{\min} \leq \eta_{\min}^{\text{port}}$ and the coarse estimate of the denominator in the (B.6).

In case of a lossless N-port antenna *modal efficiencies* can be expressed in terms of modal reflectances as

$$\eta_{\min} = 1 - |\Gamma_{\max}|^2, \quad \eta_{\max} = 1 - |\Gamma_{\min}|^2 \tag{B.7}$$

which together with (B.5) leads to

$$|\rho_{mn}| \leq \frac{|\Gamma_{\max}|^2 - |\Gamma_{\min}|^2}{2 - |\Gamma_{\max}|^2 - |\Gamma_{\min}|^2}. \tag{B.8}$$

Note, that the relative increase of the nominator is smaller than that of the denominator if $|\Gamma_{\min}|$ is replaced by zero. For unknown $|\Gamma_{\min}|$ one can, therefore, take recourse to the coarser estimate

$$|\rho_{mn}| \leq \frac{|\Gamma_{\max}|^2}{2 - |\Gamma_{\max}|^2}. \tag{B.9}$$

For $|\Gamma_{\max}| \ll 1$ the bound given by (B.9) can be approximated by neglecting the term $|\Gamma_{\max}|^2$ in the denominator of (B.9). The overlap is always small if a lossless antenna is sufficiently well matched.

Appendix C

Implementation of characteristic mode analysis

For calculation of characteristic modes EMCoS Antenna VirtualLab [145] and MATLAB [146] were used. Fig. C.1 shows a simplified schematic of the interaction between EMCoS software and routines programmed in MATLAB. The routines written in MATLAB allow for data exchange between different functions and modules of the program. EMCoS allows to easily create a new CAD simulation model or import one and edit it according to the requirements. Moreover, the system matrix $\widehat{\mathbf{Z}}$ of an arbitrary structure is directly available from EMCoS. EMCoS also allows the results to be interactively displayed. The main advantage of this program is its transparency and convenient data exchange based on human-readable ASCII files. Further, it permits for a simple integration with custom written code. The input data for the implemented routines in MATLAB comprises: CAD model of the structure, frequency range of analysis, and angular resolution of the radiation pattern. The output data from EIG module is inserted into a single file which contains *raw eigencurrents* (i.e. current coefficients) and *eigenvalues* which can be directly normalized using (3.13). The output of the RWG module is a set of multiple

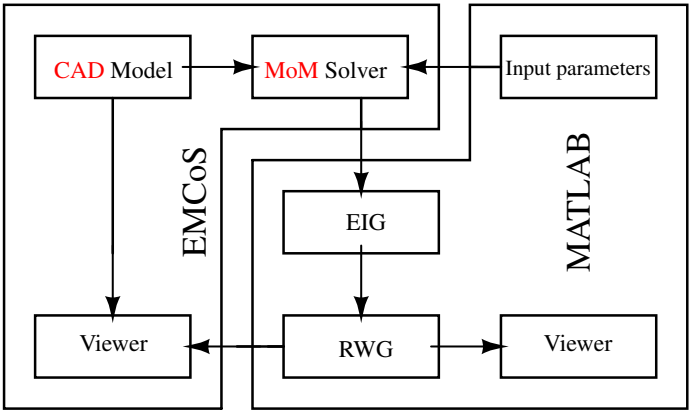

Fig. C.1.: Simplified schematic representation of the program implemented for calculating characteristic modes of a conducting body.

files for each characteristic mode and frequency which contains *surface current density*, *charge density* and *electric field* of both the near-field (optional) and far-field in EMCoS-specific ASCII file format.

The sequence of operation of the program is given in Fig. C.1. Once the input data is delivered the first function of the program invokes EMCoS 3D MoM solver in order to obtain the system matrix $\widehat{\mathbf{Z}} = \widehat{\mathbf{R}} + \mathrm{j}\,\widehat{\mathbf{X}}$. The second module (denoted by EIG, Fig. C.1) uses Linear Algebra PACKage (LAPACK), available in MATLAB as a set of high level functions, to perform generalized eigenvalue decomposition, given by relation (3.12)

$$\widehat{\mathbf{X}}\boldsymbol{I}_p = \lambda_p \widehat{\mathbf{R}}\boldsymbol{I}_p, \tag{C.1}$$

where $\boldsymbol{I}_p$ is the pth eigenvector comprising real coefficients and λ_p is its eigenvalue. Eigenvalues are sorted per frequency and therefore tracking [147] over frequency is required. It is accomplished by calculating overlap matrix $\mathbf{K}$ as in [148]. The elements of the overlap matrix $\mathbf{K}$ are the inner products between two vectors of the current coefficients $\boldsymbol{I}_p$ and $\boldsymbol{I}_\ell$ taken at frequency f_1 and f_2, respectively

$$K_{p,\ell}(f_1, f_2) = \boldsymbol{I}_p{}^{\top}(f_2)\boldsymbol{I}_\ell(f_1). \tag{C.2}$$

For small frequency difference $\Delta f = f_2 - f_1$ between adjacent samples the overlap coefficient $K_{p,\ell}$ approaches one for two corresponding eigenvalues and

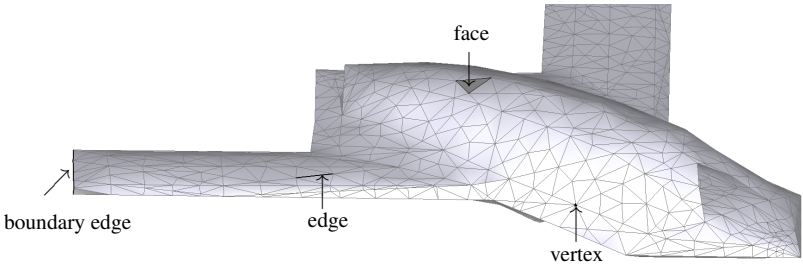

Fig. C.2.: Surface of the X45A modeled by triangular patches [152, 153].

zero otherwise. Therefore, by calculating the overlap matrix eigenvalues can be tracked over frequency. Sorted eigencurrents contain the coefficients of edge currents (i.e. current coefficients $\boldsymbol{I}_p = (I_{p,1}, ..., I_{p,n}, ..., I_{p,N})^\top$, where n refers to n-th edge of all N internal edges of the triangulated surface S of a conducting body) and therefore require transformation to the surface current density representation (currents on triangle) via RWG basis functions [149]. This is realized by the RWG module (Fig. C.1) of the program in which the vector basis functions given in [150] are implemented. Detailed description is given further in three subsequent subsections of the present appendix. The output is in form of human-readable ASCII file which can be read by either EMCoS or MATLAB using customized routines. Additional MATLAB routines are used to postprocess the data and e.g. to calculate electric field expansion coefficients given by (3.58).

Triangular patch modeling

Typically, in the MoM the surface S of a conducting body is approximated by a suitable set of faces, edges, vertices and boundary edges as shown in Fig. C.2 often using Delaunay triangulation [151]. Basis functions suitable for use with MoM and triangular patch modeling were given in [154]. Details related to the mathematical representation and properties of the triangular patch models can be found in [155, 156].

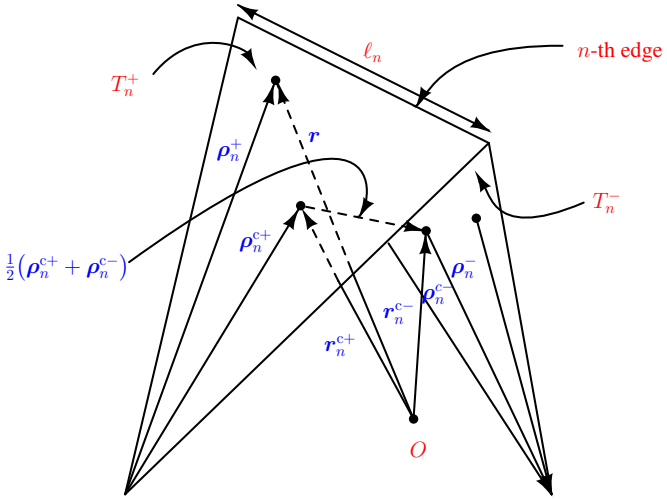

Fig. C.3.: Pair of adjacent triangles and geometrical quantities associated with the internal edge after [149].

RWG Basis Functions

The vector basis function associated with the n-th edge was given in [149]. Fig. C.3 shows an interior edge for which the basis functions was defined. It shows two triangles T_n^+ and T_n^-. The position of any point on the surface of the triangle T_n^+ can be referenced to either the observation point O (vector $\boldsymbol{r}$) or the free vertex (vector $\boldsymbol{\rho}_n^+$). Similar remarks also apply to triangle T_n^-, except that vector $\boldsymbol{\rho}_n^-$ has direction toward the free vertex. It is assumed that the direction of the current is from T_n^+ toward T_n^-. If the ℓ_n in the length of the edge and $A^\pm$ is the area of the triangle $T_n^\pm$ then the vector basis function after [149] is given by

$$\boldsymbol{f}_n(\boldsymbol{r}) = \begin{cases} \frac{\ell_n}{2A_n^+}\boldsymbol{\rho}_n^+, & \boldsymbol{r} \in T_n^+ \\ \frac{\ell_n}{2A_n^+}\boldsymbol{\rho}_n^-, & \boldsymbol{r} \in T_n^- \\ \mathbf{0}, & \text{otherwise.} \end{cases} \tag{C.3}$$

The basis function $\boldsymbol{f}_n(\boldsymbol{r})$ approximately represents the surface current density. The divergence over the surface S of the vector function $\boldsymbol{f}_n(\boldsymbol{r})$

$$\nabla_S \boldsymbol{f}_n(\boldsymbol{r}) = \begin{cases} \frac{\ell_n}{A_n^+}, & \boldsymbol{r} \in T_n^+ \\ -\frac{\ell_n}{A_n^-}, & \boldsymbol{r} \in T_n^- \\ \mathbf{o}, & \text{otherwise}, \end{cases} \tag{C.4}$$

is proportional to the surface charge density. The surface charge density is constant in each triangle. The total charge density of the pair of T_n^+ and T_n^- triangles is zero.

The current on surface S (here given with respect to k-th triangle) can be approximated using vector basis functions $\boldsymbol{f}_n(\boldsymbol{r})$ (C.3) as

$$\boldsymbol{J}_k = \sum_{n=1}^{N} I_n \boldsymbol{f}_n(\boldsymbol{r}), \quad \text{where} \quad \boldsymbol{r} \in T_k \tag{C.5}$$

where I_n is the current coefficient and N is the number of internal edges. The coefficient I_n is interpreted as the normal component of the current density flowing through the n-th edge. The dipole moment $\boldsymbol{m}$ of the m-th dipole is given by

$$\boldsymbol{m}_n = \ell_n I_n (\boldsymbol{r}_n^{\mathrm{c}+} - \boldsymbol{r}_n^{\mathrm{c}-}). \tag{C.6}$$

The magnitude of the current over the whole surface S is given by

$$I^2 = \sum_{n=1}^{N} (\ell_n I_n)^2, \tag{C.7}$$

where the summation takes place over all N internal edges of the surface S. For a dipole the magnitude of the current I^2 after (C.7) has simple physical interpretation since the surface current density $\boldsymbol{J}_\mathrm{s}$ has a single direction along the length of the dipole.

System Matrix

The element mn of the $N \times N$ system matrix is described by the vector potential $\boldsymbol{A}$ and the scalar potential Φ

$$Z_{nm} = \ell_n \left(\mathrm{j}\,\omega \left(\boldsymbol{A}^{+}_{nm} \frac{\boldsymbol{\rho}^{\mathrm{c}+}_{n}}{2} + \boldsymbol{A}^{-}_{nm} \frac{\boldsymbol{\rho}^{\mathrm{c}-}_{n}}{2} \right) + \Phi^{-}_{nm} - \Phi^{+}_{nm} \right) \tag{C.8}$$

The nm-th vector potential $\boldsymbol{A}$ and the nm-th element of the scalar potential Φ has a form

$$\boldsymbol{A}^{\pm}_{nm} = \mu \int_S \boldsymbol{f}_m(\boldsymbol{r}') \boldsymbol{g}^{\pm}_n(\boldsymbol{r}^{\mathrm{c}\pm}_n, \boldsymbol{r}')\,\mathrm{d}S' \tag{C.9}$$

and

$$\Phi^{\pm}_{nm} = -\frac{1}{\mathrm{j}\,\omega\epsilon} \int_S \nabla'_S \boldsymbol{f}_m(\boldsymbol{r}') \boldsymbol{g}^{\pm}_n(\boldsymbol{r}^{\mathrm{c}\pm}_n, \boldsymbol{r}')\,\mathrm{d}S', \tag{C.10}$$

respectively. ϵ denotes permittivity, μ is permability and k is the wavenumber. The Green's function has well-known form

$$\boldsymbol{g}^{\pm}_n(\boldsymbol{r}^{\mathrm{c}\pm}_n, \boldsymbol{r}') = \frac{\mathrm{e}^{-\mathrm{j}\,k\left|\boldsymbol{r}^{\mathrm{c}\pm}_n - \boldsymbol{r}'\right|}}{4\pi \left|\boldsymbol{r}^{\mathrm{c}\pm}_n - \boldsymbol{r}'\right|} \tag{C.11}$$

Electric and Magnetic Fields

The radiated magnetic and electric fields from n-th infinitesimally small dipole, featuring dipole moment $\boldsymbol{m}_n$ at the point $\boldsymbol{r}$ located at distance r from the observation point O are given by [149, 150]

$$\boldsymbol{H}_n(\boldsymbol{r}) = \frac{\mathrm{j}\,k}{4\pi} (\boldsymbol{m}_n \times \boldsymbol{r}) C \mathrm{e}^{-\mathrm{j}\,kr}, \quad \text{where} \quad C = \frac{1}{r^2}\left(1 + \frac{1}{\mathrm{j}\,kr}\right) \tag{C.12}$$

$$\boldsymbol{E}_n(\boldsymbol{r}) = \frac{\eta_0}{4\pi}\left(\boldsymbol{M} - \boldsymbol{m}_n \right)\left(\frac{\mathrm{j}\,k}{r} + C \right) + 2\boldsymbol{M}C \Big) \mathrm{e}^{-\mathrm{j}\,kr}, \text{ where } \boldsymbol{M} = \frac{(\boldsymbol{r}\boldsymbol{m}_n)\boldsymbol{r}}{r^2} \tag{C.13}$$

The distance from the observation point O to the center of the two triangles is $r = |\boldsymbol{r}|$. η_0 denotes impedance of the free space. It is important to understand

that both relations while allow to obtain electric and magnetic field at any point in space (not only in the far-field region) feature certain practical limitation. The length ℓ_n of the n-th edge located in the vicinity of the observation point O has to be smaller than the distance r.

The total electric and magnetic fields at the observation point O are the respective sums of contributions from N electric dipoles, where N is the number of internal edges, and are given by

$$\boldsymbol{E}(\boldsymbol{r}) = \sum_{n=1}^{N} \boldsymbol{E}_n \left(\boldsymbol{r} - \frac{1}{2}(\boldsymbol{r}_n^+ + \boldsymbol{r}_n^-) \right), \quad \boldsymbol{H}(\boldsymbol{r}) = \sum_{n=1}^{N} \boldsymbol{H}_n \left(\boldsymbol{r} - \frac{1}{2}(\boldsymbol{r}_n^+ + \boldsymbol{r}_n^-) \right). \tag{C.14}$$

Appendix D

Useful design equations

Lumped element realization of 180° hybrid

The bandwidth requirements for a fixed-impedance MDN for multiport symmetric antennas (see Chapter 4) dictate use of 180° hybrids which feature either narrow or wide bandwidth. A lumped element realization derived from transmission matrices (see the next subsection of the present appendix) of 180° hybrids was reported in [117]. The topology of the network and the values of the lumped elements are easy to obtain using simple design equations which were extracted from the analysis of a 180° hybrid using transmission ($ABCD$) matrix. Fig. D.1 shows the lumped element realization of a 180° hybrid which features fractional bandwidth of about $20\ \%$ about the center frequency. The values of inductors and capacitors are given by

$$L = \frac{Z}{\omega} \quad \text{and} \quad C = \frac{1}{\omega Z}, \tag{D.1}$$

respectively, where Z is the impedance of a hybrid given by $Z = Z_{\mathrm{L}}\sqrt{2}$ and $\omega = 2\pi f_0$ (with Z_{L} denoting load impedance and f_0 being the center frequency). The design equations for a broadband lumped element 180° hybrid (see Fig. D.2) are given by

$$L_1 = \frac{Z}{\omega\sqrt{2}}, \quad C_1 = \frac{\sqrt{2}-1}{\omega Z}, \quad L_2 = \frac{Z}{\omega(\sqrt{2}-1)}, \quad C_2 = \frac{\sqrt{2}}{\omega Z}, \tag{D.2}$$

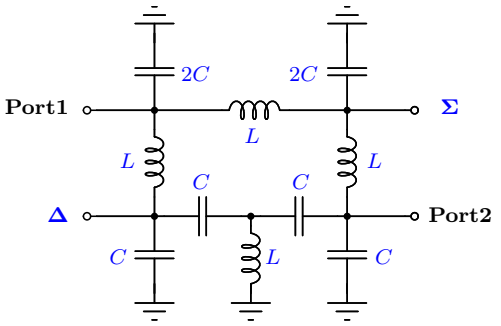

Fig. D.1.: Lumped element realization of 180° hybrid after [117].

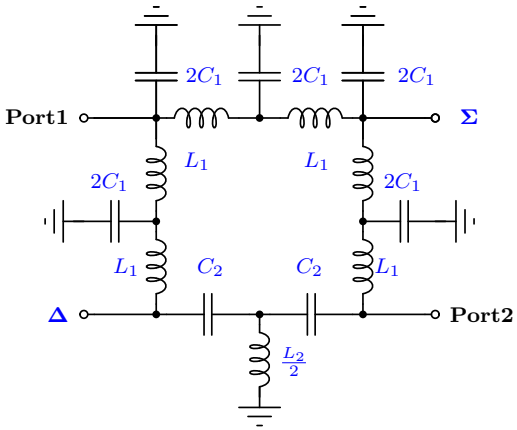

Fig. D.2.: Lumped element realization of 180° broadband hybrid after [117].

where $Z = Z_{\mathrm{L}}\sqrt{2}$. The fractional bandwidth of this 180° hybrid is about $70\ \%$.

The transmission matrix

In practice since many circuits used in e.g. matching of antennas are either 2-port or due to their symmetry can be decomposed to 2-port networks it is not only convenient but also useful to define transmission ($ABCD$) matrix. It allows to cascade 2-port network much easier than using S-parameters of Z-matrix representation of the network. The $ABCD$ matrix is defined in terms of voltages and currents using the matrix form

$$\begin{pmatrix} V_1 \\ I_1 \end{pmatrix} = \begin{pmatrix} A & B \\ C & D \end{pmatrix} \begin{pmatrix} V_2 \\ I_2 \end{pmatrix}, \tag{D.3}$$

where I_1 is incoming current at port 1 and I_2 is outgoing current from port 2. It can easily be proved that the $ABCD$ matrix of the cascade connection of the two networks is equal to the product of the $ABCD$ matrices representing the individual 2-port networks. Due to the fact that matrix multiplication is not commutative the networks must be arranged in the same order as the multiplication of $ABCD$ matrices. The scattering matrix $\mathbf{S}$ of a 2-port network is given in terms of $ABCD$ parameters as [157]

$$\mathbf{S} = \frac{1}{A+B/Z_0+CZ_0+D} \begin{pmatrix} A+B/Z_0-CZ_0-D & 2(AD-BC) \\ 2 & -A+B/Z_0-CZ_0+D \end{pmatrix}. \tag{D.4}$$

The impedance matrix $\mathbf{Z}$ is given in terms of $ABCD$ parameters as [157]

$$\mathbf{Z} = \frac{1}{C} \begin{pmatrix} A & AD-BC \\ 1 & D \end{pmatrix}. \tag{D.5}$$

The summary of $ABCD$ Parameters and S-parameters of the basic circuits, used in practice, is given in Tab. D.1. The importance of practical usefulness of the $ABCD$ matrix representation is in the fact that a library comprising the basic 2-port networks after Tab. D.1 is sufficient to built more complicated networks in a systematic fashion.

Tab. D.1.: S-parameters (the first column) and $ABCD$ parameters (the second column) of some 2-port circuits after [157].

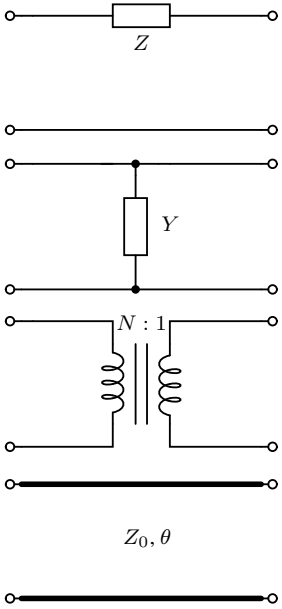

$$\begin{pmatrix} 1 & Z \\ 0 & 1 \end{pmatrix}, \qquad \frac{1}{2Z_\mathrm{L}+Z}\begin{pmatrix} Z & 2 \\ 2 & Z \end{pmatrix}$$

$$\begin{pmatrix} 1 & 0 \\ Y & 1 \end{pmatrix}, \qquad \frac{1}{2+YZ_\mathrm{L}}\begin{pmatrix} -YZ_\mathrm{L} & 2 \\ 2 & -YZ_\mathrm{L} \end{pmatrix}$$

$$\begin{pmatrix} N & 0 \\ 0 & \frac{1}{N} \end{pmatrix}, \qquad \frac{1}{N^2+1}\begin{pmatrix} N^2-1 & 2N \\ 2N & -N^2+1 \end{pmatrix}$$

$$\begin{pmatrix} \cos\theta & \mathrm{j}\,Z_0\sin\theta \\ \mathrm{j}\,Y_0\sin\theta & \cos\theta \end{pmatrix}, \qquad \mathbf{S}_\mathrm{TL} \text{ is given by}$$

$$\mathbf{S}_\mathrm{TL} = \frac{1}{2\cos\theta + \alpha\,\mathrm{j}\sin\theta}\begin{pmatrix} \beta\,\mathrm{j}\sin\theta & 2 \\ 2 & \beta\,\mathrm{j}\sin\theta \end{pmatrix},$$

where coefficients α and β have the form

$$\alpha = \frac{Z_0}{Z_\mathrm{L}} + \frac{Z_\mathrm{L}}{Z_0} \quad \text{and} \quad \beta = \frac{Z_0}{Z_\mathrm{L}} - \frac{Z_\mathrm{L}}{Z_0}$$

with Z_0 denoting the line impedance and Z_L being the load impedance.

Appendix E

Numerical evaluation of MDN tuning capabilities

The present appendix shows a numerical study of the tuning capabilities of the electrically tunable MDN [112] proposed in Chapter 5. For the purpose of the present analysis it was assumed that the element L_{12} is incorporated into the antenna physical structure in order to maximize the total efficiency of the *differential mode* (see Fig. E.1). Therefore, this element was not taken into account in the analysis of the MDN tuning capabilities. High quality factor 0603 wirewound inductors from Johansontechnology were chosen for the purpose of the present analysis. TCN1-10 from MiniCircuits was selected as a common mode choke.

Design details: *Common mode* matching network

The electrically tunable ΣMN has a π-type topology which consist of two shunt and a single series LC tank (see Fig. E.1). It is well known that this basic network topology brings about a coverage of nearly the entire Smith chart [133] within a useful frequency range. Three inductors L_1^c, L_2^c and L_1^c have fixed values while capacitors C_1^c, C_2^c and C_3^c are tunable. The *common mode* is used for the transmit mode of operation so that only highly linear tunable RF-MEMS

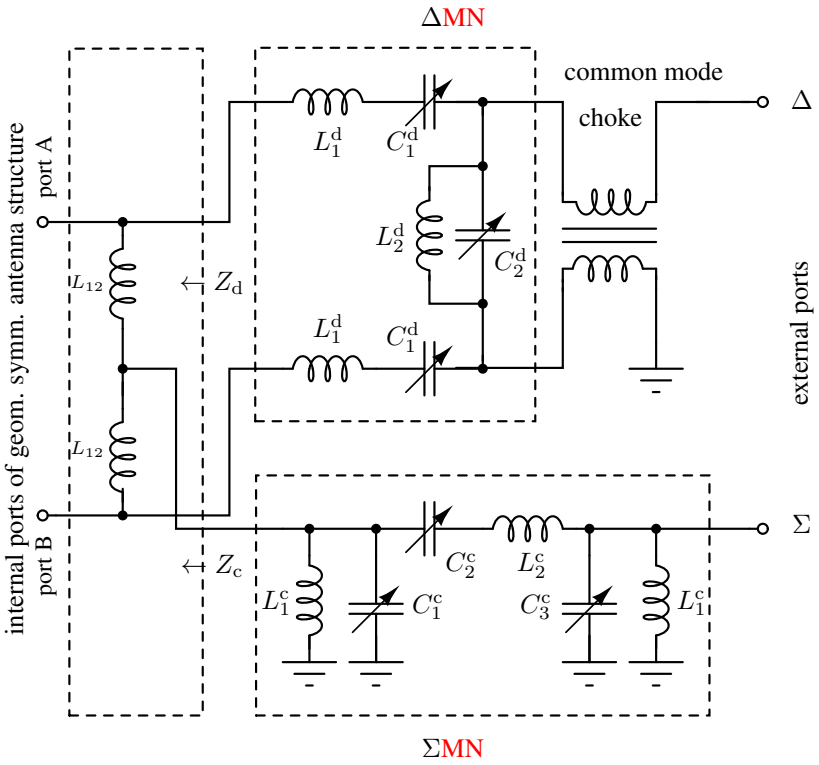

Fig. E.1.: Electrically tunable MDN for a symmetric 2-port DL-MIMO electrically small dipole antenna comprising separate ΣMN and ΔMN. MDN uses center-tapped inductance $2L_{12}$ as part of the antenna physical structure.

capacitors or Complementary Metal-Oxide-Semiconductor (CMOS) DTCs can be considered in a design.

Design details: *Differential mode* matching network

The tunable ΔMN comprises L-type matching network that consists of a series LC and a shunt LC tank (see Fig. E.1). In addition, in order to suppress the *common mode* in the *differential mode* branch a common mode choke has to be used. Isolation between external ports Σ and Δ depends on the Common Mode Rejection Ratio (CMRR) of the choke. The tuning range of the network is limited in comparison to ΣMN due to restriction to L-type topology. However, it is not a constraint as this network should only allow to match the *differential mode* within no more than few percent of its resonance frequency for a low-loss design. This is due to the fact tat coarse switching by means of switches in the antenna structure itself is assumed here. Moreover, due to a strong *common mode* signal present at the differential mode branch the capacitance C_1^{d} has to be realized by a highly linear component. C_2^{d} does not have to comply with this restriction. Nevertheless, in practice, it is convenient to utilize the same kind of components.

Finding the optimum values of fixed inductors and switching states of DTCs

The values of inductances $\boldsymbol{L} = \{L_1^{\mathrm{c}}, L_2^{\mathrm{c}}\}$ or $\boldsymbol{L} = \{L_1^{\mathrm{d}}, L_2^{\mathrm{d}}\}$ for the *common mode* and the *differential mode* matching network, respectively are not arbitrary. The minimum value is constrained by a size of an SMD element. Typically, they are above 1 nH for 0603 size components. The maximum value of inductors is limited by the SRF. This restricts possible values of 0603 size SMDs inductors to 20 nH since covering also LTE mid-band (from 1710 MHz to 2170 MHz), at least by ΣMN, is of high interest. The S-parameters of inductors from Johansontechnology with discrete values $\{1.8, ..., 18\}$ nH were used in the evaluation. In order to find the optimum values of inductors which maximize the efficiency of either *radiation mode* given by $|s_{21}|^2$ within given frequency range a sweep over all given discrete values was performed. The frequency range for ΣMN tuning capabilities evaluation extends from 700 MHz to 2200 MHz. For the ΔMN it was limited to the LTE low-band due to use of the TCN1-10 common mode choke.

Tab. E.1.: The optimum element values (given in pF and nH) of the tunable MDN after Fig. E.1.

element	L_1^{d}	L_2^{d}	L_1^{c}	L_2^{c}	C
value	5.8	3.9	6.8	5.8	from 0.7 to 4.6

The procedure for finding the optimum value of $\boldsymbol{L}$, denoted by $\boldsymbol{L}^{\mathrm{opt}}$ can be decomposed into an inner loop and an outer loop optimization problem. The least squared error type penalty function for the outer loop is given by

$$\boldsymbol{L}^{\mathrm{opt}} = \arg\max_{\{\boldsymbol{L}\}} \sum_m \sum_k \left| s_{21}(f_m, Z_k, \boldsymbol{C}_{m,k}^{\mathrm{opt}}(\boldsymbol{L}), \boldsymbol{L}) \right|^2, \tag{E.1}$$

where $\boldsymbol{C}_{m,k}^{\mathrm{opt}}(\boldsymbol{L})$ denotes the optimum value of $\boldsymbol{C}_{m,k}(\boldsymbol{L})$ for a given value of $\boldsymbol{L}$ at the m-th frequency of interest f_m and the k-th modal impedance Z_k. In order to determine the optimum tuning states of DTCs i.e. $\boldsymbol{C}_{m,k}^{\mathrm{opt}}$ in the inner loop in either matching network with a given value of $\boldsymbol{L}$ to match k-th modal impedance Z_k so as to maximize efficiency at frequency f_m we used the following least squared error type penalty function

$$\boldsymbol{C}_{m,k}^{\mathrm{opt}}(\boldsymbol{L}) = \arg\max_{\{\boldsymbol{C}\}} \left| s_{21}(f_m, Z_k, \boldsymbol{C}, \boldsymbol{L}) \right|^2, \tag{E.2}$$

where $\boldsymbol{C} = \{C_1^{\mathrm{c}}, C_2^{\mathrm{c}}, C_3^{\mathrm{c}}\}$ or $\boldsymbol{C} = \{C_1^{\mathrm{d}}, C_2^{\mathrm{d}}\}$ contains nominal capacitance values of DTCs which yield $\left|s_{21}\right|^2$ and $\boldsymbol{C}_{m,k}^{\mathrm{opt}}$ is the optimum solution. Switching states of DTCs are given by $(0.129 \cdot n + 0.6)$ pF, where $n = 0, ..., 31$. Optimization is performed for all K values i.e. over a complete set of complex modal impedances Z_k for $k = 1, ..., 360$ which are matched to maximize $\left|s_{21}\right|^2$ by changing DTC switching states. Note, that the values of $\boldsymbol{C}$ and $\left|s_{21}\right|^2$ for different impedances Z_k depend on different topologies of ΣMN and ΔMN and given value of $\boldsymbol{L}$ and frequency f_m. The results $\sum_m \sum_k \left|s_{21}\right|^2$ are stored as a function of $\boldsymbol{L}$. In the end the optimum value of $\boldsymbol{L}$ was found so as to maximize the area on the Smith chart which can be matched with total efficiency higher than $50\ \%$ at the lowest and the highest frequency of analysis. The values of inductors in both MNs are smaller than 10 nH. The nominal values of the SMD components are given in Table. E.1.

Results

Using optimization criterion given by (E.1) and (E.2) for the optimum values of inductors the maximum values of efficiency were found at the lowest and the highest frequencies of LTE low-band and LTE mid-band for the *common mode* matching network. The results are shown in Figs. E.2 and E.3. The tunable ΣMN provides match which results in efficiency higher than $50\ \%$ over most of the Smith chart area in the frequency range from $700\ \mathrm{MHz}$ to $2200\ \mathrm{MHz}$. The tuning capabilities of ΔMN are constrained to LTE low-band due to restricted bandwidth of the *common mode choke*. In terms of impedances which can be effectively matched the tuning range covers smaller than in case of the *common mode* but still useful region of the Smith chart as can be seen from Fig. E.4.

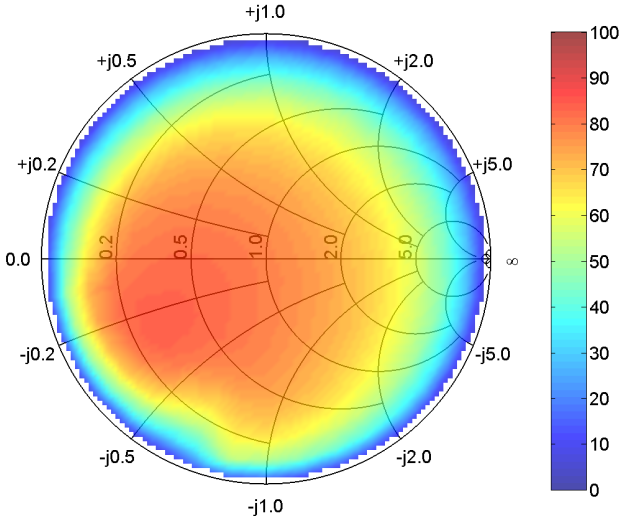

a) 704 MHz

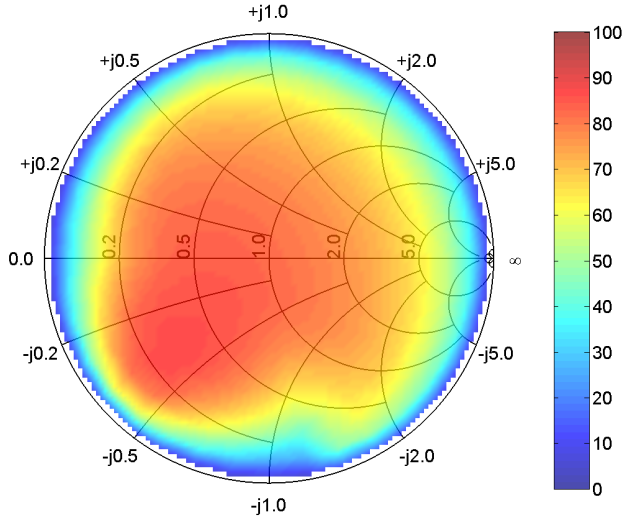

b) 960 MHz

Fig. E.2.: Matching capabilities of a lossy ΣMN at the lowest and the highest frequency of the LTE low-band. Different colors indicate different values of efficiency (assuming lossless antenna) which can be achieved for a different *common mode* impedance of an antenna.

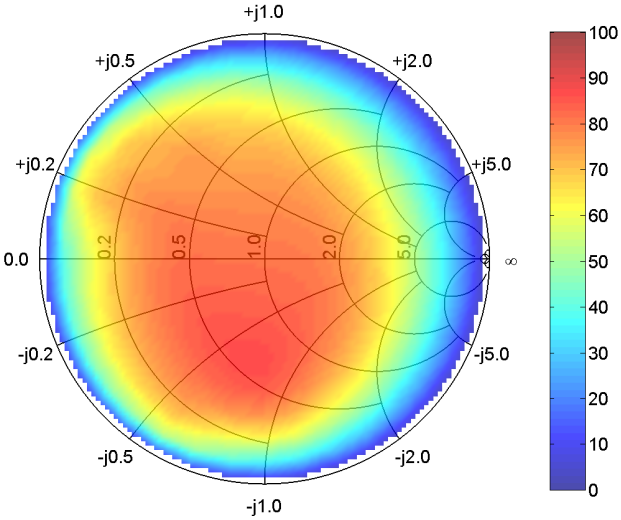

a) 1710 MHz

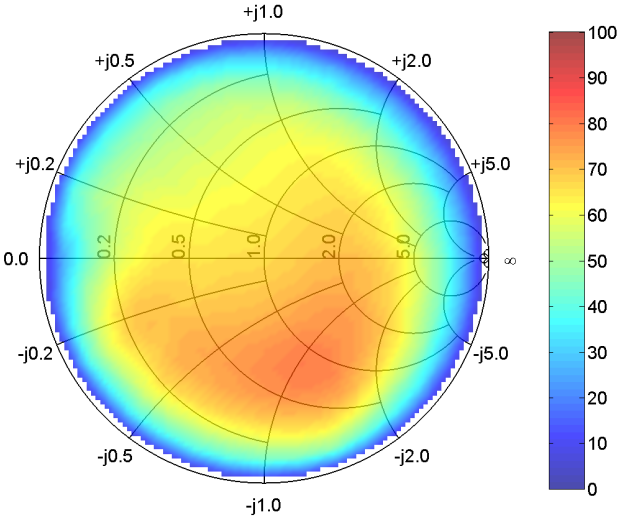

b) 2170 MHz

Fig. E.3.: Matching capabilities of a lossy ΣMN at the lowest and the highest frequency of the LTE mid-band. Different colors indicate different values of efficiency (assuming lossless antenna) which can be achieved for different *common mode* impedances of an antenna.

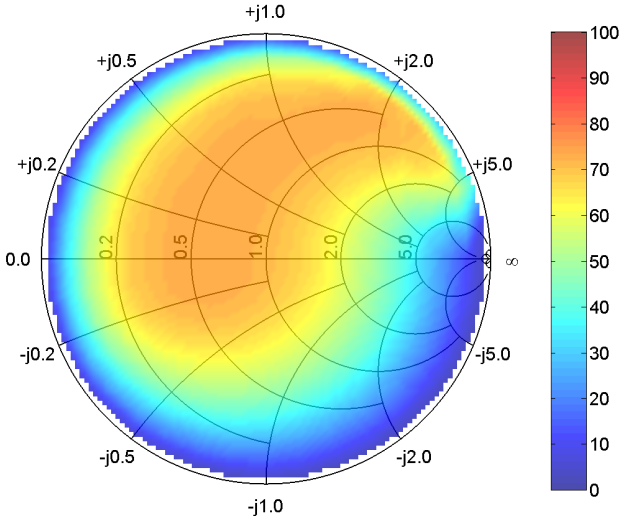

a) 741 MHz

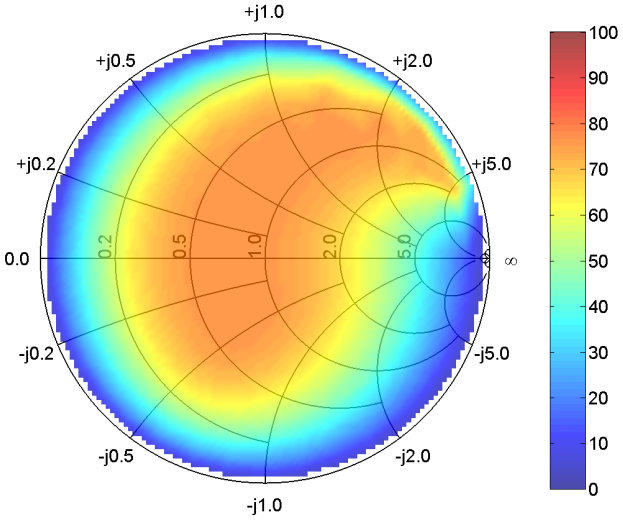

b) 945 MHz

Fig. E.4.: Matching capabilities of a lossy ΔMN. Different colors indicate different values of efficiency (assuming lossless antenna) which can be achieved for different *differential mode* impedances of an antenna.

Appendix F

Derivation of characteristic mode radiation quality factors based on EM field theory

For evaluation of quality factors it is necessary to calculate separately the time-average stored magnetic and electric energies given by $\langle W_{\mathrm{M}} \rangle$ and $\langle W_{\mathrm{E}} \rangle$, respectively. With reference to Fig. F.1 the complex Poynting theorem for a lossless source free region G is given by Harrington in [92]

$$\oiint_{\partial G} \frac{1}{2}(\boldsymbol{E} \times \boldsymbol{H}^*)\boldsymbol{n}\,\mathrm{d}S + 2\,\mathrm{j}\,\omega \iiint_{G} \left(\frac{\mu}{4}|\boldsymbol{H}|^2 - \frac{\epsilon}{4}|\boldsymbol{E}|^2\right)\mathrm{d}V = 0 \quad \text{(F.1)}$$

which with the help of $\langle W_{\mathrm{M}} \rangle = \frac{\mu}{4}\boldsymbol{H}\boldsymbol{H}^*$ and $\langle W_{\mathrm{E}} \rangle = \frac{\epsilon}{4}\boldsymbol{E}\boldsymbol{E}^*$ can be written in the form

$$\langle W_{\mathrm{M}} \rangle - \langle W_{\mathrm{E}} \rangle = \frac{-1}{2\,\mathrm{j}\,\omega} \oiint_{\partial G} \frac{1}{2}(\boldsymbol{E} \times \boldsymbol{H}^*)\boldsymbol{n}\,\mathrm{d}S. \quad \text{(F.2)}$$

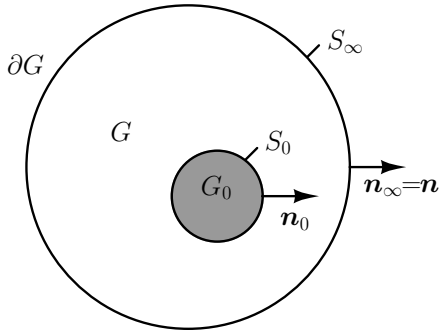

Fig. F.1.: A region G containing source free region G_0.

The region of interest is the free space around the radiating object. It is bounded by the surface S_0 of the object and S_∞, a sphere in the far field region.

In order to evaluate the individual terms on the lhs of (F.2) a second equation is needed. The required expression for the sum of the time averaged stored magnetic and electric energies was given by Harrington in [92] (see chapter 8.4, eq.(8-53)) and used by Fante [140] in the context of the bandwidth-radiation quality factor relation

$$\begin{aligned}\langle W_\mathrm{M}\rangle + \langle W_\mathrm{E}\rangle &= \frac{1}{4}\iiint_G \left(\mu\,|\boldsymbol{H}|^2 + \epsilon\,|\boldsymbol{E}|^2\right)\mathrm{d}V \\ &= \frac{\mathrm{j}}{4}\oiint_{\partial G}\left(\frac{\partial \boldsymbol{E}}{\partial\omega}\times\boldsymbol{H}^* - \frac{\partial \boldsymbol{H}}{\partial\omega}\times\boldsymbol{E}^*\right)\boldsymbol{n}\,\mathrm{d}S \qquad \text{(F.3)}\end{aligned}$$

By combining (F.2) and (F.3) it is possible to derive the quality factor without taking recourse to any equivalent circuit model.

Evaluation of the difference between the time averaged stored magnetic and electric energies

The integral on the rhs of (F.2) contains a contribution from S_0 and from S_∞, therefore

$$\oiint_{\partial G} \frac{1}{2}(\boldsymbol{E}\times\boldsymbol{H}^*)\boldsymbol{n}\,\mathrm{d}S = -\oiint_{S_0} \frac{1}{2}(\boldsymbol{E}\times\boldsymbol{H}^*)\boldsymbol{n}_0\,\mathrm{d}S + \oiint_{S_\infty} \frac{1}{2}(\boldsymbol{E}\times\boldsymbol{H}^*)\boldsymbol{n}_\infty\,\mathrm{d}S, \tag{F.4}$$

where now vector $\boldsymbol{n}_0$ is the outer normal on S_0 (pointing into G) and vector $\boldsymbol{n}_\infty$ is the outer normal on S_∞. Since in the far field the following relation between electric and magnetic field holds

$$\eta_0\,\boldsymbol{H}|_{S_\infty} = \boldsymbol{n}\times\boldsymbol{E}|_{S_\infty}\,, \tag{F.5}$$

where η_0 is the impedance of the free space ($\eta_0 \approx 377\ \Omega$). At this point of derivation it is necessary to introduce the treatment of characteristic modes. The second integral on the rhs of (F.4) is just P_0 due to power scaling $\left\langle \boldsymbol{J}_{\mathrm{s},m} \middle| \widehat{\mathbf{R}}\boldsymbol{J}_{\mathrm{s},m} \right\rangle = 2P_0$. On the geometrical surface of the body surface current density of the m-th characteristic mode $\boldsymbol{J}_{\mathrm{s},m}$ is given the tangential magnetic field strength is then also known from the boundary condition

$$\boldsymbol{H}_m|_{S_0} = -\boldsymbol{n}_0\times\boldsymbol{J}_{\mathrm{s},m}. \tag{F.6}$$

This allows to express the first term under integral on the rhs of (F.4) in terms of electric field and the surface current density

$$(\boldsymbol{E}_m\times\boldsymbol{H}_m^*)\boldsymbol{n}_0 = (\boldsymbol{E}_m\times(-\boldsymbol{n}_0\times\boldsymbol{J}_{\mathrm{s},m}))\boldsymbol{n}_0 = -\boldsymbol{n}_0(\boldsymbol{E}\boldsymbol{J}_{\mathrm{s},m}))\boldsymbol{n}_0 = -\boldsymbol{E}\boldsymbol{J}_{\mathrm{s},m} \tag{F.7}$$

and

$$-\oiint_{S_0} \frac{1}{2}(\boldsymbol{E}_m\times\boldsymbol{H}_m^*)\boldsymbol{n}_0\,\mathrm{d}S = \oiint_{S_0} \frac{1}{2}\boldsymbol{E}\boldsymbol{J}_{\mathrm{s},m}\,\mathrm{d}S. \tag{F.8}$$

The surface current density of the m-th characteristic mode the tangential electric field on S_0 which is due to $\boldsymbol{J}_{\mathrm{s},m}$ is given by

$$\boldsymbol{E}_m|_{S_0} = -\widehat{\mathbf{Z}}[\boldsymbol{J}_{\mathrm{s},m}]. \tag{F.9}$$

The negative sign follows the definition of the operator $\widehat{\mathbf{Z}}$ as given by Harrington and Mautz in [10]. Hence, due to power scaling $\langle \boldsymbol{J}_{\mathrm{s},m} | \widehat{\mathbf{R}} \boldsymbol{J}_{\mathrm{s},m} \rangle = 2P_0$

$$-\oiint_{S_0} \frac{1}{2}(\boldsymbol{E}_m \times \boldsymbol{H}_m^*)\boldsymbol{n}_0 \,\mathrm{d}S = -\frac{1}{2}\langle \boldsymbol{J}_{\mathrm{s},m} | \widehat{\mathbf{Z}} \boldsymbol{J}_{\mathrm{s},m} \rangle_{S_0} = -\frac{1}{2}(1+\mathrm{j}\,\lambda_m)2P_0 \tag{F.10}$$

Since the second term on the rhs of (F.4) equals P_0 it is easy to find the difference between the time averaged stored magnetic and electric energies

$$\langle W_{\mathrm{M},m} \rangle - \langle W_{\mathrm{E},m} \rangle = \frac{-1}{2\,\mathrm{j}\,\omega}\big(-(1+\mathrm{j}\,\lambda_m)P_0 + P_0 \big) = \frac{\lambda_m P_0}{2\omega} \tag{F.11}$$

which is proportional to eigenvalue and inversely proportional to the frequency. Due to the fact that eigenvalues change rapidly over frequency the difference between the time averaged stored electric and magnetic energies does also.

Evaluation of the sum of the time averaged stored magnetic and electric energies

The integral on the rhs of (F.3) contains a contribution from $\partial G = S_0 \cup S_\infty$, therefore

$$\begin{aligned}
&\frac{\mathrm{j}}{4}\oiint_{\partial G}\left(\frac{\partial \boldsymbol{E}}{\partial \omega} \times \boldsymbol{H}^* - \frac{\partial \boldsymbol{H}}{\partial \omega} \times \boldsymbol{E}^*\right)\boldsymbol{n}\,\mathrm{d}S \\
&\qquad = -\frac{\mathrm{j}}{4}\oiint_{S_0}\left(\frac{\partial \boldsymbol{E}}{\partial \omega} \times \boldsymbol{H}^* - \frac{\partial \boldsymbol{H}}{\partial \omega} \times \boldsymbol{E}^*\right)\boldsymbol{n}_\mathbf{o}\,\mathrm{d}S \\
&\qquad\qquad + \frac{\mathrm{j}}{4}\oiint_{S_\infty}\left(\frac{\partial \boldsymbol{E}}{\partial \omega} \times \boldsymbol{H}^* - \frac{\partial \boldsymbol{H}}{\partial \omega} \times \boldsymbol{E}^*\right)\boldsymbol{n}_\infty\,\mathrm{d}S
\end{aligned} \tag{F.12}$$

The first terms on the rhs shall be denoted by A_0 and A_∞, respectively, below. Since the sum $A_0 + A_\infty$ must be real and non-negative, the sum of the integrals alone (without the imaginary unit in front of them) must be purely imaginary and the imaginary part must be negative in order for the sum $\langle W_\mathrm{M} \rangle + \langle W_\mathrm{E} \rangle$ to be real. The minus sign in front of the integral A_0 is due to the use of $\boldsymbol{n}_0$ instead of $\boldsymbol{n}$.

Contribution of $\mathbf{A_0}$

In order to evaluate rhs of (F.3) on the surface S_0 it is necessary to find individual terms inside the integral using (F.6)

$$\left(\frac{\partial \boldsymbol{E}}{\partial \omega} \times \boldsymbol{H}^*\right) \boldsymbol{n}_0 = -\frac{\partial \boldsymbol{E}}{\partial \omega} \boldsymbol{J}_\mathrm{s}^* \tag{F.13}$$

and

$$-\left(\frac{\partial \boldsymbol{H}}{\partial \omega} \times \boldsymbol{E}^*\right) \boldsymbol{n}_0 = \left(\boldsymbol{E}^* \times \frac{\partial \boldsymbol{H}}{\partial \omega}\right) \boldsymbol{n}_0 = -\boldsymbol{E}^* \frac{\partial \boldsymbol{J}_\mathrm{s}}{\partial \omega}\,. \tag{F.14}$$

For the purpose of simple notation the contribution from S_0 to the rhs of (F.3) is denoted by A_0. It is given by

$$A_0 = -\frac{\mathrm{j}}{4} \oiint_{S_0} \left(\frac{\partial \boldsymbol{E}}{\partial \omega} \times \boldsymbol{H}^* - \frac{\partial \boldsymbol{H}}{\partial \omega} \times \boldsymbol{E}^*\right) \boldsymbol{n}_0 \,\mathrm{d}S = \frac{\mathrm{j}}{4} \oiint_{S_0} \left(\boldsymbol{J}_\mathrm{s}^* \frac{\partial \boldsymbol{E}}{\partial \omega} + \boldsymbol{E}^* \frac{\partial \boldsymbol{J}_\mathrm{s}}{\partial \omega}\right) \mathrm{d}S. \tag{F.15}$$

In application to a characteristic mode (with modal surface current density $\boldsymbol{J}_{\mathrm{s},m}$) the integral becomes

$$\begin{aligned} A_0 &= \frac{\mathrm{j}}{4} \oiint_{S_0} \left(\boldsymbol{J}_\mathrm{s}^* \frac{\partial \boldsymbol{E}}{\partial \omega} + \boldsymbol{E}^* \frac{\partial \boldsymbol{J}_\mathrm{s}}{\partial \omega}\right) \mathrm{d}S \\ &= -\frac{\mathrm{j}}{4} \oiint_{S_0} \left(\boldsymbol{J}_{\mathrm{s},m} \frac{\partial}{\partial \omega} \widehat{\mathbf{Z}}[\boldsymbol{J}_{\mathrm{s},m}] + \widehat{\mathbf{Z}}^*[\boldsymbol{J}_{\mathrm{s},m}] \frac{\partial \boldsymbol{J}_{\mathrm{s},m}}{\partial \omega}\right) \mathrm{d}S, \end{aligned} \tag{F.16}$$

where the minus sign in front of the integral is in agreement with definition of $\widehat{\mathbf{Z}}$ after (F.9). With inner product notation over a complex Hilbert space the notation changes to

$$\begin{aligned} A_0 &= -\frac{\mathrm{j}}{4} \left(\langle \boldsymbol{J}_{\mathrm{s},m} | \frac{\partial}{\partial \omega} \widehat{\mathbf{Z}} \boldsymbol{J}_{\mathrm{s},m} \rangle_{S_0} + \langle \boldsymbol{J}_{\mathrm{s},m} | \widehat{\mathbf{Z}}^* \frac{\partial \boldsymbol{J}_{\mathrm{s},m}}{\partial \omega} \rangle_{S_0}\right) \\ &= -\frac{\mathrm{j}}{4} \left(\langle \boldsymbol{J}_{\mathrm{s},m} | \frac{\partial \widehat{\mathbf{Z}}}{\partial \omega} \boldsymbol{J}_{\mathrm{s},m} \rangle_{S_0} + \langle \boldsymbol{J}_{\mathrm{s},m} | \widehat{\mathbf{Z}} \frac{\partial \boldsymbol{J}_{\mathrm{s},m}}{\partial \omega} \rangle_{S_0} + \langle \boldsymbol{J}_{\mathrm{s},m} | \widehat{\mathbf{Z}}^* \frac{\partial \boldsymbol{J}_{\mathrm{s},m}}{\partial \omega} \rangle_{S_0}\right). \end{aligned} \tag{F.17}$$

By exploiting $\widehat{\mathbf{Z}} + \widehat{\mathbf{Z}}^{\dagger} = \widehat{\mathbf{Z}} + \widehat{\mathbf{Z}}^{*} = 2\widehat{\mathbf{R}}$ it is easy to find that

$$A_0 = -\frac{\mathrm{j}}{4}\left(\left\langle \boldsymbol{J}_{\mathrm{s},m}\right| \frac{\partial \widehat{\mathbf{Z}}}{\partial \omega}\boldsymbol{J}_{\mathrm{s},m}\right\rangle_{S_0} + 2\left\langle \boldsymbol{J}_{\mathrm{s},m}\right| \widehat{\mathbf{R}}\frac{\partial \boldsymbol{J}_{\mathrm{s},m}}{\partial \omega}\left.\right\rangle_{S_0}\right) \tag{F.18}$$

$$= -\frac{\mathrm{j}}{4}\left(\left\langle \boldsymbol{J}_{\mathrm{s},m}\right| \frac{\partial \widehat{\mathbf{R}}}{\partial \omega}\boldsymbol{J}_{\mathrm{s},m}\right\rangle_{S_0} + \mathrm{j}\left\langle \boldsymbol{J}_{\mathrm{s},m}\right| \frac{\partial \widehat{\mathbf{X}}}{\partial \omega}\boldsymbol{J}_{\mathrm{s},m}\right\rangle_{S_0} + 2\left\langle \boldsymbol{J}_{\mathrm{s},m}\right| \widehat{\mathbf{R}}\frac{\partial \boldsymbol{J}_{\mathrm{s},m}}{\partial \omega}\left.\right\rangle_{S_0}\right). \tag{F.19}$$

Furthermore, the power scaling $\left\langle \boldsymbol{J}_{\mathrm{s},m}\right| \widehat{\mathbf{R}}\boldsymbol{J}_{\mathrm{s},m}\left\rangle_{S_0} = 2P_0\right.$ implies that its frequency derivative equals zero

$$\frac{\partial}{\partial \omega}\left\langle \boldsymbol{J}_{\mathrm{s},m}\right| \widehat{\mathbf{R}}\boldsymbol{J}_{\mathrm{s},m}\left\rangle_{S_0} = \left\langle \boldsymbol{J}_{\mathrm{s},m}\right| \frac{\partial \widehat{\mathbf{R}}}{\partial \omega}\boldsymbol{J}_{\mathrm{s},m}\right\rangle_{S_0} + 2\left\langle \boldsymbol{J}_{\mathrm{s},m}\right| \widehat{\mathbf{R}}\frac{\partial \boldsymbol{J}_{\mathrm{s},m}}{\partial \omega}\left.\right\rangle_{S_0} = 0 \tag{F.20}$$

Using (F.20) the relation (F.18) simplifies to its final form

$$A_0 = \frac{1}{4}\left\langle \boldsymbol{J}_{\mathrm{s},m}\right| \frac{\partial \widehat{\mathbf{X}}}{\partial \omega}\boldsymbol{J}_{\mathrm{s},m}\left\rangle_{S_0}. \right. \tag{F.21}$$

Contribution of $\mathbf{A}_{\infty}$

The contribution from the far field sphere S_{∞}, denoted by A_{∞}, can be simplified by means of (F.5) to

$$A_{\infty} = \frac{\mathrm{j}}{4}\oiint_{S_{\infty}}\left(\frac{\partial \boldsymbol{E}}{\partial \omega}\times\boldsymbol{H}^{*} - \frac{\partial \boldsymbol{H}}{\partial \omega}\times\boldsymbol{E}^{*}\right)\boldsymbol{n}_{\infty}\,\mathrm{d}S = \frac{\mathrm{j}}{2\eta_0}\oiint_{S_{\infty}}\frac{\partial \boldsymbol{E}}{\partial \omega}\,\boldsymbol{E}^{*}\,\mathrm{d}S. \tag{F.22}$$

The electric field in the far-field can be described as

$$\boldsymbol{E}_m(r,\omega) = u_m(\omega)\frac{\mathrm{e}^{-\mathrm{j}\,kr}}{r}\boldsymbol{C}_m(\boldsymbol{e}_{\mathrm{r}},\omega) \tag{F.23}$$

where propagation constant $k = \omega/c$, where c is the speed of light. $u_m(\omega)$ is a frequency dependent amplitude (presumably only slight frequency dependence) and $\boldsymbol{C}_m$ is a dimensionless tangential vector field over the unit sphere

which depends on the direction of radiation, described by $\boldsymbol{e}_\mathrm{r}$, and can be normalized as

$$\oiint_\Omega \boldsymbol{C}_m^*(\boldsymbol{e}_\mathrm{r},\omega)\boldsymbol{C}_m(\boldsymbol{e}_\mathrm{r},\omega)\,\mathrm{d}\Omega = 1. \tag{F.24}$$

The origin of the sphere is located in the geometrical center of the body. Due to power scaling of characteristic modes $\left\langle \boldsymbol{J}_{\mathrm{s},m}\middle|\widehat{\mathbf{R}}\boldsymbol{J}_{\mathrm{s},m}\right\rangle_{S_0} = 2P_0$

$$P_0 = \frac{u_m^2}{2\eta_0} = \frac{u^2}{2\eta_0} \tag{F.25}$$

with frequency independent value of u the same for all characteristic modes. Now, the rhs of (F.22) can be obtained, as a function of r as

$$\begin{aligned} A(r) &= \frac{\mathrm{j}}{2\eta_0}\oiint_{S(\mathbf{o},r)} \frac{\partial \boldsymbol{E}_m}{\partial\omega}\boldsymbol{E}_m^*\,\mathrm{d}S = \frac{\mathrm{j}}{2\eta_0}\oiint_{S(\mathbf{o},r)} \frac{\partial \boldsymbol{E}_m}{\partial\omega}\boldsymbol{E}_m^* r^2\,\mathrm{d}\Omega \\ &= \frac{\mathrm{j}}{2\eta_0}\left(\frac{\mathrm{d}}{\mathrm{d}\omega}u\frac{\mathrm{e}^{-\mathrm{j}\,kr}}{r}\right)\left(u^*\frac{\mathrm{e}^{\mathrm{j}\,kr}}{r}\right)r^2 = \frac{\mathrm{j}}{2\eta_0}\left(-\mathrm{j}\,\frac{r}{c}u^2\right) = \frac{1}{2\eta_0}\frac{r}{c}u^2. \end{aligned} \tag{F.26}$$

Use of the power normalization after (F.25) leads to

$$A(r) = \frac{r}{c}P_0 = T(r)P_0 \tag{F.27}$$

where $T(r)$ is the time a wavefront emerging from a point source at the origin $\mathbf{o}$ needs to reach the sphere $S(\mathbf{o},r)$. Hence, $T(r)P_0$ is the part of the energy which corresponds to the radiating field between the source point $\mathbf{o}$ and surface $S(\mathbf{o},r)$. This energy has to be omitted from the present considerations because it is does not correspond to reactive energy.

Characteristic mode radiation quality factors

Addition and subtraction of (F.11) and (F.21) lead to the following relations for $\langle W_{\mathrm{M},m}\rangle$ and $\langle W_{\mathrm{E},m}\rangle$

$$2\langle W_{\mathrm{M},m}\rangle = \frac{\lambda_m P_0}{2\omega} + \frac{1}{4}\left\langle \boldsymbol{J}_{\mathrm{s},m}\middle|\frac{\partial\widehat{\mathbf{X}}}{\partial\omega}\boldsymbol{J}_{\mathrm{s},m}\right\rangle_{S_0} \tag{F.28}$$

$$2\langle W_{\mathrm{E},m}\rangle = -\frac{\lambda_m P_0}{2\omega} + \frac{1}{4}\left\langle \boldsymbol{J}_{\mathrm{s},m}\middle|\frac{\partial\widehat{\mathbf{X}}}{\partial\omega}\boldsymbol{J}_{\mathrm{s},m}\right\rangle_{S_0} \tag{F.29}$$

The radiation quality factor of the m-th characteristic mode over some frequency range can be found from the definition

$$Q_{\mathrm{rad},m}(\omega) = \frac{2\omega \max(\langle W_{\mathrm{M},m}\rangle, \langle W_{\mathrm{E},m}\rangle)}{P_0} = \max\left(\frac{\omega}{4P_0}\left\langle \boldsymbol{J}_{\mathrm{s},m}\middle|\frac{\partial \widehat{\mathbf{X}}}{\partial\omega}\boldsymbol{J}_{\mathrm{s},m}\right\rangle_{S_0} \pm \frac{\lambda_m}{2}\right) \tag{F.30}$$

It is shown in section 3.3 that at resonance $\omega = \omega_{m,0}$, the eigenvalue $\lambda_m = 0$, one recovers an old expression given in [10, 12].

Investigation of possible simplification of (F.30)

In order to investigate if (F.30) can be expressed in a different form consider the derivative of X_m

$$\begin{aligned}\frac{\partial X_m}{\partial\omega} &= \frac{\partial}{\partial\omega}\left(\frac{\left\langle \boldsymbol{J}_{\mathrm{s},m}\middle|\widehat{\mathbf{X}}\boldsymbol{J}_{\mathrm{s},m}\right\rangle_{S_0}}{\left\langle \boldsymbol{J}_{\mathrm{s},m}\middle|\boldsymbol{J}_{\mathrm{s},m}\right\rangle_{S_0}}\right)\\ &= \frac{1}{\left\langle \boldsymbol{J}_{\mathrm{s},m}\middle|\boldsymbol{J}_{\mathrm{s},m}\right\rangle_{S_0}}\frac{\partial}{\partial\omega}\left\langle \boldsymbol{J}_{\mathrm{s},m}\middle|\widehat{\mathbf{X}}\boldsymbol{J}_{\mathrm{s},m}\right\rangle_{S_0} - \frac{\left\langle \boldsymbol{J}_{\mathrm{s},m}\middle|\widehat{\mathbf{X}}\boldsymbol{J}_{\mathrm{s},m}\right\rangle_{S_0}}{\left\langle \boldsymbol{J}_{\mathrm{s},m}\middle|\boldsymbol{J}_{\mathrm{s},m}\right\rangle^2_{S_0}}\frac{\partial}{\partial\omega}\left\langle \boldsymbol{J}_{\mathrm{s},m}\middle|\boldsymbol{J}_{\mathrm{s},m}\right\rangle_{S_0}\\ &= \frac{1}{\left\langle \boldsymbol{J}_{\mathrm{s},m}\middle|\boldsymbol{J}_{\mathrm{s},m}\right\rangle_{S_0}}\frac{\partial}{\partial\omega}\left\langle \boldsymbol{J}_{\mathrm{s},m}\middle|\widehat{\mathbf{X}}\boldsymbol{J}_{\mathrm{s},m}\right\rangle_{S_0} + \left\langle \boldsymbol{J}_{\mathrm{s},m}\middle|\widehat{\mathbf{X}}\boldsymbol{J}_{\mathrm{s},m}\right\rangle_{S_0}\frac{\partial}{\partial\omega}\left\langle \boldsymbol{J}_{\mathrm{s},m}\middle|\boldsymbol{J}_{\mathrm{s},m}\right\rangle^{-1}_{S_0}.\end{aligned} \tag{F.31}$$

Using orthogonality relation (3.15) and the definition of the characteristic mode radiation resistance (3.29) it is easy to see that (F.31) is given by

$$\frac{\partial X_m}{\partial\omega} = R_m\frac{\partial\lambda_m}{\partial\omega} + \lambda_m\frac{\partial R_m}{\partial\omega}, \tag{F.32}$$

which should be obvious since $X_m = \lambda_m R_m$. Consider closely the first term on the rhs of (F.31)

$$\frac{1}{\left\langle \boldsymbol{J}_{\mathrm{s},m} \middle| \boldsymbol{J}_{\mathrm{s},m} \right\rangle_{S_0}} \frac{\partial}{\partial \omega} \left\langle \boldsymbol{J}_{\mathrm{s},m} \middle| \widehat{\mathbf{X}} \boldsymbol{J}_{\mathrm{s},m} \right\rangle_{S_0} = 2 \frac{\left\langle \frac{\partial \boldsymbol{J}_{\mathrm{s},m}}{\partial \omega} \middle| \widehat{\mathbf{X}} \boldsymbol{J}_{\mathrm{s},m} \right\rangle_{S_0}}{\left\langle \boldsymbol{J}_{\mathrm{s},m} \middle| \boldsymbol{J}_{\mathrm{s},m} \right\rangle_{S_0}} + \frac{\left\langle \boldsymbol{J}_{\mathrm{s},m} \middle| \frac{\partial \widehat{\mathbf{X}}}{\partial \omega} \boldsymbol{J}_{\mathrm{s},m} \right\rangle_{S_0}}{\left\langle \boldsymbol{J}_{\mathrm{s},m} \middle| \boldsymbol{J}_{\mathrm{s},m} \right\rangle_{S_0}}. \tag{F.33}$$

In order to proceed to further simplify (F.33) it is convenient to use (3.12) which yields

$$\frac{1}{\left\langle \boldsymbol{J}_{\mathrm{s},m} \middle| \boldsymbol{J}_{\mathrm{s},m} \right\rangle_{S_0}} \frac{\partial}{\partial \omega} \left\langle \boldsymbol{J}_{\mathrm{s},m} \middle| \widehat{\mathbf{X}} \boldsymbol{J}_{\mathrm{s},m} \right\rangle_{S_0} = 2 \frac{\left\langle \frac{\partial \boldsymbol{J}_{\mathrm{s},m}}{\partial \omega} \middle| \widehat{\mathbf{R}} \boldsymbol{J}_{\mathrm{s},m} \right\rangle_{S_0}}{\left\langle \boldsymbol{J}_{\mathrm{s},m} \middle| \boldsymbol{J}_{\mathrm{s},m} \right\rangle_{S_0}} \lambda_m + \frac{\left\langle \boldsymbol{J}_{\mathrm{s},m} \middle| \frac{\partial \widehat{\mathbf{X}}}{\partial \omega} \boldsymbol{J}_{\mathrm{s},m} \right\rangle_{S_0}}{\left\langle \boldsymbol{J}_{\mathrm{s},m} \middle| \boldsymbol{J}_{\mathrm{s},m} \right\rangle_{S_0}} \tag{F.34}$$

Use of (F.20) leads to

$$\frac{1}{\left\langle \boldsymbol{J}_{\mathrm{s},m} \middle| \boldsymbol{J}_{\mathrm{s},m} \right\rangle_{S_0}} \frac{\partial}{\partial \omega} \left\langle \boldsymbol{J}_{\mathrm{s},m} \middle| \widehat{\mathbf{X}} \boldsymbol{J}_{\mathrm{s},m} \right\rangle_{S_0} = - \frac{\left\langle \boldsymbol{J}_{\mathrm{s},m} \middle| \frac{\partial \widehat{\mathbf{R}}}{\partial \omega} \boldsymbol{J}_{\mathrm{s},m} \right\rangle_{S_0}}{\left\langle \boldsymbol{J}_{\mathrm{s},m} \middle| \boldsymbol{J}_{\mathrm{s},m} \right\rangle_{S_0}} \lambda_m + \frac{\left\langle \boldsymbol{J}_{\mathrm{s},m} \middle| \frac{\partial \widehat{\mathbf{X}}}{\partial \omega} \boldsymbol{J}_{\mathrm{s},m} \right\rangle_{S_0}}{\left\langle \boldsymbol{J}_{\mathrm{s},m} \middle| \boldsymbol{J}_{\mathrm{s},m} \right\rangle_{S_0}}. \tag{F.35}$$

Introduction of the following definitions, in order to simplify the notation,

$$\frac{\left\langle \boldsymbol{J}_{\mathrm{s},m} \middle| \frac{\partial \widehat{\mathbf{R}}}{\partial \omega} \boldsymbol{J}_{\mathrm{s},m} \right\rangle_{S_0}}{\left\langle \boldsymbol{J}_{\mathrm{s},m} \middle| \boldsymbol{J}_{\mathrm{s},m} \right\rangle_{S_0}} = \frac{\partial \widetilde{R}_m}{\partial \omega} \tag{F.36}$$

and

$$\frac{\left\langle \boldsymbol{J}_{\mathrm{s},m} \middle| \frac{\partial \widehat{\mathbf{X}}}{\partial \omega} \boldsymbol{J}_{\mathrm{s},m} \right\rangle_{S_0}}{\left\langle \boldsymbol{J}_{\mathrm{s},m} \middle| \boldsymbol{J}_{\mathrm{s},m} \right\rangle_{S_0}} = \frac{\partial \widetilde{X}_m}{\partial \omega}, \tag{F.37}$$

allows to write the derivative of X_m as

$$\frac{\partial X_m}{\partial \omega} = \frac{\partial \widetilde{X}_m}{\partial \omega} - \lambda_m \frac{\partial \widetilde{R}_m}{\partial \omega} + \lambda_m \frac{\partial R_m}{\partial \omega} \,. \tag{F.38}$$

In the general case $\frac{\partial X_m}{\partial \omega} \neq \frac{\partial \widetilde{X}_m}{\partial \omega}$. Only if $\frac{\partial \widetilde{R}_m}{\partial \omega} = \frac{\partial R_m}{\partial \omega}$ or at resonance (i.e when $\lambda_m = 0$) $\frac{\partial X_m}{\partial \omega} = \frac{\partial \widetilde{X}_m}{\partial \omega}$. From (F.33) the approximation holds if the surface current density $\boldsymbol{J}_{\mathrm{s},m}$ does not change significantly over frequency. Numerical results show that it is approximately satisfied for e.g. a linear thin long wire.

Acronyms and Abbreviations

AoA	Angle of Arrival
3GPP	3rd Generation Partnership Project
ARC	Active Reflection Coefficient
BC	band class
CAD	Computer-aided Design
CECC	Complex Envelope Correlation Coeffient
CMOS	Complementary Metal-Oxide-Semiconductor
CMRR	Common Mode Rejection Ratio
CPE	Customer Premises Equipment
CSI	Channel State Information
CL-SM	Closed-loop Spatial Multiplexing
DAC	digital to analog converter
DC	Direct Current
DL	Downlink
DTC	Digitally Tunable Capacitor
DVB-T	digital video broadcasting – terrestrial
ECM	Equivalent Circuit Model
EM	Electromagnetic
eNB	evolved Node-B
E-UTRA	Evolved Universal Terrestrial Radio Access
ESR	Equivalent series resistance
EGC	Equal Gain Combining

FDD	Frequency Division Duplex
FDTD	Finite-difference time-domain method
FET	Field-effect transistor
IFA	inverted-F antenna
IL	insertion loss
LTE	Long Term Evolution
MDN	Mode Decomposition Network
MEMS	Micro Electro-Mechanical System
MIMO	Multiple Input – Multiple Output
SU	Single User
MN	Matching Network
MoM	Method of Moments
MIM	Metal-Insulator-Metal
MRC	Maximum Ratio Combining
MRL	Multi-Port Return Loss
PCB	printed circuit board
PCS	Personal Communication Services
PECC	Power Envelope Correlation Coeffient
PIFA	planar inverted-F antenna
PIN	PIN diode
RD	Receive Diversity
RF	radio frequency
RL	Return Loss
RX	Receiver
SOI	Silicon-On-Insulator
SOS	Silicon-On-Silicon
SM	Spatial Multiplexing
SMD	Surface Mount Device

SNR	Signal to Noise Ratio
SPI	Serial Peripheral Interface
SRF	Self-resonant frequency
SPST	Single Pole, Single Throw
TARC	Total Active Reflection Coefficient
TE	Transversal Electric
TM	Transversal Magnetic
TMRL	Total Multiport Return Loss
TX	Transmitter
UE	User Equipment
UL	Uplink
USB	Universal Serial Bus
VNA	Vector Network Analyzer
VSWR	Voltage Standing Wave Ratio
WLAN	Wireless Local Area Network

List of Symbols

$(\cdot)^{\dagger}$	Hermitian transpose
$(\cdot)^{\top}$	transpose
$(\cdot)^{*}$	complex conjugate
G	gain of a single port antenna
P_{diss}	dissipated power
P_{rad}	total radiated power
Q_{rad}	radiation quality factor
R_{loss}	loss resistance
R_{rad}	radiation resistance
S	surface
Y_{L}	load admittance
Z_0	line impedance
Z_{L}	load impedance
Γ_{tot}	total multiport reflectance
$\mathbf{C}$	modal efficiency matrix
$\mathbf{D}$	dissipation matrix
$\mathbf{R}$	radiation matrix
$\mathbf{S}$	scattering matrix

$\mathbf{T}$	compound pattern
$\mathbf{Y}$	admittance matrix
$\mathbf{\Gamma}$	modal reflectance matrix
$\mathbf{\Pi}$	permutation matrix
$\mathbf{\Psi}$	arbitrary unitary matrix
Ω	angular position
$\boldsymbol{E}^{\mathrm{ex}}$	incident electric field
$\boldsymbol{E}^{\mathrm{ex}}_{\mathrm{tan}}$	tangential component of an incident electric field
$\boldsymbol{E}_{\mathrm{rad}}$	radiated electric field vector
$\boldsymbol{E}_{\mathrm{rec}}$	received electric field vector
$\boldsymbol{J}_{\mathrm{s}}$	vector of the surface current density
$\boldsymbol{J}_{\mathrm{s},m}$	vector of the surface current density of the mth characteristic mode
$\boldsymbol{V}_n$	nth *radiation mode*
$\boldsymbol{a}$	vector of incoming wave quantities
$\boldsymbol{b}$	vector of outgoing wave quantities
$\boldsymbol{\zeta}$	modal impedance matrix
η_0	characteristic impedance of the free space
η_{rad}	radiation efficiency
η_{tot}	total efficiency
λ_0	wavelength in the free space
λ_m	eigenvalue of the mth characteristic mode
$\langle W_{\mathrm{E}} \rangle$	time-average stored electric field
$\langle W_{\mathrm{M}} \rangle$	time-average stored magnetic field

ω	angular frequency
$\overline{\eta_{\mathrm{tot}}}$	total multiport efficiency
ρ_{mn}	radiation pattern overlap
$b^{7\mathrm{dB}}$	fractional $7\mathrm{dB}$ bandwidth
k_0	propagation constant in the free space
$\|\| \cdot \|\|_{\mathrm{F}}$	Frobenius norm of a matrix

References

[1] S. Stein, "On cross coupling in multiple-beam antennas," *IRE Transactions on Antennas and Propagation*, vol. 10, no. 5, pp. 548–557, Sep. 1962.

[2] H. J. Chaloupka, X. Wang, and J. C. Coetzee, "Performance enhancement of smart antennas with reduced element spacing," in *IEEE Wireless Communications and Networking (WCNC)*, vol. 1, New Orleans, LA, USA, Mar. 2003, pp. 425–430.

[3] H. J. Chaloupka and X. Wang, "Novel approach for diversity and MIMO antennas at small mobile platforms," in *15th IEEE International Symposium on Personal, Indoor and Mobile Radio Communications (PIMRC)*, vol. 1, Barcelona, Spain, Sep. 2004, pp. 637–642.

[4] H. . J. Chaloupka, D. Esser, and X. Wang, "Port decoupling for antennas with narrow element spacing," in *7th European Conference on Wireless Technology*, Amsterdam, The Netherlands, May 2004, pp. 221–224.

[5] D. Esser and H. J. Chaloupka, "Design approach for a class of compact multiport antennas," in *IEEE International Symposium on Microwave, Antenna, Propagation and EMC Technologies for Wireless Communications (MAPE)*, vol. 1, Beijing, China, Aug. 2005, pp. 144–147.

[6] C. Volmer, J. Weber, R. Stephan, K. Blau, and M. Hein, "Decoupling and matching network for miniaturised 3-port antenna arrays based on 180° couplers," in *2nd International ITG Conference on Antennas (INICA)*, Munich, Germany, Mar. 2007, pp. 63–66.

[7] T.-I. Lee and Y. E. Wang, "Oversampled antenna array: Supergain and diversity performance," in *International Workshop on Antenna Technology: Small and Smart Antennas Metamaterials and Applications iWAT*, Cambridge, UK, Mar. 2007, pp. 211–214.

[8] ——, "A mode-based supergain approach with closely coupled monopole pair," in *IEEE Antennas and Propagation Society International Symposium*, Honolulu, HI, Jun. 2007, pp. 5901–5904.

[9] H. D. Foltz and J. S. McLean, "Bandwidth limitations on antenna systems with multiple isolated input ports," *John Wiley and Sons, Inc. Microwave Opt Technol Lett*, vol. 19, pp. 301–304, Apr. 1998.

[10] R. F. Harrington and J. R. Mautz, "Theory of characteristic modes for conducting bodies," *IEEE Transactions on Antennas and Propagation*, vol. 19, no. 5, pp. 622–628, Sep. 1971.

[11] P. Vainikainen, J. Ollikainen, O. Kivekaes, and I. Kelander, "Resonator-based analysis of the combination of mobile handset antenna and chassis," *IEEE Transactions on Antennas and Propagation*, vol. 50, no. 10, pp. 1433–1444, Oct. 2002.

[12] C. T. Famdie, W. L. Schroeder, and K. Solbach, "Numerical analysis of characteristic modes on the chassis of mobile phones," in *First European Conference on Antennas and Propagation EuCAP 2006*, Nice, France, Nov. 2006.

[13] ——, "Optimal antenna location on mobile phones chassis based on the numerical analysis of characteristic modes," in *European Microwave Conference 2007*, Munich, Germany, Oct. 2007, pp. 987–990.

[14] S. K. Chaudhury, W. L. Schroeder, and H. J. Chaloupka, "MIMO antenna system based on orthogonality of the characteristic modes of a mobile device," in *2nd International ITG Conference on Antennas (INICA)*, Munich, Germany, Mar. 2007, pp. 58–62.

[15] ——, "Multiple antenna concept based on characteristic modes of mobile phone chassis," in *The Second European Conference on Antennas and Propagation (EuCAP) 2007*, Edinburgh, UK, Nov. 2007.

[16] S. K. Chaudhury, H. J. Chaloupka, and A. Ziroff, "Novel MIMO antennas for mobile terminal," in *Proceedings of the 38th European Microwave Conference (EuMC)*, Amsterdam, The Netherlands, Oct. 2008.

[17] ——, "Multiport antenna systems for MIMO and diversity," in *Proceedings of the Fourth European Conference on Antennas and Propagation (EuCAP)*, Barcelona, Spain, Apr. 2010.

[18] S. K. Chaudhury, "MIMO antenna concept for small devices based on characteristic modes," Ph.D. dissertation, Bergische Universitaet Wuppertal, 2010.

[19] R. Martens, E. Safin, and D. Manteuffel, "Selective excitation of characteristic modes on small terminals," in *Proceedings of the 5th European Conference on Antennas and Propagation (EuCAP)*, Rome, Italy, Apr. 2011, pp. 2492–2496.

[20] ——, "Inductive and capacitive excitation of the characteristic modes of small terminals," in *Loughborough Antennas and Propagation Conference (LAPC)*, Loughborough, UK, Nov. 2011.

[21] R. Martens and D. Manteuffel, "A feed network for the selective excitation of specific characteristic modes on small terminals," in *6th European Conference on Antennas and Propagation (EuCAP)*, Prague, Czech Republic, Mar. 2012, pp. 1842–1846.

[22] ——, "2-port antenna based on the selective excitation of characteristic modes," in *IEEE Antennas and Propagation Society International Symposium (APSURSI)*, Chicago, IL, USA, Jul. 2012.

[23] Z. Miers, H. Li, and B. K. Lau, "Design of multi-antenna feeding for MIMO terminals based on characteristic modes," in *IEEE International Symposium on Antennas and Propagation (APSURSI)*, Orlando, FL, USA, Jul. 2013.

[24] Z. Miers, H. Li, and B. Lau, "Design of bandwidth enhanced and multiband MIMO antennas using characteristic modes," *IEEE Antennas and Wireless Propagation Letters*, vol. PP, no. 99, Nov. 2013.

[25] J. W. Wallace and M. A. Jensen, "Termination-dependent diversity performance of coupled antennas: Network theory analysis," *IEEE Transactions on Antennas and Propagation*, vol. 52, no. 1, pp. 98–105, Jan. 2004.

[26] ——, "Mutual coupling in MIMO wireless systems: A rigorous network theory analysis," *IEEE Transactions on Antennas and Propagation*, vol. 3, no. 4, pp. 1317–1325, Jul. 2004.

[27] B. K. Lau, J. B. Andersen, G. Kristensson, and A. F. Molisch, "Impact of matching network on bandwidth of compact antenna arrays," *IEEE Transactions on Antennas and Propagation*, vol. 54, no. 11, pp. 3225–3238, Nov. 2006.

[28] J. Weber, C. Volmer, K. Blau, R. Stephan, and M. A. Hein, "Miniaturized antenna arrays using decoupling networks with realistic elements," *IEEE Transactions on Microwave Theory and Techniques*, vol. 54, no. 6, pp. 2733–2740, Jun. 2006.

[29] J. Weber, "Entwurf miniaturisierter antennengruppen," Ph.D. dissertation, Technische Universitaet Ilmenau, 2009.

[30] W. K. Kahn, "Active reflection coefficient and element efficiency in arbitrary antenna arrays," *IEEE Transactions on Antennas and Propagation*, vol. 17, no. 5, pp. 653–654, Sep. 1969.

[31] C. Volmer, J. Weber, R. Stephan, K. Blau, and M. Hein, "An eigen-analysis of compact antenna arrays and its application to port decoupling," *IEEE Transactions on Antennas and Propagation*, vol. 56, no. 2, pp. 360–370, Feb. 2008.

[32] D. Youla, "Weissfloch equivalents for lossless 2n-ports," *IRE Transactions on Circuit Theory*, vol. 7, no. 3, pp. 193–199, Sep. 1960.

[33] C. Volmer, "Compact antenna arrays in mobile communications: A quantitative analysis of radiator coupling," Ph.D. dissertation, Technische Universitaet Ilmenau, May 2009.

[34] W. P. Geren, C. E. Curry, and J. Andersen, "A practical technique for designing multiport coupling networks," *IEEE Transactions on Microwave Theory and Techniques*, vol. 44, no. 3, pp. 364–371, Mar. 1996.

[35] J. Andersen and H. Rasmussen, "Decoupling and descattering networks for antennas," *IEEE Transactions on Antennas and Propagation*, vol. 24, pp. 841–846, Nov. 1976.

[36] A. C. K. Mak, C. R. Rowell, and R. D. Murch, "Isolation enhancement between two closely packed antennas," *IEEE Transactions on Antennas and Propagation*, vol. 56, no. 11, pp. 3411–3419, Nov. 2008.

[37] G. Park, M. Kim, T. Yang, J. Byun, and A. S. Kim, "The compact quad-band mobile handset antenna for the LTE 700 MIMO application," in *IEEE Antennas and Propagation Society International Symposium (APSURSI)*, Charleston, SC, USA, Jun. 2009.

[38] W. L. Schroeder and A. Krewski, "Total multi-port return loss as a figure of merit for MIMO antenna systems," in *European Microwave Conference (EuMC)*, Paris, France, Sep. 2010, pp. 1742–1745.

[39] A. Krewski and W. L. Schroeder, "Equivalent circuit model for closely coupled symmetrical two-port MIMO antennas in small volume," in *IEEE Antennas and Propagation Society International Symposium (APSURSI)*, Toronto, ON, Canada, Jul. 2010.

[40] M. T. Montgomery, F. M. Caimi, J. Paul A. Tornatta, and L. Chen, "Multimode antenna structure," US Patent 7,688,275 B2, Mar., 2010.

[41] M. T. Montgomery, F. M. Caimi, and M. W. Kishler, "Multimode antenna structure," US Patent 7,688,273 B2, Mar., 2010.

[42] M. T. Montgomery, "High isolation antenna system," US Patent US 2011/0 050 528, 2011.

[43] M. T. Montgomery, F. M. Caimi, and M. W. Kishler, "Multimode antenna structure," US Patent US 2011/0 080 332, 2011.

[44] T. Ohishi, N. Oodachi, S. Sekine, and H. Shoki, "A method to improve the correlation coefficient and the mutual coupling for diversity antenna," in *IEEE Antennas and Propagation Society International Symposium*, vol. 1A, Washington DC, USA, Jul. 2005, pp. 507–510.

[45] T. Kokkinos, E. Liakou, and A. Feresidis, "Decoupling antenna elements of PIFA arrays on handheld devices," *Electronics Letters*, vol. 44, no. 25, p. 1442, Dec. 2008.

[46] M.-S. Han and J. Choi, "Multiband MIMO antenna with a band stop filter for high isolation characteristics," in *IEEE Antennas and Propagation Society International Symposium (APSURSI)*, Charleston, SC, USA, Jun. 2009.

[47] Z. H. Hu, P. S. Hall, P. Gardner, and Y. Nechayev, "Wide tunable balanced antenna for mobile terminals and its potential for MIMO applications," in *Loughborough Antennas and Propagation Conference (LAPC)*, Loughborough, UK, Nov. 2011.

[48] Z. Hu, P. Hall, and P. Gardner, "Reconfigurable dipole-chassis antennas for small terminal MIMO applications," *Electronics Letters*, vol. 47, no. 17, pp. 53–955, Aug. 2011.

[49] S. Yoon and N. G. Alexopoulos, "Multiple antenna high isolation apparatus and application thereof," US Application 2010/022 022A1, Sep. 2, 2010. [Online]. Available: http://www.google.com/patents/US20100220022

[50] A. Tatomirescu, O. Alrabadi, and G. Pedersen, "Orthogonal antenna architecture for MIMO handsets," in *6th European Conference on Antennas and Propagation (EuCAP)*, Prague, Czech Republic, Mar. 2012, pp. 1989–1991.

[51] H. Li, B. K. Lau, Z. Ying, and S. He, "Decoupling of multiple antennas in terminals with chassis excitation using polarization diversity, angle diversity and current control," *IEEE Transactions on Antennas and Propagation*, vol. 60, no. 12, pp. 5947–5957, Dec. 2012.

[52] J. Ilvonen, O. Kivekaes, A. Azremi, R. Valkonen, J. Holopainen, and P. Vainikainen, "Isolation improvement method for mobile terminal antennas at lower UHF band," in *Proceeding of the 5th European Conference on Antennas and Propagation (EuCAP)*, Apr. 2011, pp. 1307–1311.

[53] M. Han and J. Choi, "Compact multiband MIMO antenna for next generation USB dongle application," in *IEEE Antennas and Propagation Society International Symposium (APSURSI)*, Toronto, ON, Canada, Jul. 2010.

[54] ——, "Dual-band MIMO antenna using a symmetric slotted structure for 4G USB dongle application," in *IEEE International Symposium on Antennas and Propagation (APSURSI)*, Spokane, WA, USA, Jul. 2011, pp. 2223–2226.

[55] J. Choi and M. Han, "Multiband MIMO antenna using a symmetric slotted structure for next generation USB dongle application," in *IEEE MTT-S International Microwave Workshop Series on Intelligent Radio for Future Personal Terminals (IMWS-IRFPT)*, Daejeon, South Korea, Aug. 2011.

[56] B. Kim, Y. Park, H. Wi, M.-J. Park, Y. Choi, J. Lee, W. Jung, D. Kim, and B. Lee, "Isolation enhancement of USB dongle MIMO antenna in LTE 700 band applications," *IEEE Antennas and Wireless Propagation Letters*, vol. 11, pp. 961–964, 2012.

[57] J. Guterman, D. W. Browne, Y. Rahmat-Samii, A. A. Moreira, and C. Peixeiro, "Design of integrated antenna arrays for MIMO enabled laptops," in *IEEE Antennas and Propagation Society International Symposium*, Honolulu, HI, USA, Jun. 2007, pp. 2421–2424.

[58] K.-L. Wong, W.-J. Chen, L.-C. Chou, and M.-R. Hsu, "Bandwidth enhancement of the small-size internal laptop computer antenna using a parasitic open slot for penta-band WWAN operation," *IEEE Transactions on Antennas and Propagation*, vol. 58, no. 10, pp. 3431–3435, Oct. 2010.

[59] E. A. Vazquez, R. Caballero, B. Chiang, R. A. G. Angulo, Y. Jiang, D. B. Kough, R. W. Schlub, and G. A. Springer, "Dielectric window antennas for electronic

devices," US Application US20 100 321 253 A1, Dec. 23, 2010. [Online]. Available: http://www.google.com/patents/US20100321253

[60] E. L. Camacho, B. Chiang, D. B. Kough, and H. Xu, "Electronic device antenna," US Grant US8 269 674 B2, Sep. 18, 2012. [Online]. Available: http://www.google.com/patents/US8269674

[61] Y. Feng, W. L. Schroeder, C. von Gagern, A. Tankielun, and T. Kaiser, "Metrics and methods for evaluation of over-the-air performance of MIMO user equipment," *International Journal of Antennas and Propagation*, vol. 2012, no. 598620, p. 15, 2012.

[62] J. Wallace, H. Ozcelik, M. Herdin, E. Bonek, and M. Jensen, "Power and complex envelope correlation for modeling measured indoor MIMO channels: A beamforming evaluation," in *IEEE 58th Vehicular Technology Conference, VTC 2003-Fall*, vol. 1, Orlando, FL, USA, Oct. 2003, pp. 363–367.

[63] S. Blanch, J. Romeu, and I. Corbella, "Exact representation of antenna system diversity performance from input parameter description," *Electronics Letters*, vol. 39, no. 9, pp. 705–707, May 2003.

[64] J. Thaysen and K. B. Jakobsen, "Envelope correlation in (N, N) MIMO antenna array from scattering parameters," *Microwave and Optical Technology Letters*, vol. 48, no. 5, pp. 832–834, May 2006.

[65] B. Rembold, "Relation between diagram correlation factors and s-parameters of multiport antenna with arbitrary feeding network," *Electronics Letters*, vol. 44, no. 1, pp. 5–7, Jan. 2008.

[66] C. Volmer, J. Weber, R. Stephan, and M. A. Hein, "A descriptive model for analyzing the diversity performance of compact antenna arrays," *IEEE Transactions on Antennas and Propagation*, vol. 57, no. 2, pp. 395–405, Feb. 2009.

[67] R. A. Horn and C. R. Johnson, *Matrix Analysis*. Cambridge University Press, 1985.

[68] A. Krewski, W. L. Schroeder, and K. Solbach, "Bandwidth limitations and optimum low-band LTE MIMO antenna placement in mobile terminals using modal analysis," in *European Conference on Antennas and Propagation (EuCAP)*, Rome, Italy, Apr. 2011, pp. 142–146.

[69] W. K. Kahn, "Scattering equivalent circuit for common symmetrical junctions," *IRE Transactions on Circuit Theory*, vol. 3, no. 2, pp. 121–127, Jun. 1956.

[70] H. F. Pues and A. R. V. de Capelle, "An impedance-matching technique for increasing the bandwidth of microstrip antennas," *IEEE Transactions on Antennas and Propagation*, vol. 37, no. 11, pp. 1345–1354, Nov. 1989.

[71] A. D. Yaghjian and S. R. Best, "Impedance, bandwidth, and Q of antennas," *IEEE Transactions on Antennas and Propagation*, vol. 53, no. 4, pp. 1298–1324, Apr. 2005.

[72] R. E. Collin and S. Rothschild, "Evaluation of antenna Q," *IEEE Transactions on Antennas and Propagation*, vol. AP-12, pp. 23–27, 1964.

[73] J. Volakis, C.-C. Chen, and K. Fujimoto, *Small Antennas: Miniaturization Techniques and Applications*. McGraw-Hill Professional, 2011.

[74] W. Geyi, P. Jarmuszewski, and Y. Qi, "The foster reactance theorem for antennas and radiation Q," *IEEE Transactions on Antennas and Propagation*, vol. 48, no. 3, pp. 401–408, Mar. 2000.

[75] L. J. Chu, "Physical limitations of omni-directional antennas," *Journal of Applied Physics*, vol. 19, pp. 1163–1175, 1948.

[76] W. Kahn, "Element efficiency: A unifying concept for array antennas," *IEEE Antennas and Propagation Magazine*, vol. 49, no. 4, pp. 48–56, Nov. 2007.

[77] Y. Feng, "Over-the-air (OTA) measurement method for mimo-enabled mobile terminals," Ph.D. dissertation, University Duisburg-Essen, Apr. 2013.

[78] H. Li, X. Lin, B. K. Lau, and S. He, "Calculating signal correlation in lossy dipole arrays using scattering parameters and efficiencies," in *7th European Conference on Antennas and Propagation (EuCAP)*, Gothenburg, Sweden, Apr. 2013.

[79] ——, "Equivalent circuit based calculation of signal correlation in lossy MIMO antennas," *IEEE Transactions on Antennas and Propagation*, vol. 61, no. 10, pp. 5214–5222, Oct. 2013.

[80] A. Stjernman, "Relationship between radiation pattern correlation and scattering matrix of lossless and lossy antennas," *Electronics Letters*, vol. 41, no. 12, pp. 678–680, Jun. 2005.

[81] A. Krewski, W. L. Schroeder, and K. Solbach, "Upper bound on pattern correlation of lossy N-port antennas in terms of modal efficiencies," in *7th European Conference on Antennas and Propagation (EuCAP)*, Gothenburg, Sweden, Apr. 2013.

[82] A. Krewski and W. L. Schroeder, "Tight upper bound on radiation pattern correlation for N-port MIMO antennas," *Electronics Letters*, vol. 49, no. 23, pp. 1427–1428, Nov. 2013.

[83] A. Tatomirescu, O. Alrabadi, and G. F. Pedersen, "Optimal placement of MIMO antenna pairs with different quality factors in smart-phone platforms," in *7th European Conference on Antennas and Propagation (EuCAP)*, Gothenburg, Sweden, Apr. 2013, pp. 726–729.

[84] J. Rahola, "Simultaneous multiport matching circuit optimization for multiantenna systems," in *7th European Conference on Antennas and Propagation (EuCAP)*, Gothenburg, Sweden, Apr. 2013, pp. 2700–2703.

[85] M. Manteghi and Y. Rahmat-Samii, "Broadband characterization of the total active reflection coefficient of multiport antennas," in *IEEE Antennas and Propagation Society International Symposium*, vol. 3, Jun. 2003, pp. 20–23.

[86] R. Garbacz and R. Turpin, "A generalized expansion for radiated and scattered fields," *IEEE Transactions on Antennas and Propagation*, vol. 19, no. 3, pp. 348–358, May 1971.

[87] J. Holopainen, R. Valkonen, O. Kivekas, J. Ilvonen, and P. Vainikainen, "Broadband equivalent circuit model for capacitive coupling element-based mobile terminal antenna," *IEEE Antennas and Wireless Propagation Letters*, vol. 9, pp. 716–719, Jul. 2010.

[88] M. C. Fabres, "Systematic design of antennas using the theory of characteristic modes," Ph.D. dissertation, Universitat Politecnica de Valencia, Feb. 2007.

[89] K. A. Obeidat, "Design methodology for wideband electrically small antennas (ESA) based on the theory of characteristic modes (CM)," Ph.D. dissertation, Ohio State University, 2010.

[90] J. Ethier, "Antenna shape synthesis using characteristic mode concepts," Ph.D. dissertation, University of Ottawa, 2012.

[91] V. H. Rumsey, "Reaction concept in electromagnetic theory," *Physical Review*, vol. 95, no. 6, p. 1705, Jun. 1954.

[92] R. F. Harrington, *Time-Harmonic Electromagnetic Fields*, ser. IEEE Press Series on Electromagnetic Wave Theory. Wiley-IEEE Press, Sep. 2001.

[93] B. A. Austin and K. P. Murray, "The application of characteristic-mode techniques to vehicle-mounted NVIS antennas," *IEEE Antennas and Propagation Magazine*, vol. 40, no. 1, pp. 7–21, Feb. 1998.

[94] J. Ethier and D. McNamara, "Through the looking glass: A characteristic mode view of electromagnetic modeling & design," in *14th International Symposium on Antenna Technology and Applied Electromagnetics & the American Electromagnetics Conference (ANTEM-AMEREM)*, Ottawa, ON, Canada, Jul. 2010.

[95] J. Adams and J. Bernhard, "Broadband equivalent circuit models for antenna impedances and fields using characteristic modes," *IEEE Transactions on Antennas and Propagation*, vol. 61, no. 8, pp. 3985–3994, Aug. 2013.

[96] J. Chalas, K. Sertel, and J. Volakis, "Computation of the Q limits for arbitrary-shaped antennas using characteristic modes," in *IEEE International Symposium on Antennas and Propagation (APSURSI)*, Spokane, WA, USA, Jul. 2011, pp. 772–774.

[97] ——, "Q limits for arbitrary shape antennas using characteristic modes," in *6th European Conference on Antennas and Propagation (EUCAP)*, Prague, Czech Republic, Mar. 2012, pp. 1672–1673.

[98] R. F. Harrington and J. R. Mautz, "Control of radar scattering by reactive loading," *IEEE Transactions on Antennas and Propagation*, vol. AP-20, no. 4, pp. 446–454, Jul. 1972.

[99] J. Thal, H.L., "Gain and Q bounds for coupled TM-TE modes," *IEEE Transactions on Antennas and Propagation*, vol. 57, no. 7, pp. 1879–1885, Jul. 2009.

[100] M. Gustafsson, C. Sohl, and G. Kristensson, "Illustrations of new physical bounds on linearly polarized antennas," *IEEE Transactions on Antennas and Propagation*, vol. 57, no. 5, pp. 1319–1327, May 2009.

[101] J. McLean, "A re-examination of the fundamental limits on the radiation Q of electrically small antennas," *IEEE Transactions on Antennas and Propagation*, vol. 44, no. 5, pp. 672–676, May 1996.

[102] M. Gustafsson, *AntennaQ*, http://www.mathworks.com/matlabcentral/ fileexchange/26806-antennaq, Mar. 2010, computes physical bounds on Q and D/Q for antennas.

[103] A. Yee and R. Garbacz, "Self- and mutual-admittances of wire antennas in terms of characteristic modes," *IEEE Transactions on Antennas and Propagation*, vol. 21, no. 6, pp. 868 – 871, Nov. 1973.

[104] W. L. Schroeder, A. A. Vila, and C. Thome, "Extremely small, wide-band mobile phone antennas by inductive chassis mode coupling," in *36th European Microwave Conference*, Manchester, UK, Sep. 2006.

[105] E. Rosa, "The self and mutual inductances of linear conductors," *Bulletin of the Bureau of Standards*, vol. 4, no. 2, p. 301ff, 1908.

[106] A. Krewski, W. L. Schroeder, and K. Solbach, "Multi-band 2-port MIMO LTE antenna design for laptops using characteristic modes," in *Loughborough Antennas and Propagation Conference (LAPC)*, Loughborough, UK, Nov. 2012.

[107] ——, "Multi-band 2-port MIMO antenna design for LTE-enabled 13" monocoque laptop," in *IEEE International Symposium on Antennas and Propagation (APSURSI)*, Orlando, FL, USA, Jul. 2013.

[108] ——, "MIMO LTE antenna design for laptops based on theory of characteristic modes," in *6th European Conference on Antennas and Propagation*, Prague, Czech Republic, Mar. 2012.

[109] A. Krewski, W. Schroeder, and J. Vercruysse, "Antenna system for portable wireless device," WO Patent WO 2013/060 683 A1, 10, 2012.

[110] J. Coetzee and Y. Yu, "Design of decoupling networks for circulant symmetric antenna arrays," *IEEE Antennas and Wireless Propagation Letters*, vol. 8, pp. 291–294, 2009.

[111] A. Krewski, W. L. Schroeder, and K. Solbach, "Matching network synthesis for mobile MIMO antennas based on minimization of the total multi-port reflectance," in *Loughborough Antennas and Propagation Conference (LAPC)*, Loughborough, UK, Nov. 2011.

[112] A. Krewski and W. L. Schroeder, "Electrically tunable mode decomposition network for 2-port MIMO antennas," in *Loughborough Antennas & Propagation Conference (LAPC)*, Loughborough, UK, Nov. 2013, pp. 553–558.

[113] J. J. Lynch, "A modal description of multiport antennas," *International Journal of Antennas and Propagation*, vol. 2011, p. 12, 2011.

[114] T.-I. Lee and Y. Wang, "A planar multipolar antenna for MIMO applications," in *IEEE Antennas and Propagation Society International Symposium*, Honolulu, HI, USA, Jun. 2007, pp. 2429–2432.

[115] A. Krewski and W. L. Schroeder, "N-port DL-MIMO antenna system realization using systematically designed mode matching and mode decomposition network," in *42nd European Microwave Conference (EuMC)*, Amsterdam, The Netherlands, Nov. 2012, pp. 156–159.

[116] F. D. Flaviis, L. Jofre, J. Romeu, and A. Grau, *Multiantenna Systems for MIMO Communications*, 1st ed. Morgan & Claypool Publishers, 2008.

[117] S. J. Parisi, "180 lumped element hybrid," in *IEEE MTT-S International Microwave Symposium Digest*, Long Beach, CA, USA, Jun. 1989, pp. 1243–1246.

[118] J. C. Coetzee and Y. Yu, "Port decoupling for small arrays by means of an eigenmode feed network," *IEEE Transactions on Antennas and Propagation*, vol. 56, no. 6, pp. 1587–1593, Jun. 2008.

[119] T.-I. Lee and Y. E. Wang, "Mode-based information channels in closely coupled dipole pairs," *IEEE Transactions on Antennas and Propagation*, vol. 56, no. 12, pp. 3804–3811, Dec. 2008.

[120] R. Tian and B. K. Lau, "Uncoupled antenna matching for performance optimization in compact MIMO systems using unbalanced load impedance," in *IEEE Vehicular Technology Conference (VTC)*, Singapore, May 2008, pp. 299–303.

[121] L. K. Yeung and Y. E. Wang, "A decoupling technique for compact antenna arrays in handheld terminals," in *IEEE Radio and Wireless Symposium (RWS)*, New Orleans, LA, USA, Jan. 2010, pp. 80–83.

[122] H. Wheeler, "Fundamental limitations of small antennas," *Proceedings of the IRE*, vol. 35, no. 12, pp. 1479–1484, Dec. 1947.

[123] J. Thal, H.L., "Exact circuit analysis of spherical waves," *IEEE Transactions on Antennas and Propagation*, vol. 26, no. 2, pp. 282–287, Mar. 1978.

[124] J. Herbert L. Thal, "New radiation Q limits for spherical wire antennas," *IEEE Transactions on Antennas and Propagation*, vol. 54, no. 10, pp. 2757–2763, Oct. 2006.

[125] S. R. Best, "The radiation properties of electrically small folded spherical helix antennas," *IEEE Transactions on Antennas and Propagation*, vol. 52, no. 4, pp. 953–960, Apr. 2004.

[126] H. Wheeler, "The radiansphere around a small antenna," *Proceedings of the IRE*, vol. 47, no. 8, pp. 1325–1331, Aug. 1959.

[127] H. A. Wheeler, "Small antennas," *IEEE Transactions on Antennas and Propagation*, vol. 23, no. 4, pp. 462–469, Jul. 1975.

[128] C. A. Balanis, *Antenna Design: Analysis and Design*, 2nd ed. New York, USA: John Wiley and Sons, Inc., 1982.

[129] G. S. Smith, "Efficiency of electrically small antennas combined with matching networks," *IEEE Transactions on Antennas and Propagation*, vol. 25, no. 3, pp. 369–373, May 1977.

[130] J. T. Aberle, "Two-port representation of an antenna with application to non-foster matching networks," *IEEE Transactions on Antennas and Propagation*, vol. 56, no. 5, pp. 1218–1222, May 2008.

[131] E. Microsemi and C. Pin, "Microsemi-watertown the PIN diode circuit designers' handbook," 1992.

[132] *Infineon Technologies AG*, Neubiberg, Germany, 1999 - 2013.

[133] R. Whatley, T. Ranta, and D. Kelly, "CMOS based tunable matching networks for cellular handset applications," in *IEEE MTT-S International Microwave Symposium Digest (MTT)*, Jun. 2011.

[134] L. Huang and P. Russer, "Electrically tunable antenna design procedure for mobile applications," *IEEE Trans. Microwave Theory Tech.*, vol. 56, no. 12, pp. 2789 – 2797, Dec. 2008.

[135] K.-S. S. Ang and Y.-C. C. Leong, "Converting baluns into broad-band impedance-transforming 180° hybrids," *IEEE Transactions on Microwave Theory and Techniques*, vol. 50, no. 8, pp. 1990–1995, Aug. 2002.

[136] A. Krewski, W. L. Schroeder, and K. Solbach, "2-port DL-MIMO antenna design for LTE-enabled USB dongles," *IEEE Antennas and Wireless Propagation Letters*, vol. 12, pp. 1436–1439, Nov. 2013.

[137] X. Tang, K. Mouthaan, and J. Coetzee, "Tunable decoupling and matching network for diversity enhancement of closely spaced antennas," *IEEE Antennas and Wireless Propagation Letters*, vol. 11, pp. 268–271, 2012.

[138] *SEMCAD X ver. 14.6.1 Aletsch*, Schmid & Partner Engineering AG, Zurich, Switzerland, 2004-2011.

[139] J. Andersen and S. Berntsen, "Comments on "the foster reactance theorem for antennas and radiation Q"," *IEEE Transactions on Antennas and Propagation*, vol. 55, no. 3, pp. 1013–1014, Mar. 2007.

[140] R. Fante, "Quality factor of general ideal antennas," *IEEE Transactions on Antennas and Propagation*, vol. 17, no. 2, pp. 151–155, Mar. 1969.

[141] R. Hansen, *Electrically Small, Superdirective, and Superconducting Antennas*, 1st ed. Hoboken, New Jersey: A John Wiley & Sons, Inc., Publication, Jun. 2006.

[142] H. W. Bode, *Network Analysis and Feedback Amplifier Design*. New York: Van Nostrand, 1945.

[143] R. M. Fano, "Theoretical limitations on the broadband matching of arbitrary impedances," Massachusetts Institute of Technology, Tech. Rep. 41, Jan. 1948.

[144] A. Lopez, "Review of narrowband impedance-matching limitations," *IEEE Antennas and Propagation Magazine*, vol. 46, no. 4, pp. 88–90, Aug. 2004.

[145] *EMCoS Ltd., EMCoS Antenna VirtualLab, Version 1.0, www.emcos.com*.

[146] MATLAB, *version 7.10.0 (R2010a)*, The MathWorks Inc., Natick, MA, 1994–2013.

[147] M. Capek, P. Hazdra, P. Hamouz, and J. Eichler, "A method for tracking characteristic numbers and vectors," *Progress In Electromagnetics Research B*, vol. 33, pp. 115–134, 2011. [Online]. Available: http://www.jpier.org/pierb/pier.php?paper=11060209

[148] R. T. Maximov, C. L. Zekios, and G. A. Kyriacou, "MIMO antenna design exploiting the characteristic modes eigenanalysis," in *32nd ESA Antenna Workshop on Antennas for Space Applications*, Noordwijk, The Netherlands, Oct. 2010.

[149] S. M. Rao, D. R. Wilton, and A. W. Glisson, "Electromagnetic scattering by surface of arbitrary shape," *IEEE Transactions on Antennas and Propagation*, vol. AP-30, no. 3, pp. 409–418, May 1982.

[150] S. N. Makarov, *Antenna and EM Modelling with Matlab*. Wiley, Jul. 2002.

[151] B. Delaunay, "Sur la sphere vide," *Bulletin de l'Academie des Sciences de l'URSS*, no. 6, pp. 793–800, 1934.

[152] *X-45A UCAV 3D model*, http://thefree3dmodels.com, Nov. 2012.

[153] A. Krewski, "2-port MIMO antenna system for high frequency data link with UAVs using characteristic modes," in *IEEE Antennas and Propagation Society International Symposium (APSURSI)*, Orlando, FL, USA, Jul. 2013.

[154] A. W. Glisson, "On the development of numerical techniques for treating arbitrarily-shaped surfaces," Ph.D. dissertation, University of Mississippi, Jan. 1978.

[155] D. R. Wilton, S. S. M. Rao, and A. W. Glisson, "Electromagnetic scattering by arbitrary surfaces," Rome Air Development Center, Griffiss AFB, Tech. Rep. RADC-TR-79-325, Mar. 1980.

[156] S. U. Hwu and D. R. Wilton, "Electromagnetic scattering and radiation by arbitrary configurations of conducting bodies and wires," University of Houston, Tech. Rep. 1325, Aug. 1988.

[157] D. M. Pozar, *Microwave engineering, 3rd ed.* John Wiley & Sons, Inc, 2005.